Quantum dot devices in silicon and dopant-free GaAs/AlGaAs heterostructures

by

Brandon Buonacorsi

A thesis
presented to the University of Waterloo
in fulfillment of the
thesis requirement for the degree of
Doctor of Philosophy
in
Physics (Quantum Information)

Waterloo, Ontario, Canada, 2021

© Brandon Buonacorsi 2021

Examining Committee Membership

The following served on the Examining Committee for this thesis. The decision of the Examining Committee is by majority vote.

External Examiner:	Xuedong Hu Professor, Dept. of Physics, University at Buffalo
Supervisors:	Jonathan Baugh Associate Professor, Dept. of Chemistry, University of Waterloo
	Raymond Laflamme Professor, Dept. of Physics and Astronomy, University of Waterloo
Internal Member:	Kevin Resch Professor, Dept. of Physics and Astronomy, University of Waterloo
Internal-External Member:	Michael Reimer Assistant Professor, Dept. of Electrical and Computer Engineering, University of Waterloo
Other Member:	Na Young Kim Associate Professor, Dept. of Electrical and Computer Engineering, University of Waterloo

Author's Declaration

This thesis consists of material all of which I authored or co-authored: see Statement of Contributions included in the thesis. This is a true copy of the thesis, including any required final revisions, as accepted by my examiners.

I understand that my thesis may be made electronically available to the public.

Statement of Contributions

The following publications and preprints, of which I am the primary author, have been adapted into material for Chapters 2, 3, and 4 respectively of this thesis:

- **Buonacorsi, B.**, Cai, Z., Ramirez, E.B., Willick, K.S., Walker, S.M., Li, J., Shaw, B.D., Xu, X., Benjamin, S.C., and Baugh, J. (2019). Network architecture for a topological quantum computer in silicon. *Quantum Science and Technology, 4*(2), 025003.
- **Buonacorsi, B.**, Shaw, B., and Baugh, J. (2020). Simulated coherent electron shuttling in silicon quantum dots. *Physical Review B, 102*(12), 125406.
- **Buonacorsi, B.**, Korkusinski, M., Khromets, B., and Baugh, J. (2020). Optimizing lateral quantum dot geometries for reduced exchange noise. *arXiv preprint arXiv:2012.10512*.

Chapters 1, 5, and 6 are not directly based on a publication or preprint and were authored solely by myself. Chapters 2-5 begin with a detailed breakdown of the specific contributions to the material presented in each chapter.

Abstract

Single spin quantum dot qubits in silicon are a promising candidate for a scalable quantum processor due to their long coherence times, compact size, and ease of integration into existing fabrication technologies. Realizing a large quantum processor composed of thousands or more logical qubits requires the integration of conventional transistor circuitry and wiring interconnects to control each individual dot in the processor. The high density of control wiring required for these processors presents many engineering challenges. In this thesis, we propose a surface code quantum processor for silicon quantum dot qubits based on a node/network architecture. Local nodes consisting of just seven quantum dots are spatially separated on the order of microns to facilitate space for the necessary high density wiring. Entanglement is distributed between individual nodes via shuttling of entangled electron pairs throughout the network. X or Z stabilizer operations, necessary for operating the surface code, are realized by distributing three electron spin singlet pairs across four local nodes followed by local gate operations and ancilla measurements. Simulations of electron shuttling indicate that adiabatic transport is possible on timescales that do not bottleneck the processor speed. Phase rotation of the shuttled spin, induced by the Stark shift, can lower the overall shuttling fidelity; however, the error can be mitigated by proper electrostatic tuning of the stationary electron's g-factor. Using realistic noise models, we estimate error thresholds with respect to single and two-qubit gate fidelities as well as singlet dephasing errors during shuttling.

Electron shuttling is a key resource of the proposed network architecture. We continue the shuttling simulations by presenting an algorithm for finding constant-adiabatic shuttling control pulses, which enables a more rigorous study of how different conditions impact the shuttling speed and fidelity. These constant adiabatic pulses are used to optimize the physical device geometry to maximize charge shuttling speeds up to $\sim$300 nm/ns in the single-valley case. We then switch to an effective Hamiltonian representation where spin and valley degrees of freedom are accounted for during shuttling. Using realistic device and material parameters, shuttle speeds in the range $10-100$ nm/ns with high spin entanglement fidelities are obtained when the tunneling energy exceeds the Zeeman energy. High fidelity shuttling also requires the inter-dot valley phase difference to be below a threshold determined by the ratio of tunneling and Zeeman energies, so that spin-valley-orbit mixing is weak. In this regime, we find that the primary source of infidelity is a coherent spin rotation that is correctable, in principle, using single spin rotations.

Two-qubit gates in the network architecture are mediated by the exchange interaction, an interaction that stems from the Coulomb interaction but manifests as a rotation between the $|\uparrow\downarrow\rangle$ and $|\downarrow\uparrow\rangle$ two qubit states. Realizing fault tolerant two-qubit gates has proven diffi-

cult in silicon quantum dots due to charge noise which perturbs the electron orbitals states, causing decoherence. Quantitatively accurate modelling of exchange in general quantum dot networks is important towards realizing fault tolerant gates. Traditional modelling methods, such as a full configuration interaction approach, are cumbersome due to significant computational overhead required when accounting for the electron-electron interactions in the calculation. We present a modified linear combination of harmonic orbitals configuration interaction (LCHO-CI) approach which significantly reduces the computational time for obtaining quantitatively accurate estimations of exchange. The method works by approximating the single electron orbitals of the quantum dot network using an orthogonal basis of harmonic orbitals. This choice of orthogonal basis allows a pre-calculated library of matrix elements to be used in evaluating the Coulomb interactions, which speeds up the LCHO-CI calculation. The modified LCHO-CI approach is then used to study how the physical device geometry impacts the charge noise sensitivity of a double quantum dot system. We find that, in general, geometries which increase the dot charging energy and decrease the gate lever arms improve the system's sensitivity to charge noise.

We conclude this thesis by pivoting away from theoretical studies of silicon quantum dots and towards experimental studies of electron transport in dopant-free GaAs heterostructures. In modulation doped GaAs heterostructures, a doping layer is used to induce a two-dimensional electron gas (2DEG) at the heterojunction. Dopant-free GaAs lack the doping layer which makes fabrication more difficult as local electron reservoirs must be used to bring carriers and induce a 2DEG. The lack of the doping layer offers several advantages over modulation doped heterostructures, such as gate-ability of the 2DEG and ability to make ambipolar devices (both n- and p-type ohmic contacts). Realizing n- and p-type ohmic contacts requires etching a recess pit and depositing the ohmic material at an angle in order to preventing screening of the top gate when inducing a 2DEG or two-dimensional hole gas (2DHG). Magnetotransport experiments are used to characterize an induced 2DEG and 2DHG in a Hall bar fabricated on a 310 nm deep single heterojunction. The carrier mobility and density can be tuned using the top gate, and we achieve peak mobility values of 4.5×10^6 cm^2/Vs and 0.65×10^6 cm^2/Vs for the 2DEG and 2DHG respectively. We then move to a one-dimensional system and study electron transport through a quantum point contact. Conductance quantization is observed, and subband spectroscopy measurements indicate a 1D subband spacing of 4.5 meV. Finally, we study dynamically driven electron transport in a zero-dimensional system using a tunable-barrier quantum dot acting as a single electron pump. Single electron pumping is observed up to $T = 5$ K, and fits to the electron cascade model suggests pumping errors of 1.87 ppm when operated at a driving frequency of $f = 500$ MHz.

Acknowledgements

This thesis would not have been completed without the vast magnitude of support I have received throughout my time here. In particular, I am extremely grateful for the financial support provided to me from the University of Waterloo, the Institute for Quantum Computing, and Defence Research and Development Canada.

I would like to thank my supervisor, Dr. Jonathan Baugh, who provided constant support during my time here and allowed me to research such a diverse range of topics. I am privileged to have studied underneath such a great scientist and researcher. Additionally, I would like to thank my co-supervisor, Dr. Raymond Laflamme, who I enjoyed working with closely during my first few months here and was more than gracious when I asked to pivot my research towards silicon quantum dot devices.

I would also like to thank the members of my examination committee Dr. Kevin Resch, Dr. Michael Reimer, Dr. Na Young Kim, and Dr. Xuedong Hu for taking the time provide helpful comments and feedback on my research.

The work presented in this thesis would not have been possible with the extensive help I have received from members of the Coherent Spintronics Group at the University of Waterloo. Almost everything I know about nanofabrication, III-V physics, and experimental measurements comes from Dr. François Sfigakis, who has never ceased to challenge my thinking and has become a great friend. I am extremely grateful to my office mates Eduardo Barrera-Ramirez and Sean Walker for the extensive support they offered. I am additionally thankful to Dr. Greg Holloway, Dr. Kyle Willick, Annelise Bergeron, Bohdan Khromets, Kaveh Gharavi, Dr. Ferhat Aydinoglu, and Dr. Milad Khoshnegar who all have taught me something throughout my time in the CSG group.

I am also grateful to Dr. Lin Tian and Nachiket Sherlekar of the QPD group at the University of Waterloo who I had the joy of learning optics from. An extra thank you goes to Dr. Marek Korkusinski of the National Research Council who was very patient with me while learning the ins and outs of exchange calculations. Without him, there would be no Chapter 4 of this thesis.

I would like to thank my family for their love and support, specifically my mother, who was my very first educator back when I was homeschooled. Additionally my wife, Alicia, has provided never ending support and encouragement through every high and low of my Ph.D. I sincerely could not have done this without her help and guidance. My children, Asher and Oliver, turned every hard day into a good one with their excitement whenever I would come home from the lab.

Dedication

This is dedicated to Asher and Oliver, the best souvenirs I could have asked for during my time in Canada, and to Alicia, for her endless love, support, and encouragement.

Table of Contents

List of Tables xiii

List of Figures xiv

1 Introduction 1

1.1 Introduction . . . 1

1.2 Thesis Overview . . . 2

1.3 Background . . . 4

1.3.1 Electron transport through quantum dots . . . 4

1.3.2 Single spins in quantum dots as qubits . . . 10

1.3.3 An outlook on quantum dot spin qubits . . . 16

2 Network architecture for a topological quantum computer in silicon 20

2.1 Introduction . . . 20

2.2 Node/network surface code for quantum dots . . . 23

2.2.1 Stabilizer circuit . . . 26

2.2.2 Readout of the ancilla qubits . . . 29

2.2.3 Network layout . . . 32

2.3 Single electron transport . . . 34

2.3.1 Shuttling simulations . . . 35

2.3.2 Stark effect and singlet phase rotation error . . . 38

2.3.3 Stabilizer repetition rate and other considerations 41
2.4 Surface code error thresholds 43
2.4.1 Errors associated with the control-Z gate 44
2.4.2 Twirling 46
2.4.3 Threshold simulation results 46
2.5 Conclusions 50

3 Simulated coherent electron shuttling in silicon quantum dots 52
3.1 Introduction 52
3.2 Constant-adiabaticity control sequences 54
3.3 Charge shuttling 56
3.3.1 Modelling the electrostatic potential 57
3.3.2 Trade-off between fidelity and shuttle speed 59
3.3.3 Device geometry optimization 62
3.4 Spin and valley effects on electron shuttling 67
3.4.1 Valley-orbit Hamiltonian 67
3.4.2 Validity of the single valley approximation in charge shuttling . . . 69
3.4.3 The effective spin-orbit Hamiltonian 71
3.4.4 Spin-valley-orbit Hamiltonian 74
3.4.5 Spin transport simulations: $t_c > E_z$ 76
3.4.6 Spin transport simulations: $t_c < E_z$ 81
3.5 Discussion 84
3.6 Conclusions 88

4 Calculating the exchange interaction in lateral quantum dot networks 89
4.1 Introduction 89
4.2 The modified LCHO-CI method 92
4.2.1 Building single electron states in a quantum dot network using harmonic orbitals 92

4.2.2 Constructing the many-electron Hamiltonian 94
4.2.3 Choosing an optimal harmonic orbital basis 99
4.2.4 Comparison to Heitler-London and Hund-Mülliken methods 103
4.3 Charge noise sensitivity of a double quantum dot device 106
4.3.1 Device model 107
4.3.2 Charging energies and lever arms 110
4.3.3 Exchange calculations for different gate geometries 112
4.3.4 Zero bias potentials 121
4.4 Conclusion 123

5 Electron transport in dopant-free GaAs 125

5.1 Introduction 125
5.2 n- and p-type ohmic contacts to dopant-free GaAs single heterojunctions . 129
5.2.1 Overview of ohmic fabrication 130
5.2.2 Magnetotransport in a 2D system 134
5.2.3 Experimental results 138
5.3 Quantum point contacts in dopant-free GaAs single heterojunctions 142
5.3.1 Electron transport in 1D 143
5.3.2 1D subband spectroscopy of a quantum point contact 147
5.4 Single electron pumping in dopant-free GaAs single heterojunctions 152
5.4.1 Experimental results 156
5.5 Conclusions 161

6 Conclusions 163

6.1 Outlook and future work 165

References 168

APPENDICES 197

A Elliptical harmonic orbital Coulomb matrix elements **198**

B Fabrication recipes for dopant-free GaAs devices **202**

B.1 Sample cleaning 202
B.2 Mesa pattern 203
B.3 n-type ohmic contacts 204
B.4 p-type ohmic contacts 206
B.5 Oxide insulator and etching via holes 208
B.6 Top gate and bond pads 208
B.7 Electron beam lithography and metal deposition 209

List of Tables

4.1 Tunnel gate voltages at zero bias which yield $J = 1$ μeV for different double dot dimensions 122

List of Figures

1.1 Schematic of single quantum dot 5
1.2 Simulated current through a single quantum dot 7
1.3 Using a charge sensor to monitor a nearby quantum dot 9
1.4 Spin qubit initialization in a single quantum dot 11
1.5 Spin-to-charge conversion techniques for spin readout using a charge sensor 15

2.1 Schematic of spatial separation of a spin singlet state via shuttling 24
2.2 Sequence of steps in the stabilizer operation on four neighboring nodes . . 25
2.3 Device concept for a node 27
2.4 Explicit circuit diagram corresponding to one stabilizer cycle on a group of 4 nodes 30
2.5 Scheduling of the full stabilizer cycle 31
2.6 A method for reading out the ancilla qubits 32
2.7 Illustration of a proposed network layout showing a plaquette of four nodes and how they connect beyond to form a 2D surface code 33
2.8 Setup for the electron shuttling simulations 36
2.9 Adiabaticity threshold for a 3-dot shuttling simulation 37
2.10 Stark effect and singlet phase rotation error for the 3-dot shuttling simulation 39
2.11 Stark effect and singlet phase rotation error for the 3-dot shuttling simulation 42
2.12 Simplified diagram of the stabilizer check circuit 47
2.13 Twirling circuit for control-Z errors 47

2.14 Fault tolerance thresholds for $\sqrt{\text{SWAP}}$ gates 48
2.15 Fault tolerance thresholds for electron shuttling 49

3.1 Effect of a single electron on a self-consistent calculation of a double well potential 58
3.2 Schematic of a triple linear quantum dot chain with a simplified gate geometry 60
3.3 Constant-adiabatic shuttling pulse calculated for a linear triple dot system 61
3.4 Relationship between adiabatic parameter, final orbital state infidelity, and pulse length 62
3.5 Non-adiabatic and adiabatic electron shuttling simulations through a triple quantum dot chain 63
3.6 Orbital spacing versus plunger gate length 65
3.7 Optimizing simplified gate geometry for fast shuttling 66
3.8 Valley-orbit energy spectrum for a double quantum dot with single electron occupation 69
3.9 Fidelity of shuttling a charge with and without valley physics 71
3.10 Relationship between the ratio t_c/E_z and $\delta\phi_{\text{th}}$ 76
3.11 Shuttling one member of a singlet pair, for $t_c > E_z$ 78
3.12 Error due single-spin rotation during shuttling 80
3.13 Shuttling one member of a singlet pair, for $t_c < E_z$ 83
3.14 Shuttling one member of a singlet pair, for $t_c < E_z$ 85
3.15 Comparison of shuttling singlet infidelity for different spin-orbit coupling strengths 86

4.1 Approximating single electron states using harmonic orbitals 94
4.2 Optimizing choice of ω for LCHO-CI calculation 102
4.3 Comparison of Heitler-London and Hund-Mülliken methods to the LCHO-CI approach 105
4.4 Schematic of a double quantum dot gate geometry 108
4.5 Convergence of exchange with respect to basis size 109

4.6 Relationship between bias voltage and inter-dot detuning 111
4.7 Dependence of exchange on dot size 114
4.8 Dependence of exchange on tunnel gate width 116
4.9 Dependence of exchange on oxide thickness 118
4.10 Dependence of exchange on dot eccentricity 120
4.11 1D potential slices of the zero bias potentials 123

5.1 Band structure for modulation doped and dopant-free single heterojunctions 127
5.2 Ohmic contacts for modulation doped and dopant-free heterostructures . . 131
5.3 Ohmic contacts to deep and shallow dopant-free single heterojunctions . . 133
5.4 Landau levels and filling factors for a 2D system 137
5.5 Optical image of a Hall bar and schematic for a Hall measurement 139
5.6 Characterization of a n-type Hall bar in a 310 deep single heterojunction . 140
5.7 Characterization of a p-type Hall bar in a 310 deep single heterojunction . 143
5.8 Quantized conductance through a saddle point 1D potential. 146
5.9 Quantized conductance in an etched quantum point contact 148
5.10 Subband spectroscopy of an etched QPC 150
5.11 SEM image of a single electron pump 153
5.12 Operation of a tunable-barrier single electron pump 155
5.13 Single electron pumping at different driving frequencies 157
5.14 Two-dimensional pump map at 500 MHz 159
5.15 Temperature dependence of single electron pumping 161

Let us hold fast the confession of our hope without wavering, for He who promised is faithful.

-*Hebrews 10:23*

Chapter 1

Introduction

1.1 Introduction

There has been significant interest in utilizing quantum mechanics to realize novel technologies for metrology [85, 254], communications [86], sensing [169, 52], and computing [195]. Quantum computers are believed to be capable of solving a set computational problems much faster than could be done on a classical computer, such as prime number factorization [240], database search [93], and simulation of quantum materials [67]. Classical computers work by performing gate operations on a regular bit of information, which can be stored in either a 0 or 1 state. Quantum computers utilize quantum superposition to encode quantum bits (i.e. qubits) as a superposition of both 0 and 1 states. Other quantum phenomena, such as entanglement and interference, give quantum computers unique properties that enable them to outperform their classical counterparts. Quantum computers are getting closer to demonstrating 'quantum supremacy', where a quantum computer performs a particular computational task faster than ever could be possible on a classical computer. Recently, quantum supremacy has been claimed for a computation involving pseudo-random quantum circuit sampling [3]. Such milestones will become only more commonplace in the upcoming years as quantum technologies continue to mature.

There are numerous implementations for realizing a quantum processor including superconducting circuits [40, 272, 78], nuclear magnetic resonance [45, 171], optical systems [144], trapped ions [97], topologically protected states [232], diamond nitrogen vacancies [37], phosphorus donors in silicon [129, 211], spins in quantum dots [170, 142], and more not listed here. Each implementation has its own advantages and disadvantages which typically revolve around the ability scale to larger qubit systems or difficulties in achiev-

ing high qubit gate fidelities. The particular implementation focused on in this thesis is spins in quantum dots. Quantum dots are regions where electrons (or holes) are trapped in a zero-dimensional system, confined in all three spatial directions [99]. Quantum dots are very small, ranging from 10s to 100s nm in size depending on the material system, which enables dense packing of these qubits within a quantum processor. The tight confinement of the dot gives rise to discrete energy levels forming *s*-, *p*-, *d*-, orbital 'shells'. Electron fill these shells according to Hunds rule leading quantum dots to often be referred to as 'artificial atoms' [38, 162]. The number of electrons occupying the a quantum dot can be precisely tuned from ∼100 electrons down to just a single electron. For quantum information purposes, dots are typically operated in the single to few electron regime.

In this thesis, we focus on quantum dots that are formed laterally in a semiconductor heterostructure using electrostatic gates. A heterostructure consists of two or more different semiconductor materials stacked on top of each other, such as Si/SiO_2 or GaAs/AlGaAs. By bending the band structure of these materials, either though electrostatic gating or doping of the material system, a thin conductive layer of free electrons can become trapped in a 2-dimensional plane along the interface of the host materials. The free electrons in the conductive layer behave like a gas and as such, are referred to as a two-dimensional electron gas (2DEG). Gate electrodes deposited on top of the heterostructure can be used to locally tune the potential landscape to reduce the system from 2D to 0D, forming a quantum dot. By manipulating the voltages applied to these gate electrodes, the quantum dots and the electrons within them can be electrostatically controlled.

1.2 Thesis Overview

The rest of this chapter provides an introduction of electron transport through quantum dots, followed by a brief discussion of how single electron spins in dots can be used as qubits. This is by no means a comprehensive introduction into the fundamentals of quantum dot systems, and additional material can be found in the reviews of Hanson *et al.* [99], Van der Wiel *et al.* [262], Kloeffel *et al.* [142], Kouwenhoven *et al.* [150], and Zwanenburg *et al.* [295] where the last one focuses specifically on silicon quantum devices.

Chapter 2 presents a proposal of a node/network architecture for a scalable quantum processor using silicon quantum dot spin qubits. Individual nodes in the network are composed of seven quantum dots, and nodes are separated on the order of microns to open up space for electronic wiring and classical control circuity. Neighboring nodes are connected via linear chains of empty quantum dots which facilitate entanglement distribution by shuttling electrons from singlet pairs between nodes. A circuit for realizing X and Z stabilizer

operations, which are necessary for implementing the surface code, is presented in terms of elementary quantum dot qubit operations. One of these elementary operations, inter-node electron shuttling, is simulated to study how fast shuttling operations can occur while still maintaining adiabatic evolution of the electron state. Surface code error thresholds for the network are calculated using noise models for single and two-qubit gate errors as well as spin dephasing errors accumulated during shuttling.

Chapter 3 significantly expands upon the electron shuttling simulations done in the previous chapter. Electrons are shuttled by sequential tunneling through a linear quantum dot array where each quantum dot is formed using a simplified gate geometry. A method for finding constant-adiabatic shuttling pulses is introduced which allows for systematic comparison of shuttling speeds and fidelities across different device geometries and material parameters. Constant-adiabatic shuttling pulses are used to optimize the dimensions of the simplified gate geometry in order to maximize the shuttling speed. Bulk silicon has six-fold degenerate conduction band minima termed as "valleys" which, for a lateral quantum dot, reduces to a two-fold nearly degenerate valley system. The interplay between the orbital, valley, and spin degrees of freedom is highly relevant to silicon, as it can cause mixing and decoherence during shuttling. The shuttling simulations are extended to include valley and spin physics using an effective Hamiltonian representation. We find that high fidelity singlet shuttling can occur when the inter-dot tunnel coupling is larger than the Zeeman splitting and when the valley phase difference between adjacent quantum dots is below a threshold value, given by the ratio of tunnel coupling and Zeeman splitting.

Chapter 4 presents work done on modelling the exchange interaction in quantum dot networks. The exchange interaction can be used to implement two-qubit gates, a necessary part of operating the network architecture introduced in Chapter 2. We introduce a modified linear combination of harmonic orbitals/configuration interaction (LCHO-CI) approach for solving the many-electron eigenstates of the quantum dot network. The resultant many-electron spectra is mapped to an effective Heisenberg representation to extract the individual electron pairwise exchange interaction strengths. In the modified LCHO-CI approach, an orthogonal basis of harmonic orbitals is used to approximate the single electron states. This choice of basis significantly reduces the computation time of the CI calculation by enabling a pre-calculated library of matrix elements to be used when evaluating the Coulomb interactions. Additionally, we show how the harmonic orbital basis can be optimized to improve the accuracy of the LCHO-CI calculation without hindering the total calculation time. We use the modified LCHO-CI method to calculate exchange in a silicon double quantum dot device occupied by two electrons. The full 3D device structure is modelled, including the physical gate geometry and Si/SiO_2 heterostructure. The speed of the modified LCHO-CI calculations enables us to systematically study how the

device's geometric parameters impact the system's sensitivity to charge noise fluctuations, an important decoherence mechanism for quantum dot spin qubits.

Chapter 5 switches focus from applied theoretical studies of silicon quantum dots to focusing on experimental studies of electron transport in dopant-free GaAs material systems. The highlight of the chapter is a demonstration of single electron pumping using a dynamically driven quantum dot in dopant-free GaAs. However, the quantum dots are not made with quantum information processing in mind but rather for novel quantum optics and communications applications. The chapter begins by discussing the benefits of dopant-free systems compared to intentionally doped heterostructures. The biggest challenge with using dopant-free GaAs is forming high quality ohmic contacts to an induced 2DEG at the GaAs/AlGaAs interface. 2D magnetotransport data for a deep single heterojunction demonstrates good ohmic contacts to these structures as well as the presence of an induced conductive layer of electrons and holes. Next, 1D electron transport is studied using an etched quantum point contact. Quantized conductance is observed, and bias spectroscopy measurements show how the 1D subband spacing can be tuned as high as 4.5 meV using the top gate. Lastly, non-adiabatic electron transport is studied in a 0D system using a tunable-barrier single electron pump. When the pump is driven by an AC signal, a small integer number of electrons can be pumped through the device every cycle with high accuracy and reproducibility. Non-adiabatic pumping is observed at driving frequencies from 100 MHz to 900 MHz at relatively high cryogenic temperatures of $T = 1.4$ K. Fits to the electron cascade model suggest a pumping accuracy comparable to state of the art single electron pumps in GaAs at similar frequencies. This device is the very first demonstration of single electron pumping in a dopant-free GaAs system.

1.3 Background

1.3.1 Electron transport through quantum dots

We begin with a brief introduction of electron transport in quantum dots. Much of this section is based on the introduction in the thesis of Holloway [109]. To start, we consider just a single quantum dot that is coupled to source and drain leads, shown schematically in Figure 1.1. The source and drain leads are capacitively coupled to the quantum dot which forms tunnel barriers. The source and drain leads act as reservoirs for electrons to tunnel into and out of the quantum dot. These reservoirs can be used to initialize and measure electron spin states for quantum information purposes, as discussed in Section 1.3.2. An additional metal gate electrode with voltage V_g is capacitively coupled to the quantum

dot with strength C_g. V_g enables tuning of the energy levels within the quantum dot. Electrons fill the lowest energy states of the source and drain up to the respective chemical potentials of the leads μ_S and μ_D. By applying an external bias voltage V_{bias} to the leads, these chemical potentials can be shifted according to $eV_{\text{bias}} = \mu_S - \mu_D$. The quantum dot chemical potential $\mu(N) = U(N) - U(N-1)$ specifies the energy required to add an Nth electron to the dot, where $U(N)$ is the total energy of the quantum dot when occupied by N electrons. When $\mu(N)$ lies below μ_S and μ_D, electrons occupy the first N states of the quantum dot.

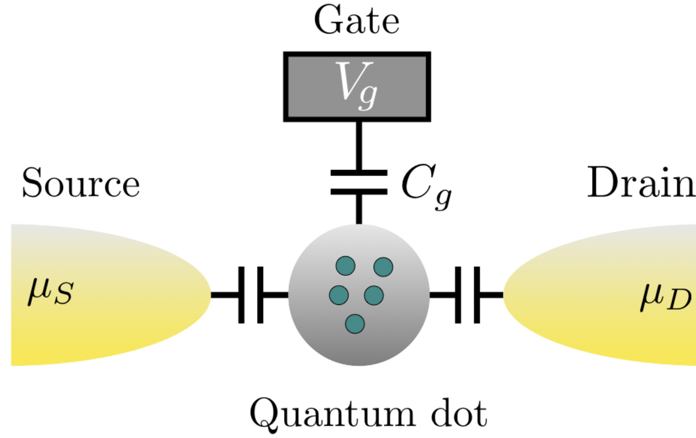

Figure 1.1: Schematic of a single quantum dot coupled to a source and drain reservoir as well as a nearby gate. Each reservoir has a corresponding chemical potential μ, and the gate voltage V_g is capacitively coupled to the dot with strength C_g.

Evaluating $\mu(N)$ from first principles is non-trivial. A good model for $\mu(N)$ can be found using the semi-classical constant interaction approach [262], which gives

$$\mu(N) = E_N + \frac{e^2(N - N_0 - 1/2)}{C} - \frac{eC_gV_g}{C} \tag{1.1}$$

where E_N is the orbital energy of the Nth electron, N_0 is the number of electrons occupying the quantum dot when $V_g = 0$ V, and C is the self-capacitance of the quantum dot. The tight confinement of the quantum dot can be treated as small 3D box, giving rise to orbital energies of the form

$$E_{\text{orb}} = \frac{\hbar^2\pi^2}{2m^*}\left(\frac{n_x}{L_x} + \frac{n_y}{L_y} + \frac{n_z}{L_z}\right) \tag{1.2}$$

where m^* is the effective mass of the electron in the host material, n_i corresponds to an orbital mode along each spatial direction, and L_i are the effective confinement length scales. We will denote the orbital energy $E_{\text{orb}}(n_x, n_y, n_z)$ of the Nth electron in the dot as E_N. The amount of energy required to add an electron to the quantum dot is simply

$$E_{\text{add}} = \mu(N) - \mu(N-1) = E_N - E_{N-1} + e^2/C \tag{1.3}$$

where the last term, e^2/C, is the quantum dot's charging energy, typically denoted as E_C. E_C accounts for the Coulomb repulsion energy that electrons need to overcome when being packed within such a tight space. Usually, the physical size of a quantum dot makes $E_C \gg E_{\text{orb}}$ so that $E_{\text{add}} \approx E_C$.

When a bias voltage is applied to shift μ_S and μ_D, $\mu(N)$ can be tuned to fall within the bias window where the quantum dot is no longer in a equilibrium charge configuration. An electron can tunnel from the source, into the accessible N^{th} dot state, and then back out of the dot into an unoccupied state in the drain. As this process repeats, a finite current is produced through the device. However, if $\mu(N)$ lies outside of the bias window, then electron tunneling through the dot is suppressed, and there is no current flow. As this effect is mainly caused by $E_{\text{add}} \approx E_C$, the current suppression is referred to as Coulomb blockade. The current through the quantum dot is given as

$$I = e\Gamma_0 \sum_N f(\mu(N) - \mu_S) - f(\mu(N) - \mu_D) \tag{1.4}$$

where $f(\mu) = [1 + \exp(\mu/k_B T)]^{-1}$ is the Fermi function with temperature T and Γ_0 is the electron tunneling rate through the dot barriers [8]. The tunnel rate Γ_0 is an average of the individual source and drain barrier tunneling rates $\Gamma_0 = \Gamma_S\Gamma_D/(\Gamma_S + \Gamma_D)$. Current through the device can be controlled three ways. The first is the applied bias voltage V_{bias}. By increasing V_{bias}, the bias window opens bringing more states, $\mu(N)$, within the window allowing for conduction through the device. The second control parameter is temperature. At higher temperatures there are free electrons with energy $> \mu_{S/D}$ and unoccupied states with energy $< \mu_{S/D}$ in the source and drain. This broadens the bias window and smears the resolution of when current is and is not blocked through the dot. The third and final parameter is V_g, which directly controls $\mu(N)$ as described in Equation 1.1. By changing V_g, $\mu(N)$ can be shifted to lie in and out of the bias window, controlling when current flows through the dot.

Figure 1.2a shows simulated current through a single quantum dot as a function of V_{bias} and V_g. The simulation parameters are $E_C = 10$ meV, $T = 1$ K, $C_g = 0.1$C, and $\Gamma_0 =$ 1 GHz. Diamond-like regions of Coulomb blockade (i.e. Coulomb diamonds) correspond

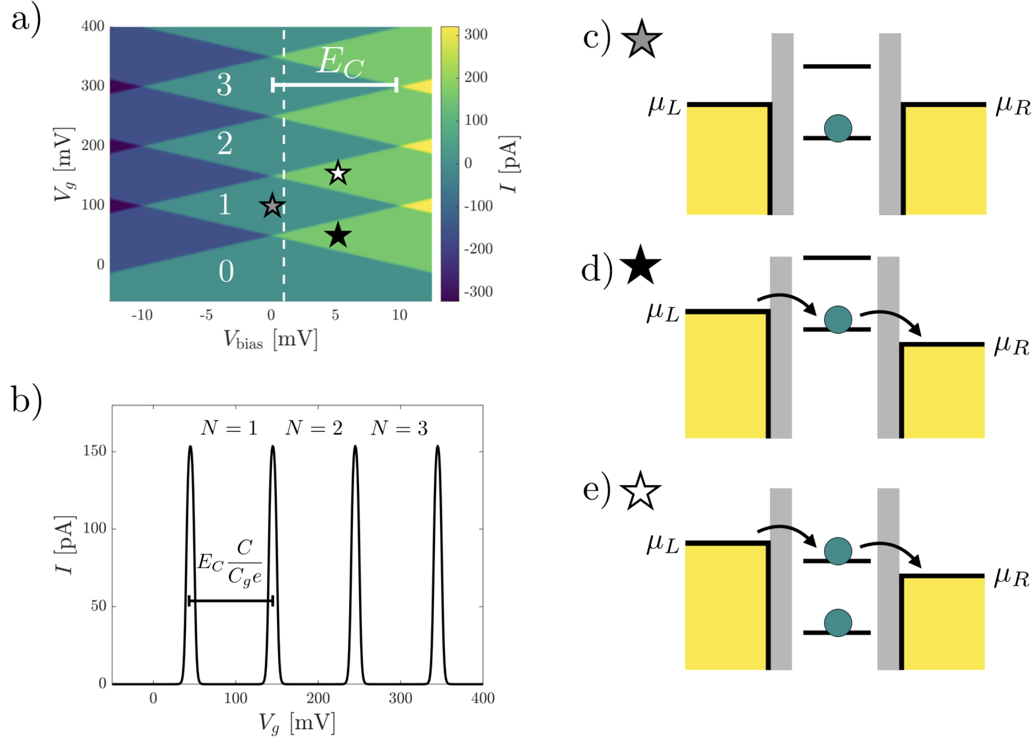

Figure 1.2: Simulated current through a single quantum dot coupled to two electron reservoirs with chemical potentials μ_L and μ_R. Simulation parameters are $E_C = 10$ meV, $T = 1$ K, $C_g = 0.1$C, and $\Gamma_0 = 1$ GHz. a) Coulomb diamonds when $V_{\rm bias}$ and V_g are swept. When no energy levels lie within the bias window, current is suppressed. As the bias increases and dot energy levels are brought within the window, electrons can tunnel from the left reservoir, into the dot, and out into the right reservoir producing current. Numbers indicate the electron occupancy of the quantum dot as a function of V_g. The width of the Coulomb diamond directly gives the dot charging energy E_C. b) Current versus V_g at $V_{\rm bias} = 1$ mV. Peaks in the current correspond to an additional electron tunneling onto the quantum dot. The spacing between peaks is related to E_C by the dot capacitance C and gate capacitance V_g. c-e) Schematics of the dot energy diagrams at different bias and gate voltage configurations taken from a).

to where no energy levels $\mu(N)$ lie within the bias window and current is suppressed. As V_g increases, each diamond indicates where an additional electron has tunneled onto the quantum dot. The respective quantum dot occupancy in each diamond is appropriately

labelled in the figure. The width of the Coulomb blockade diamonds directly gives the charging energy, providing an easy way to experimentally determine E_C. Figure 1.2b shows a 1D slice of the simulated current along $V_{\text{bias}} = 1$ mV to highlight the Coulomb blockade peaks as V_g is swept. Each peak corresponds to an additional electron tunneling onto the dot. The peak broadness is a function of both the temperature T of the electron reservoir as well as V_{bias}. At very small V_{bias}, the conductance peaks ($G = I/V$) can be fit to the expression

$$G = \frac{e^2}{h}\frac{A}{k_B T}\,\text{sech}^2\left(\frac{\alpha(V_g - V_0)}{2k_B T}\right) \tag{1.5}$$

where A is an amplitude fitting constant, α is the lever arm between V_g and the energy of the dot, V_0 is the voltage location of the peak height, and T is the estimated temperature of the electron reservoir. In the lab, heating from wiring lines or noise in the signal can raise the effective temperature of the electron reservoir above the cryostat base temperature where the device is being measured. Higher T will smear the resolution of the current measurements discussed above, and characterizing T is an important step in assessing the quality of the cryogenic measurement setup. Figures 1.2c-e show schematics of the dot's energy spectra at different bias and gate voltage configurations when current is allowed and suppressed through the device. The measurements outlined in Figure 1.2 can be used to find which voltage configurations tune the quantum dot to the regime where a single electron occupies the dot, which is relevant for quantum computing purposes.

Our above discussion has assumed the system parameters such as C_g and Γ_0 are constant in the system. In reality, both C_g and Γ_0 depend on the gate voltages that define the quantum dot system. As a quantum dot approaches the single electron occupancy regime, the tunnel rate Γ_0 through the quantum dot will fall. This is because as V_g is lowered, the barrier height between the dot and the source and drain leads is indirectly increased. As Γ_0 decreases, so does the magnitude of the current through the quantum dot. Generally at small electron occupancies, it is not possible to directly measure the current through the quantum dot due to its small magnitude. Therefore, in order to tune the quantum dot down to the single electron regime, we must utilize a charge sensor. The charge sensor is another quantum dot physically located nearby the dot of interest. The close proximity capacitively couples the two dots together as shown schematically in Figure 1.3a. The charge sensor is tuned to a higher electron occupancy regime where the tunnel rate Γ_0 through the sensor is large enough so that the sensor current I_{sensor} can be directly measured. When the charge sensor is tuned along the edge of a I_{sensor} Coulomb peak as shown in Figure 1.3b, the charge sensor becomes sensitive to electrostatic fluctuations in the surrounding environment. As electrons in the dot of interest tunnel on or off of the quantum dot, the charge sensor's energy is perturbed and a measurable change in I_{sensor} is recorded. The amplitude of

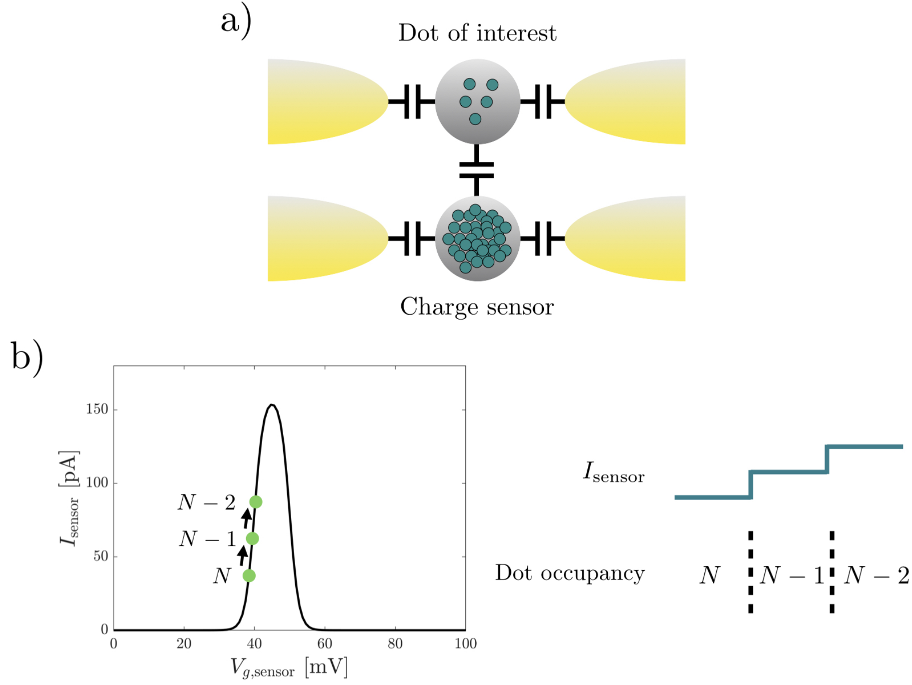

Figure 1.3: Using a charge sensor to monitor a nearby quantum dot. a) Schematic showing two quantum dots (grey) capacitively coupled together. Both dots are capacitively coupled to two electron reservoirs (yellow). The dot of interest is in a low electron occupancy regime with low tunneling rate Γ_0 where the current is too small to directly measure. The charge sensor is in a higher electron occupancy regime where the tunneling rate Γ_0 is high so that the current I_{sensor} can be resolved. b) A simulated Coulomb blockade peak for the charge sensor dot using the same dot parameters as Figure 1.2. The sensor is tuned along the edge of a Coulomb blockade peak making it sensitive to nearby electrostatic fluctuations. As electrons tunnel off of the dot of interest, the effective voltage on the charge sensor increases, shifting I_{sensor}. The right schematic indicates how I_{sensor} increases step-wise with the change in electron occupancy of the dot of interest.

those perturbations is proportional to the strength of the capacitive coupling between the dot and charge sensor. In this way, the charge sensor can monitor the dot of interest's electron occupancy down to the last electron. This ability of the charge sensor to be able to detect single charge events of dot can be utilized for spin readout as will be discussed in Section 1.3.2.

1.3.2 Single spins in quantum dots as qubits

There are several methods for encoding spins in quantum dots into a logical qubit including singlet-triplet [178, 274], hybrid [137], exchange-only [58, 221], and single-spin. In this thesis we focus on the most straightforward of the possible encodings, the single-spin qubit, first proposed by Loss and DiVincenzo [170]. The quantum processor consists of a lattice network configuration of many quantum dots coupled together each occupied by a single electron. By applying a large static magnetic field B_0, the Zeeman effect lifts the spin degeneracy forming a two-level qubit system where the logical qubit states $|0\rangle$ and $|1\rangle$ correspond to the spin states $|\uparrow\rangle$ and $|\downarrow\rangle$.

The rest of this section provides a brief introduction into four fundamental operations for these qubits: initialization, single-qubit rotations, two-qubit rotations, and measurement. While these techniques described are applicable to both silicon and GaAs material systems, our terminology will center around silicon quantum dot devices as they are the focus of Chapters 2, 3, and 4. Silicon has two distinct advantages over GaAs in its ability to realize quantum dot spin qubits. First, GaAs has many nuclear spins which can couple to the electron via the hyperfine interaction and decohere the spin state. While natural silicon has an abundance of the ^{29}Si, a spin $+\frac{1}{2}$ isotope, silicon can be purified to only have ^{28}Si, creating a nuclear spin 'vacuum' which significantly increases the coherence time of silicon spin qubits. Secondly, GaAs's zinc-blende lattice structure has bulk inversion asymmetry. This creates a strong spin-orbit coupling in GaAs and is a dominanting mechanism for spin relaxation [63, 233]. Silicon has no bulk inversion asymmetry; however, structural inversion asymmetry arises at the interface where the quantum dot is formed which causes a non-zero, but far weaker, spin-orbit coupling compared to GaAs [99, 295].

Qubit initialization

Qubits can be easily initialized into a quantum dot by coupling to an electron reservoir, as discussed in Section 1.3.1. Figure 1.4a shows the procedure for initializing a spin-up $|\uparrow\rangle$ (logical $|0\rangle$) state. The dot is tuned such that the chemical potential of the electron reservoir, μ, falls in between the ground and excited spin states. The black outline of the yellow region depicts the energy distribution of electrons in the reservoir. At $T = 0$ K, electrons do not have high enough energy to tunnel into the excited spin state $|\downarrow\rangle$ and instead only initialize into the ground spin state $|\uparrow\rangle$. The probability of initializing into $|\uparrow\rangle$ depends both on the magnitude of the Zeeman splitting E_z as well as the effective electron temperature of the reservoir. E_z is given as $E_Z = g\mu_B B_0$ where $g \approx 2$ is the electron g-factor and μ_B is the Bohr magneton. Typically $|B_0|$ is on the order of $\sim$1 T giving $E_z \approx$

110 μeV. The magnitude of E_z sets an upper bound on the allowable temperature of the reservoir. If the thermal energy $k_BT \approx E_z$, then some electrons in the reservoir have a high enough energy to load into the excited spin state as shown in Figure 1.4b. By reducing T so that $k_BT \ll E_z$, the $|\uparrow\rangle$ state can be initialized with high probability. Due to the small magnitude of E_z, T must be tens of mK, usually achieved using a dilution refrigerator.

In a large quantum dot network, it is not practical to couple reservoirs to every single dot in the network. Adding reservoirs takes up an important amount of physical space on the chip as well as introduces extra charge noise from each reservoir. In reality, only a subset of dots in the network need to be coupled to a reservoir. Electrons can be initialized in those reservoir-coupled dots and then moved elsewhere by sequential tunneling through dots in the network. In principle, as long as a quantum dot is decoupled from an electron reservoir, there is no strict requirement that $k_BT \ll E_z$ in order to operate the spin qubits. Recent experiments have demonstrated 'hot' quantum dot qubits above 1 K where cryogenic cooling requirements are eased [283, 206, 207].

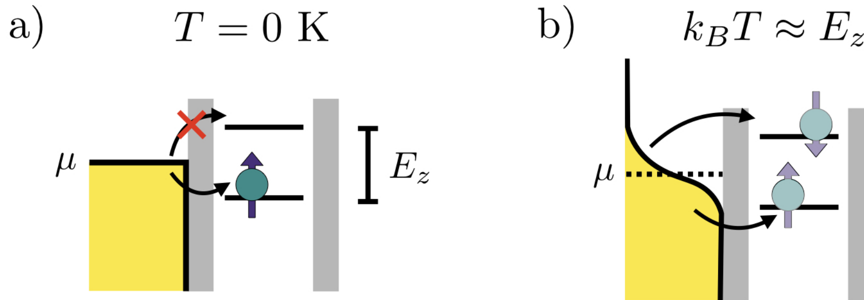

Figure 1.4: Spin qubit initialization in a single quantum coupled to an electron reservoir. The dot is tuned so that the chemical potential of the reservoir, μ, lies in between the $|\uparrow\rangle$ and $|\downarrow\rangle$ spin states. Both spin states are separated in energy by the Zeeman splitting $E_z = g\mu_B|B|$. The black outline of the yellow region corresponds to the energy distribution of electrons in the reservoir. a) At $T = 0$ K, electron tunneling into the excited spin state is suppressed, and electrons only only initialize into the ground $|\uparrow\rangle$ state. b) When the thermal energy of the reservoir is comparable to the Zeeman splitting, there is a non-zero probability of electrons tunneling into the excited $|\downarrow\rangle$ state.

One useful feature of quantum dots is their inherent ability to initialize entangled two-qubit states. When two electrons from a reservoir are loaded into a single quantum dot, they load into the same ground orbital state of the quantum dot. The Pauli exclusion principle prevents two spins of the same species from being loaded, and the electrons load

into the entangled spin singlet state $|S\rangle = \frac{1}{\sqrt{2}}(|\uparrow\downarrow\rangle - |\downarrow\uparrow\rangle)$. By tunneling one electron from the pair into a neighboring quantum dot, a distributed entangled qubit can be realized. This behavior is heavily utilized in our proposal for a scalable quantum dot processor outlined in Chapter 2.

Single-qubit rotations

A standard method for realizing single-spin qubit rotations is microwave-driven electron spin resonance (ESR) [211, 267, 269, 280]. The static magnetic field B_0 causes a precession of the electron spin. By applying an on-resonance microwave field B_1 perpendicular to B_0, the spin state can be driven between the $|\uparrow\rangle$ and $|\downarrow\rangle$ states. The precession frequency of the electron is determined by B_0 and tends to be on the order $\sim$10s of GHz. The microwave pulse can be generated either by sending power to a resonant cavity or by using an impedance matched microstrip line placed directly near the quantum dot. Using resonant cavities has proven difficult as generating a large B_1 induces a strong microwave electric field which enables photon assisted tunneling of the electron out of the dot [151, 249]. Microstrip lines placed within a few hundred nanometers of the quantum dot require less power, thereby suppressing photon assisted tunneling. However, microstrip lines tend to be bulky, taking up valuable physical space and can only control a local set of nearby quantum dots in the network. Nevertheless, microstrip lines have been used to demonstrate very high fidelity single-qubit gates >0.999 [280]. As the microwave pulse is applied perpendicular to the B_0 field, ESR can can only implement directly X and Y qubit rotations. Z gates can be achieved either by changing the reference frame of the system or by composing X and Y gates.

Local dot disorder causes the electron g-factor to vary from each dot to dot [122]. This is advantageous as it enables individual addressability of each quantum dot in the network. However, realizing global control proves problematic as it is difficult to realize a pulse with wide bandwidth while maintaining uniformly high fidelity. The small but non-zero spin orbit coupling in silicon allows the g-factor to be electrostatically tuned through the Stark shift [267]. This allows quantum dots to be brought on and off resonance with the microwave pulse enabling on-demand individual and global control.

Electron spin dipole resonance (EDSR) uses electric microwave pulses as an alternative approach for single-spin rotations [179, 44]. Electric fields couple to the qubit's spin through the spin-orbit interaction to drive rotations. In silicon, only holes have a sufficiently strong enough spin-orbit interaction to realize fast spin rotations. For electrons, the spin-orbit coupling is too weak. Strong enough microwave electric fields can be brought directly to the qubit by using one of the nearby metal gates defining the quantum dot [197, 167],

providing individual addressability. For electrons, a strong effective spin-orbit interaction can be realized by using a micromagnet [249, 271, 286, 133]. The micromagnet creates a magnetic field gradient with perpendicular and parallel fields akin to a strong effective spin-orbit interaction. Micromagnets are large compared to the quantum dot size and must be deposited as a final step on top of the device structure, thereby covering a cluster of nearby quantum dot qubits. While EDSR easily allows for individual addressibility, the magnetic field gradients are not tunable after depositing the micromagnet, nor easily reproducible, and variation from micromagnet to micromagnet on the same processor will require calibration. Additionally, the stray fields from the micromagnet will perturb the rotation axis of the qubit if the micromagnet is not properly aligned with the B_0 field. The introduction of the effective spin-orbit interaction means the qubits are more sensitive to charge noise and will decrease the qubit's coherence time [13].

Two-qubit rotations

Quantum dot qubits have a natural mechanism for implementing entangling two-spin quantum gates through the exchange interaction [269, 287, 271, 116, 276]. This interaction, with strength J, is a function of tunnel coupling as well as the energy detuning between neighboring quantum dots. While the interaction arises from the Coulomb interaction, it manifests as a rotation between the $|\uparrow\downarrow\rangle$ and $|\downarrow\uparrow\rangle$ two-qubit spin states. Since tunnel coupling and detuning can be controlled electrostatically using gates that define the quantum dot, J and the corresponding two-spin gates can be controlled electrostatically. The size of J enables π rotations of the entangling gates in the subnanosecond range [178]. Direct application of the exchange interaction results in a $\sqrt{\text{SWAP}}$ quantum gate but requires high bandwidth lines for proper control at the fastest frequencies [116]. For the logical quantum gates control-Z or CROT, extra single-spin gates must be used in tandem with the exchange interaction. In the original Loss-DiVincenzo proposal for quantum dot qubits, the control-Z was proposed using three single-spin and two $\sqrt{\text{SWAP}}$ gates [170]. However, the control-Z can also be directly implemented by creating a difference in Zeeman energy between the two quantum dots and have an exchange interaction of lesser or comparable strength. The ΔE_z can either be realized using a micromagnet as shown experimentally in Watson *et al.* [271] or through the Stark shift as in Veldhorst *et al.* [269].

Two-spin operations are significantly faster than single-spin operations. There are proposals for exchange-only quantum dot qubits which use only the exchange interaction for universal control of logical qubits, allowing for very fast processor speeds in principle [58]. The single-spin qubit requires a combination of both J and single-spin gates, so the logical two-qubit gates will be limited by the slower single-spin operations. Two-qubit gates

have only recently obtained high enough fidelities of 98.0% to allow for characterization using randomized benchmarking techniques, indicating that both single-spin and two-spin quantum gates are approaching fault tolerance levels for quantum computing [116, 276]. The difficulty in realizing high fidelity two-spin gates stems from the exchange interaction's sensitivity to charge noise, which perturbs both the detuning and tunnel coupling between the quantum dot qubits [50, 56]. Reducing charge noise's effect on the qubit can be done through operating the qubits near the symmetric operating point which makes the qubit first order insensitive to charge noise [221, 177]. Furthermore, the impact of the charge noise can be reduced using appropriately designed control pulses [29, 94] and refocusing composite pulses [64]. Charge noise can induce correlated errors on the qubits which can adversely affect fault tolerant encoding protocols [251]; however, we show in Chapter 2 that the SWAP error in the $\sqrt{\text{SWAP}}$ gate can be converted to Pauli noise through twirling. The exchange interaction and its sensitivity to charge noise is one of the focuses of Chapter 4.

Qubit Measurement

Directly measuring the spin of a single electron is challenging due its small magnetic moment. The most commonly used method for spin readout relies on converting the electron spin state into a unique charge configuration which can in turn be measured using a charge sensor [212, 281, 184]. One drawback in charge sensing is the need for dynamic control over the tuning of the charge sensor in order to maintain an optimal charge sensitivity throughout a wide voltage range measurement [281]. The first spin-to-charge conversion technique discussed is spin-dependent tunnelling as shown in Figure 1.5a [63]. When the quantum dot is coupled to an electron reservoir, the dot's energy levels can be pulsed so that the chemical potential of the reservoir μ lies between the two spin energy levels. If the electron is in the ground $|\uparrow\rangle$ state, it cannot tunnel out of the dot. As the charge configuration of the dot remains unchanged, so does the charge sensor's current I_{sensor}. On the other hand, if the dot is in the excited $|\downarrow\rangle$ state, then the electron can tunnel out of the quantum dot into the reservoir. I_{sensor} will response to the change in the electrostatic environment with a change in the sensor current. After the electron has tunneled out of the dot, a new electron can tunnel into the ground state which returns I_{sensor} to it's idle configuration. The main disadvantage of this readout technique is that the electron and the spin state is lost when the measured electron tunnels into the reservoir.

An alternative approach, which does not require the electron to be lost to the reservoir, employs Pauli spin blockade in a double quantum dot system [157], schematically shown in Figure 1.5b. Two electrons in a double quantum dot system form either a singlet or one of three triplet spin states corresponding to $S_z = -1$, 0, or +1. When the ground

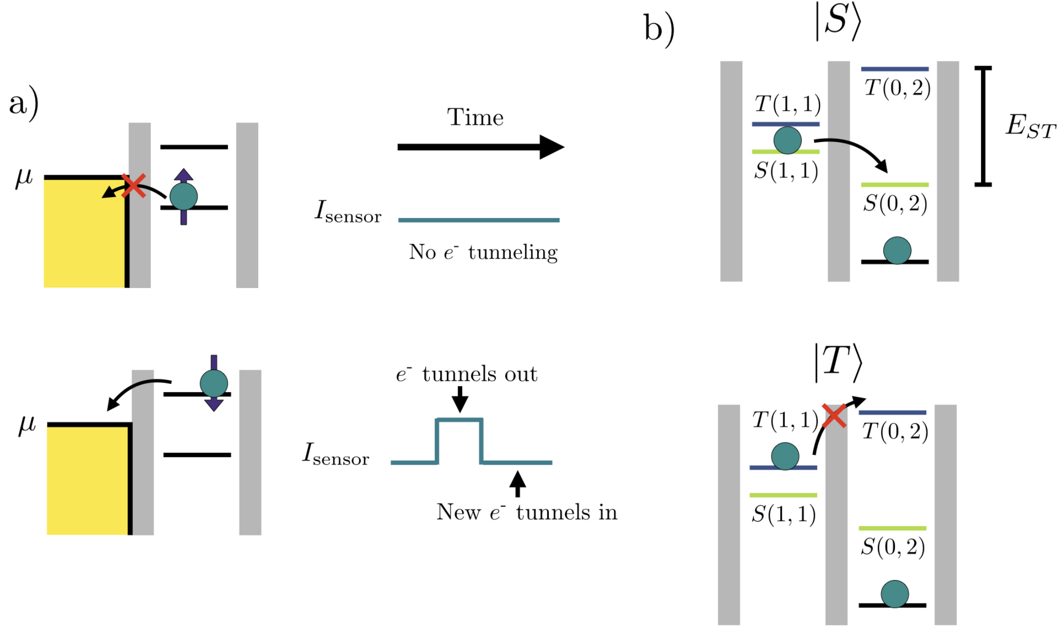

Figure 1.5: Spin-to-charge conversion techniques for spin readout using a charge sensor. a) In spin-dependent tunneling, the dot is coupled to a electron reservoir with chemical potential μ. The dot energy levels are pulsed such that μ lies between the two spin states. When the electron is in the $|\uparrow\rangle$ state, the electron remains trapped in the dot, and the charge sensor sees no response in its current I_{sensor}. When the electron is in the $|\downarrow\rangle$ state, the electron tunnels out of the dot manifesting as a blip in I_{sensor} until a new electron tunnels into the dot. b) When a small bias is applied to a double dot system with two electrons, the leftmost electron wants to tunnel into the right dot taking the system from a $(1,1) \rightarrow (0,2)$ charge configuration. This transition only occurs when the electrons are in the singlet $|S\rangle$ as the doubly occupied triplet $|T\rangle$ is separated by an energy splitting E_{ST} due to the Pauli exclusion principle.

state energy levels in each quantum dot are aligned, each electron occupies a single dot in a $(1,1)$ charge configuration (where each number corresponds to the electron occupancy of the left/right dot). When a small bias is applied to the dots as shown in Figure 1.5b, an electron will try and tunnel into the other dot forming a $(0,2)$ charge configuration. The doubly occupied energy levels for the singlet S and triplet T states are separated by a large energy splitting E_{ST} due to the Pauli exclusion principle. For small biases, the electron can only tunnel into the right dot if the electron pair are in the singlet state $S(1,1) \rightarrow S(0,2)$.

When in the triplet state, the $T(1,1) \nrightarrow T(0,2)$ transition is suppressed. A nearby charge sensor can monitor the respective $(1,1)$ or $(0,2)$ charge configuration of the double dot system in order to extract the two-electron spin state.

The need for a charge sensor to perform spin readout increases the density of metal gate lines and device complexity. An alternative and more scalable spin readout method is gate dispersive readout which uses radio frequency (RF) reflectometry techniques to probe the charge configuration of the quantum dot [89, 46, 224]. An LC tank circuit is directly connected to one of the metal gates used to define the quantum dot, eliminating the need for a charge sensor. The LC circuit elements consist of a surface mount inductor and the parasitic capacitance of the metal gate. Changes in the charge configuration of the quantum dot shift the load capacitance ΔC at the metal gate which manifests as a dispersive phase response $\Delta\phi \approx \pi Q \Delta C / C_p$ of the reflected RF signal where Q is the quality factor of the LC circuit [182]. Homodyne detection on the reflected RF signal can be used to measure $\Delta\phi$ and detect changes in the charge configuration.

1.3.3 An outlook on quantum dot spin qubits

This section gives a brief summary of the current state of quantum dot spin qubits and an outlook on what next steps are necessary in order to scale up these devices to the tens of qubit level. Some of the discussion here will be explored in further detail elsewhere in this thesis. While electron spin quantum dot qubits are a promising candidate for a scalable quantum processor, state of the art devices so far consist of at most 10 quantum dots [181, 185]. In contrast, Google's Sycamore quantum processor, which was claimed to have demonstrated quantum supremacy, is composed of 54 superconducting qubits [3]. Quantum dot devices are beginning to demonstrate the basic operations needed to scale up to larger qubit systems. Demonstrating simple quantum algorithms, like the Deutsch–Josza algorithm, has been realized in a two-qubit silicon quantum dot device [271]. Additional experiments, such as conditional quantum teleportation, have recently been realized in a GaAs quadruple quantum dot device [214].

Scaling to larger quantum dot devices is not prohibited by the physical size of a quantum dot. Quantum dots take up a remarkably small area, with GaAs dots being around 100s of nm in size and silicon dots being around 10s of nm. Scaling to larger qubit systems is mainly prohibited by other aspects of quantum dot qubits, such as current state of the art two-qubit gate fidelities, device variability, cryogenic cooling capabilities, and wiring/control complexity. Single qubit gates with very high fidelities have been demonstrated for silicon (0.9996) [283] and GaAs (0.995) [31]. However, two-qubit gates have struggled to achieve

similarly high gate fidelities due to charge noise (charge noise is explored in detail in Chapter 4). Only recently have fidelities for two-qubit gates reached 98% in Si/SiO_2 quantum dot devices [116] and 92% in Si/SiGe devices [276]. In GaAs, two-spin entangling gates have demonstrated fidelities of 90% in a double dot system [191]. Additionally, quantum teleportation was achieved in a GaAs four-dot system using two-qubit gates [214]; however, the low teleportation fidelities ($\sim$0.71) indicate that two-qubit gates in GaAs are still far from fault tolerant thresholds.

Device variability is another bottleneck in scaling up quantum dot processors. Because quantum dots are so small, local variations from device fabrication or material quality can introduce significant dot to dot variations. For example, measurements of nominally similar silicon quantum dot devices showed that the electron g-factor can vary by up to 0.3% from dot to dot [122]. The magnetic fields typically used to create two-level spin systems in quantum dots give a Zeeman splitting of $\sim$40 GHz, implying that the energy splitting could vary by up to $\sim$120 MHz from dot to dot. If global microwave control fields are used to facilitate single qubit rotations, then there is no guarantee that all qubits would be on resonance with the common microwave pulse. Of the possible material systems for quantum dot qubits (GaAs, Si/SiO_2, and Si/SiGe), Si/SiO_2 is the worst offender for device variability, due to imperfections at the Si/SiO_2 interface and defects within the SiO_2. For GaAs and Si/SiGe, variability from background dopants or intentional dopants in the material system give rise to device non-uniformity. Material systems such as GaAs and SiGe bury the electrons in the quantum dot within the wafer heterostructure, where device reproducibility is improved [155]. Improvements in fabrication techniques have already demonstrated multi-dot devices with reduced variation [14, 106]. Some proposals for silicon dot devices suggest using floating gates placed nearby the quantum dot to fine-tune the dot's electrostatic potential and reduce dot to dot variation [18]. However, the use of this technique in practice remains to be seen.

Another main bottleneck for device scaling lies in cryogenic cooling of the quantum dot processor. Quantum dot devices are typically operated in dilution refrigerator systems which can cool down the devices to tens of mK. These low temperatures are necessary in order to resolve the two-level spin system when using conventional measurement techniques. However, as mentioned in the readout section of Section 1.3.2, if the quantum dots are decoupled from an electron reservoir, there is nothing, in principle, preventing them from being operated at higher temperatures. Several recent state of the art experiments have demonstrated implementing single and two-qubit gates in silicon quantum dot devices above 1 K [283, 206, 207]. At these temperatures, conventional pumped ^{4}He cryogenic systems can be used to cool the devices. Quantum dots require high control wiring density in order to precisely control the qubits. To handle the high density, it has been proposed to

bring conventional CMOS control circuitry into the cryostat and even onto the same chip as the quantum dots [164, 264, 16, 275]. However, these conventional CMOS circuits have significant power dissipation, which proves problematic for dilution refrigerators. Pumped ^{4}He cryostats have orders of magnitude larger cooling power compared to dilution refrigerators and can easily reach 1.4 K temperatures, which could enable the integration of CMOS control circuitry. As such, raising the operating temperature of quantum dot qubits above 1 K is key towards their scalability.

We have discussed several material systems which can host quantum dot spin qubits: GaAs, Si/SiO_2, and Si/SiGe. GaAs quantum dots are larger and easier to fabricate, and as such they were realized earlier than silicon quantum dot spin qubits. However, GaAs has a strong hyperfine interaction, due to the presence of nuclear spins, which results in intrinsic electron spin coherence times T_2^* on the order of 10 ns [208, 146] (although dynamical decoupling techniques have demonstrated T_2's up to ∼1 ms [176]). When isotopically purified of the naturally occurring ^{29}Si isotope, silicon is nuclear spin free. This has proven effective in enabling long coherence times on the order of $T_2^* = 120$ ms and $T_2 = 28$ ms in early Si/SiO_2 silicon spin qubit experiments [267]. GaAs also has a strong spin-orbit interaction while silicon does not, making it easier to facilitate long range spin state transfer in silicon. In bulk silicon, the conduction band minima have six-fold degeneracy, termed valleys. At the interfaces where the quantum dots are formed, the degeneracy is lifted, resulting in two low energy states. The presence of these valley states can be a major source of mixing for silicon quantum dot spin qubits, particularly when the valley splitting is equal to the Zeeman splitting [282, 115]. The valley splitting energy is determined by the sharpness of the interface, as well as other electric fields present in the system. As the Si/SiO_2 interface is sharper than the Si/SiGe interface, the former material tends to have larger valley splittings compared to the latter; however, both materials have demonstrated valley splittings >100 μeV [79] (note that typical Zeeman splittings are <100 μeV). Local disorder at the interface can cause the valley splitting to vary between dots, which not only causes unwanted dot to dot variation, but can also suppress the inter-dot coupling strength [294, 20]. The conduction band of GaAs has no degeneracy resulting in a single valley material. However, the hyperfine and spin-orbit effects of GaAs still make silicon a more attractive material system overall in terms of scalability. Si/SiGe materials have intrinsic strain which makes the wafers more difficult to grow and fabricate devices [255]. In contrast, the Si/SiO_2 interface is not as strained, making it comparatively easier to grow and fabricate devices. Charge traps in the SiO_2 layer are problematic for device noise and variation; however, forming gas annealing is effective at suppressing those defects [139, 138]. Conventional CMOS technology readily uses Si/SiO_2 material, which makes it a natural fit for current foundry processing as well as integration of classical circuits onto the physical

quantum processor chip. Taking all of these considerations into account, we anticipate that Si/SiO_2 will be the material of choice for realizing quantum dot spin qubits, at least for the nearer-term.

Chapter 2

Network architecture for a topological quantum computer in silicon

Chapter contributions: The network architecture was initially conceived by Dr. Jonathan Baugh and further refined with input from myself, Eduardo B. Ramirez, Dr. Kyle S. Willick, and Sean M. Walker. Jiahao Li and Benjamin D. Shaw assisted with nextnano++ simulations for Section 2.3. Error models for the quantum gates were proposed by myself and Dr. Jonathan Baugh with input from Zhenyu Cai and Dr. Simon C. Benjamin. Simulations of the surface code error thresholds in Section 2.4 were done by Zhenyu Cai.

This chapter is adapted from the publication:

Buonacorsi, B., Cai, Z., Ramirez, E.B., Willick, K.S., Walker, S.M., Li, J., Shaw, B.D., Xu, X., Benjamin, S.C., and Baugh, J. (2019). Network architecture for a topological quantum computer in silicon. *Quantum Science and Technology, 4*(2), 025003.

2.1 Introduction

Building a large-scale, universal quantum computer would enable major technological advances, yet presents a significant challenge. Solid-state qubits based on superconducting circuits [78, 272], semiconductor quantum dots [99, 142], semiconductor donor spins [129, 295, 211], or topologically protected quantum states [232] offer exciting prospects for a quantum computer chip, in analogy to classical CMOS devices. The standard circuit

model for quantum computation, however, requires a staggering error correction overhead to achieve fault tolerance. Topological stabilizer codes acting on two-dimensional qubit arrays, i.e. surface codes [220, 75], can tolerate relatively high error thresholds and are considered one of the most promising approaches to scaling up. Fowler *et al.* [72] estimate that ∼100 million physical qubits would be required to factor a 2000 bit semiprime (i.e. RSA) number via Shor's algorithm on a surface code processor. In that estimate, the ratio of logical to physical qubits is $\sim 10^{-4}$. Scaling to this size, while maintaining the requisite precision of quantum control and the necessary cryogenic environment, is far beyond what is possible today. Superconducting qubit processors are rapidly advancing from several qubits [189, 242, 126] to the $50 - 100$ qubit scale [3], while competing platforms such as semiconductor quantum dots are still developing at the few-qubit scale [271, 269, 64, 286, 289]. Ultimately, the qubit footprint matters for a large-scale monolithic chip to be possible. Quantum dot and donor qubits have the advantage of a small (tens of nanometers) footprint compared to other platforms like superconducting or trapped ion qubits, making an area density of $\sim 10^{10}$ physical qubits per cm^2 a theoretical possibility. A rigorous analysis based on a compact exchange-only silicon double dot qubit, accounting for technological and physical constraints as a function of CMOS technology node, predicts that a 10^{10} cm^{-2} density of physical qubits is possible at the 7 nm CMOS node, corresponding to $\sim 10^4 - 10^6$ cm^{-2} logical qubits depending on the error correction scheme chosen [225]. The ability to integrate classical components on the quantum chip to facilitate multiplexing of control and readout signals will be advantageous. Semiconductor qubits also have an advantage in this respect, especially those based on silicon platforms. We will refer to realizing electron or hole spin qubits in a silicon MOS device structure [179, 267, 102, 121] at cryogenic temperatures as 'QMOS'. A QMOS approach can benefit from the vast investments and advances that have been made in conventional CMOS device processing, and is naturally compatible with CMOS integration. In this chapter, we propose a QMOS architecture that is based on a network/node approach and is distinct from existing proposals [107, 200, 210, 266, 164]. This approach is advantageous because it separates the surface code operation into two fundamental parts: local node operations that should be feasible to demonstrate in the near-term, and medium-range entanglement distribution that is more challenging but can be developed in parallel. Our scheme provides greater isolation of the data qubits (data qubits hold the computational quantum states of the surface code) than a conventional close-packed 2D array, and naturally opens up useful space to ease wiring density constraints and allow integration of supporting components to facilitate multiplexing of control and readout signals.

While much early progress in quantum dot spin qubits was achieved in GaAs 2DEG devices, silicon offers the possibility of a nuclear spin free lattice, which has been demon-

strated to yield electron spin coherence times of order seconds for donor electrons [256, 187] and up to tens of milliseconds for MOS quantum dot spin qubits [269]. The intrinsic spin-orbit interaction for electrons at the conduction band edge in silicon is weak compared to III-V semiconductors, which leads to longer spin relaxation and decoherence times. An enhanced spin-orbit interaction arises at the Si/SiO_2 interface due to inversion asymmetry leading to variation in the electronic g-factor, however this can be tuned near zero by the orientation of the external magnetic field [121]. The variation in g, of order 10^{-2} at most [268, 65, 267], is tunable by the vertical electric field strength and can be used for addressing individual spins with a global microwave ESR field, or as a second control axis for singlet-triplet qubit rotations [121]. Disadvantages of silicon compared to III-V's include the valley degeneracy problem [49, 282] and greater difficulty in accurately modelling two-qubit exchange energies [163]. Valley splittings are enhanced at interfaces, and have been observed for MOS dots up to several hundred μeV but vary considerably depending on local electric fields and disorder [79, 168]. While Si/SiGe quantum wells present less disorder in the electrostatic potential and are thus 'cleaner', valley splittings are found to be smaller on average for quantum dots in this material [15, 190, 288].

While for MOS quantum dots the microscopic roughness of the SiO_2 interface leads to an unavoidable degree of intrinsic variation in electrostatic and qubit parameters, the large scale uniformity of the Si/SiO_2 material system is remarkable and has been critically important to the scaling of classical CMOS. Many engineering challenges, however, can be foreseen with developing large scale QMOS: (i) qubit sensitivity to charge noise, (ii) control line cross-talk, (iii) variability in device tuning parameters, (iv) need for high density 3D wiring interconnects, (v) need for multiplexing and parallel operations, (vi) ultra-low power dissipation, (vii) high precision / high bandwidth / low noise voltage controls, etc. Existing proposals make use of 2D quantum dot arrays as a basis for a surface code quantum computer. Veldhorst *et al.* [266] suggest a two-layer structure, with a closely-packed 2D dot array at a lower ^{28}Si/SiO2 interface, and an upper Si transistor layer to enable a word-line/bit-line qubit addressing scheme using floating gates. Each dot is singly charged and has four nearest neighbours with exchange interactions that must be separately controlled. Single-qubit rotations are achieved via global microwave field and gate tuning of individual electronic g-factors. This approach utilizes shared control lines and is therefore scalable in principle, but requires a high interconnect density with feature sizes well below present technological capabilities. All qubits, both data and measure, experience the same local noise environment and capacitive cross-coupling to many electrodes, so that both control line cross-talk and gate voltage noise would present challenges. Furthermore, the power dissipated by conventional transistors would make it difficult to maintain mK temperatures, either requiring very large cooling powers or qubit operation at temperatures approaching

1 K. Li *et al.* [164] propose an alternate scheme using shared control that makes use of a half-filled 2D lattice, so that, between operations, qubits are better isolated. It relies on shuttling electrons between adjacent lattice sites to accomplish two-qubit interactions, and uses dc currents in a subset of control lines to tune local ESR frequencies in concert with a global ESR field. Since the dots and tunnel barriers are all controlled by a crossed array of common lines, this scheme requires a high degree of device uniformity, at least an order of magnitude beyond what has yet been demonstrated in experiments. To avoid practical issues with scaling a qubit array beyond ∼1000 qubits, it was proposed to join arrays in a network, making use of electron shuttling 'highways' consisting of linear dot arrays to transmit quantum information. Hence, both local and long-range electron shuttling are critical elements of Li *et al.*'s proposal. Our scheme also makes essential use of electron shuttling to distribute entanglement between adjacent nodes; however, these are small nodes of fewer than 10 quantum dots, so that the nodes and their corresponding local quantum operations are nearly within the reach of present experimental capabilities.

2.2 Node/network surface code for quantum dots

It is well understood that a universal quantum computer could be constructed by networking together many simple processor cells, rather than building a single complex device [193, 140, 39, 192]. Key to this approach is the ability to distribute entanglement between such cells, or network nodes. Nickerson *et al.* [193] showed that even with realistically noisy entanglement distribution, with raw error rates approaching 10%, entanglement purification strategies could be used to reduce the effective error rates to tolerable levels. Combined with sufficiently high fidelity local gate operations, state preparation and measurement, a stabilizer protocol was described that enables a two-dimensional surface code to be implemented [193]. This method is straightforwardly applicable to systems like trapped ion qubits, where spatially separated traps can be linked photonically [117, 17, 183]. However, successful entanglement distribution via a photonic link is currently probabilistic and slow, with typical rates on the scale of a few Hz, limiting practical processor speeds. Here we propose to apply the network model to a monolithic silicon QMOS chip, with internode distance on the micron scale. We exploit the natural property of spin qubits to form a singlet ground state in a doubly occupied quantum dot to create the entanglement resource, and the weak spin-orbit interaction in silicon to allow coherent shuttling of electron spins via inter-dot tunnelling, as illustrated in Figure 2.1. Thus, entanglement distribution becomes effectively deterministic. Although our approach is monolithic and thus returns to 'building a single complex device', we gain significant advantage by separating the scaling

problem into two distinct parts, and by creating useful space between these very compact qubits to improve qubit isolation and make wiring/integration more practical. Numerical simulations show that electron shuttling on the micron scale can be carried out with high fidelity in principle, and on the timescale of single-qubit ESR gate operations so that shuttling does not create a speed bottleneck. Further, we show that phase error in the singlet state due to Stark effect modulation of the g-factor during shuttling can be reduced to negligible levels with appropriate electrostatic tuning. Finally, we obtain threshold values for errors in gate and shuttling operations that would be required for a scaled up network to be fault tolerant, using reasonable noise models and the Gottesman-Knill theorem [91, 1] to efficiently simulate large networks.

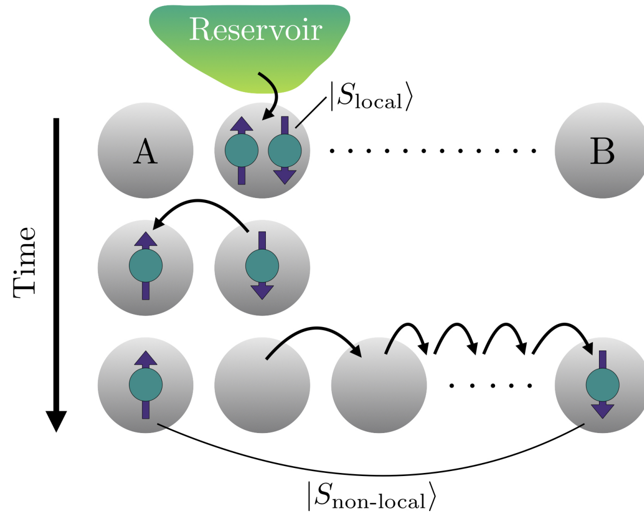

Figure 2.1: Spatial separation of the spin singlet state $|S\rangle$ across distant quantum dots A and B, via spin shuttling through a linear chain of normally empty quantum dots. The two-electron ground state singlet is loaded into a quantum dot tunnel coupled to the reservoir. The singlet is separated into a (1,1) charge state with one electron in dot A, then the other electron is shuttled to a distant dot B. Both the weakness of the spin-orbit interaction for conduction electrons in silicon and the isotopic removal of ^{29}Si nuclear spins help to preserve spin coherence during transport over micron scales.

For simplicity, we will assume that spatial separation of the singlet states can be done with high fidelity, so that entanglement purification is not needed. This allows for a minimal node consisting of one data and two ancilla qubits. Additional ancillae and entanglement distribution operations could be used for entanglement purification if needed, as described

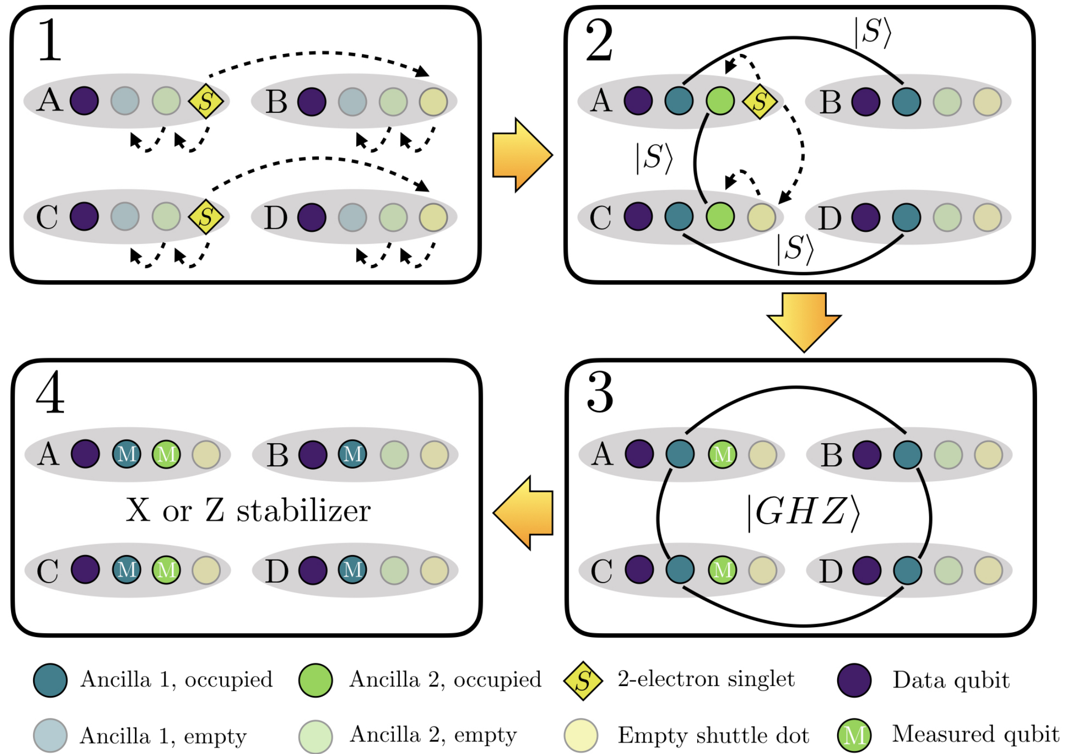

Figure 2.2: Sequence of steps in the stabilizer operation on four neighbouring nodes labeled A-D. Prior to step 1, all dots are empty except for the data qubit dots. Dashed lines indicate electron internode and intranode tunneling events. In **step 1**, singlets created at nodes A and C are shared between nodes A/B and between C/D, populating the ancilla 1 qubits. Long dashed lines indicate internode shuttling. **Step 2**: a singlet created at A is shared between ancilla 2 qubits on nodes A/C. **Step 3**: ancilla 2 qubits on nodes A/C are measured, which projects the four ancilla 1 qubits into the shared GHZ state with probability 1/2, or with equal probability into a state that is transformed to the GHZ state by local gate operations. **Step 4**: conditional quantum gates (control-NOT or control-Z) are performed between ancilla 1 and data qubits, followed by measurement of the ancilla 1 qubits, realizing a stabilizer operation on the data qubits. Step numbers are color-coded to match circuit segments in Figure 2.4

in [193]. A four-qubit GHZ state is formed across four neighbouring nodes, making use of singlet separation and the ancilla qubits in each node, as shown in Figure 2.2. The GHZ resource shared among ancilla 1 qubits, together with conditional logic gates (control-NOT or control-Z) applied to the data qubits, allows for the X or Z stabilizer operation to be carried out. In addition to the three quantum dots hosting the data and ancilla qubits, $1-2$ additional dots are present in the node to facilitate the distribution of singlet states, which we will refer to as 'shuttle' dots. A conceptual device-level illustration of a node is shown in Figure 2.3. In this version, there are two shuttle dots, which ensures no more than three tunnel couplings per dot. The node is connected to a single electron reservoir via one of the shuttle dots, providing a means for initializing the charge state of the device and loading singlets into the shuttle dot prior to their distribution. All reservoirs are kept at a fixed potential of 0 V. The node in Figure 2.3 is based on a simplified gate geometry in which each quantum dot is defined by a single 'via' accumulation gate electrode (see Figure 3.2 in Chapter 3 for an example). Additional barrier gates between intranode dots allow for fine control of exchange. A double dot, aligned perpendicular to the data/ancilla linear array, allows for readout of both ancilla qubits, as will be described in Section 2.2.2. A global microwave field acts in concert with electrostatic tuning of the electronic g-factors to realize arbitrary single-qubit rotations via ESR. Dots forming the shuttle pathway are each formed by single gate electrodes, with no additional barrier gates, as we show in Section 2.3.

2.2.1 Stabilizer circuit

In order to simulate the performance of the proposed network architecture, we must first write out the explicit stabilizer circuit in terms of the basis operations possible with quantum dot qubits: inter-dot tunneling, single qubit X, Y, and Z rotations, and two-qubit $\sqrt{\mathrm{SWAP}}$ gates. The four-node stabilizer sequence shown in Figure 2.2 begins with all dots empty except for the data qubit. The explicit circuit diagram corresponding to the stabilizer sequence is shown in Figure 2.4.

We outline the mathematical details underlying the part of the circuit used to construct the distributed four-qubit GHZ state. In our notation, commas separate nodes from each other as $|\mathrm{A,B,C,D}\rangle$. Within a particular node, the first qubit represents the ancilla 1 qubit and the second (if written) indicates the ancilla 2 qubit. A blank space in the ancilla 2 location means that qubit is not present. For instance $|01,01,01,01\rangle$ indicates that all nodes have a $|0\rangle$ state in the ancilla 1 qubit and a $|1\rangle$ state in the ancilla 2 qubit. While the state $|01,0,01,01\rangle$ indicates that all nodes have a $|0\rangle$ state in the ancilla 1 qubit and while all but the B node have a $|1\rangle$ state in the ancilla 2 qubit (where the B node actually

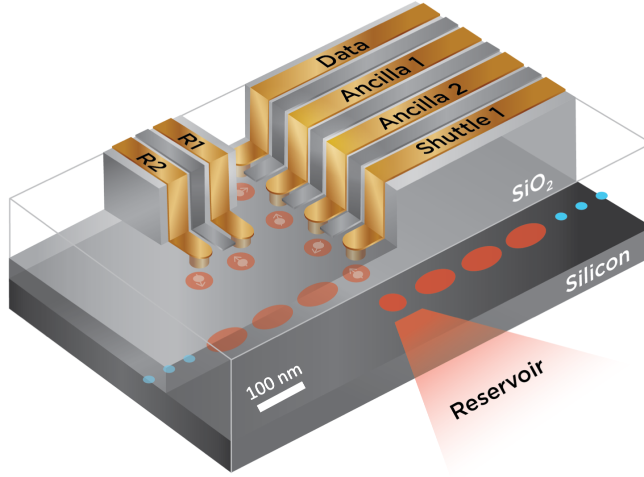

Figure 2.3: Device concept for a node. Accumulation mode MOS quantum dots are formed by single 'via' gate electrodes (gold color), with additional gates to control inter-dot tunneling (silver color). All quantum dots (red circles and ovals) form in Si just below the interface with SiO_2. For clarity, gate electrodes forming the electron shuttling pathways (oval dots) and the electron reservoir are not shown. The intranode dots are identified by the labels on the via gate electrodes. In this version of the node there are two shuttle dots (note that only one is labelled explicitly), one tunnel coupled to the shuttle path going left, the other to the path going right and to the reservoir. This geometry ensures no more than three tunnel couplings per dot. The labels $R1, R2$ indicate the double dot that allows for readout of the ancilla qubits, using the singlet-triplet spin basis together with RF reflectometry. Gate electrodes to control exchange between the ancilla qubits and $R1$ are not shown but are implied. The oval-shaped dots making up the shuttle pathway are each defined by a single gate, with no additional barrier gates.

has no qubit present in the ancilla 2 location). A two-electron spin singlet state is loaded from the reservoir into the shuttle dots in nodes A and C, and then distributed across A-B and C-D via internode shuttling. This populates the ancilla 1 qubits giving the initialized state

$$|\Psi\rangle = \frac{1}{\sqrt{2}}\Big(|0,1\rangle_{\mathrm{AB}} - |1,0\rangle_{\mathrm{AB}} \Big) \otimes \frac{1}{\sqrt{2}}\Big(|0,1\rangle_{\mathrm{CD}} - |1,0\rangle_{\mathrm{CD}} \Big) \tag{2.1}$$

$$= \frac{1}{2}\Big(|0,1,0,1\rangle_{\mathrm{ABCD}} - |0,1,1,0\rangle_{\mathrm{ABCD}} - |1,0,0,1\rangle_{\mathrm{ABCD}} + |1,0,1,0\rangle_{\mathrm{ABCD}} \Big) \tag{2.2}$$

From here on out, we will drop the $|\rangle_{\mathrm{ABCD}}$ notation. Next, a fresh singlet loaded in node

A is distributed across the ancilla 2 qubits in nodes A-C giving the state

$$
\begin{aligned}
|\Psi\rangle = \frac{1}{2\sqrt{2}}\Big(&|00,1,01,1\rangle - |00,1,11,0\rangle - |10,0,01,1\rangle + |10,0,11,0\rangle \\
&- |01,1,00,1\rangle + |01,1,10,0\rangle + |11,0,00,1\rangle - |11,0,10,0\rangle \Big)
\end{aligned} \tag{2.3}
$$

The first step of segment 3 in Figure 2.4 is a $Y(\pi)$ rotation on the ancilla 1 qubits in nodes A and C and on the ancilla 2 qubit in A. This transforms the singlets into the $|\Phi^+\rangle = \frac{1}{\sqrt{2}}(|00\rangle + |11\rangle)$ Bell states, and the total state becomes

$$
\begin{aligned}
|\Psi\rangle = \frac{-i}{2\sqrt{2}}\Big(&|11,1,11,1\rangle + |11,1,01,0\rangle + |01,0,11,1\rangle + |01,0,01,0\rangle \\
&+ |10,1,10,1\rangle + |10,1,00,0\rangle + |00,0,10,1\rangle + |00,0,00,0\rangle \Big)
\end{aligned} \tag{2.4}
$$

Next, we perform a control-Z operation between the ancilla 1 and ancilla 2 qubits in nodes A and C,

$$
\begin{aligned}
|\Psi\rangle = \frac{-i}{2\sqrt{2}}\Big(&|11,1,11,1\rangle - |11,1,01,0\rangle - |01,0,11,1\rangle + |01,0,01,0\rangle \\
&+ |10,1,10,1\rangle + |10,1,00,0\rangle + |00,0,10,1\rangle + |00,0,00,0\rangle \Big)
\end{aligned} \tag{2.5}
$$

To create the 4-qubit GHZ state distributed across all four ancilla 1 qubits, we perform an X basis measurement on the ancilla 2 qubits in nodes A and C. Rewriting the state above in the X basis, it is easy to find the state of the ancilla 1 qubits conditional on the four measurement outcomes:

$$
\begin{aligned}
+_A, +_C &\rightarrow \frac{1}{\sqrt{2}}\Big(|0,0,0,0\rangle + |1,1,1,1\rangle \Big) \quad & -_A, -_C &\rightarrow \frac{1}{\sqrt{2}}\Big(|0,0,0,0\rangle + |1,1,1,1\rangle \Big) \\
+_A, -_C &\rightarrow \frac{1}{\sqrt{2}}\Big(|0,0,1,1\rangle + |1,1,0,0\rangle \Big) \quad & -_A, +_C &\rightarrow \frac{1}{\sqrt{2}}\Big(|0,0,1,1\rangle + |1,1,0,0\rangle \Big)
\end{aligned}
$$

Since the four outcomes above occur with equal probability, the even parity outcomes give the GHZ state with probability 1/2. The odd parity outcomes give a state with equal probability 1/2 that is transformed into the GHZ state by applying an $X(\pi)$ rotation on the ancilla 1 qubits in two of the nodes (either A-B or C-D). Therefore, four-qubit GHZ state preparation is deterministic. The GHZ state provides the shared entanglement resource that allows the data qubits to be stabilized. A control-NOT (or control-Z) between the local ancilla 1 and data qubits, followed by measurement of the ancilla 1 qubits, performs

a 4-qubit X (or Z) stabilizer on the data qubits. The resulting stabilizer measurement outcomes are fed to a classical data processing module in order to determine if any nodes require a unitary rotation to correct any errors in the code. The ancilla dots can then be emptied of electrons (via shuttling to the reservoir) to prepare for the next stabilizer operation.

A full surface code cycle requires 4 separate stabilizer operations in sequence, since any two neighbouring 4-node plaquettes cannot be stabilized simultaneously. Both the Z and X plaquettes are split into two non-adjoining subsets, and each of the 4 subsets are stabilized sequentially (see Figure 2.5). As pointed out in [193], the stabilizer superoperator allows projectors and errors to be commuted so that errors occurring in between subsets can be corrected. Note that the control-NOT and control-Z operations in steps 3 and 4 of Figure 2.4 require single-qubit rotations on the data, ancilla 1 and ancilla 2 qubits. To simplify the device, however, one could restrict single-qubit control to ancilla 1 only, and use SWAP operations to realize gates on the neighbouring qubits. While this approach is more costly in terms of two-qubit gate error, it reduces control complexity by requiring only one dot per node to be on-resonance with the global ESR field. Since exchange gates are typically much faster than ESR rotations, this does not present a bottleneck to processor speed.

2.2.2 Readout of the ancilla qubits

Measuring ancilla qubits quickly and with high fidelity is a critical requirement for any surface code processor, including the network approach proposed here. One method for projectively measuring the electron spin is to use spin-dependent tunneling together with a local charge sensor [63, 184]. However, this would require bringing both an electron reservoir and a charge sensor in close proximity to the ancilla qubits, both of which we aim to avoid in order to keep the data and ancilla qubits well isolated and reduce the number of local gate electrodes. Instead, we propose to use a double quantum dot placed so that it can be controllably tunnel coupled to both ancilla dots. The double dot is not coupled to a reservoir, but is coupled via local gate to an RF reflectometry circuit, as shown in Figure 2.6. The double dot is operated in the two-electron singlet/triplet basis. The readout sequence for the ancilla state $|\psi\rangle$ is the following: (1) initialize the double dot in the singlet (0,2) charge configuration, (2) separate into the $(1,1)$ singlet, (3) perform a control-Z gate operation between the ancilla and the adjacent member of the double dot, (4) tune the double dot to favour the (0,2) configuration and use gate-dispersive RF reflectometry [205, 224, 88] to distinguish the $T(1,1)$ and $S(0,2)$ spin(charge) states. This charge detection method works by sensing the quantum capacitance associated with inter-dot tunnelling

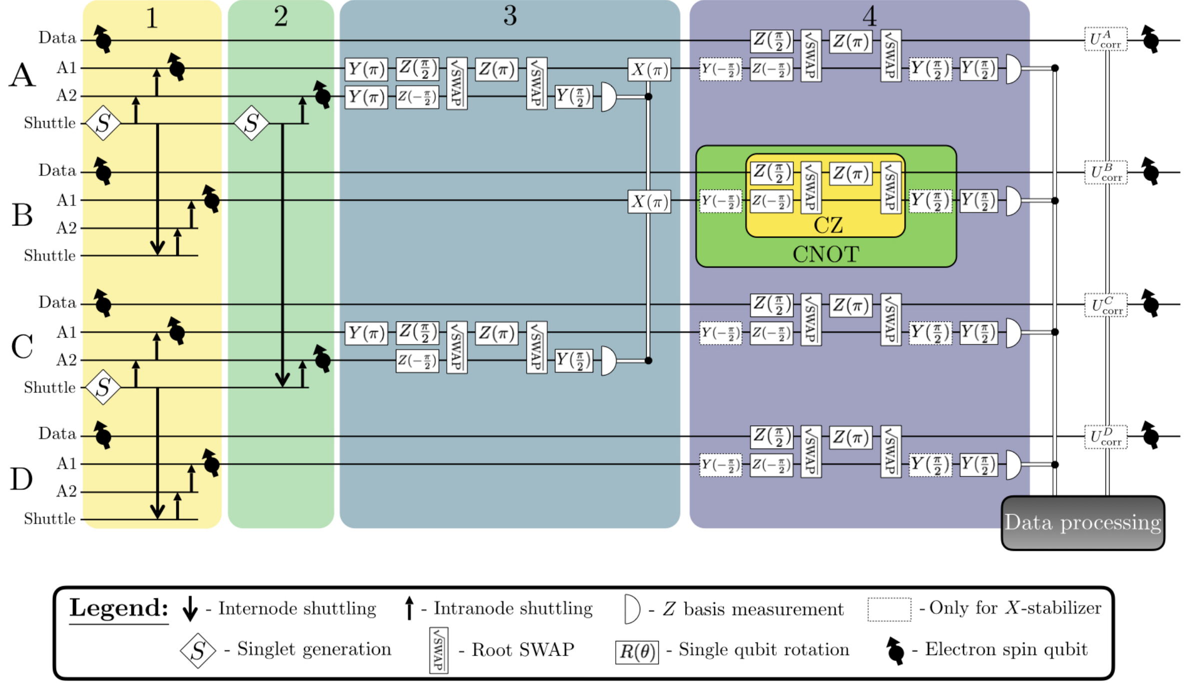

Figure 2.4: Circuit diagram corresponding to the four-node operations shown in Figure 2.2. The labels 1-4 at the top correspond to the steps in Figure 2.2; entanglement distribution is carried out in steps 1-2, the GHZ state is formed at the end of step 3, and the stabilizer operation is step 4. A1 and A2 refer to ancilla qubits 1 and 2, respectively. Other symbols are defined in the legend below. The notation $R(\theta)$ indicates a spin rotation about the R axis in the Bloch sphere by an angle θ. Conditional $X(\pi)$ gates applied to the A1 qubits in nodes A and B ensure the GHZ state is created with 100% probability in the absence of measurement and gate errors. Control-Z gates in step 4 correspond to a Z-stabilizer, whereas additional $Y(\pi/2)$ rotations transform these to control-NOT gates which yield the X-stabilizer. The stabilizer measurement outcomes are sent to a classical data processing node to determine which (if any) nodes require a corrective unitary rotation U_{corr}. In the diagram we assume the ability to perform single qubit rotations on the data and both ancilla qubits, however, use of additional SWAP gates could restrict this requirement to one qubit, e.g. single qubit gates on A1 only. The control-Z sequences could be replaced by direct gates under certain circumstances [271], reducing the number of single-qubit gates and increasing processor speed. Steps to empty the ancilla dots are not shown explicitly, but will directly follow the final measurements.

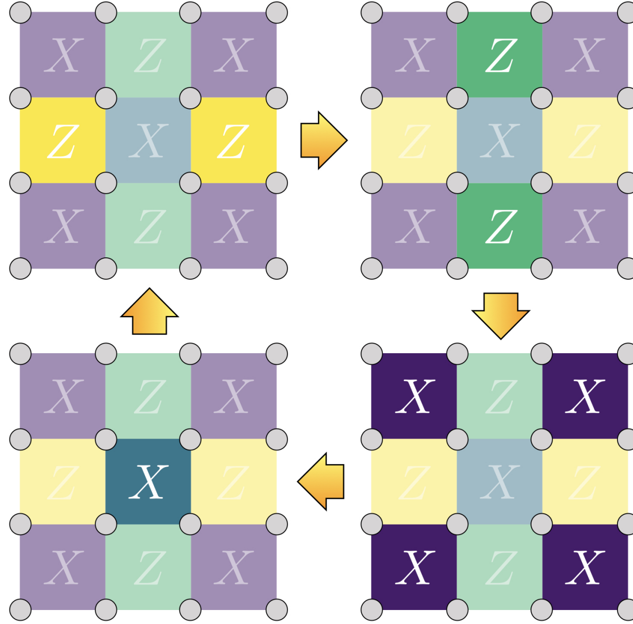

Figure 2.5: A full stabilizer cycle consists of the four steps indicated in the figure, since adjacent 4-node plaquettes cannot be stabilized at the same time. Starting at the upper left, the Z stabilizer is split into two steps, followed by the two-step X stabilizer. The cycle then repeats. Dark color indicates which stabilizer operations are being performed in the current step.

(see Mizuata *et al.* [182] for a description of quantum capacitance). When the ancilla qubit is in the logical $|1\rangle$ state, the control-Z gate rotates the singlet to a triplet, which remains in the $(1, 1)$ charge state due to the Pauli spin blockade. The conventional control-Z gate sequence requires two-qubit exchange and single-qubit rotations on both qubits, but it may be advantageous to restrict single-qubit rotations to the ancilla qubit by using SWAP gates. We note that single electron charge detection using gate-dispersive methods has demonstrated sensitivities allowing for measurement on few-nanosecond timescales [89], therefore, qubit readout times could be limited by the gate operations and not by charge detection. The presence of valley states in silicon complicates the spin-blockade based readout but is not a fundamental obstacle to achieving high readout fidelities [247]. We note that current state of the art experiments using gate dispersive methods have achieved readout fidelities of >98% for a two-qubit state in silicon within a time frame of 6 μs [293]. Obtaining these fidelities at the 1-100 ns regime is critical to ensuring that readout does not significantly bottleneck the overall processor speed.

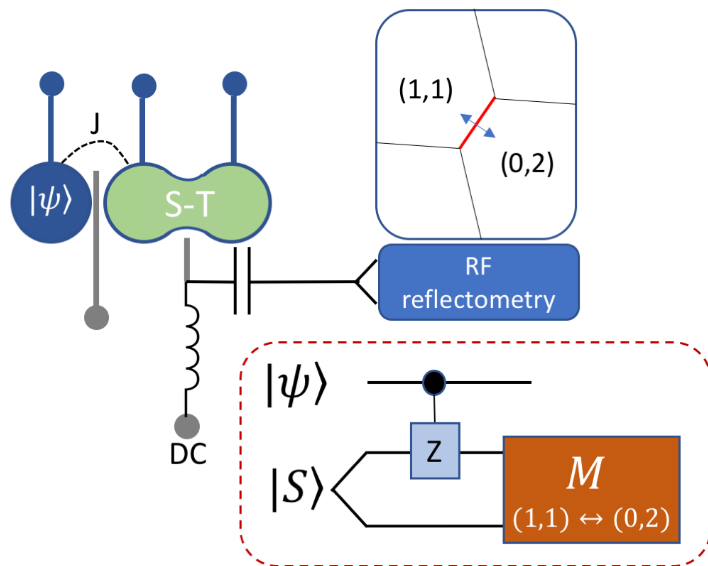

Figure 2.6: A method for reading out the ancilla qubits. A double quantum dot is operated in the two electron singlet-triplet basis (labeled $S-T$). A local gate electrode (gray) couples the quantum capacitance of the double dot to an RF reflectometry circuit for gate dispersive charge readout. A second (gray) gate electrode controls exchange (J) between the ancilla dot and the double dot. Initialized in the $(1,1)$ singlet state, a control-Z gate conditioned on the state $|\psi\rangle$ of the ancilla qubit acts on the dot adjacent to it. The ancilla states $|0\rangle$ and $|1\rangle$ thus map to the singlet and triplet states, respectively. The Pauli blockade prevents the $T(1,1)$ state from tunnelling to the $S(0,2)$ state, and thus the dispersive charge detection allows the two states to be distinguished. The conventional control-Z sequence requires control of the exchange coupling and single-qubit rotations, the latter of which can be restricted to the ancilla qubit using SWAP gates.

2.2.3 Network layout

A proposed layout of the nodes forming a network is presented in Figure 2.7. N-type ion implanted regions, kept well separated from the nodes to reduce charge noise, allow reservoirs to be brought to each node using accumulation gates. The shuttle dots in each node connect to north/south shuttle pathways (linear dot arrays). The version shown here and in Figure 2.3 has two shuttle dots so that no dot has more than three tunnel couplings that must be separately controlled. The data qubit dot is coupled only to the first ancilla, providing isolation for this all-important qubit. East/west shuttle paths can be

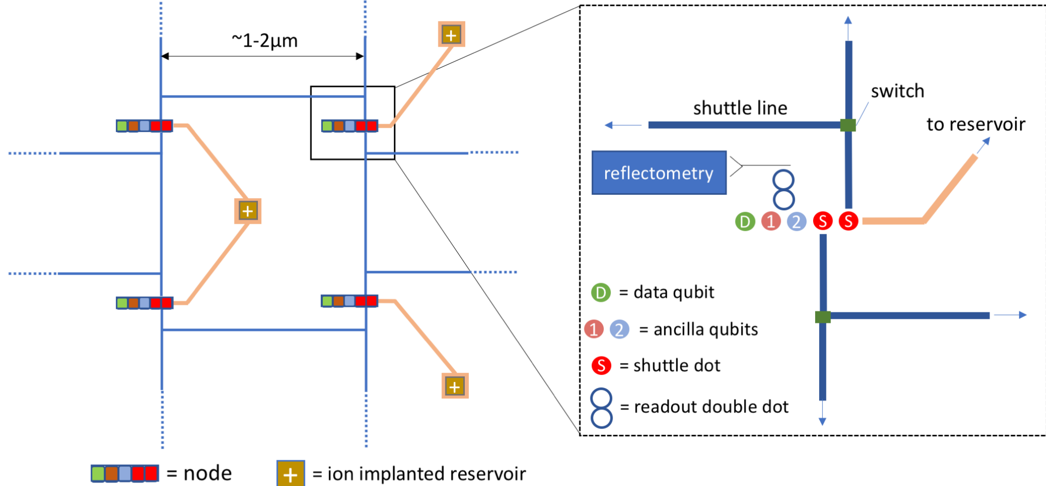

Figure 2.7: Illustration of a proposed network layout showing a plaquette of four nodes and how they connect beyond to form a 2D surface code. Ion implanted regions indicated by '+' symbols provide electron reservoirs that are brought to each node with accumulation gates (gold color). The enlarged section at right shows the dot layout in each node relative to the reservoir and shuttling paths, the latter here indicated as lines that represent linear (empty) dot arrays. Each switch is a T-junction of quantum dots in which the tunnelling direction is controlled by local gate electrodes. Gate electrodes that form the dots and enable quantum control (not shown) connect vertically (out of plane) to wiring in upper interconnect layers. Gate electrodes controlling shuttling can be shared, since singlet distribution occurs in parallel across the entire device. The RF reflectometry circuit indicated by the blue box represents a combination of on-chip and off-chip components and probes the charge state of the double dot by the gate-dispersive readout technique. Nodes in the main figure are not to scale.

chosen at T-junctions, where local gate electrodes control the tunnelling direction. Thus, each node is connected to all four neighbouring nodes. The internode distance can be scaled to optimize wiring density and integration of classical CMOS components while minimizing shuttle errors, and we expect this to be on the scale of $\sim$1 to a few microns. For an internode spacing of 1.5 μm, the node (data qubit) density is 4.4×10^7 cm^{-2}, still a high density compared to superconducting and ion trap qubits. It is about 2 orders of magnitude less dense than the estimates given in [225] for close-packed silicon-based qubits, but would still give a few times 10^3 cm^{-2} logical qubits, enough to factor a 2000-

bit semiprime number using Shor's algorithm with a 10 cm^2 size chip (assuming ∼10,000 logical qubits) [225, 72]. The internode space could be used to add floating gate circuits to correct for small electrostatic variations in qubit device parameters, allowing for widely shared control lines.

2.3 Single electron transport

Spatial separation of the spin singlet pairs is fundamental to the proposed network approach, and occurs in parallel across the device at the beginning of every stabilizer cycle. To coherently translate an electron spin across a distance requires confinement of the wavefunction be maintained. Single electron transport via 'moving quantum dots' has been realized with surface acoustic waves in piezoelectric materials [131, 260, 10]. This idea was recently applied even in silicon, with an appropriate piezoelectric material attached to the surface [25]. Surface acoustic wave generation, however, requires bulky interdigitated electrodes, and confining the waves to desired pathways is challenging. A more exotic possibility is the generation of a soliton wave [134, 60], which would render unnecessary the requirement for a moving potential well. Unfortunately, solitons can only be generated from a Fermi sea, and not (as far as we know) from single particle levels in quantum dots. To create a moving confining potential without acoustic waves, one can use a set of gate electrodes to form a linear array of quantum dots [76, 68]. In the limit of many fine gate electrodes, a moving dot could be approximated. With realistic gate dimensions, however, it is more practical to define adjacent dots and force electrons to tunnel successively between them. We adopt a simplified model in which each dot is formed by a single accumulation (plunger) gate, and there are no explicit gates to control tunnelling. Instead, plunger gate voltages and the electrode geometry are used to control tunnelling. Two main topics are addressed: (1) what shuttling speeds are feasible in realistic devices while adiabatically maintaining the electronic ground state, and (2) how large is the shuttle-induced modulation of the electronic g-factor due to the Stark effect, how much error does this cause in the singlet state fidelity, and can it be mitigated? The results presented here are only an introduction into the feasibility of sequential electron shuttling through a quantum dot chain as it relates the network architecture proposal. These results are expanded upon in significantly more detail in Chapter 3. Although unrealistic for silicon [247], we assume a single valley model in this chapter as a first step. Coherent spin transport through a series of dots is unlikely to succeed in cases for which the energy splitting between the two lowest valley states, Δ_{vs}, is comparable to the Zeeman and/or tunnelling energies, E_z and t_c, respectively. In such cases, even a weak spin-orbit coupling causes levels with different

spin and valley indices to anti-cross, so that diabatic transitions that mix spin and valley states are difficult to avoid [291, 165]. Thus, our approach would require that $\Delta_{vs} \gg E_z, t_c$, so that the higher valley state would play a role similar to an excited dot orbital state. This condition is more likely to be achievable in MOS dots compared to Si/SiGe. The g-factor modulation is an indirect effect of the spin-orbit coupling and causes a phase rotation of the singlet state. Direct spin-orbit induced rotations along $\hat{x}, \hat{y}$ are expected to yield weaker errors, but are non-negligible for long shuttle paths, as we discuss below. Charge decoherence, which can occur when the system is biased near zero-detuning [209], is also neglected in our simulations, but will be an important factor to consider in future work. As a side note, there is a closely related method referred to as coherent transfer by adiabatic passage (CTAP) which is analogous to the STIRAP (Stimulated Raman Adiabatic Passage) technique in optics for population transfer in a three-level atomic system (Λ system) [92, 216]. CTAP, in a 3-dot linear array, relies on quantum interference to transfer an electron from dot 1 to dot 3 without it ever being in dot 2. This can be generalized to an N-dot system (for odd N). This method, however, is not feasible with the simplified gate geometry of our simulations because CTAP requires independent control of tunnel couplings and dot potentials, implying more gate electrodes are needed. CTAP is also sensitive to dephasing throughout the entire sequence, whereas shuttling is only sensitive during the tunnel events. For these reasons we have not included CTAP in our simulations, but it remains a possible alternative.

2.3.1 Shuttling simulations

Figure 2.8a shows an example of the gate electrode geometry and potential landscape for a five-dot linear array. This is simulated using a 3D self-consistent Poisson equation solver in the nextnano++ software [11]. The 'via' gate electrodes are 40 nm wide at the base, with center-center separation of 60 nm. The base of the via gate is separated from the Si interface by 17 nm of SiO_2, and the potential profile is shown 0.5 nm below the Si/SiO_2 interface. Figure 2.8b shows the sequence of gate voltages applied in a five-dot shuttling simulation, with V_1 (V_5) corresponding to the leftmost (rightmost) gate electrodes. The gate voltage sequence for shuttling was designed using a set of 1D potentials calculated using nextnano++. The electron is first initialized in dot 1 with $V_1 > V_2$. To transfer the electron to dot 2, we first sweep V_2 linearly in the positive direction while holding V_1 fixed. This can be done very quickly over the range of V_2 for which the wavefunction localized in dot 1 is insensitive to V_2. This fast sweep ends when inter-dot tunnelling 'turns on' and there is a small probability for the electron to be in dot 2; we chose an arbitrary threshold of $\sim$0.1% probability. V_2 is then swept slowly enough to continue to satisfy the

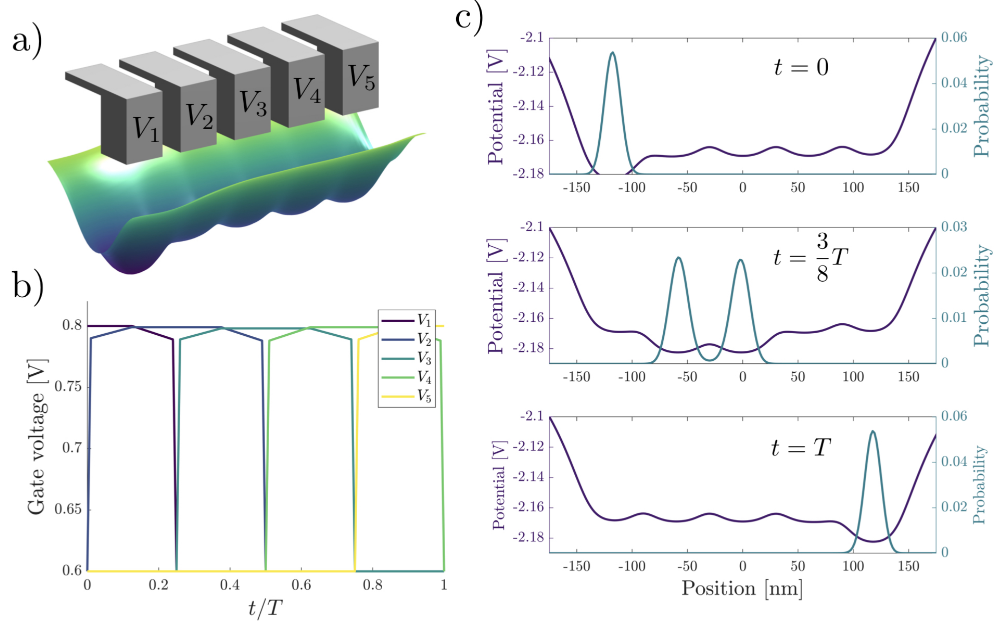

Figure 2.8: Setup for the electron shuttling simulations. a) A linear chain of five quantum dots is formed by single 'via' gate electrodes with applied voltages $V_1 - V_5$. The corresponding electrostatic potential in Si just below the Si/SiO$_2$ interface is shown. b) Gate voltage sweep sequence for moving an electron from dot 1 (left) to dot 5 (right), with time $T/4$ per shuttle. Voltage is swept more slowly near the resonant tunnelling point to preserve adiabaticity. c) Snapshots of the 1D potential and ground state electronic probability density $|\psi|^2$ at $t = 0$, $3T/8$ and T. Note that potential differences are meaningful but the potential offset (absolute value) is arbitrary, and the sign of the potential is reversed as though the electron charge were positive. Coherent tunnelling between dots 2 and 3 can be seen at $t = 3T/8$. The minimum T for which shuttling remains adiabatic is determined by the size of the tunnel coupling, the orbital energy spacing and other factors.

approximate adiabatic condition [42]

$$\sum_{m \neq 0} \hbar \left| \frac{\langle \psi_m(t) | \frac{d}{dt} | \psi_0(t) \rangle}{E_0(t) - E_m(t)} \right| \ll 1, \tag{2.6}$$

where $\frac{d}{dt}|\psi_0(t)\rangle$ is the time derivative of the instantaneous ground state $|\psi_0(t)\rangle$ and $|\psi_m\rangle$ is the mth excited state orbital. $E_0(t)$ and $E_m(t)$ are the instantaneous eigenenergies of the ground and m^{th} excited state. As the resonant tunnelling point $V_2 \simeq V_1$ is approached,

the relevant energy gap for adiabaticity is given by $2\epsilon_t$ where ϵ_t is the tunnelling energy. In a linear dot array, cross-capacitances between gates affect the dot potentials so that the exact resonant tunnelling points occurs when $V_i \simeq V_j$ rather than at $V_i = V_j$ for adjacent dots j and k. The correct resonant tunnelling points are identified by the electron having equal probability to be in both dots, and this is taken into account in the construction of the gate voltage sequences.

After the resonant tunnelling point $V_1 \simeq V_2$, V_1 is then swept slowly in the negative direction with V_2 fixed, until the tunnel coupling is sufficiently 'off' that V_1 can be swept quickly without affecting the wavefunction now localized in dot 2. This procedure is then repeated for the rest of the dots in the linear chain to generate the full voltage shuttling sequence.

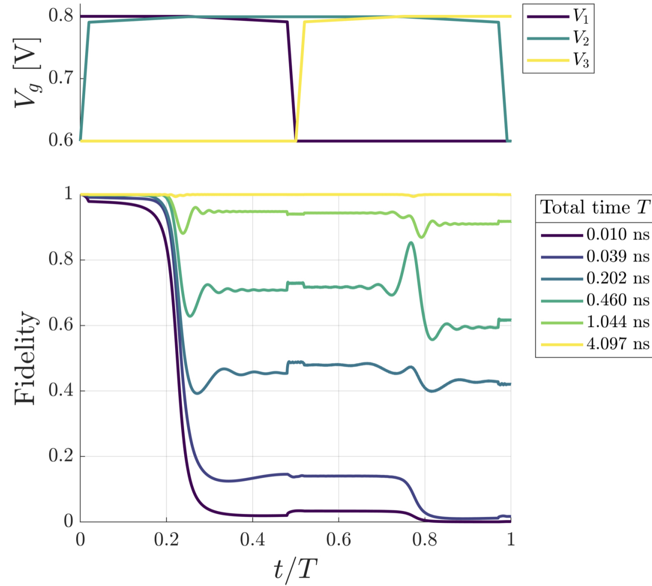

Figure 2.9: Adiabaticity threshold for a 3-dot shuttling simulation (i.e. two shuttle steps). The fidelity between the ground state wavefunction $\psi_0(t)$ and the actual wavefunction $\psi(t)$ is defined as $F = |\langle\psi_0(t)|\psi(t)\rangle|^2$. The total sequence time is T, and the normalized time t/T is given on the horizontal axis. The corresponding gate voltages are shown in the panel above, sharing the same time axis. The process is adiabatic for $T = 4.1$ ns, but non-adiabatic for $T \leq 1$ ns. For a final state fidelity $F > 0.99$, the adiabatic threshold for these simulations is $T_{th} \approx 3$ ns, or roughly 1.5 ns per shuttle step.

Figure 2.8(c) shows the central one-dimensional (1D) slice of the electrostatic potential that was used for shuttling simulations, together with the electronic ground state wavefunction at three different points in the sequence (i.e. the actual wavefunction in the ideal adiabatic limit $T \to \infty$). The snapshot at $t = 3T/8$ shows the electron tunnelling between dots 2 and 3. Here, the tunnel coupling is $t_c = 25$ μeV, giving a resonant tunnel rate $\Gamma = 24$ GHz, based on the level anti-crossing in the spectrum of two dots at zero detuning. At the end of the sequence ($t = T$), the electron is ideally localized in the rightmost dot and remains in the ground orbital state. To simulate shuttling, we solved the 1D time-dependent Schrödinger equation numerically. Results for a 3-dot simulation are shown in Figure 2.9. For T larger than a threshold value T_{th}, the shuttling is adiabatic, and the simulated wavefunction has a large overlap with the ground state at all times. Non-adiabatic behaviour occurs for $T < T_{th}$. The state fidelity is defined as $|\langle\psi_0(t)|\psi(t)\rangle|^2$, where $\psi_0(t)$ is the ground state wavefunction at time t, and $\psi(t)$ is the actual simulated state. The data in Figure 2.9 indicate $T_{th} \approx 3$ ns. For shorter sequence times, the electronic wavefunction develops appreciable overlap with excited orbital states and is not properly localized in the target dot at the end of the sequence. For the non-adiabatic curves in Figure 2.9, the initial drop in fidelity occurs when dots 1 and 2 are near the resonant tunnelling point, where the energy gap between ground and excited states is determined by the tunnel coupling. A larger tunnel coupling allows for faster shuttling, although this is limited by the condition $t_c \ll \Delta E_{\text{orb}}$, where ΔE_{orb} is the energy gap between ground and first excited orbital states in an isolated dot. Additional features can be seen in the middle of the sequence when V_1 and V_3 are swept rapidly, and near the second resonant tunnelling point. In our simulated dot, $\Delta E_{\text{orb}} \approx 3$ meV, whereas valley splittings Δ_{vs} are typically a few hundred μeV in MOS dots. Thus, including the first excited valley state is expected to require slower sweeps to remain adiabatic; however, it is mainly the faster portions of the sweep that will be modified, as the slowest segments are still governed by t_c (as long as $t_c \ll \Delta_{vs}$). The sharp but jumps in fidelity near the beginning, middle and end of the shuttling sequence are caused by discontinuities in the derivative of the shuttling pulse sequence, and using smooth voltage pulses would mitigate these jumps in fidelity.

2.3.2 Stark effect and singlet phase rotation error

A consequence of the weak (but non-zero) spin-orbit interaction in silicon together with a gate-induced local electric field is the Stark shift of the electronic g-factor [267, 121]. The fractional variation of g is typically of order $\sim 10^{-3}$ or less for practical gate voltages, but can be as large as 10^{-2}. The normal component of the electric field, $E_z = -(\vec{\nabla} V)_z$, perturbs the g value, which can be expressed as $\frac{\Delta g}{g} = \eta |E_z|^2$, where the Stark coefficient η

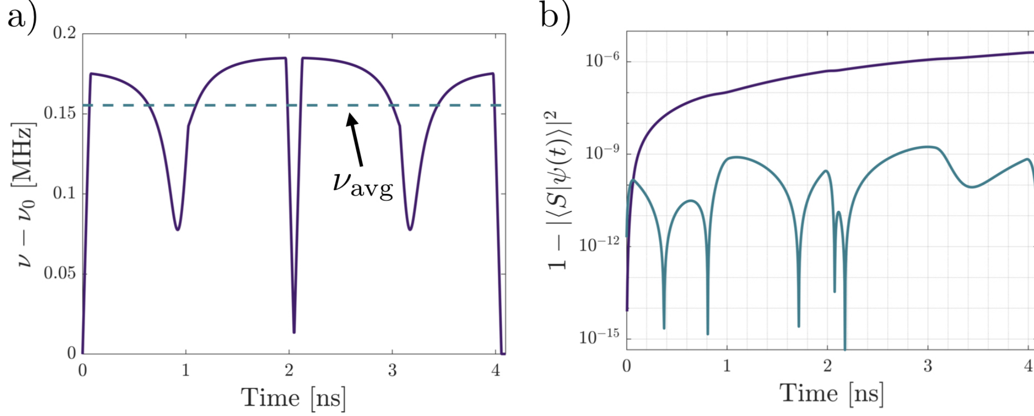

Figure 2.10: Stark effect and singlet phase rotation error for the 3-dot shuttling simulation. a) Resonance frequency shift of the moving electron relative to its initial value $\nu_0 = 40$ GHz. The average value over the full duration, $\nu_{\rm avg}$, is indicated by the red dotted line. b) Phase error quantified as $1 - F$, where $F = |\langle S|\psi(t)\rangle|^2$, $|S\rangle$ is the ideal singlet state and $\psi(t)$ is the actual spin state, a superposition of the singlet and $m_z = 0$ triplet states. The blue curve is for the case when the static electron has resonance frequency ν_0. The red curve is the result of tuning the static dot so that its electron resonance frequency is $\nu_{\rm avg}$, in which case the net phase error cancels out.

contains microscopic information and is normally determined experimentally [215]. During the shuttling process, the electronic wavefunction experiences a time-dependent field E_z which gives rise to modulation of g. For internode singlet distribution, this leads to errors since a difference in the g-factors of the static and moving electrons forming the singlet pair will cause a phase rotation of the state away from the singlet, towards the $m_z = 0$ triplet. In order to gauge the size of this error, we calculate the time-dependent g-factor of the moving dot using the instantaneous expectation value of the normal electric field, $\langle E_z(t)\rangle = \int dx\, \psi^* E_z(x,t)\psi$, with respect to the numerically calculated wavefunctions $\psi(x,t)$. We take $\eta = 2.2$ $(\mathrm{nm/V})^2$ based on the empirical results reported in [267]. Figure 2.10 shows the results from a 3-dot shuttling simulation with the same parameters used in Figure 2.9. Figure 2.10a shows the shift in resonance frequency $\nu = g\mu_B B_0/h$ as a function of time, where μ_B is the Bohr magneton, and we take $B_0 = 1.43$ T so that the initial resonance frequency is $\nu_0 = \nu(t = 0) = 40$ GHz. The resonance frequency varies on a scale of $\sim$0.2 MHz, with broad dips at the inter-dot tunneling transitions and abrupt changes corresponding to the large/fast voltage sweeps. Figure 2.10b shows the error accumulation $\epsilon = 1 - |\langle S|\psi\rangle|^2$ in terms of the overlap between the ideal singlet state $|S\rangle$ and the spin

state at time t, $|\psi(t)\rangle$. The purple curve shows the case when the resonance frequency of the static qubit is ν_0. The error surpasses 10^{-6} after these two shuttling steps. The net phase rotation error is coherent and due only to the offset between the *average* value of g for the moving dot versus the static value, and thus the error should increase with time as $\epsilon \approx 1 - \cos^2(\pi(\Delta\nu)t)$. For $\Delta\nu \approx 0.16$ MHz and $t = 4$ ns for two shuttle steps, this yields $\epsilon \approx 4 \times 10^{-6}$. For 30 shuttle steps (i.e. 1.74 μm travel distance), this would correspond to an error of about 0.1%. However, by tuning the g-factor of the static qubit to match ν_{avg} (blue dashed line in Figure 2.10a), the phase rotations are made to cancel over the course of the sequence and a much reduced error is obtained, as shown by the blue curve in Figure 2.10b. In the latter case, the maximum error is $\sim 10^{-9}$, and returns to a negligibly small value at the end of the sequence. The Stark dephasing error can thus be mitigated with proper electrostatic tuning of the static qubit. Equivalently, one can think of the tuning correction as applying a small Z rotation to one of the qubits to compensate for the net phase pickup of the shuttling sequence.

From these simulations, we find that the modulation amplitude for g scales roughly linearly with the range over which the gate voltages are swept, i.e. about 1 MHz/V. The voltage sweep range should thus be kept as low as possible to reduce the potential for Stark dephasing error. Fast noise in the electrostatic potential due to fluctuating charge defects or gate voltage noise from external sources should also be considered, as it would lead to irreversible dephasing of the singlet state. For an experimentally viable level of rms gate voltage noise of several μeV, the noise-induced fluctuation range for g would be negligibly small, only $\sim$10 Hz. Direct spin-orbit effects, on the other hand, are expected to produce larger errors. Spin-orbit coupling in a silicon 2DEG has been estimated to be of order $\sim$2 μeV$\cdot$nm [213], which yields a spin-orbit length $\sim$200 μm. For an electron travel of 1.5 μm this would produce an error in the singlet fidelity $\sim 1.4\times 10^{-4}$ due to spin rotation about a vector in the $\hat{x} - \hat{y}$ plane. Like the Stark effect phase rotation above, this is a coherent error, and is correctable by a suitable local rotation at the end of the process, in principle. Therefore, the *average* error across a large ensemble of shuttled electrons (e.g. the many shuttling lines operating in parallel across the device) is correctable by local rotations, but the error spread due to non-uniformity of devices is not. The error spread, likely of the magnitude of the average error or less, should be tolerable by the surface code. We show in the next section that a threshold of nearly 1% is obtained for dephasing error during shuttling when single and two-qubit gate errors are much smaller than the dephasing error. Multi-axis error such as weighted depolarizing noise during shuttling would likely have a lower threshold, however. Above-threshold errors would have to be mitigated by performing entanglement purification at the cost of additional ancilla qubits and gate operation overhead. We leave a more detailed analysis of the error mechanisms

associated with spin shuttling to Chapter 3.

2.3.3 Stabilizer repetition rate and other considerations

The time required to distribute a singlet between neighbouring nodes is $\approx \frac{L}{D}\tau$, where L is the internode distance, D is the dot dimension and τ is the time for a single shuttle operation. For a dot size of $D = 50$ nm and internode distance of $L = 1.5$ μm, the shuttling path consists of $\sim$30 dots (this corresponds to a total of $\sim$35 physical quantum dots per each data qubit). The shuttling parameters in Figures 2.9 and 2.10 yield $\tau = 2$ ns, for a total time of 60 ns. Single-qubit ESR rotations typically require tens of nanoseconds at least, and with the equivalent of 16.5 π rotations per subcycle, internode shuttling is not necessarily a bottleneck for the processor speed. With the inclusion of valley states and spin-orbit coupling, we expect the adiabaticity condition to be more stringent, reducing the attainable shuttling velocity. However, even if internode shuttling is an order of magnitude slower than our estimate above, the timescales of shuttling and intranode operations would still be comparable. Reducing τ further should be possible with optimization of voltage sweep and dot parameters. Elongating the dots along the shuttling direction would reduce the number of dots required and could improve the operation fidelity. Since the orbital energy spacing decreases as D^{-2}, however, the adiabaticity condition will require slower operations as D increases. Finding the optimal dot dimensions to maximize shuttling velocity while remaining adiabatic, along with designing optimal, smooth voltage sweep functions and optimizing tunnel rates is explored in Chapter 3. We emphasize that internode shuttling operations are global in that they proceed in parallel across the entire network for each stabilizer sequence (note, however, each subcycle of the surface code involves a distinct set of shuttle lines). Therefore, the electrodes controlling the shuttle path dots can be wired to common lines, assuming sufficiently high device uniformity. We expect that shuttling will be more tolerant of variations in dot parameters than qubit operations (i.e. as long as potential disorder is smaller than the minimum ground/excited state gap), although this should be investigated with numerical simulations. With common lines for shuttling, the number of external control wires can therefore remain manageable, of the order required for several plaquettes. We also emphasize that tuning the inter-dot tunnelling without explicit barrier gates relies only on the geometry of the dot gates and the voltage sequence, simplifying the device to a bare minimum of electrodes/wires.

The timescale for a full surface code cycle can be estimated by assuming realistic values for all operations in the subcycle of Figure 2.4. A full cycle consists of four subcycles (see Figure 2.2). The times we assume for singlet loading, internode shuttling, $\sqrt{\text{SWAP}}$ gates, emptying the ancilla dots and dispersive charge detection are 20 ns, 60 ns, 1 ns, 10 ns

and 10 ns, respectively. Each subcycle has the equivalent of 16.5 π rotations, including the control-Z operation involved in each ancilla readout (Z rotations are synthesized from X and Y rotations). Single-qubit ESR gates therefore make the dominant contribution to the cycle time for Rabi frequencies below ∼100 MHz. For an ESR Rabi frequency of (100, 10, 1) MHz, a full cycle requires approximately (1.2, 4.1, 33.9) μs. A plot of the full cycle rate versus ESR Rabi frequency is given in Figure 2.11. Although we have not considered logical qubit operations, which involve alternate stabilizer sequences on a subset of nodes, the four-qubit stabilizer rate should still give a reasonable estimate of processor speed for computation. The timescale for factoring a large number using Shor's algorithm has been estimated based on the surface code protocols for implementing logic gates described in [72]. To factor a 2000-bit number in a scaled-up version of our network/node processor we estimate would require ∼23 (∼7) days at 10 MHz (100 MHz) single-qubit Rabi frequency.

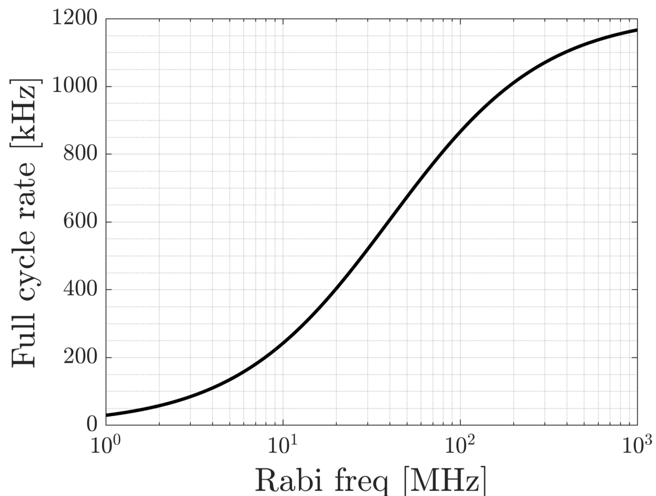

Figure 2.11: Rate for the full stabilizer cycle (both X and Z stabilizers) versus the single-qubit control Rabi frequency. Below ∼100 MHz, the cycle rate is dominated by single-qubit operations and is a linear function of the Rabi frequency. Above ∼100 MHz, the cycle rate reaches a plateau limited by the durations of all other operations. Here we assume the following operation times: singlet loading = 20 ns, internode shuttling = 60 ns, $\sqrt{\mathrm{SWAP}}$ gate = 1 ns, and gate-dispersive charge detection = 10 ns.

Although we have so far assumed a global ESR field (e.g. placing the device chip inside a macroscopic microwave cavity), the highest Rabi frequencies are typically achieved with micromagnets [286, 199, 271]. With the latter approach, direct control-Z gates also become

possible when the Zeeman energy difference between neighbouring qubits is comparable to the inter-dot tunnel coupling [271]. These gates could be significantly faster than the standard control-Z sequence we consider above, and potentially yield higher fidelities. Since micromagnets are not compatible with the singlet-triplet readout scheme proposed herein, a different method would be required, such as spin-dependent tunnelling to a reservoir together with fast charge sensing [63]. This would eliminate the control-Z gates used in the ancilla measurements in our scheme, potentially speeding up the processor. On the other hand, we expect that spin shuttling will be adversely affected by the presence of micromagnets, in general. As discussed in [291], an inhomogeneous magnetic field along the inter-dot axis together with a valley splitting comparable to Zeeman energy can yield a high probability for spin flip during shuttling. The stray field along the spin quantization axis (external field direction) would also lead to significant phase rotation in the $m_z = 0$ singlet-triplet subspace. However, since the micromagnet field is static and the shuttling voltage sequence can be fixed, the phase pickup at the end of the sequence is, in principle, correctable by an appropriate local Z rotation.

2.4 Surface code error thresholds

In quantum error correction, if the error rate of the physical components is below a certain threshold, the error rate of the logical qubits can be reduced by scaling up the code. The error threshold of surface codes is highly dependent on the way the stabilizer check circuit is implemented and the error models of the physical components. Its exact value can be obtained via simulations of the error correction circuit using the Gottesman-Knill theorem [91, 1]. Assuming depolarizing noise for all the physical components, the error threshold of surface codes can take values between $0.5\% \sim 1\%$ under different circuit implementations [244]. In our proposed quantum dot network architecture, $\sqrt{\text{SWAP}}$ is the basic building block of two-qubit gates instead of control-Z or control-NOT gates. Failures of $\sqrt{\text{SWAP}}$ will predominantly lead to SWAP errors instead of depolarizing errors which we show in Section 2.4.1. For the shuttling process, we consider dephasing noise instead of depolarizing noise based on the findings of Section 2.3 that phase rotation due to g-factor modulation should dominate the singlet state error. Although this is a coherent error for each shuttled electron, there is a spread in the errors across the device, and this justifies the use of a dephasing model. Therefore, the error types we consider in the stabilizer check circuit are the following:

- Single-qubit gates, initialization and measurement: depolarizing errors with proba-

bility p_{1q}

$$\rho \to (1-p_{1q})\rho + \frac{p_{1q}}{3}\left(X\rho X + Y\rho Y + Z\rho Z\right)$$

- $\sqrt{\text{SWAP}}$ gate: SWAP errors with probability p_{swap}

$$\rho \to (1-p_{swap})\rho + p_{swap}\text{SWAP}\cdot\rho\cdot\text{SWAP}$$

- Shuttling process: dephasing errors (due to g-factor modulation) with probability p_{sh}

$$\rho \to (1-p_{sh})\rho + p_{sh}Z\rho Z$$

2.4.1 Errors associated with the control-Z gate

Here we will justify the $\sqrt{\text{SWAP}}$ error model used to calculate the surface code error thresholds. The effective Hamiltonian for the exchange interaction between two electron spin qubits is written as $H = J\,\vec{\sigma}_1\cdot\vec{\sigma}_2$ where J is the exchange interaction strength. We assume that before the two-qubit gate, the gate voltages of the system are tuned such that $J = 0$. At the start of the two-qubit gate, J is quickly raised to a non-zero value and remains constant during the gate evolution. Afterwards, the voltages are tuned to return J to 0. The unitary evolution operator acting on the basis spin states $\{|\uparrow\uparrow\rangle, |\uparrow\downarrow\rangle, |\downarrow\uparrow\rangle, |\downarrow\downarrow\rangle\}$ is

$$\hat{U}_{ex}(\tau) = \begin{bmatrix} e^{-iJ\tau/2} & 0 & 0 & 0 \\ 0 & \cos\left(\frac{J\tau}{2}\right) & -i\sin\left(\frac{J\tau}{2}\right) & 0 \\ 0 & -i\sin\left(\frac{J\tau}{2}\right) & \cos\left(\frac{J\tau}{2}\right) & 0 \\ 0 & 0 & 0 & e^{-iJ\tau/2} \end{bmatrix} \tag{2.7}$$

If we substitute $\frac{J\tau}{2} = \theta$, we have

$$\hat{U}_{ex}(\theta) = \cos(\theta)\,I - i\sin(\theta)\,\text{SWAP} \tag{2.8}$$

A SWAP gate corresponds to $\theta = \pi/2$, and a $\sqrt{\text{SWAP}}$ gate corresponds to $\theta = \pi/4$. In experiments, over and under rotations of exchange occur due to imprecise pulse timing or fluctuation of exchange strength due to charge noise. If during the execution of $\sqrt{\text{SWAP}}$ gate, there is an equal probability of a over and under rotation by $\epsilon \ll 1$, then the applied

operator is

$$\hat{U}_{ex}\left(\frac{\pi}{4}\pm\epsilon\right) = \cos\left(\frac{\pi}{4}\pm\epsilon\right)I - i\sin\left(\frac{\pi}{4}\pm\epsilon\right)\text{SWAP} \tag{2.9}$$

$$= \frac{1}{\sqrt{2}}(I - i\text{SWAP}) \pm \frac{\epsilon}{\sqrt{2}}(-I - i\text{SWAP}) \tag{2.10}$$

$$= \hat{U}_{ex}\left(\frac{\pi}{4}\right) \pm \epsilon\,\hat{U}_{ex}\left(\frac{3\pi}{4}\right) \tag{2.11}$$

This gives the overall effective operation on a density matrix ρ as

$$\frac{1}{2}\hat{U}_{ex}\left(\frac{\pi}{4}+\epsilon\right)\rho\hat{U}^{\dagger}_{ex}\left(\frac{\pi}{4}+\epsilon\right)+ \frac{1}{2}\hat{U}_{ex}\left(\frac{\pi}{4}-\epsilon\right)\rho\hat{U}^{\dagger}_{ex}\left(\frac{\pi}{4}-\epsilon\right) = \hat{U}_{ex}\left(\frac{\pi}{4}\right)\rho\hat{U}^{\dagger}_{ex}\left(\frac{\pi}{4}\right) + \epsilon^2\,\hat{U}_{ex}\left(\frac{3\pi}{4}\right)\rho\hat{U}^{\dagger}_{ex}\left(\frac{3\pi}{4}\right) \tag{2.12}$$

$$= \sqrt{\text{SWAP}}\rho\sqrt{\text{SWAP}}^{\dagger} + \epsilon^2\left(\text{SWAP}\sqrt{\text{SWAP}}\right)\rho\left(\text{SWAP}\sqrt{\text{SWAP}}\right)^{\dagger} \tag{2.13}$$

From this, we either have a perfect $\sqrt{\text{SWAP}}$ or a ϵ^2 probability of having a SWAP error on top of $\sqrt{\text{SWAP}}$. This justifies the noise model for the $\sqrt{\text{SWAP}}$ gate adopted in these simulations:

$$\rho \to (1 - p_{swap})\rho + p_{swap}\text{SWAP}\cdot\rho\cdot\text{SWAP}$$

where p_{swap} is the error associated with the $\sqrt{\text{SWAP}}$ gate. Similar arguments can be applied to other symmetric over/under-rotation distributions that center on the correct rotation angles.

Given this noise model, we now discuss the different non-Pauli errors that can occur during the execution of a control-Z gate. In the stabilizer circuit (see Figure 2.4), control-Z gates are implemented as

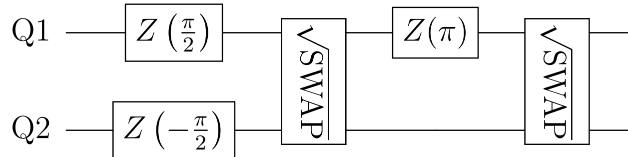

where Q1 and Q2 simply denote qubit 1 and qubit 2. There are three types of non-Pauli noise that can occur:

- SWAP error after second $\sqrt{\text{SWAP}}$ $\Rightarrow$ SWAP error after the control-Z
- SWAP error after first $\sqrt{\text{SWAP}}$ $\Rightarrow$ $(Z_1Z_2)\cdot$SWAP error after the control-Z
- σ_1^i error (for $i = x, y, z$) after $Z(\pi)$ $\Rightarrow$ $\sqrt{\text{SWAP}}\cdot\sigma_1^i\cdot\sqrt{\text{SWAP}}^\dagger$ error after the control-Z.

To efficiently simulate the error correction circuit using the Gottesman-Knill theorem, these non-Pauli error operators must be converted into Pauli noise by twirling.

2.4.2 Twirling

Twirling is used for converting arbitrary error channels into Pauli channels by conjugating the noise with Pauli gates randomly chosen from the twirling gate set [27]. The Pauli channel we obtain is the incoherent superposition of the Pauli basis of the original noise. For example, after twirling, a swap noise SWAP $= \frac{1}{2}(I_1I_2 + X_1X_2 + Y_1Y_2 + Z_1Z_2)$ will be transformed into $\frac{1}{4}(\widehat{I_1I_2} + \widehat{X_1X_2} + \widehat{Y_1Y_2} + \widehat{Z_1Z_2})$, where $\widehat{\ }$ denotes a super-operator (i.e. $(\widehat{A}+\widehat{B})\rho = A\rho A^\dagger + B\rho B^\dagger$). Twirling is proven to be effective in error threshold simulations [80, 95].

To run error threshold simulations, we must first obtain the error distribution for each round of the stabilizer check. This can be obtained via a full quantum simulation of the stabilizer check circuit, shown in Figure 2.12. In this circuit, the non-Pauli errors arise from the failures of the elements comprising the control-Z gates as discussed above in Section 2.4.1. Using conventional twirling on these two-qubit errors requires the full Pauli set of the size $4^2 = 16$ as the twirling gate set [9, 61]. Hence, if we want the exact error distribution for each round of stabilizer check, 16^6 possibilities must be iterated over since there are 6 control-Z gates in the circuit. In the stabilizer check circuit, control-Z gates are always followed by an X measurement whose results are forgotten at the end; we only record the parity of the X measurements in both the preparation and the stabilizer check stage. Using the method proposed in [27], it is found that the gate set $\{I, X_2\}$ of size 2 is sufficient for twirling. Thus, we only need to iterate over 2^6 possibilities instead of $16^6 = 2^{24}$ to obtain the exact error distribution. The twirling circuit is shown in Figure 2.13.

2.4.3 Threshold simulation results

If we assume no dephasing error during shuttling ($p_{sh} = 0$), and fix the error ratio between single-qubit errors (p_{1q}) and SWAP errors (p_{swap}), we obtain the threshold plots for p_{swap}

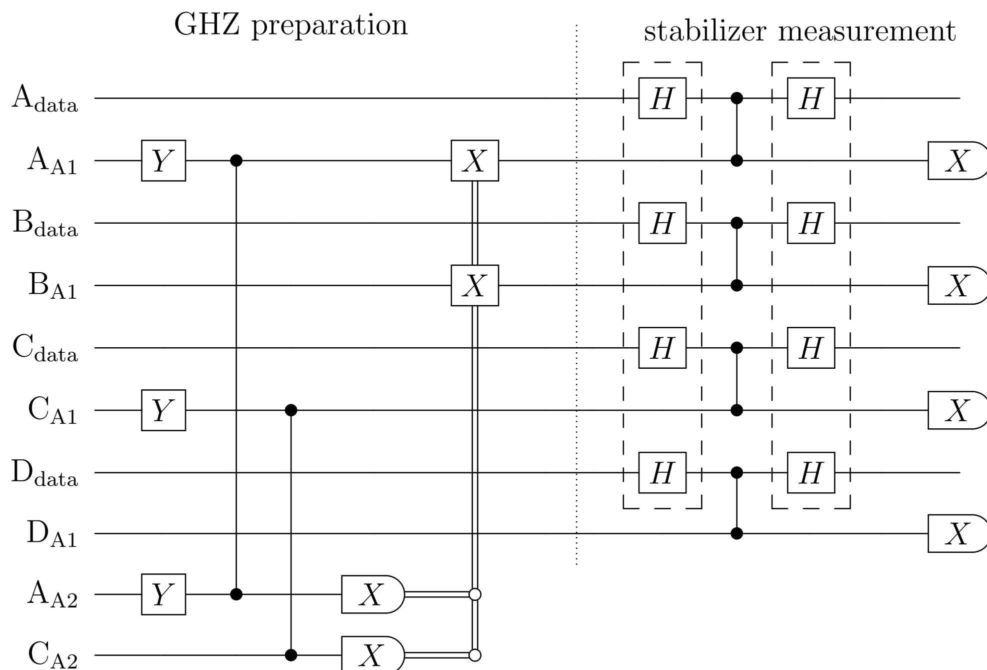

Figure 2.12: Simplified diagram of the stabilizer check circuit. Control-Z gates are indicated by the vertical lines connecting dots. The following input pairs are initialized as singlets: (A_{A1}, B_{A1}), (C_{A1}, D_{A1}), (A_{A2}, C_{A2}). The Hadamard (H) gates in the dashed boxes are used only for the X stabilizer. When the parity of the measurement results on A_{A2} and C_{A2} is odd, two additional X gates are applied on A_{A1}, B_{A1} to produce the GHZ state.

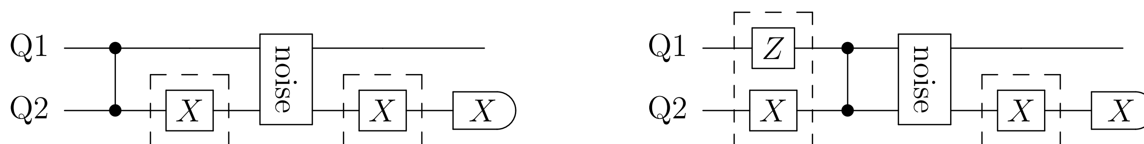

Figure 2.13: **Left circuit:** If it were the case that the noise existed as a separate physical process from the ideal gate, then one could target the noise directly by twirling operations (shown in dashed boxes). **Right circuit:** In reality the noise process is inseparable from the ideal gate, therefore we permute one of the twirling operations back through that gate to obtain the physically achievable twirling protocol.

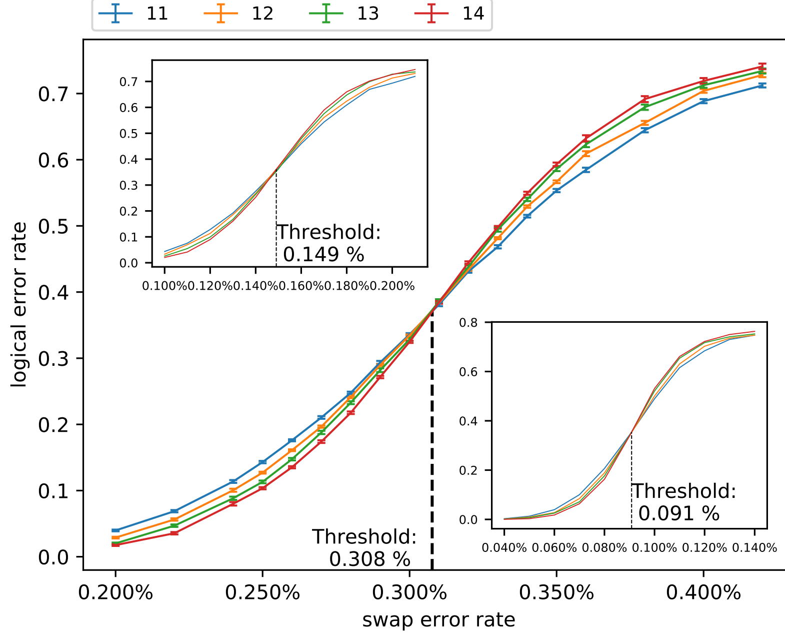

Figure 2.14: Fault tolerance thresholds with respect to error in $\sqrt{\text{SWAP}}$ gates, with $p_{sh} = 0$ and different ratios $\frac{p_{1q}}{p_{swap}}$. **Main plot:** $\frac{p_{1q}}{p_{swap}} = 0.1$. **Top left:** $\frac{p_{1q}}{p_{swap}} = 0.5$. **Bottom right:** $\frac{p_{1q}}{p_{swap}} = 1.0$. The legend shows curves of different colours corresponding to different code distances d. The corresponding number of nodes (data qubits) in our network is $d^2+(d-1)^2$. The dashed lines indicate the threshold values.

as shown in Figure 2.14. The threshold is defined as the gate error rate at which there is a crossover between the logical error rate increasing with code size (above threshold) and the error rate decreasing with code size (below threshold). The threshold can be seen here for code distances ranging from $d = 11$ to 14, where the corresponding number of nodes (or data qubits) in our network is $d^2 + (d-1)^2$. Single-qubit operations are typically achieved with higher fidelity than two-qubit operations. Under the realistic assumption that $\frac{p_{1q}}{p_{swap}} = 0.1$, we obtain a threshold of 0.31% for p_{swap}, which is of the same order as the threshold for a depolarizing noise model (0.5% $\sim$ 1% [244]). Keeping the assumption that $\frac{p_{1q}}{p_{swap}} = 0.1$, and fixing p_{swap} to a below-threshold value 0.2%, we obtain the threshold of the shuttling dephasing error to be 0.79% as shown in Figure 2.15. This threshold approaches 2% in the limit $p_{swap}, p_{1q} \to 0$. This shows a relatively high tolerance of the surface code to spin dephasing errors during internode shuttling. As noted in Section 2.2.1, each Z

and X stabilizer is split into two sequential operations since any two neighbouring 4-node plaquettes cannot be stabilized simultaneously. In these simulations, we have neglected this by assuming that idle data qubits decohere at a much slower rate than those experiencing active gate operations.

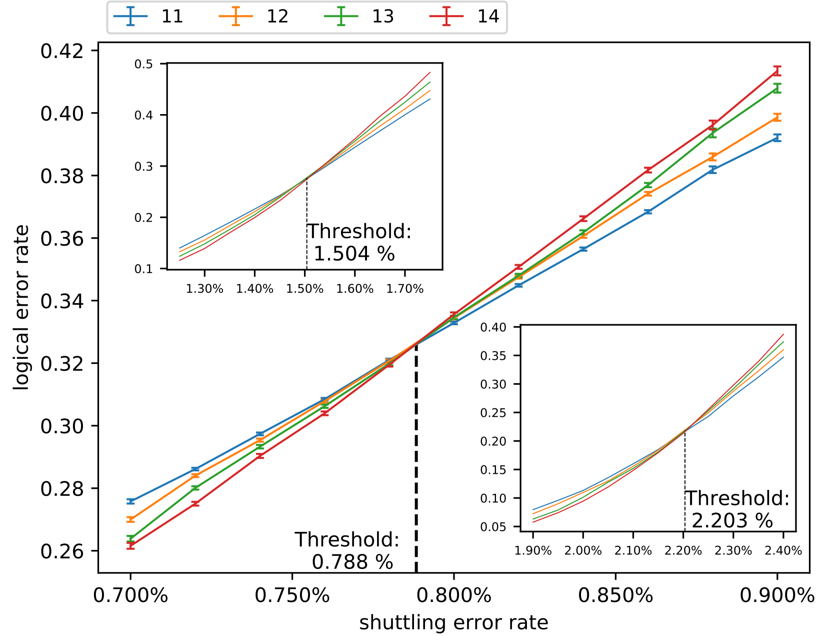

Figure 2.15: Fault tolerance thresholds with respect to dephasing errors during shuttling, with $\frac{p_{1q}}{p_{swap}} = 0.1$ and different values of p_{swap}. **Main plot:** $p_{swap} = 0.2\%$. **Top left:** $p_{swap} = 0.1\%$. **Bottom right:** $p_{swap} = 0$. The legend shows curves of different colours corresponding to different code distances d. The dashed lines indicate the threshold values.

Finally, we note that demonstrated electron spin coherence times in MOS dots (with isotopic enhancement to remove ^{29}Si nuclear spins) are compatible with fault tolerance in our architecture. [269] reports dephasing times $T_2^* \approx 120\mu$s and $T_2 \approx 28$ ms under CPMG refocusing. This should be compared to our estimated stabilizer cycle time $\sim$2 μs. Thus, with refocusing, the probability of a phase flip error purely due to T_2 is of order 10^{-4} per cycle, which should be well below the fault tolerance threshold for the surface code.

2.5 Conclusions

In summary, we have proposed a surface code realization for quantum dot spin qubits in silicon based on a network of nodes. The spatial separation of the nodes allows data qubits to be better isolated and will ease constraints on wiring density and integration of classical circuit elements to support control and readout functions. As each node contains fewer than 10 quantum dots, demonstrating a fully functional node is nearly within the grasp of current technology. Connecting nodes relies on shuttling of electrons over medium-range distances ($\sim$1 μm) and maintaining the fidelity of the distributed spin singlet states. We find value in separating the scaling problem into these two streams - local operations and entanglement distribution - that can be developed in parallel. Realistic simulations with the simplest possible gate electrode geometry show that adiabatic shuttling can be realized on timescales that do not necessarily present a speed bottleneck to the processor. Simulations suggest that the dominant error in a clean system is uncontrolled phase rotation due to the modulation of the electronic g-factor during shuttling, owing to the Stark effect. While this error $\sim$0.1% may be tolerable by a scaled-up surface code, we show how it can be much further reduced by appropriate tuning of the stationary electron's g-factor. These shuttling results, however, do not tell the whole story because we have not included multiple valleys, direct spin-orbit coupling or charge state decoherence in the simulations. The combined effects of these factors could indeed make coherent spin transport over many dots difficult or impossible and are studied in Chapter 3. While we have chosen to focus on spin shuttling in this chapter, of course, any viable method for internode entanglement distribution can be used in its place.

Achieving fault tolerance is a critical goal for a scalable processor. Using reasonable noise models, we estimate error thresholds with respect to single and two-qubit gate fidelities as well as dephasing errors due to shuttling. A twirling protocol allows us to transform the non-Pauli noise associated with exchange gate operations into Pauli noise, making it possible to use the Gottesman-Knill theorem to efficiently simulate large codes. Not surprisingly, the surface code is found to be more robust to singlet dephasing errors than to errors in $\sqrt{\text{SWAP}}$ operations. A $\sqrt{\text{SWAP}}$ error threshold of 0.31% was found when the probability of single-qubit error is 0.1 times that of the two-qubit exchange gate. A dephasing (shuttling) threshold of 0.79% was found when $\sqrt{\text{SWAP}}$ and single-qubit error probabilities are 0.2% and 0.02%, respectively. Thus, compared to the current state of the art in silicon spin qubits [271, 269, 64, 286], both single-qubit and two-qubit gate infidelities must be reduced by at least an order of magnitude to achieve fault tolerant levels (of course, this statement applies equally well to other realizations and error correction schemes). The error models used to estimate fault tolerance thresholds will become

more realistic as they are further informed by experiments at progressively finer levels of control. We also expect that the uniformity of tuning parameters/properties of nominally identical dots must improve by at least an order of magnitude compared to what has been demonstrated experimentally so far [289]. This is so that shared control lines, a practical necessity for scalability, can be feasible. Taking advantage of the internode spacing in our architecture, we envision that local floating gate electrodes could be programmed to apply small electrostatic corrections to the quantum dots forming the nodes, allowing control pulse sequences to be applied globally. On the other hand, we expect that electron shuttling can be made robust to sufficiently small variations in dot uniformity, so that shared global control of spin transport will be feasible without the need for correction gates. The robustness of shuttling operations is a subject for future work.

Similar to [193], we have only considered the case that all nodes perform four-qubit stabilizer operations, which is equivalent to logical qubit storage rather than computation. It is expected that error thresholds for computation will be similar, since the four-qubit stabilizer constitutes the bulk of operations and alternative stabilizers needed for computation are only required at boundaries. It remains to determine the precise operations within boundary nodes during computations. Clearly, we must have the ability to address boundary nodes individually, as well as the bulk nodes collectively, noting that the boundaries move during computations and thus can involve many, if not all, nodes at some point in the computation. Individual addressing of nodes will also be required during initial calibration, e.g. for setting the values of correction floating gates. An appropriate multiplexing scheme utilizing conventional transistor circuits as in [266] could be applied, noting that our scheme can make available enough space for 3D interconnects using present-day CMOS technologies (power dissipation at mK temperatures remains a challenge). Performing massively parallel readout operations in any surface code architecture is another challenge for which relatively little has been discussed in literature. Both time and frequency multiplexing can be used with RF reflectometry, but it is not yet obvious how this can be done at large scale while keeping measurement latency within acceptable bounds [32].

Chapter 3

Simulated coherent electron shuttling in silicon quantum dots

Chapter contributions: Benjamin D. Shaw assisted with early nextnano++ simulations.

This chapter is adapted from the publication:

Buonacorsi, B., Shaw, B., and Baugh, J. (2020). Simulated coherent electron shuttling in silicon quantum dots. *Physical Review B, 102*(12), 125406.

3.1 Introduction

The small footprint of a gate-defined quantum dot (QD), ∼50−100 nm in scale, means that high qubit density is a long-term advantage for scaling, but also brings significant practical challenges. The ability to rapidly transport quantum information over intermediate length scales would mitigate some of these challenges and be a valuable resource from an architecture design perspective. Recent architecture proposals such as the one presented in Chapter 2 as well as Li *et al.* [164] feature coherent spin shuttling as a primary resource. Chapter 2 showed how shuttling can be used to share entanglement between small neighbouring computational nodes, enabling the 2D surface code to be mapped to a network-of-nodes architecture. Separating the scaling problem into intra-node and inter-node operations is advantageous, and creates space for practical wiring interconnects while maintaining a high qubit density compared to state of the art ion trap and superconducting qubit technologies.

Coherent transport of quantum information encoded in the electron spin can be realized in several ways. Surface acoustic waves (SAWs) in a piezoelectric material such as GaAs have been used to deterministically transport single charges over several microns [131, 260, 10, 248]. Silicon is not piezoelectric, but a thin ZnO layer was shown to enable SAW-driven charge transport in silicon [25]. One drawback of the SAW approach is that it requires transducers that are large compared to QDs. Another approach is to manipulate the exchange interaction in a linear array of singly-charged QDs. An arbitrary spin state can be transported either via a sequence of SWAP gates [127] or by an "all-on" method such as coherent transfer by adiabatic passage (CTAP) [92, 216]. This has the advantage of a fixed charge state for all dots, but requires fine-tuned control of tunnel barriers and therefore has a limited resilience to charge and voltage noise. In this chapter, we extend the results from Section 2.3 and focus on coherent shuttling: electrostatically-driven, sequential tunneling of a single charge/spin through a chain of empty QDs. Coherent spin shuttling was demonstrated in GaAs QD devices [76, 68], despite the presence of nuclear-spin induced decoherence. In silicon, shuttling of a single charge across a linear array of nine dots in 50 ns has been reported [181], and recently coherent spin shuttling was demonstrated as well [285]. It is anticipated that the weak spin-orbit interaction for electrons in silicon, together with the ability to remove nuclear spins through isotopic purification, could set the stage for maintaining spin coherence over long shuttling distances. Prior theoretical studies have examined the impact of spin-orbit and valley physics on spin transport fidelities [165, 291, 84]. It was found that the presence of multiple valley states and variation in valley phase can give rise to significant error, although this can be mitigated by operating away from so-called leakage hot spots.

In this chapter, we expand on the shuttling simulations performed in Section 2.3. We connect the shuttling problem to realistic devices, developing tools to optimize both the shuttling voltage sequences and the device geometry. First, an algorithm for constructing voltage sequences is designed that maintains a constant adiabatic parameter. These constant-adiabaticity control sequences are a useful tool for systematic comparison and optimization, and they will be used throughout the paper. The device layout investigated is a simplified MOS geometry in which each accumulation mode QD is formed by a single plunger gate electrode, with no explicit tunnel barrier gates. Tunnel rates are controlled both by the voltages on adjacent plunger gates and by the fixed spatial gaps between electrodes. Potentials from a 3D finite element device model are mapped to 1D potentials to simulate shuttling along a chain of dots. Charge shuttling in the absence of spin and valley effects is first investigated, to test the performance of the adiabatic control sequences with respect to the speed and fidelity of single charge transport. We use an effective Hamiltonian, in which detuning and orbital excitation energies are determined based on the finite

element potentials, to optimize the device geometry for shuttling speed and fidelity. Subsequently, we implement spin and valley physics in an effective Hamiltonian, and gauge the fidelity of maintaining a desired spin state. This is quantified by the entanglement fidelity of a spin singlet pair, in which one member of the pair is shuttled and the other is static, with the two electrons assumed to be well separated. In the regime that Zeeman energy is smaller than the resonant tunneling energy, we identify a parameter range in which high shuttling fidelities and speeds up to ∼80 m/s are possible. The implications of these results for coherent spin transport in ^{28}Si MOS qubit architectures are discussed.

3.2 Constant-adiabaticity control sequences

For an adiabatic tunneling process, an electron initialized in the orbital ground state, $|\psi_0\rangle$, remains in the ground state at all times. The adiabaticity of the process is quantified by the approximate adiabatic parameter [42]

$$\xi(t) = \sum_{m\neq 0} \hbar \left| \frac{\langle \psi_m(t)| \frac{d}{dt} |\psi_0(t)\rangle}{E_0(t) - E_m(t)} \right| \tag{3.1}$$

where the index m runs over all excited states, and $E_m(t)$ is the energy of the eigenstate $|\psi_m\rangle$ at time t. When $\xi(t) \gtrapprox 1$, diabatic transitions to excited orbital states occur with high probability. Conversely, when $\xi(t) \ll 1$, the orbital state retains a large overlap with the ground state. The condition $\xi(t) \ll 1$ is achieved when the Hamiltonian changes slowly with respect to the frequency corresponding to the ground-excited state gap.

Tunneling between two QDs is achieved by sweeping the inter-dot detuning $\epsilon = \epsilon_1 - \epsilon_2$, where ϵ_i corresponds to the orbital ground state energy of the ith QD. In previous theoretical studies [18, 291] and experimental demonstrations [181, 76] of shuttling/tunneling, linear detuning pulses were used. While practically convenient, linear pulses do not maintain constant adiabaticity, and discontinuities in the pulse shape can cause undesired excitations. In order to systematically compare shuttling simulations with different geometrical and voltage parameters, and to optimize the device design for shuttling speed, it is convenient to use pulses that maintain a constant ξ. We design such pulses using an algorithm described below. Fidelity of a pulse is defined by the overlap of the final orbital state, in which the electron is located in the target dot, with the ground orbital state in the target dot. The fidelity of an adiabatic pulses can be tuned to an arbitrary value by choice of ξ, if only the orbital state is considered (spin and valley physics neglected).

Consider a linear chain of n QDs described by the Hamiltonian $H(\vec{V}) = \frac{-\hbar^2}{2m^*}\nabla^2 + v(V_1, ..., V_n)$ where v is the electrostatic potential. Here, only the orbital component of the electron wavefunction is considered (spin will be considered in later sections), and we assume there is no ground state degeneracy. $\{V_i\}$ are the voltages applied to the gate electrodes that each define an individual accumulation-mode QD and tune the energy levels ϵ_i. The set of these voltage parameters is vectorized as $\vec{V}$. We wish to find a pulse sequence $\vec{V}(t)$ that shuttles the electron through the n-dot chain while keeping ξ fixed. In later sections, we will use an effective Hamiltonian expressed directly in terms of the dot potentials ϵ_i. In that case, the vector of dot potentials $\vec{\epsilon}(t)$ is input into the the algorithm as the set of control variables. The algorithm is presented below for a double QD system, but readily generalizes to an n-dot chain.

1. Choose voltage configurations $\{\vec{V}(A), \vec{V}(B), \vec{V}(C)\}$ at three time points (A, B, C) that the Hamiltonian should pass through during the shuttling process.
   (a) $\vec{V}(A)$ tunes H so that the electron is fully localized in QD #1 ($\epsilon < 0$).
   (b) $\vec{V}(B)$ tunes H so that the electron resonantly tunnels between the two QDs ($\epsilon = 0$).
   (c) $\vec{V}(C)$ tunes H so that the electron is fully localized in QD #2 ($\epsilon > 0$).
2. Select a sufficiently large number, N, of voltage configurations interpolated between $\vec{V}(A)$, $\vec{V}(B)$ and $\vec{V}(C)$, and choose a desired adiabatic parameter ξ'.
3. For each interpolated voltage configuration $\vec{V}(i)$:
   (a) Solve for the eigenstates of the Hamiltonians $H(\vec{V}(i))$ and $H(\vec{V}(i) + \delta\vec{V}(i))$ where $\delta\vec{V}(i)$ is a small difference in the control pulse.
   (b) Use the calculated eigenstates and $\delta\vec{V}(i)$ to approximate $\frac{d}{d\vec{V}(i)}|\psi_0(\vec{V}(i))\rangle$.
   (c) Find $\frac{d\vec{V}(i)}{dt}$ such that $\frac{d\vec{V}(i)}{dt}\frac{d}{d\vec{V}(i)}|\psi_0(\vec{V}(i))\rangle$ when used in Equation 3.1 gives $\xi = \xi'$.
4. Let $\vec{V}(t_i)$ correspond to voltage configuration $\vec{V}(i)$ at time t_i. Set the initial condition as $\vec{V}(t_0 = 0) = \vec{V}(A)$. Then convert each voltage configuration index $V(i)$ to $V(t_i)$ by $t_i = t_{i-1} + \frac{dt}{d\vec{V}(i)}(\vec{V}(i+1) - \vec{V}(i))$.

The algorithm above does not assume a fixed pulse duration, but converges to a certain length based on the chosen value of ξ. Convergence requires selecting a sufficiently large

number of interpolation points in step 2 (N is deemed sufficiently large when the final pulse does not vary with increasing N). The relationship between the applied voltages $\vec{V}$ and the electrostatic potential is evaluated using a self-consistent 3D Poisson solver based on the chosen device geometry (this is not required when using the effective Hamiltonians of Sections 3.3.3 and 3.4 expressed directly in terms of the dot potentials ϵ_i). A large set of gate voltage configurations are simulated in order to provide a 'library' of potential landscapes to be used in the algorithm. The discrete set of potentials are interpolated to provide a quasi-continuous distribution (step 2). We approximate the true potentials by ignoring the effect of the single electron charge and solving the Poisson equation in the limit of zero charge density. While quantitatively approximate, this allows us to qualitatively study shuttling dynamics while avoiding the technical difficulty of maintaining a fixed charge in a Schrödinger-Poisson solver. In the Section 3.3.1, the effect of an electron charge on a double QD potential is calculated, showing that at resonant tunneling, reduction of the tunnel barrier height is the main effect. This can be compensated for, in principle, by suitable adjustment of the gate geometry and pulse design. In the effective Hamiltonian simulations of Sections 3.3.3 and 3.4.2, we use the Schrödinger-Poisson method to determine orbital energy spacings and to determine the tunnel coupling as a function of double QD geometry.

Longer QD chains are treated by adding more voltage configurations at step 1 ($2n-1$ configurations for shuttling through n dots). For example, shuttling to a third dot is realized by including configurations $\{\vec{V}(D), \vec{V}(E)\}$. It is assumed that there is no ground state degeneracy during shuttling, as this causes Equation 3.1 to diverge and the algorithm to fail. Shuttling pulses can also be found for an electron in the kth excited state by substituting $|\psi_k\rangle$ for $|\psi_0\rangle$ in Equation 3.1, assuming the orbital relaxation rate is slow compared to shuttling. Our approach for designing adiabatic control pulses is valid for any Hamiltonian of the form $H = H_0 + H_c(u_\alpha, u_\beta, \dots)$ where H_0 is static and H_c is a time-varying term with control parameters $\{u_\alpha, u_\beta, \dots\}$. However, if H is complex or contains oscillatory terms, evolution under the pulse may not adiabatic, as Equation 3.1 does not guarantee adiabaticity for Hamiltonians of that form [42].

3.3 Charge shuttling

This section investigates the performance of adiabatic pulses by simulating electron shuttling along a triple QD linear chain, considering only single-valley orbital states and neglecting both spin and valley physics. This pertains to the physical case of charge shuttling, in which the metric of interest is the fidelity of remaining in the orbital ground state. In

the single-valley case the ground state is unique; in the presence of valley physics, it is a ground state manifold. While the simulations presented in this section neglect multiple valley states, in Section 3.4.2 we have confirmed that the results are equivalent to having equal valley splittings and zero valley phase difference between adjacent dots, with valley degrees of freedom traced out at the end of the calculation. The purpose of this section is also to introduce the device geometry of interest, the application of constant-adiabaticity pulses, and a method for optimizing device geometry for speed and fidelity of charge shuttling. Each accumulation-mode QD is defined by a single plunger gate, and there are no explicit gates to control tunnelling barriers [18, 217]. Tunnelling is controlled both by the applied gate voltages and the fixed geometric gap separating adjacent gates.

3.3.1 Modelling the electrostatic potential

The full device structure of the QD linear chain, including the metal gates and the Si/SiO_2 heterostructure, is simulated using a self-consistent 3D Poisson solver in nextnano++ [11] to determine the relationship between the electrostatic potential of the quantum dot device and the applied gate voltages. A large set of gate voltage configurations are simulated in order to provide a 'library' of potential landscapes to be used in the constant adiabatic control algorithm. The discrete set of potentials are interpolated to provide a quasi-continuous distribution used in step 2 of the algorithm. We approximate the true potentials by ignoring the effect of the single electron charge and solving the Poisson (P) equation in the limit of zero charge density. While quantitatively approximate, this allows us to qualitatively study shuttling dynamics while avoiding the technical difficulty of maintaining a fixed charge in a Schrödinger-Poisson (SP) solver. However, SP calculations provide more realistic simulations of nanoscale QD structures compared to P calculations as they properly model the quantum effect of the accumulated electron density on the potential landscape. It is worthwhile to quantify the impact that using just a P calculation has on the simulations.

Electron shuttling through a linear QD chain can be realized by sweeping the inter-dot detuning using the plunger gates that define each QD. In a real linear QD chain, sweeping the plunger gates does not change the total electron occupancy if the QDs are well separated from a nearby electron reservoir. However, in a P or SP simulation, the electron density can change continuously as the plunger gate are swept. This varying electron density makes it difficult to compare potential landscapes for different plunger gate voltage configurations. Ideally, the integrated electron density could remain fixed during the SP calculation so the impact of the accumulated electron on the electrostatic potential is consistent; however, this is not possible in standard P and SP calculations. For the shuttling simulations done

in this section, the plunger gate voltages were tuned below the device's turn-on voltage so that the integrated electron density was 0 e^- for all voltage configurations. In this 0 e^- regime, P and SP calculations provide the same potential landscape and is why P calculations were used in this section.

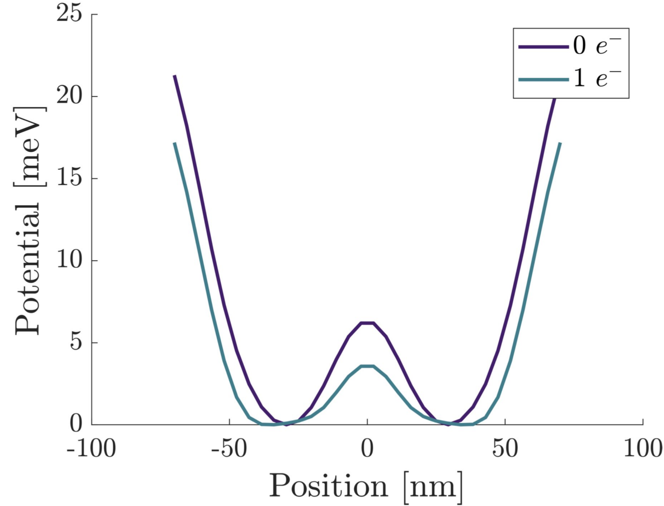

Figure 3.1: Effect of a single electron on a self-consistent calculation of a double well potential. The 1D 0 e^- (purple) and 1 e^- (blue) potentials were extracted from a 3D self-consistent Poisson calculation and a 3D self-consistent Schrödinger-Poisson calculation respectively. The electric field from the single electron lowers the barrier height between the two potential wells which raises the inter-dot tunnel coupling while simultaneously widening the individual potential well widths which lower the QD orbital spacing.

We now quantify how neglecting the electron in the P calculation impacts the electron shuttling results presented in Section 3.3.2 where these calculations are used. To do so, a 3D simulation of a double QD was done in nextnano++, and the respective plunger gate voltages were set equal to form a symmetric double well potential. The plunger gate voltages were tuned to both the 0 e^- regime just below the device turn-on and the 1 e^- regime and are simulated using a P and SP calculation respectively. 1D extractions of the 3D potentials are plotted in Figure 3.1. The 1D cuts are taken 1 nm below the Si/SiO_2 interface along the of QD chain (white dashed line in Figure 3.2b). The addition of the electron increases the inter-dot tunnel coupling from $t_c \approx 25$ μeV (0 e^-) to $t_c \approx 60$ μeV (1 e^-) due a reduction in the barrier height. Increasing t_c does not qualitatively impact the results shown later in Section 3.3.2, and simply increases the shuttle speed by reducing the

constant-adiabaticity pulse length. This increase in t_c can be compensated for by suitable adjustment of the gate geometry and pulse design. The electron has the additional effect of widening the individual potential wells which decreases the orbital spacing for each QD. For QD geometries where the orbital spacing is much greater than t_c, the lower orbital spacing will not affect shuttling performance. However, if the orbital spacing and t_c are comparable, then the lower orbital spacing can cause longer shuttling pulses in order to maintain adiabaticity as seen in Section 3.3.3. In the effective Hamiltonian simulations of Sections 3.3.3 and 3.4.2, we use the SP method to determine orbital energy spacings and to determine the tunnel coupling as a function of double QD geometry.

3.3.2 Trade-off between fidelity and shuttle speed

Figure 3.2a shows a 3D view of a triple QD model and a 2D slice of a simulated potential landscape taken 1 nm below the Si/SiO$_2$ interface. The corresponding plunger gate voltages were $V_1 = 0.3$ V and $V_2 = V_3 = 0.2$ V. Figure 3.2b shows a 2D top view of the potential landscape with an outline of the plunger gates superimposed. The plunger gate heads are 40 nm $\times$ 40 nm, and the edge to edge separation between them is 30 nm. Figure 3.2c shows a side view of the device structure taken along the black dotted line in Figure 3.2b. This view highlights the plunger gate's vertical design in which electrons only accumulate below the thinner oxide section, which is 17 nm thick in this model. The pulse control parameters are the plunger gate voltages $\{V_1, V_2, V_3\}$. Approximately 1000 potentials were calculated using plunger gate voltage configurations ranging from $[0.2, 0.3]$ V in steps of 0.01 V for each gate. Potentials at voltage configurations in between these points are obtained by linear interpolation. The potential term in the Hamiltonian is $v(V_1, V_2, V_3)$ where v is a 1D slice of the potential landscape taken along the white dashed line in Figure 3.2c, 1 nm below the Si/SiO$_2$ interface. A 1D potential is used here to reduce computational resources, but 2D or 3D potentials could be used in principle.

A constant-adiabaticity pulse for electron shuttling using $\xi = 0.02$ and a voltage range of $[0.2, 0.3]$ V is plotted in Figure 3.3. The left panel is an enlarged view that shows the smooth nature of the pulses near the corners. At time $T = 0$, $V_1 = 0.3$ V and $V_2 = V_3 = 0.2$ V which localizes the electron in dot 1. At $T \approx 155$ ns, $\epsilon = 0$ ($V_1 \approx V_2$) and the electron resonantly tunnels between dots 1 and 2. V_1 is swept to $V_1 = 0.2$ V at $T \approx 315$ ns which fully localizes the electron in dot 2. A similar process is carried out to shuttle the electron from dot 2 to dot 3. When the detuning $|\epsilon| \gg 0$, gate voltages can be swept quickly without harming adiabicity since the ground-excited state energy gap is large. When $\epsilon \approx 0$ (at $T \approx 155$ ns and $T \approx 465$ ns), the gap is small and the voltages must be swept slowly to maintain adiabaticity. The 1D potentials calculated with the Poisson solver naturally

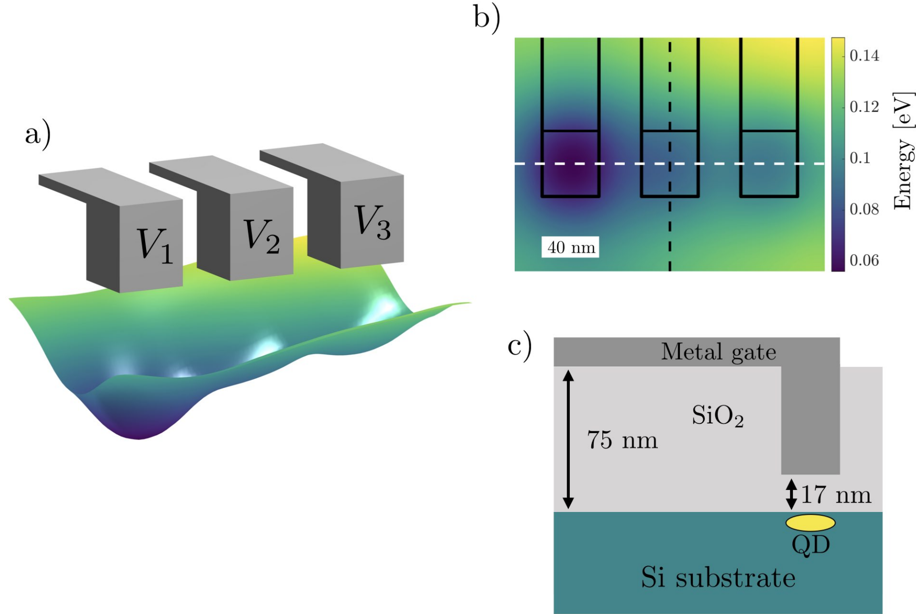

Figure 3.2: Schematic of a triple linear quantum dot chain using a 'via' gate geometry with no explicit tunnel barrier gates. a) 3D render of the gate geometry with a plot of a simulated electrostatic potential obtained with a self-consistent Poisson calculation . b) A 2D top view of the potential with plunger gates outlined. The potential is a 2D slice taken 1 nm below the Si/SiO_2 interface. Darker color indicates a more attractive potential for electrons. The white horizontal dashed line indicates the 1D potential slice used in the shuttling simulations. c) Side-view of a plunger gate taken along the black line in (b) showing the vertical plunger gate design. The yellow ellipse indicates electron accumulation in a quantum dot.

take into account cross-capacitances. This manifests as the zero detuning point ($\epsilon = 0$) occurring at $V_1 > V_2$ rather than $V_1 = V_2$, for example. The dot-to-dot shuttle duration in this example is about 325 ps.

We now examine the fidelity of shuttling using the constant-adiabaticity pulses described previously. The electron is initialized in the orbital ground state of the potential $v(\vec{V}(0))$. State evolution is calculated by solving the time-dependent Schrödinger equation (TDSE). Numerically, the TDSE is solved using the split-operator approach [57] with a time step $\Delta t = 5 \times 10^{-16}$ s. The instantaneous fidelity of the orbital state with the ground state is defined as $F(t) = |\langle\psi_0(t)|\psi_{\text{sim}}(t)\rangle|^2$, where $|\psi_0(t)\rangle$ is the ground state for the po-

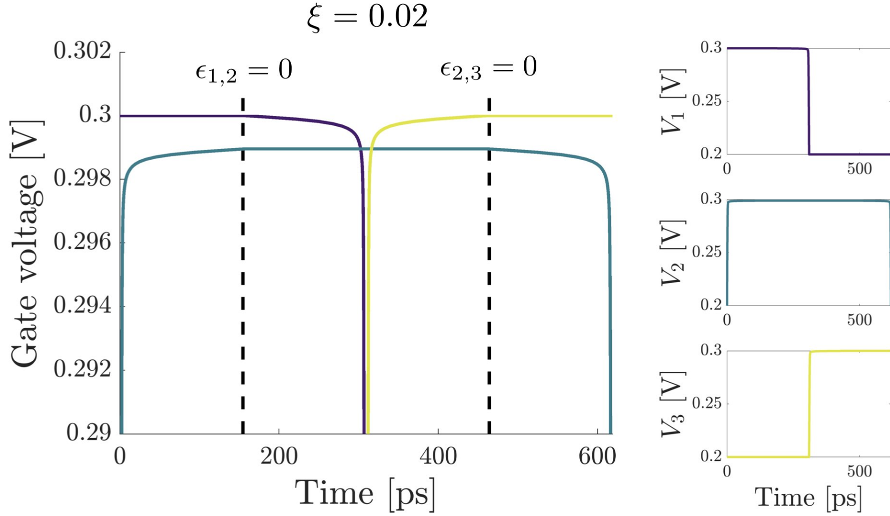

Figure 3.3: A constant-adiabaticity shuttling pulse calculated for the linear triple dot system, with $\xi = 0.02$. The electron is initially localized in dot 1 and then shuttled through dots 2 and 3 by sweeping the three plunger gates. When $V_1 \approx V_2$ or $V_2 \approx V_3$, the detuning between neighbouring dots is $\epsilon_{i,j} = \epsilon_i - \epsilon_j \approx 0$. The right inset figures show the pulse shapes over the full voltage range, while the main (left) panel is an enlarged view showing the smooth nature of the pulse shape near the upper corners.

tential $v(\vec{V}(t))$, and $|\psi_{\text{sim}}(t)\rangle$ is the simulated orbital state of the shuttled electron. The quality of a pulse of length T is defined as the final orbital state fidelity $F(T)$. We note that decoherence in the charge basis is neglected in these simulations. Figure 3.4 summarizes the trade-off between final orbital state infidelity $1 - F(T)$ and pulse duration T as the adiabatic parameter is varied. An explicit comparison between an adiabatic ($T = 650$ ps) and non-adiabatic ($T = 150$ ps) shuttling process is shown in Figure 3.5.

Apart from ξ, the resonant tunnel coupling t_c between two neighboring QDs determines the pulse length. The slowest parts of the pulse occur at the $\epsilon = 0$ anti-crossings where the energy spacing between the ground and first excited orbital state is $2|t_c|$. In the device geometry considered here, there are no gates to directly tune the tunnel barriers between dots. Instead, t_c is determined by the geometry of the gate electrodes and the inter-electrode gaps, as well as the applied gate voltages. For the device geometry in Figure 3.2, $t_c \approx 25$ μeV which gives sub-nanosecond shuttling pulses with orbital state fidelities $> 99\%$. We used a similar geometry and t_c values in Section 2.3 with linear pulses. The present results show a threshold time of ≈ 325 ps per dot-to-dot shuttling step for a final orbital state fidelity $> 99\%$, a factor of 5 improvement in speed over the linear

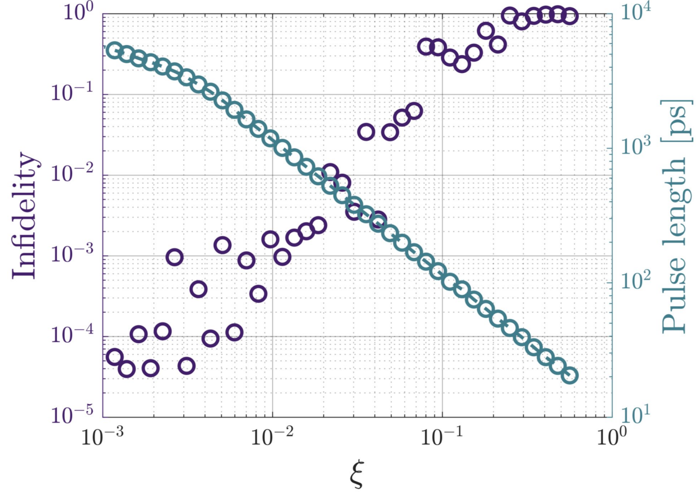

Figure 3.4: Relationship between the adiabatic parameter ξ, final orbital state infidelity $1-F(T)$, and pulse length T. Pulses with arbitrarily high fidelity can be found by reducing ξ at the cost of increased pulse length.

pulses used in Section 2.3. While superior to linear pulses, constant-adiabaticity pulses are not time optimal, and we expect that faster high-fidelity pulses could be designed by allowing ξ to vary and using optimal control methods.

3.3.3 Device geometry optimization

In this section, we use simulations of the constant-adiabaticity control pulses to optimize the gate electrode design of Figure 3.2 for maximum shuttling velocity. Stretching out the QDs in the direction of transport increases the distance travelled per shuttle, however, this also reduces the QD orbital energy spacing and requires slower pulses to maintain adiabaticity. To investigate this trade-off, we find shuttling pulses for double QDs with varying plunger gate length D and gate separation G and quantify the shuttling speed. An effective, approximate Hamiltonian describing the orbital dynamics of the shuttled electron

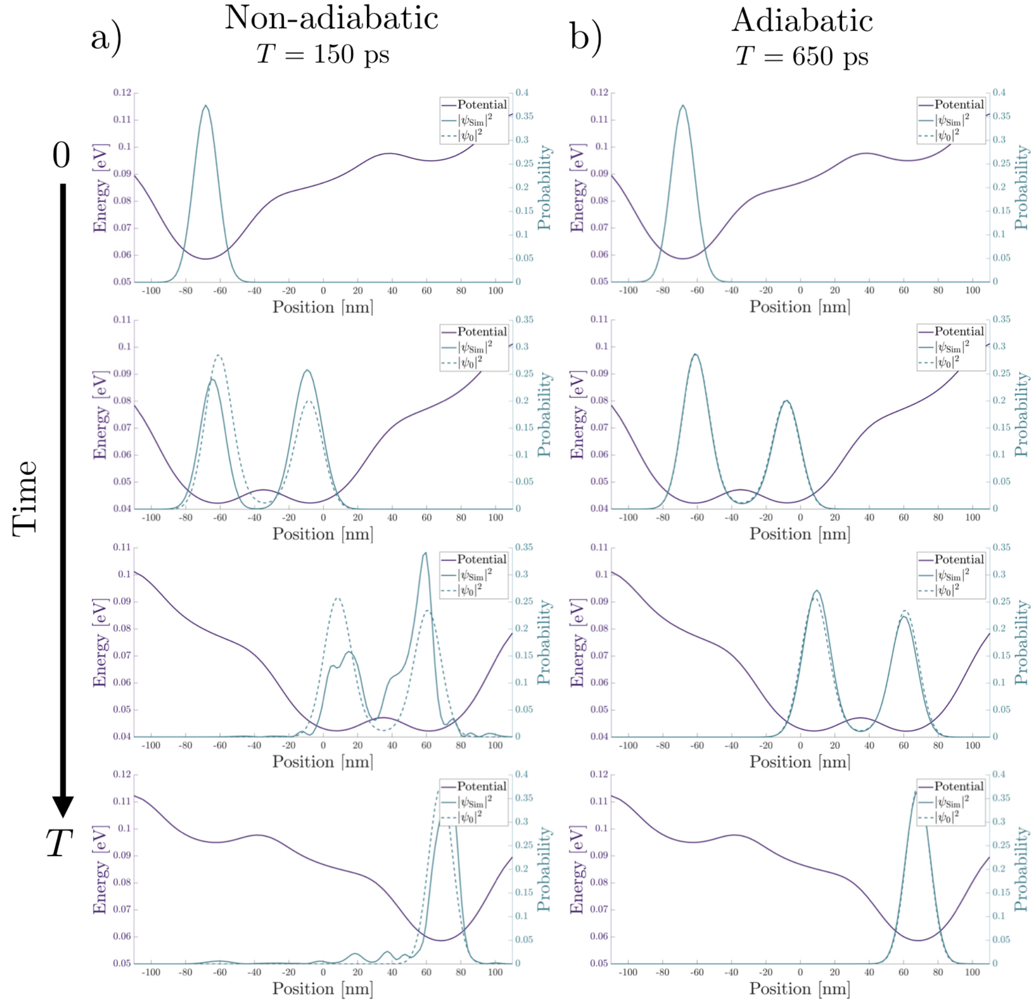

Figure 3.5: Electron shuttling simulations through a linear triple QD chain showing non-adiabatic (left column) and adiabatic (right column) evolution. The non-adiabatic (adiabatic) pulse was calculated using $\xi = 0.08$ ($\xi = 0.02$) giving a total pulse length $T = 150$ ps ($T = 650$ ps). For both simulations, the electron is initialized initialized in the orbital ground state and simulated according to the time-dependent Shcrödinger equation using the split-operator method with a time step $\Delta t = 5 \times 10^{-16}$ s. In each panel the instantaneous potential landscape (solid purple), orbital ground state (dashed blue) and simulated orbital state (solid blue) are plotted. In the non-adiabatic case, the simulated orbital wave function deviates from the orbital ground state due to the faster pulse's sweep rate. Conversely, in the adiabatic case, the simulated orbital state remains in the orbital ground state throughout the entire pulse sequence.

is used. The Hamiltonian for the double QD is

$$H = \begin{bmatrix} \epsilon_L & 0 & t_c & t_c \\ 0 & \epsilon_L + \Delta E_L & t_c & t_c \\ t_c & t_c & \epsilon_R & 0 \\ t_c & t_c & 0 & \epsilon_R + \Delta E_R \end{bmatrix} \tag{3.2}$$

where $d = L, R$ refers to the left and right dots, ϵ_d is the ground state energy, ΔE_d is the ground to first excited orbital splitting, and t_c is the resonant tunnel coupling. Here t_c is treated as an independent parameter and not a function of the dot size; we will discuss the dependence of t_c on the dot geometry below.

The orbital spacing $\Delta E = \Delta E_L = \Delta E_R$ is determined as a function of dot size D by simulating a triple linear QD chain using a self-consistent Schrödinger-Poisson solver in nextnano++. The three plunger gates have the same length D, a 40 nm width, and a 30 nm edge-to-edge separation. The middle plunger gate is used to define a central QD, and the outside plunger gates are included to model the impact of the QD chain on the central QD's orbital spacing. For a given plunger gate length D, the middle plunger gate voltage V is tuned so that the integrated electron density is $1 \pm 0.05\ e^-$ in the central QD. The outer gate voltages are offset -0.1 V with respect to V which tunes the outer dots to zero electron occupancy. From the resulting simulation, the energy difference between the ground and first excited energy states give the orbital spacing ΔE. Figure 3.6 shows how the orbital spacing varies with D. The data are fit to a power-law $f(D) = aD^b$ with $a = 0.58$ eV$\cdot$nm^b and $b = -1.47$.

For various QD lengths D, constant-adiabaticity pulses are found with $\xi = 0.005$ and inserting $\Delta E(D)$ into the Hamiltonian above. Here, the control parameters for the pulses are the ground state energies of each dot ϵ_i rather than the applied gate voltages as was done in Section 3.3.2. In a real device, ϵ_i is related to the set of gate voltage $\vec{V}$ by a linear transformation that can be experimentally measured [181]. Once the pulse length T is known for given parameters D and t_c, the shuttling velocity is $(G + D)/T$, where G is the inter-electrode gap set to 30 nm. Figure 3.7a summarizes the relationship between shuttling velocity and dot size D for different tunnel couplings ranging from $t_c = 10\ \mu$eV to 100 μeV. The shuttling speed initially increases with D, but then saturates at a maximum value and gradually decreases thereafter. The initial positive slope is due to a greater distance covered per shuttle step, but as D further increases, the effect of reduced orbital energy spacing dominates, increasing the time T needed to maintain adiabaticity. As expected, the shuttle velocity is a monotonically increasing function of t_c.

Above, we took t_c as a chosen parameter, however in practice t_c will be determined by a combination of the geometrical parameters (G, D) and the applied voltages. To get a

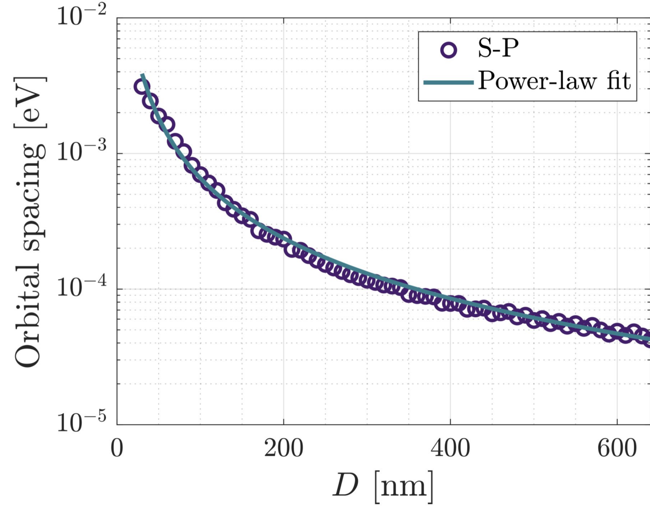

Figure 3.6: Orbital spacing versus plunger gate length D. The orbital spacings are extracted using a self-consistent Schrödinger-Poisson calculation and fit to a power-law $f(D) = aD^b$ with $a = 0.58$ eV·nm^b and $b = -1.47$.

sense of the range of practical tunnel coupling values, t_c for a double QD was calculated using a 3D Schrödinger-Poisson solver over a range of (G, D) values. Figure 3.7b shows the modelled four dot geometry, where the outer gate voltages were fixed at -0.1 V with respect to the central gates which were set to $V_1 = V_2 = V_p$. V_p was tuned such that a single electron occupies the symmetric inner double QD potential. The splitting of the lowest two eigenenergies determines t_c [262]. The results are plotted in Figure 3.7c, where t_c decreases monotonically as both D and G increase, with a higher sensitivity to variation in G. Assuming a practical fabrication limit of $G = 10$ nm, achievable electron velocities in Figure 3.7a are restricted to the green shaded region. The solid green line bounding the shaded region corresponds to $G = 10$ nm, whereas $G > 10$ nm for the rest of the shaded region. The highest practical shuttle velocities for this device geometry, $\sim$0.3 μm/ns, occur for $D \approx 100$ nm and $G \approx 10$ nm. On the other hand, to reduce the number of shuttle steps, D can be extended to ≈ 300 nm at the cost of reducing the velocity by a factor $\sim$3. These results demonstrate that a simplified gate geometry (one electrode per QD) can be optimized for single electron shuttling, without the need for additional gates to tune tunnel couplings, effectively reducing the required number of electrodes by two for a linear shuttling array.

We note two assumptions used when constructing H using Equation 3.2. The first is

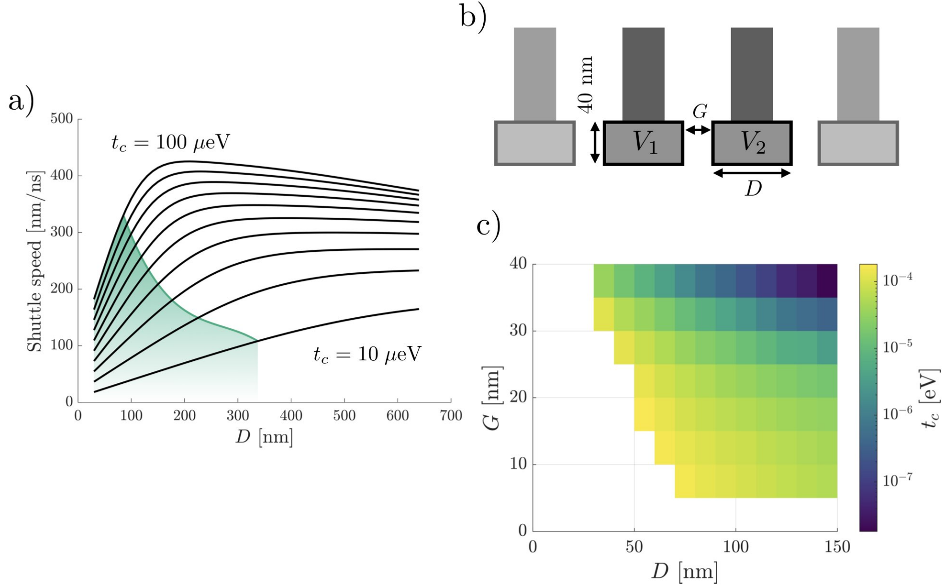

Figure 3.7: Optimizing the gate electrode geometry for fast shuttling. a) Shuttling velocity $(G + D)/T$ determined by finding a constant-adiabaticity pulse of duration T for given values of D and t_c. The ten curves corresponds to values of t_c ranging from 10 to 100 μeV in steps of 10 μeV. The shaded (green) region corresponds to the range of (D, t_c) values achievable in the geometry of (b) with $G \geq 10$ nm. Smaller gap values are considered impractical for realistic device fabrication. b) Top-down schematic view of the four-electrode model used to calculate t_c as a function of geometrical parameters G and D. The two central gates form the double QD used to model shuttling, while the outer gates are set to fixed potentials to make the double dot potential realistic. The dot length D and inter-electrode gap G are varied uniformly for all four gates. c) Dependence of t_c on D and G resulting from a 3D Schrödinger-Poisson calculation of the four-electrode model, with a single electron occupying the central double dot.

that the inter-dot coupling strength t_c is assumed to be equal between all orbital pairs. In reality, this is unlikely to be the case. Different t_c values will certainly cause the quantitative results in Figure 3.7 to change. We anticipate that when matrix elements of the form $\langle L, 0| H |R, 1\rangle$ (where 0 and 1 correspond to the ground and excited orbital states) increase in magnitude, the impact the orbital states have on the shuttling process is amplified. As such, when $\langle L, 0| H |R, 1\rangle$ is increased, we expect the optimal shuttle speed to occur at smaller D values. The second assumption in constructing H is that only a single excited orbital is considered. It is known that in quantum dot systems, the excited orbital state is

nearly doubly-degenerate (consider the degenerate first and second excited orbital states of a simple 2D harmonic potential well). We expect that incorporating the second excited orbital state should serve to reduce the overall shuttle speeds but not significantly impact which D values give the optimal shuttle speeds. Exploring both of these assumptions of H in greater detail would be a worthwhile endeavour.

3.4 Spin and valley effects on electron shuttling

Thus far, we have only considered the electronic orbital state dynamics in a single-valley setting and ignored spin. For quantum information processors based on QDs in silicon, shuttling of electron spin qubits, especially one member of an entangled pair, would be a critically important resource [18, 164]. To examine this possibility, an effective Hamiltonian model that accounts for spin and valley degrees of freedom is used to study the limits of coherent single spin transport by shuttling. We use the entanglement fidelity of a two-spin state to gauge the fidelity of the process, however, the second spin is considered to be static and never physically close to the shuttled spin.

3.4.1 Valley-orbit Hamiltonian

Bulk silicon has six-fold degenerate conduction band minima referred to as valleys. In a Si/SiO_2 hetero-structure, strong confinement along the vertical ($\hat{z}$) direction and strain at the Si/SiO_2 interfaces raises the energy of the four in-plane valleys, leaving a 2-fold degeneracy of the out-of-plane valley states $|z\rangle$ and $|\tilde{z}\rangle$ [2]. The sharp change in potential at the Si/SiO_2 interface couples $|z\rangle$ and $|\tilde{z}\rangle$, lifting the degeneracy and giving two valley eigenstates $|\pm\rangle = \frac{1}{\sqrt{2}}(|z\rangle \pm e^{i\phi}|\tilde{z}\rangle)$ [236, 228]. The eigenstates $|\pm\rangle$ are separated in energy by the valley splitting $\Delta = |\Delta|e^{i\phi}$, where ϕ is the phase of the electron's Bloch wave function [247, 49]. Disorder at the Si/SiO_2 interface causes $|\Delta|$ and ϕ to vary randomly between QDs [51, 79].

The valley phase difference between two neighboring QDs, $\delta\phi = \phi_1 - \phi_2$, can strongly affect how fast the electron can be adiabatically shuttled. First consider a single electron in a double quantum system consisting of two orbital states $|L\rangle$ and $|R\rangle$ where each state corresponds to the electron orbital occupying the left or right QD. Both QDs have a ground state energy ϵ_d (with $d = L, R$) and are coupled with strength t_c. Each QD has its own complex valley splitting $\Delta_d = |\Delta_d|e^{i\phi_d}$ which couples the two valley states $|z\rangle$ and $|\tilde{z}\rangle$. The

Hamiltonian of this valley-orbit subspace has the form

$$H_{VO} = \sum_{d=L,R} \epsilon_d k_d \otimes \tau_0 + \sum_{d=L,R} (\Delta_d k_d \otimes \tau_+ + h.c) + t_c k_x \otimes \tau_0 \tag{3.3}$$

where k and τ are two-level operators acting on the orbital and valley subspaces respectively. In terms of a dummy two-level operator A, the operators appearing in Equation 3.3 are defined as $A_L = \frac{1}{2}(I + \sigma_z)$, $A_R = \frac{1}{2}(I - \sigma_z)$, $A_0 = I$, $A_x = \sigma_x$, $A_y = \sigma_y$, $A_z = \sigma_z$, and $A_\pm = \frac{1}{2}(\sigma_x \pm i\sigma_y)$, where σ_j are the Pauli matrices and I is the identity matrix. The four basis states are $\{d, \nu\}$ with $d = L, R$ (left and right orbital ground states) and $\nu = z, \tilde{z}$ (valley states).

To better understand the impact of valley splitting on the system, it is useful to re-write the Hamiltonian in the valley eigenbasis $|\pm\rangle = |z\rangle \pm e^{i\phi_d} |\tilde{z}\rangle$. This is done via the matrix transformation $B = \sum_{L,R} k_d \otimes B_d$ where

$$B_d = \begin{bmatrix} 1 & 1 \\ e^{-i\phi_d} & -e^{-i\phi_d} \end{bmatrix} \tag{3.4}$$

After the change of basis, the valley-orbit Hamiltonian becomes

$$H'_{VO} = B^\dagger H_{VO} B = \sum_{d=L,R} \epsilon_d k_d \otimes \tau'_0 + \sum_{d=L,R} |\Delta_d| k_d \otimes \tau'_z + (t_{c,+} k_+ \otimes \tau'_0 + h.c) + (t_{c,-} k_- \otimes \tau'_x + h.c) \tag{3.5}$$

where τ'_i are two-level Pauli operators acting on this new valley eigenbasis. The basis states are defined by $\{d, \nu'\}$ with $d = L, R$ and $\nu' = -, +$ (valley eigenstates). Setting $\phi_L = 0$ and $\phi_R = \delta\phi$ gives $t_{c,+} = \frac{t_c}{2}(1 + e^{-i\delta\phi})$ and $t_{c,-} = \frac{t_c}{2}(1 - e^{-i\delta\phi})$. In this representation, the tunnel coupling t_c term has transformed into two distinct forms: $t_{c,+}$ and $t_{c,-}$. The *intra-valley* tunnel coupling $t_{c,+}$ allows tunneling events between QD orbitals with the same valley eigenstate ($|L, \pm\rangle$ and $|R, \pm\rangle$), whereas the *inter-valley* tunnel coupling $t_{c,-}$) couples opposite valley eigenstates ($|L, \pm\rangle$ and $|R, \mp\rangle$) [291]. Most importantly, their respective coupling strengths depend on the magnitude of the valley phase difference $\delta\phi$. From the expression for $t_{c,+}$ ($t_{c,-}$), the coupling between orbital states from the same (different) valley eigenstate varies from being strongest (0) when $\delta\phi = 0$ to 0 (strongest) when $\delta\phi = \pi$.

Figure 3.8 shows a valley-orbit energy diagram for a silicon double QD with the four anti-crossings formed by $t_{c,-}$ and $t_{c,+}$ labelled. The two $t_{c,+}$ and two $t_{c,-}$ anti-crossings occur at energies $\epsilon = \pm(|\Delta_L| - |\Delta_R|)$ and $\epsilon = \pm(|\Delta_L| + |\Delta_R|)$, respectively. Sweeping the inter-dot detuning $\epsilon = \epsilon_R - \epsilon_L$ adiabatically through any of these four anti-crossings moves an electron from one QD to the other.

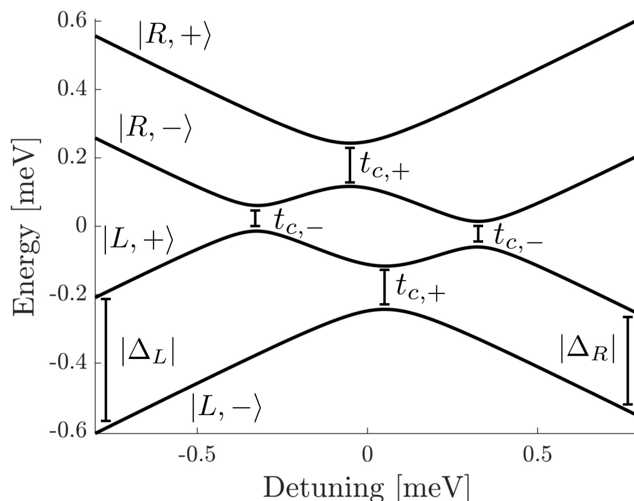

Figure 3.8: Valley-orbit energy spectrum for a double quantum dot with single electron occupation. The Hamiltonian parameters are $|\Delta_L| = 200$ μeV, $|\Delta_R| = 150$ μeV, and $\delta\phi = \pi/3$. The four eigenstates when $\epsilon \ll 0$ are labelled on the left side. The intra-valley and inter-valley tunnel couplings are labelled $t_{c,+}$ and $t_{c,-}$, respectively.

As discussed in Section 3.3.2, for an electron in the ground state, the tunnel coupling t_c limits the adiabatic shuttling speed. In the valley-orbit Hamiltonian, $t_{c,+}$ will limit the shuttling speed instead. Because the couplings $t_{c,+}$ and $t_{c,-}$ are dependent on $\delta\phi$, the highest shuttling speed is obtained when $\delta\phi = 0$ and $|t_{c,+}| = t_c$. With increasing $\delta\phi$, $|t_{c,+}|$ decreases, requiring longer constant-adiabaticity pulses. For $\delta\phi = \pi$, $|t_{c,+}| = 0$ and intra-valley tunneling is completely suppressed. At the $t_{c,-}$ anti-crossing, the opposite occurs; inter-valley tunneling cannot occur for $\delta\phi = 0$, whereas for $0 < \delta\phi < \pi$, $|t_{c,-}|$ is finite and yields an anti-crossing that mixes the $|L, \pm\rangle$ and $|R, \mp\rangle$ valley-orbit states. When $\delta\phi = \pi$, $|t_{c,-}| = t_c$ and the inter-valley gap is completely opened.

3.4.2 Validity of the single valley approximation in charge shuttling

Here we justify the the single-valley approximation used in the charge shuttling simulations in Section 3.3. First, consider the single-valley effective Hamiltonian used in Equation 3.2 which includes both the ground and first excited state orbital degrees of freedom for a

double quantum dot system.

$$H_{\text{orb}} = \begin{bmatrix} \epsilon_L & 0 & t_c & t_c \\ 0 & \epsilon_L + \Delta E_L & t_c & t_c \\ t_c & t_c & \epsilon_R & 0 \\ t_c & t_c & 0 & \epsilon_R + \Delta E_R \end{bmatrix} \tag{3.6}$$

ΔE_d with $d = L, R$ is the orbital spacing in the left and right dots, and t_c is the inter-dot tunnel coupling. The basis states of H_{orb} are $\{d, n\}$ where $n = 0, 1$ (ground and first excited state). This effective Hamiltonian can be generalized to include valley states as

$$H_{VO} = H_{\text{orb}} \otimes \tau_0 + \sum_{d=L,R} (\Delta_d k_d \otimes I_2 \otimes \tau_+ + h.c.) \tag{3.7}$$

where the k operator acts on the left and right QD state subspace and τ acts on the valley subspace as described in Equation 3.3 of the main text. The 2×2 identity operator denoted I_2 acts on the ground and first excited state subspace. The basis states of this Hamiltonian are $\{d, n, \nu\}$ where $\nu = z, \tilde{z}$ (valley states).

Constant-adiabaticity single electron shuttling simulations are performed using both H_{orb} and H_{VO} in order to compare dynamics resulting from the single-valley and the valley-orbit effective Hamiltonians. To begin, a constant-adiabatic pulse with $\xi = 0.005$ in which the detuning $\epsilon = \epsilon_L - \epsilon_R$ from -1.5 meV to $+1.5$ meV is calculated using H_{orb}. For both H_{orb} and H_{VO}, the state is initialized in the ground state of the respective Hamiltonian and subsequently evolved according to the pulse shape. The infidelity of the shuttling process is calculated as $1 - |\text{Tr}[\rho_{\text{orb}}(T)|R, 0\rangle\langle R, 0|]|^2$ where $\rho_{\text{orb}}(T)$ is the orbital density matrix after shuttling. For simulations of H_{VO}, $\rho_{\text{orb}}(T)$ is found by tracing out the valley degree of freedom of the final density matrix.

The fixed Hamiltonian parameters used are $t_c = 50$ μeV and $|\Delta_R| = 150$ μeV. The dots are assumed to be of equal size $\Delta E_L = \Delta E_R$. Dot size is mapped to an orbital energy spacing ΔE using the fit parameters from Section 3.3.3. Figure 3.9 shows the infidelity of the shuttling simulations as a function of dot size for different combinations of $\delta\phi$ and $|\Delta_L|$. The infidelity increases with dot size for all simulations; this is due to increased overlap of the final state with excited orbital states $|L, 1\rangle$ and $|R, 1\rangle$ with increasing dot size. We see that the single-valley Hamiltonian H_{orb} (dashed black) and the valley Hamiltonian produce the same shuttling dynamics when $\Delta_L = \Delta_R = 150$ μeV and $\delta\phi = 0$ (solid yellow). When $\Delta_L \neq \Delta_R$ (solid purple) or $\delta\phi \neq 0$ (solid blue-green), the two Hamiltonians produce different dynamics, but with infidelities still of similar order. This shows that the charge shuttling simulations presented in Section 3.3, which only took into account the single-valley orbital states, should give a reasonable approximation to the physically relevant

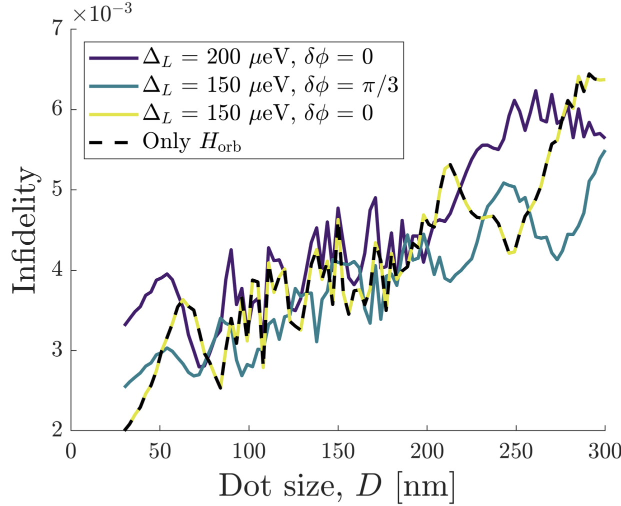

Figure 3.9: Fidelity of shuttling a charge with and without valley physics. The fixed Hamiltonian parameters are $t_c = 50$ μeV and $|\Delta_R| = 150$ μeV. The orbital infidelity is plotted on the vertical axis, defined as $1 - |\text{Tr}[\rho_{\text{orb}}(T)|R,0\rangle\langle R,0|]|^2$, where $\rho_{\text{orb}}(T)$ is the orbital density matrix after shuttling. The dashed black line corresponds to simulations of H_{orb} where no valley physics is considered. Simulations of H_{VO} that include valley physics are shown for three different cases: equal valley splitting and no valley phase difference (yellow), non-equal valley splitting and no valley phase difference (purple), and equal valley splitting and non-zero valley phase difference (blue-green).

case of charge shuttling in the presence of valley states. However this is only strictly true if the inter-dot valley splittings are equal and there is no valley phase difference.

3.4.3 The effective spin-orbit Hamiltonian

The small but non-zero spin-orbit coupling in silicon's conduction band mixes spin and valley eigenstates and is a source of spin decoherence for shuttled electrons [282, 66]. Here we show how to construct an effective Hamiltonian representation of the spin-orbit Hamiltonian H_{SO} including Rashba and Dresselhaus terms [26, 59] which will be used to build a full spin-valley-orbit Hamiltonian next in Section 3.4.4. In real space, the spin-orbit Hamiltonian takes the standard form

$$H_{SO} = \alpha(\kappa_x s_y - \kappa_y s_x) + \beta(\kappa_x s_x - \kappa_y s_y) \tag{3.8}$$

where α and β are the Rashba and Dresselhaus interaction coefficients, κ_x and κ_y are the electron wave operators along the [100] and [010] crystal lattice directions respectively. s is a two-level operator acting on the spin subspace (defined similarly as the operators k and τ from Equation 3.3). We also assume there is a static magnetic along the $+\hat{z}$ direction with strength B_z giving $|\uparrow\rangle$ as the ground eigenstate of s_z. The generalized electron wave operators take the form $\vec{\kappa} = -i\vec{\nabla} + \frac{e}{\hbar}\vec{A}$ (with electron momentum $\vec{p} = \hbar\vec{\kappa}$) with the gauge chosen such that the magnetic vector potential is $\vec{A} = \frac{B_z}{2}(-y, x, 0)$.

We consider a double quantum dot system composed of two harmonic potential wells giving the orbital Hamiltonian

$$H_0 = \frac{\hbar^2\vec{\kappa}^2}{2m*} + \frac{m^*\omega_0^2}{2}\min[(x \pm a)^2 + y^2] \tag{3.9}$$

where m^* is the material effective mass, ω_0 is the harmonic frequency, and $2a$ is the dot separation. We take the localized electron orbital states in each quantum dot to be the Fock-Darwin states. Considering only the ground s-orbital state, the localized electron orbitals in the left (L) and right (R) dots are

$$|L/R\rangle = \frac{1}{l_0}\sqrt{\frac{b}{\pi}} e^{\frac{\mp iay}{2l_B^2}} e^{-\frac{b}{2l_0^2}[(x\pm a)^2+y^2]} \tag{3.10}$$

where $l_0 = \sqrt{\hbar/m\omega_0}$ is the effective Bohr radius, $l_B = \sqrt{\hbar/eB_z}$ is the effective magnetic length, $b = \omega/\omega_0 = \sqrt{1 + \omega_L^2/\omega_0^2}$ is the magnetic compression factor, and $\omega_L = eB_z/2m^*$ is the Larmor frequency. The phase factor containing l_B arises due to the gauge freedom when choosing $\vec{A}$.

In order to convert H_{SO} to an effective Hamiltonian representation, we first need to evaluate a number of matrix elements for the shifted Fock-Darwin states and the spin states. The orbital overlap matrix element is

$$\langle L|R\rangle = S = \exp\left[-\frac{a^2}{l_0^2}\left(2b - \frac{1}{b}\right)\right]$$

which we have denoted as S. The position operator matrix elements are

$$\langle L|\, x \,|L\rangle = -\langle R|\, x \,|R\rangle = -a, \qquad \langle L|\, y \,|R\rangle = \frac{ial_0^2}{2bl_B^2}S$$

$$\langle L|\, x \,|R\rangle = \langle L|\, y \,|L\rangle = \langle R|\, y \,|R\rangle = 0$$

Next, the derivative operator matrix elements are

$$\langle L|\frac{\partial}{\partial x}|L\rangle = \langle R|\frac{\partial}{\partial x}|R\rangle = 0, \qquad \langle L|\frac{\partial}{\partial x}|R\rangle = -\langle R|\frac{\partial}{\partial x}|L\rangle = \frac{ba}{l_0^2}S$$

$$\langle L|\frac{\partial}{\partial y}|L\rangle = -\langle R|\frac{\partial}{\partial y}|R\rangle = \frac{-ia}{2l_B^2}, \qquad \langle L|\frac{\partial}{\partial y}|R\rangle = 0$$

Finally, we list a few trivial spin matrix elements

$$\langle\downarrow| s_x |\uparrow\rangle = \langle\uparrow| s_x |\downarrow\rangle = 1, \qquad \langle\downarrow| s_y |\uparrow\rangle = -\langle\uparrow| s_y |\downarrow\rangle = -i$$

Now the effective Hamiltonian can be assembled in the basis of spin-orbital states $\{|L,\downarrow\rangle, |L,\uparrow\rangle, |R,\downarrow\rangle, |R,\uparrow\rangle\}$. Because H_{SO} contains only s_x and s_y spin operators, any matrix elements without a spin flip (i.e. $\langle L,\uparrow| H_{SO} |L,\uparrow\rangle$ or $\langle L,\downarrow| H_{SO} |R,\downarrow\rangle$) will be 0. The first non-zero matrix element considered is $\langle L,\downarrow| H_{SO} |L,\uparrow\rangle$ which yields

$$\begin{aligned}
\langle L,\downarrow| H_{SO} |L,\uparrow\rangle &= \alpha \langle L,\downarrow| k_x s_y |L,\uparrow\rangle - \alpha \langle L,\downarrow| k_y s_x |L,\uparrow\rangle \\
&\quad + \beta \langle L,\downarrow| k_x s_x |L,\uparrow\rangle - \beta \langle L,\downarrow| k_y s_y |L,\uparrow\rangle \\
&= \alpha(0) - \alpha\left[-i\left(\frac{-ia}{2l_B^2}\right) + \frac{1}{2l_B^2}(-a)\right](1) \\
&\qquad + \beta(0) - \beta\left[-i\left(\frac{-ia}{2l_B^2}\right) + \frac{1}{2l_B^2}(-a)\right](-i) \\
\langle L,\downarrow| H_{SO} |L,\uparrow\rangle &= \frac{a}{l_B^2}(\alpha - i\beta) \equiv \eta_1
\end{aligned} \tag{3.11}$$

The next non-zero term we consider is a cross-orbital term $\langle R,\downarrow| H_{SO} |L,\uparrow\rangle$ which gives

$$\begin{aligned}
\langle L,\downarrow| H_{SO} |R,\uparrow\rangle &= \alpha \langle L,\downarrow| k_x s_y |R,\uparrow\rangle - \alpha \langle L,\downarrow| k_y s_x |R,\uparrow\rangle \\
&\quad + \beta \langle L,\downarrow| k_x s_x |R,\uparrow\rangle - \beta \langle L,\downarrow| k_y s_y |R,\uparrow\rangle \\
&= \alpha\left[-i\left(\frac{ab}{l_0^2}S\right) - \frac{1}{2l_B^2}\left(\frac{ial_0^2}{2bl_B^2}\right)S\right](-i) - \alpha(0) \\
&\qquad + \beta\left[-i\left(\frac{ab}{l_0^2}S\right) - \frac{1}{2l_B^2}\left(\frac{ial_0^2}{2bl_B^2}\right)S\right](1) - \beta(0) \\
&= -\frac{ab}{l_0^2}\left[1 + \frac{l_0^4}{4b^2 l_B^4}\right] S(\alpha + i\beta) \\
\langle L,\downarrow| H_{SO} |R,\uparrow\rangle &= -\frac{a}{l_0^2}\left[2b - \frac{1}{b}\right] S(\alpha + i\beta) \equiv \eta_2
\end{aligned} \tag{3.12}$$

Evaluating all of the remaining non-zero matrix elements gives the full effective spin-orbit Hamiltonian

$$H_{SO,\text{eff}} = \begin{bmatrix} 0 & \eta_1^\dagger & 0 & \eta_2^\dagger \\ \eta_1 & 0 & -\eta_2 & 0 \\ 0 & -\eta_2^\dagger & 0 & -\eta_1^\dagger \\ \eta_2 & 0 & -\eta_1 & 0 \end{bmatrix} \tag{3.13}$$

An equivalent form written in terms of the two-level operators for the orbital and spin degrees of freedom is

$$H_{SO,\text{eff}} = (\eta_1 k_z \otimes s_- + h.c) + (\eta_2\, ik_y \otimes s_- + h.c.) \tag{3.14}$$

where k is the two-level operator acting on the L, R orbital subspace as defined in Equation 3.3. Silicon lacks any bulk inversion asymmetry meaning that the Dresselhaus coefficient $\beta = 0$. This condenses the effective Hamiltonian to

$$H_{SO,\text{eff}} = \eta_1 k_z \otimes s_x + \eta_2 k_y \otimes s_y \tag{3.15}$$

This form of $H_{\text{SO,eff}}$ is the same form used in Zhao *et al.* [291] and is what we use for later spin shuttling simulations.

At the Si/SiO_2 interface, interface inversion asymmetry induces a Dresselhaus-like spin-orbit Hamiltonian term. The strength of this Dresselhaus-like is usually larger than the Rashab spin-orbit strength [226, 65, 66, 250]. Setting $\beta = 0$ is physically akin to saying the electron wavefunction has little overlap with the interface and spends more time in the 'bulk' material. Properly accounting for the this effect would be an important generalization of the following spin shuttling simulations. Additionally, when $H_{SO,\text{eff}}$ is used later on, it is assumed that $|L\rangle$ and $|R\rangle$ are orthogonal ($S = 0$). While this is a good approximation for combinations of smaller ω_0 and larger a parameters, if ω_0 is large and a is small, then $S \not\approx 0$. In that case, $|L\rangle$ and $|R\rangle$ can be orthogonalized as $|\tilde{L}/\tilde{R}\rangle = (|L/R\rangle - g\,|R/L\rangle)/\sqrt{1 - 2Sg + g^2}$ where $g^2 = (1 - \sqrt{1 - S^2})/S$. The spin-orbit matrix elements η_1 and η_2 should be reevaluated in this new basis.

3.4.4 Spin-valley-orbit Hamiltonian

Here the Hamiltonian given in Equation 3.3 is extended to include the electron's spin degree of freedom. The spin-valley-orbit effective Hamiltonian for a double quantum dot

system is [291]

$$
\begin{aligned}
H_{SVO} = \sum_{d=L,R} (\epsilon_d k_d \otimes \tau_0 \otimes s_0) + t_c k_x \otimes \tau_0 \otimes s_0 + \sum_{d=L,R} (\Delta_d k_d \otimes \tau_+ \otimes s_0 + h.c.) \\
+ E_z k_0 \otimes \tau_0 \otimes s_z + \eta_1 k_z \otimes \tau_0 \otimes s_x + \eta_2 k_y \otimes \tau_0 \otimes s_y
\end{aligned} \tag{3.16}
$$

where k, τ, ϵ, t_c, and Δ are all defined the same as in Equation 3.3. The 8 basis states are defined by $\{d, \nu, s\}$, where $d = L, R$ (left and right orbital ground states), $\nu = z, \tilde{z}$ (valley states), $s^i = \uparrow, \downarrow$ (spin eigenstates). $E_z = \frac{1}{2} g \mu_B B$ is the Zeeman splitting caused by a static magnetic field of strength B. η_1 and η_2 describe the spin-orbit interaction with $\eta_1 = \langle L, \nu, \downarrow | H_{SO} | L, \nu, \uparrow \rangle$ and $\eta_2 = \langle L, \nu, \downarrow | H_{SO} | R, \nu, \uparrow \rangle$ as derived in Section 3.4.3.

In order to understand the interplay between the spin-orbit interaction and valley splitting, we will rewrite H_{SVO} in the valley eigenbasis. Applying the transformation B from Equation 3.4 onto H_{SVO} results in

$$
\begin{aligned}
H'_{SVO} &= (B^\dagger \otimes s_0) H_{SVO} (B \otimes s_0) \\
&= \sum_{d=L,R} \epsilon_d k_d \otimes \tau'_0 \otimes s_0 + \sum_{d=L,R} |\Delta_d| k_d \otimes \tau'_z \otimes s_0 + E_z k_0 \otimes \tau'_0 \otimes s_z \\
&\quad + (t_{c,+} k_+ \otimes \tau'_0 \otimes s_0 + h.c) + (t_{c,-} k_- \otimes \tau'_x \otimes s_0 + h.c) \\
&\quad + \eta_1 k_z \otimes \tau'_0 \otimes s_x + (\eta_{2,+} k_+ \otimes \tau'_0 \otimes i s_y + h.c) + (\eta_{2,-} k_+ \otimes \tau'_x \otimes i s_y + h.c)
\end{aligned} \tag{3.17}
$$

where $\eta_{2,+} = \frac{\eta_2}{2}(1 + e^{-i\delta\phi})$ and $\eta_{2,-} = \frac{\eta_2}{2}(1 - e^{-i\delta\phi})$. The basis states are now $\{d, \nu', s\}$ with $d = L, R$, $\nu' = -, +$ (valley eigenstates) and $s = \uparrow, \downarrow$.

In the valley eigenbasis, it is easier to see how the strength of the spin-orbit coupling terms η_1 and η_2 depend on the magnitude of the valley phase difference $\delta\phi$. The η_2 spin-orbit coupling term takes on two different forms $\eta_{2,+}$ and $\eta_{2,-}$, similarly to how the tunnel coupling t_c transforms in this valley eigenbasis as well. These two terms $\eta_{2,+}$ and $\eta_{2,-}$ couple spin-orbit states from either the same or different valley eigenstate respectively. The coupling strengths of $\eta_{2,+}$ and $\eta_{2,-}$ are directly controlled by the magnitude of $\delta\phi$. When $\delta\phi = 0$, $\eta_{2,+}$ (which couples spin-orbital states from the same valley eigenstate) is maximal in strength. However as $\delta\phi \to \pi$, $\eta_{2,+}$ is suppressed and fully turned off at $\delta\phi = 0$. The converse is true for $\eta_{2,-}$ which couples spin-orbital states from different valley eigenstates. When $\delta\phi \to 0$, $\eta_{2,-}$ becomes suppressed, and $\eta_{2,-}$ is maximal when $\delta\phi = \pi$.

For the η_1 term, when the detuning is large $|\epsilon| \gg 0$, the orbital eigenstates are $|L\rangle$ and $|R\rangle$. The η_1 term then acts as a single-spin X rotation operator with no dependence on $\delta\phi$. As the detuning is swept near the $t_{c,+}$ and $t_{c,-}$ anti-crossings, the orbital eigenstates

become a super-position of $|L\rangle$ and $|R\rangle$, and the η_1 term couples both the orbital and spin states. The strength of the spin-orbit coupling near these anti-crossing is tied to the strength of $t_{c,+}$ and $t_{c,-}$. As $t_{c,+}$ increases (decreases), spin-orbital coupling between spin-orbital states from the same valley eigenstate is stronger (suppressed). Similarly as $t_{c,-}$ increases (decreases), spin-orbital coupling between spin-orbital state from different valley eigenstates is stronger (suppressed). Because both $t_{c,+}$ and $t_{c,-}$ depend on $\delta\phi$, the spin-orbit coupling from η_1 near these anti-crossing depends on $\delta\phi$ as well.

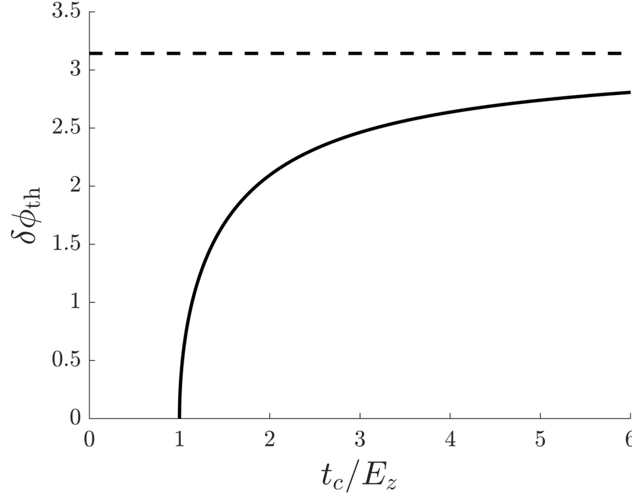

Figure 3.10: Relationship between the ratio t_c/E_z and the threshold value of valley phase difference, $\delta\phi_{\text{th}}$, where strong SVO mixing occurs.

When $t_c < E_z$, the ground orbital, excited spin state overlaps with the excited orbital, ground spin state, and the spin-orbit terms $\eta_{1,2}$ cause SVO mixing. When $t_c > E_z$, these states do not overlap until $\delta\phi$ reaches a threshold value $\delta\phi_{\text{th}}$. For $\delta\phi < \delta\phi_{\text{th}}$, the SVO mixing from $\eta_{1,2}$ is heavily suppressed. The threshold value $\delta\phi_{\text{th}}$ occurs at $E_z = |t_{c,+}| = \frac{t_c}{2}|1 + e^{i\delta\phi_{\text{th}}}|$. The relationship between t_c/E_z and $\delta\phi_{\text{th}}$ is plotted in Figure 3.10. A larger t_c/E_z ratio provides greater tolerance for variations in $\delta\phi$ during shuttling to suppress decoherence caused by SVO mixing. For $t_c \gg E_z$, $\delta\phi_{\text{th}}$ approaches π.

3.4.5 Spin transport simulations: $t_c > E_z$

For electron shuttling to be useful in a spin-based quantum information processing device, it must retain the coherence of the spin state. The silicon material system is promising in

this respect, since the conduction band spin-orbit coupling is weak compared to that in III-V materials, and nuclear magnetism can be greatly suppressed by isotopic purification. We now incorporate spin along with orbital and valley degrees of freedom using the double QD effective Hamiltonian model H_{SVO}. Only the two lowest valleys are considered, and orbital excited states are neglected, since they are high in energy compared to typical valley splittings. Consider the preparation of a two-electron spin singlet state $|S\rangle = \frac{1}{\sqrt{2}}(|\uparrow\downarrow\rangle - |\downarrow\uparrow\rangle)$, with one spin stationary outside of the double dot (e.g. in a third adjacent dot), and the other electron shuttled from left to right within the double dot system. The spin transport fidelity is quantified by the overlap of the post-shuttle spin state with the singlet. It is important to note that satisfying the adiabatic condition Equation 3.1 is not alone sufficient for maintaining spin coherence during electron shuttling, since for example, H_{SVO} is only real if the valley phase difference between adjacent QDs is zero, and adiabatic evolution is not guaranteed if the Hamiltonian is not real [42].

The effective double QD Hamiltonian is

$$H = \Bigg[\sum_{d=L,R} (\epsilon_d k_d \otimes \tau_0 \otimes s_0^1) + t_c k_x \otimes \tau_0 \otimes s_0^1 + \sum_{d=L,R} (\Delta_d k_d \otimes \tau_+ \otimes s_0^1 + h.c.) + E_z k_0 \otimes \tau_0 \otimes s_z^1 + \eta_1 k_z \otimes \tau_0 \otimes s_x^1 + \eta_2 k_y \otimes \tau_0 \otimes s_y^1 \Bigg] \otimes s_0^2 + E_z k_0 \otimes \tau_0 \otimes s_0^1 \otimes s_z^2 \quad (3.18)$$

where the bracketed terms are just H_{SVO} from the previous section acting on the shuttled electron, and the term outside the bracket acts on the static electron. Two-level operators that act on the orbital, valley and spin subspaces are denoted by k, τ and s^i respectively. The 16 basis states are defined by the binary values of the variables $\{d, \nu, s^1, s^2\}$, where $d = L, R$ (left and right orbital ground states), $\nu = z, \tilde{z}$ (valley states), $s^i = \uparrow, \downarrow$ (spin eigenstates of the shuttled $[i = 1]$ and stationary $[i = 2]$ electrons).

An electron shuttling from L to R is simulated using the parameters $\{\epsilon_L, \epsilon_R\}$ to define an adiabatic pulse with $\xi = 0.005$. The detuning $\epsilon = \epsilon_L - \epsilon_R$ is swept from -600 μeV to $+600$ μeV. The initial state is $|\psi(0)\rangle = \frac{1}{\sqrt{2}} \left|\psi_0^{VO}(0)\right\rangle \otimes (|\uparrow\downarrow\rangle - |\downarrow\uparrow\rangle)$ where $\left|\psi_0^{VO}(0)\right\rangle$ is the ground state of the initial valley-orbit Hamiltonian. The state evolution is calculated by a discretized time-dependent Schrödinger equation. For each simulation, we calculate both the shuttle speed and the fidelity of the final spin state with respect to the singlet. An effective speed is based on the electron travel of 60 nm per shuttle, and corresponding duration of the adiabatic pulse T. The fidelity of maintaining the singlet state is $|\mathrm{Tr}[\rho(T)(I_4 \otimes |S\rangle\langle S|)]|^2$, where $\rho(T)$ is the density matrix describing the post-shuttle state and I_4 is the 4×4 identity matrix.

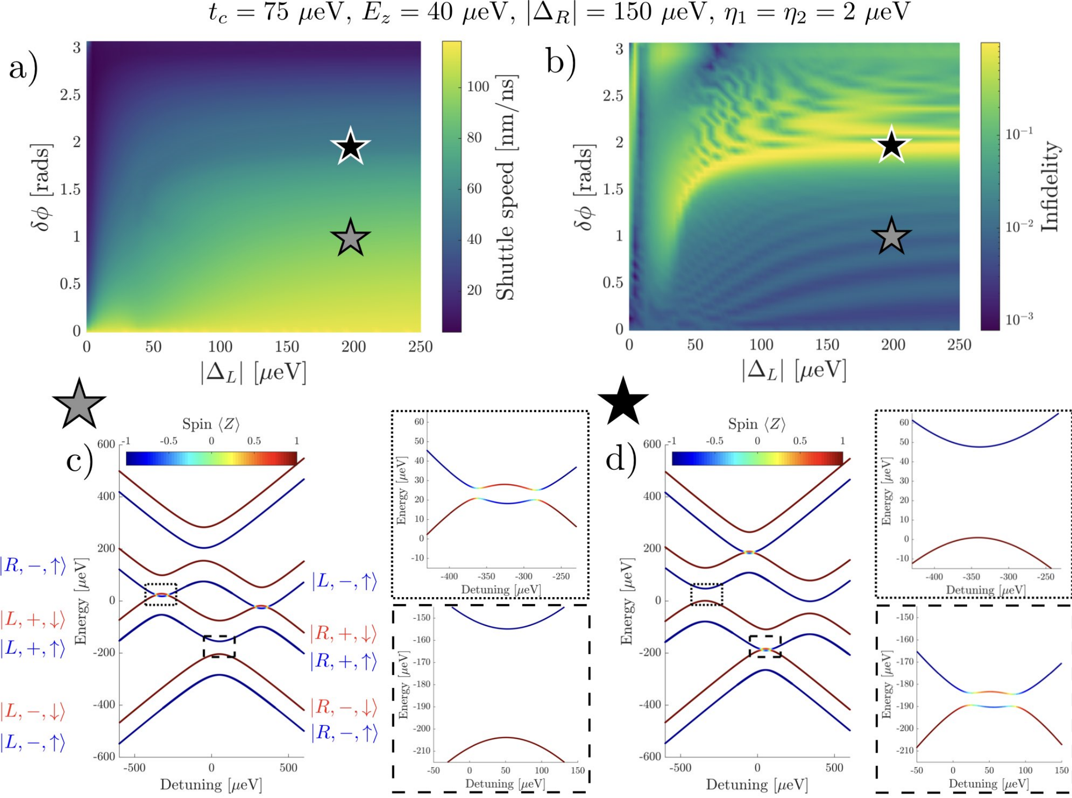

Figure 3.11: Shuttling one member of a singlet pair, for $t_c > E_z$. For all panels, the fixed parameters are: $\xi = 0.005$, $t_c = 75\ \mu$eV, $E_z = 40\ \mu$eV, $|\Delta_R| = 150\ \mu$eV, $\eta_1 = \eta_2 = 2\ \mu$eV. a) Variation of shuttle speed (colour scale) with the left QD valley splitting $|\Delta_L|$ and the inter-dot valley phase difference $\delta\phi$. These speeds are based on finding constant adiabaticity pulses with $\xi = 0.005$. b) The fidelity of maintaining the spin singlet state versus $|\Delta_L|$ and $\delta\phi$. Infidelity is plotted in colour scale, defined as $1 - |\mathrm{Tr}[\rho(T)(I_4 \otimes |S\rangle\langle S|)]|^2$, where $\rho(T)$ is the density matrix of the post-shuttle state. High (low) fidelity is indicated by dark blue (yellow). c), d) Energy spectra of the H_{SVO} in Equation 3.16 versus detuning $\epsilon_L - \epsilon_R$. $|\Delta_L| = 200\ \mu$eV in both panels, $\delta\phi = 1$ rad and $\delta\phi = 2$ rad for c) and d), respectively. Colour indicates the spin state, with red (blue) corresponding to spin down (up). Energy levels are labelled by the corresponding eigenstates on the left when the detuning $\ll 0$ and on the right when the detuning $\gg 0$. Enlarged views near the $t_{c,+}$ (dashed square) and $t_{c,-}$ (dotted square) anti-crossings illustrate how SVO mixing varies with $\delta\phi$.

Figure 3.11 shows the dependence of shuttle speed and spin fidelity on varying the valley splitting in the left dot, $|\Delta_L|$, and the valley phase difference, $\delta\phi$. The fixed Hamiltonian parameters are $t_c = 75$ μeV $> E_z = 40$ μeV, $|\Delta_R| = 150$ μeV, and $\eta_1 = \eta_2 = 2$ μeV. The chosen spin-orbit strength $\eta_{1,2}$ is about an order of magnitude larger than an experimentally reported value [100]. $|\Delta|_L$ is varied from from $0.1 - 250$ μeV, and $\delta\phi$ from $[0, \pi)$ rad ($\delta\phi = \pi$ is excluded because the ground state is degenerate at that point). The range $\delta\phi = (\pi, 2\pi]$ would produce a mirror image.

Since $t_c > E_z$, the lowest energy states $|L, -, \uparrow\rangle$ and $|L, -, \downarrow\rangle$ form a ground state manifold. The energy gap with respect to this manifold, set by $|\Delta_L|$ and $t_{c,+}$, determines the speed of the constant-adiabaticity pulse. This is evident in Figure 3.11a, where the shuttle speed decreases as $\delta\phi$ increases, due to the closing of the $|t_{c,+}|$ gap. The gap closing can be seen in Figures 3.11c-d, which show the energy spectra at $\Delta_L = 200$ μeV for $\delta\phi = 1$ rad and $\delta\phi = 2$ rad, respectively. Spin-valley-orbit (SVO) mixing is evident in the dashed box of Figure 3.11d when $\delta\phi = 2$ rad.

The valley splitting in the left dot, $|\Delta_L|$, has no significant impact on the shuttle speed as long as $|\Delta_L| > |t_{c,+}|$ ($|\Delta_R|$ is fixed at 150 μeV in these simulations). However, when $|\Delta_L| \leq |t_{c,+}|$, $|\Delta_L|$ represents the lowest excitation energy and therefore determines the shuttle speed. The crossover point, where $|\Delta_L| = |t_{c,+}|$, moves to smaller $|\Delta_L|$ values as $\delta\phi$ increases. This is the reason why in Figure 3.11a, for a fixed $\delta\phi$ value such as 1 rad, the shuttle speed increases with $|\Delta_L|$.

Figure 3.11b plots the infidelity (with respect to the singlet) of the post-shuttle spin state versus $\delta\phi$ and $|\Delta_L|$. Fidelities >95% are obtained when $|\Delta_L| > E_z$ and $\delta\phi$ is below about 2 rad. This corresponds to energy spectra qualitatively similar to Figure 3.11c, where the ground state manifold does not overlap with the lowest excited state. During the adiabatic pulse, the spin-entangled electron occupies only the ground state spin doublet and maintains coherence. When $\delta\phi \approx 2$ rad, the $t_{c,+}$ gap begins to close and SVO mixing occurs, rapidly degrading the state fidelity. The threshold value of $\delta\phi$ for this crossover is given approximately by $E_z \approx |t_{c,+}| = \frac{t_c}{2}|1 + e^{i\delta\phi_{th}}|$, when $|\Delta_L| > E_z$. For the parameters $t_c = 75$ μeV and $E_z = 40$ μeV used here, $\delta\phi_{th} \approx 2$ rad. For valley phase differences well above this threshold, the state fidelity improves modestly; this is due to a suppression of SVO mixing near the $t_{c,+}$ anti-crossing as $\delta\phi \to \pi$. The coupling of spin-orbit eigenstates through the η_1 term is governed by $t_{c,+}$ and $t_{c,-}$ (see Section 3.4.1). If either $t_{c,+}$ or $t_{c,-}$ equals 0, η_1 does not cause SVO mixing near the corresponding anti-crossing. In the valley eigenbasis, there are two distinct η_2 couplings: $\eta_{2,\pm} = \frac{\eta_2}{2}(1 \pm e^{-i\delta\phi})$ (see Section 3.4.4). As with $t_{c,\pm}$, $\eta_{2,+}$ ($\eta_{2,-}$) couple intra-valley (inter-valley) spin-orbit states. The $\eta_{2,+}$ term mixes states at the $t_{c,+}$ anti-crossing, but approaches zero as $\delta\phi \to \pi$.

In the high fidelity shuttling regime, where $|\Delta_L| > E_z$ and $\delta\phi < \delta\phi_{\text{th}}$, the infidelity is primarily caused by a precession of the shuttled electron's spin state about an effective axis due to the presence of the spin-orbit η_1 and η_2 terms in addition to the Zeeman term. In other words, the singlet state is not an eigenstate of the spin Hamiltonian when the spin-orbit coupling terms are non-zero. The dominant error is a phase rotation of the singlet into the $|T_0\rangle = \frac{1}{\sqrt{2}}(|\uparrow\downarrow\rangle + |\downarrow\uparrow\rangle)$ triplet state. Figure 3.12a plots the phase rotation angle with $|\Delta_L| = 200$ μeV and $\delta\phi \in [0, 1.7]$ rad. The normalized shuttling time t/T is given on the $\hat{y}$-axis, where T is the total pulse length for the constant adiabaticity shuttling pulses ($\xi = 0.005$). T increases with $\delta\phi$, causing the spin to accumulate a larger phase error at larger $\delta\phi$ values.

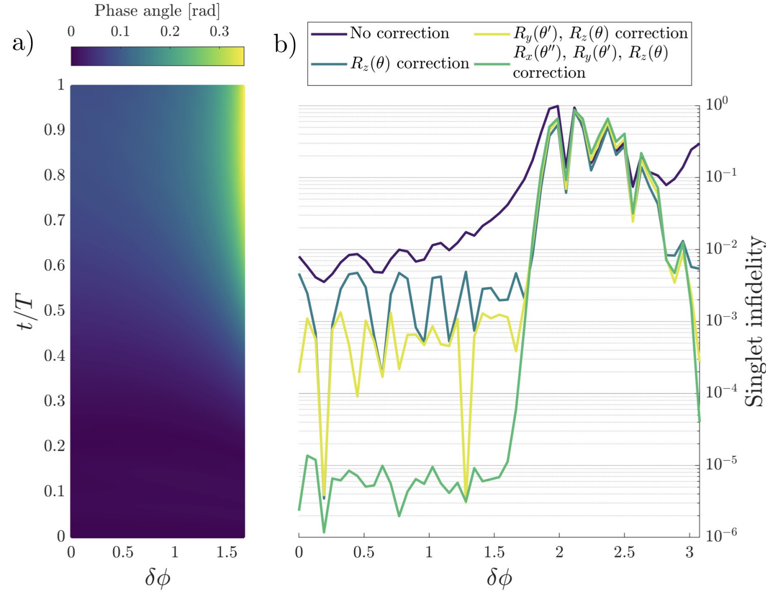

Figure 3.12: Error due single-spin rotation during shuttling. For both panels, $\xi = 0.005$, $t_c = 75$ μeV $> E_z = 40$ μeV, $|\Delta_L| = 200$ μeV, $|\Delta_R| = 150$ μeV, and $\eta_1 = \eta_2 = 2$ μeV. a) Phase (σ_z) rotation of the shuttled spin in the regime $\delta\phi \in [0, 1.67]$ rad. b) Effect of corrective rotations on the infidelity of the post-shuttle state with respect to the singlet, as a function of $\delta\phi$. (Purple) no corrective rotations are applied; (blue) $R_z(\theta)$ correction applied; (yellow) $R_z(\theta)$ and $R_y(\theta')$ corrections applied; (green) $R_z(\theta)$, $R_y(\theta')$, and $R_x(\theta'')$ corrections applied.

Figure 3.12b shows that in addition to phase rotation, the finite spin-orbit terms lead

to small rotations about σ_x and σ_y as well. Fidelity with the singlet state significantly improves as corrective rotations $R_n(\theta) = \exp(-i\theta\sigma_n/2)$, where $n = \{x, y, z\}$, are applied to the shuttled electron spin. The correction angles required for the $R_z(\theta)$, $R_y(\theta')$ and $R_x(\theta'')$ rotations are found by calculating the overlap between the final state and the $|T_0\rangle$, $\frac{1}{\sqrt{2}}(|\uparrow\uparrow\rangle + |\downarrow\downarrow\rangle)$, and $\frac{1}{\sqrt{2}}(|\uparrow\uparrow\rangle - |\downarrow\downarrow\rangle)$ states, respectively. The trace in Figure 3.12b with no corrective rotations (purple) is a line cut along $\delta\phi$ from Figure 3.11b, with $|\Delta_L| = 200$ μeV. When $\delta\phi < \delta\phi_{\text{th}}$, corrective rotations significantly improve the singlet fidelity. Above $\delta\phi_{\text{th}}$, the SVO mixing during shuttling produces a spin state with purity < 1 upon tracing out the orbital and valley degrees of freedom. As $\delta\phi$ approaches π, however, it can be seen that the corrective rotations again improve fidelity due to suppression of SVO mixing near the $t_{c,+}$ anti-crossing.

The $R_z(\theta)$ corrections remove the dominant spin rotation error, resulting in $\approx 99.5\%$ singlet fidelity below $\delta\phi_{\text{th}}$. Additional $R_y(\theta')$ and $R_x(\theta'')$ corrections further improve fidelity by nearly three orders of magnitude, giving a singlet infidelity $\approx 10^{-5}$. The remaining error after applying all three corrective rotations is due to weak SVO mixing from the $\eta_{1,2}$ Hamiltonian terms. When all three corrective pulses are applied, small variation of the adiabatic parameter ξ does not affect the singlet fidelity, indicating that the state evolution in these simulations is well inside the adiabatic regime. If any of the single spin corrections are not applied, however, slower pulses (smaller ξ) will make the fidelity worse, as more single-spin rotation error accumulates. With all corrections applied, pulses with smaller ξ (more adiabatic) slightly enlarge the high-fidelity region of $\delta\phi$ by reducing SVO mixing near the gap-closing threshold $\delta\phi_{\text{th}}$.

In the regime $|\Delta_L| < E_z$ in Figure 3.11b, the corresponding energy spectra are more complex. The states labeled (at large negative detuning) $|L, -\downarrow\rangle$ and $|L, +, \uparrow\rangle$ overlap near zero detuning, irrespective of $\delta\phi$. This explains the funnel-shaped, low-fidelity feature at low $|\Delta_L|$ and $\delta\phi$ values.

3.4.6 Spin transport simulations: $t_c < E_z$

Here we extend the results from Section 3.4.5 and present electron singlet shuttling simulations using an effective Hamiltonian where $t_c < E_z$. The fixed Hamiltonian parameters are $t_c = 40$ μeV, $E_z = 75$ μeV, $|\Delta_R| = 150$ μeV, and $\eta_1 = \eta_2 = 2$ μeV. The electron pair is initialized into the state $|\psi(0)\rangle = \frac{1}{\sqrt{2}}\left|\psi_0^{VO}(0)\right\rangle \otimes (|\uparrow\downarrow\rangle - |\downarrow\uparrow\rangle)$ where $\left|\psi_0^{VO}(0)\right\rangle$ is the ground state of the initial valley-orbit Hamiltonian, and simulation is via the time time-dependent Schrödinger equation. Figure 3.13 shows how the shuttle speed and final singlet state fidelity vary with $\delta\phi$ and $|\Delta_L|$. Both the electron velocity and final singlet

state infidelity are calculated the same as in Section 3.4.5.

Figure 3.13a shows how shuttle speed varies with $|\Delta_L|$ and $\delta\phi$. $|\Delta_L|$ is varied from $0.1 - 250$ μeV and $\delta\phi$ is varied from $[0, \pi)$. Here the shuttle speed decreases and $\delta\phi$ increases similarly to the case when $t_c > E_z$ which is discussed in Section 3.4.5 and is caused by the closing $t_{c,+}$ anti-crossing. Figures 3.13c-e show the shuttled electron energy spectra versus detuning at $|\Delta_L| = 200$ μeV and $\delta\phi = 0$, $\frac{\pi}{2}$, and π respectively. The initially $|L, -\uparrow\rangle$ and $|R, -, \uparrow\rangle$ energy levels form the $t_{c,+}$ anti-crossing near zero detuning which closes as $\delta\phi$ increases. When $|\Delta_L| > |t_{c,+}|$, the valley splitting $|\Delta_L|$ has little impact on the shuttle speed. This is because the duration of the constant-adiabaticity pulse is determined by the smallest energy scale with respect to the ground state which in this regime is the $t_{c,+}$ anti-crossing. However, when $|\Delta_L| < |t_{c,+}|$, the valley splitting becomes the smallest energy scale with respect to the ground state and controls the shuttle speed. The overall shuttle speed is lower here for $t_c < E_z$ compared to the $t_c > E_z$ simulations in Section 3.4.5 because t_c is smaller (40 μeV compared to 75 μeV).

Figure 3.13b shows the final singlet state fidelity dependence on $|\Delta_L|$ and $\delta\phi$. The colour scale corresponds to the final singlet state infidelity. Unlike when $t_c > E_z$ in Section 3.3.2, there is no clear region of good fidelity singlet shuttling. Here where $t_c < E_z$, the first and second excited energy levels cross as the detuning is swept for all values of $\delta\phi$ as seen in Figures 3.13c-e. These crossing cause SVO mixing from the η_1 and η_2 Hamiltonian terms occurs which reduces the singlet fidelity. In the region where $|\Delta_L| > E_z$, the singlet fidelity does improve modestly with $\delta\phi$. This is caused by a reduction of the SVO mixing strength between the same valley eigenstates as $\delta\phi$ increases (refer to Section 3.4.4 for details). While the singlet fidelity does improve at higher $\delta\phi$, it is an undesirable region for electron shuttling as both the shuttle speed is reduced and there is non-zero spin-orbit mixing until $\delta\phi = \pi$.

When $|\Delta_L| < E_z$, the final singlet state fidelity is low for all $\delta\phi$. In this regime, the shuttled electron's energy spectra becomes more complicated compared to the spectra shown in Figure 3.13c-e. Here, the initially $|L, -, \downarrow\rangle$ energy level always crosses with spin-orbit energy levels from both the same valley eigenstate and different valley eigenstates. Because the electron travels along the $|L, -, \downarrow\rangle$ energy level during shuttling, it experiences both types of SVO mixing (between the same and different valley eigenstates). As $\delta\phi$ increases, the SVO mixing occurring between the same valley eigenstate decreases and is strongest when $\delta\phi = 0$. Conversely, as $\delta\phi$ decreases, the SVO mixing between different valley eigenstates increases and is strongest when $\delta\phi = \pi$. Because the electron sees both types of SVO mixing during shuttling, there is never a value of $\delta\phi$ where the SVO mixing is suppressed to give good singlet shuttling fidelity.

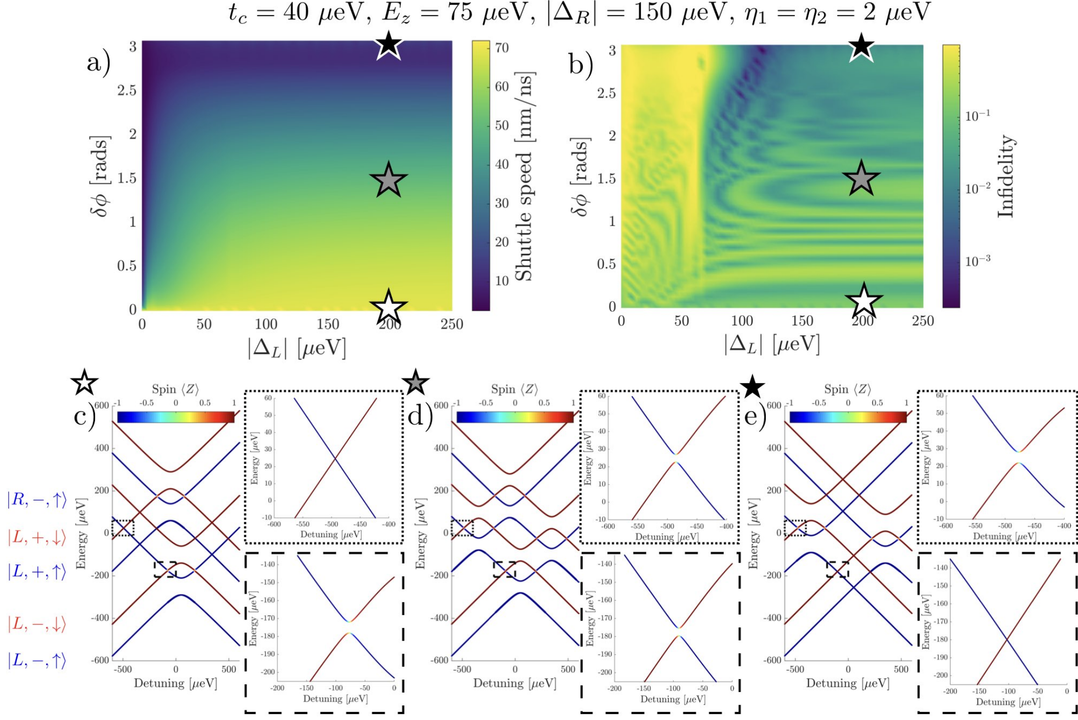

Figure 3.13: Shuttling one member of a singlet pair, for $t_c < E_z$. For all panels, the fixed Hamiltonian parameters are: $t_c = 40$ μeV, $E_z = 75$ μeV, $|\Delta_R| = 150$ μeV, $S_1 = S_2 = 2$ μeV. a) Variation of shuttle speed with the left QD valley splitting $|\Delta_L|$ and the inter-dot valley phase difference $\delta\phi$. b) Final singlet state fidelity's dependence on $|\Delta_L|$ and $\delta\phi$. The infidelity is plotted in colour scale, defined as $1 - |\text{Tr}[\rho(T)(I_4 \otimes |S\rangle\langle S|)]|^2$, where $\rho(T)$ is the density matrix of the post-shuttle state. Dark blue indicates high fidelity shuttling, yellow indicates low fidelity. c), d) and e) show the shuttled electron energy spectrum versus detuning. $|\Delta_L| = 200$ μeV in all panels, and $\delta\phi = 0$, $\frac{\pi}{2}$, and π for c), d), and e) respectively. Energy levels are labelled according to their initial energy eigenstate when the detuning $\ll 0$. Enlarged views near the $t_{c,+}$ (dashed square) and $t_{c,-}$ (dotted square) anti-crossings demonstrate how the SVO mixing varies with $\delta\phi$.

3.5 Discussion

The key results of this chapter can be summarized as follows. In Section 3.3.3, it was shown that single electron shuttling is possible using a simplified device geometry in which there is a single gate electrode per dot. Such a geometry would be highly economical for large-scale devices, reducing the required number of electrodes by two, and simplifying the applied voltage sequences. In the single-valley case, adiabatic transport is achieved at speeds up to 0.3 μm/ns. Transport speed is mainly determined by the resonant tunneling energy t_c, which can reach the 100 μeV scale in our simplified device geometry, even considering practical fabrication constraints. In Section 3.4, we studied the entanglement fidelity of a shuttled electron spin in the presence of valley states $|z\rangle$ and $|\tilde{z}\rangle$ and a small, but finite, spin-orbit coupling. It was found that the $t_c > E_z$ regime is favourable for high spin fidelity, but only for inter-dot valley phase differences $\delta\phi$ below a threshold value (≈ 2 rad for the parameters used in our simulation). Below this threshold, SVO mixing is weak, and the primary effect of the spin-orbit coupling is to generate systematic single-spin rotations that can, in principle, be corrected. With such corrections applied, very high fidelities $\sim$0.9999 are recovered, compared to 0.995 with phase correction only, and > 0.95 with no corrections. For $\delta\phi < \delta\phi_{th}$ and $|\Delta| > E_z$, average speed and fidelity (without single-qubit corrections) are estimated as 80 nm/ns and 0.99, respectively. We did not optimize the dot geometry for maximum speed in the spin/valley case, but one might expect that the dot length could be extended until the orbital energy scale is comparable to the intra-valley tunnelling gap, which could significantly increase velocity. However, spin-orbit effects will also increase with dot elongation, and this trade-off could be explored in future work using the expressions for η_1 and η_2 derived in Equations 3.11 and 3.12. Note that for spin-orbit couplings set to zero, there is no SVO mixing in any of the parameter space, which results in near-perfect spin fidelities. For $\delta\phi$ values at or above the threshold, strong SVO mixing significantly reduces the spin fidelity. The regime of high Zeeman field, $t_c < E_z$, has strong SVO mixing at nearly all values of $\delta\phi$, and is therefore unfavourable for spin shuttling. Thus, variability of the valley phase and remaining in the $t_c > E_z$ regime are two key experimental concerns. It should be noted that our simulations only pertain to the case of well-separated electrons, and do not apply to the initial steps of separating a singlet originating in a single dot. In that regime, a two-electron simulation including electron-electron interactions is necessary, and is left for future work.

What are the implications of these results for coherent spin transport, a key resource for large-scale quantum computer architectures in silicon? For entanglement distribution in a network architecture, Nickerson *et al.* showed that a raw fidelity $\sim$0.9 is sufficient, since even one round of entanglement distillation can increase the fidelity to fault tolerant

levels [193]. Consider a chain of 16 dots, with 15 shuttle events to transport an electron from dot 1 to dot 16. Each dot-to-dot shuttle requires a fidelity of ~0.993 for the whole process to be above the 0.9 threshold. In the regime of $\delta\phi < 1.5$ rad and $|\Delta| > 50$ μeV of Figure 3.11, the singlet fidelity is > 0.99 on average. Applying corrective phase rotations $R_z(\theta)$ increases the fidelity to ~0.995, which is sufficient for a 16-dot process with fidelity > 0.9. These values correspond to a spin-orbit coupling strength $\eta_{1,2} = 2$ μeV, an order of magnitude larger than what has been reported in silicon [100].

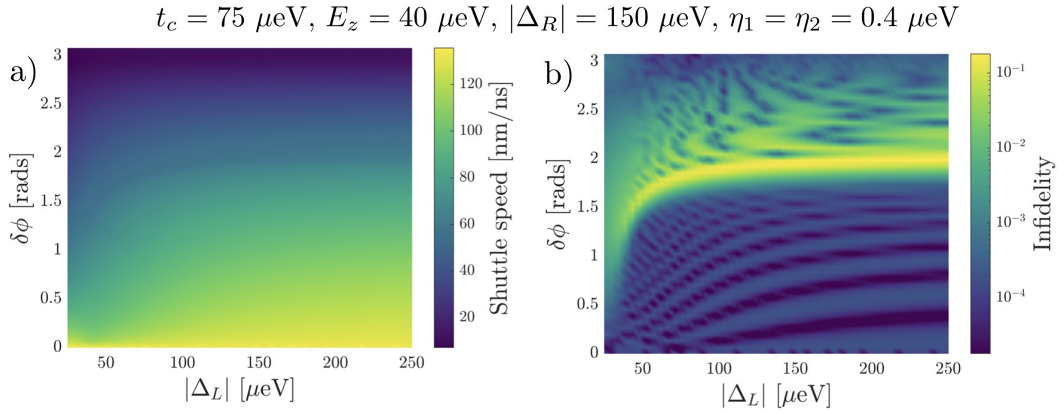

Figure 3.14: Shuttling one member of a singlet pair, for $t_c < E_z$. For all panels, the fixed Hamiltonian parameters are: $t_c = 40$ μeV, $E_z = 75$ μeV, $|\Delta_R| = 150$ μeV, $\eta_1 = \eta_2 = 0.4$ μeV. a) Variation of shuttle speed with the left QD valley splitting $|\Delta_L|$ and the inter-dot valley phase difference $\delta\phi$. b) Final singlet state fidelity's dependence on $|\Delta_L|$ and $\delta\phi$. The infidelity is plotted in colour scale, defined as $1 - |\text{Tr}[\rho(T)(I_4 \otimes |S\rangle \langle S|)]|^2 2$, where $\rho(T)$ is the density matrix after shuttling and I_4 is the 4×4 identity matrix. Dark blue indicates high fidelity shuttling, yellow indicates low fidelity.

Simulations with a weaker spin-orbit coupling $\eta_1 = \eta_2 = 0.4$ μeV are shown in Figure 3.14. All other fixed Hamiltonian parameters are the same as the simulations in Section 3.4.5 ($t_c > E_z$). The initial electron pair state, shuttle speed, and singlet infidelity are calculated the same way as in Section 3.4.5. Figure 3.15 directly compares the singlet fidelity for the larger (purple, $\eta_{1,2} = 2$ μeV) and smaller (blue, $\eta_{1,2} = 0.4$ μeV) spin-orbit coupling simulations. The traces are taken from Figures 3.11b (larger spin-orbit) and 3.15 (smaller spin-orbit) along $\delta\phi$ at $|\Delta_L| = 200$ μeV. The smaller spin orbit simulation shows ~1.5 orders of magnitude improvement in singlet fidelity for a factor of 5 reduction

in spin-orbit strength. Therefore for a smaller spin-orbit coupling strength in the same regime $\delta\phi < 1.5$ rad and $|\Delta| > 50$ μeV, the singlet fidelity is > 0.999 without any corrective rotations, which is sufficient for the 16-dot process. The timescale of this 16-dot shuttle, ~12 ns, is shorter than the fastest single-qubit gates that have been implemented for silicon spin qubits [286]. Intermediate scale shuttling, therefore, is not necessarily a speed bottleneck for a processor. Indeed, a 9-dot charge shuttle in 50 ns has already been demonstrated experimentally [181]. Moreover, the same experiment showed it is possible to shuttle multiple electrons in parallel (separated by a few dots), so that entanglement distillation would not require a doubling of shuttling times, but would require additional ancilla dots and measurements. On the other hand, the scenarios discussed above assume all dots lie within the parameter space for high fidelity shuttling; a single outlier with sufficiently large valley phase difference or small valley splitting would spoil the scheme. It remains to be seen experimentally whether material quality and device processing can yield sufficient control over these parameters.

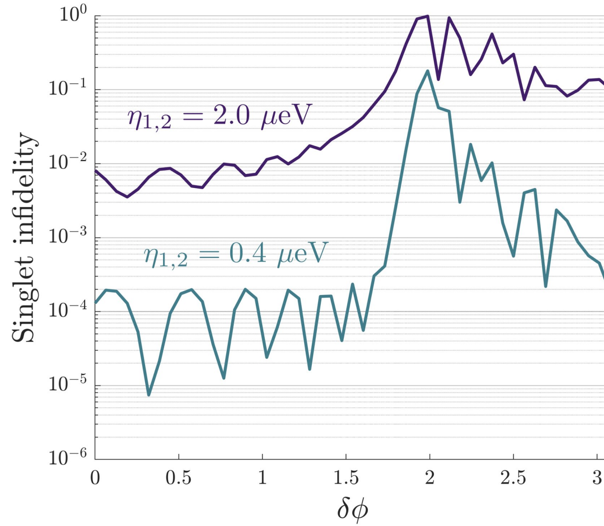

Figure 3.15: Comparison of shuttling singlet infidelity for two different spin-orbit coupling strengths: $\eta_{1,2} = 2$ μeV (purple) and $\eta_{1,2} = 0.4$ μeV (blue). Traces are taken directly from Figures 3.11b and 3.14b. These are the raw infidelities, with no single-spin correction rotations applied.

Before concluding this chapter, we will summarize here the several decoherence mechanisms relevant to electron shuttling that have been discussed in Chapters 2 and 3. The first mechanism is variation of the electron g-factor during shuttling. This variation arises

due to the changing electric field that is induced by the shuttling voltage control pulse or by local disorder that naturally shifts the g-factor from dot to dot. If the control pulse is noise-free and remains the same between shuttling events, then the control pulse should, in principle, introduce the same g-factor modulation. Additionally, if the shuttled electrons always travel along the same path during shuttling (as would be the case in the network architecture proposed in Chapter 3), then the total g-factor variation along a shuttle path should remain fixed. Therefore, the accumulated phase error due to a varying g-factor should be deterministic, allowing the error to be measured and subsequently corrected by a single qubit rotation. Of course in reality, there will be noise in the system, particularly voltage noise on the gate electrodes where the shuttling control pulse is applied. Such noise will introduce incoherent errors to the two decoherence mechanisms mentioned above. For typical cryogenic setups, voltage noise levels are in the few μV. The results in Section 2.3 showed that over a voltage range of $\sim$0.2 V, the resonance frequency varied by $\sim$0.2 MHz. This implies that for 10 μV of noise would give a corresponding resonance frequency shift of 10 Hz, which is negligible considering the length and timescales that shuttling takes place over. A second decoherence mechanism, which was discussed in detail this chapter, is spin rotations caused by the spin-orbit interaction which causes the effective magnetic axis to be tilted away from the $\hat{z}$ axis. As was shown in Section 3.4.5, when the valley phase difference between neighboring dots is small enough, these spin rotations are coherent and can be corrected by single qubit rotations on the shuttled electron. If the valley phase difference is large enough, then spin-valley-orbital mixing occurs and the spin state cannot be recovered. There are additional decoherence mechanisms related to the orbital state of the electron during shuttling: adiabaticity and charge decoherence. When the shuttling process is non-adiabatic, the electron is coherently evolves into a superposition of ground and excited orbital states. The state would quickly decohere though, due to the orbital relaxation time, which is determined by the transition dipole matrix element. Of course, by slowing down the shuttling process, adiabatic evolution is easy to obtain suppressing this decoherence mechanism. Even still, very fast shuttling sequences, in the few ns timescale, can still maintain adiabatic evolution. Therefore, we expect that experimental demonstrations of shuttling should not be limited by this decoherence mechanism, as ns shuttling timescales are more than practical for quantum information purposes. Charge decoherence is a decoherence mechanism that has been mentioned in passing but not yet discussed in any detail. When a single electron resides in a double dot system, at zero detuning, the electron is in an equal superposition of occupying either the left or right dot. If the system remains fixed at zero detuning, local device disorder causes the charge state to collapse, so that the electron occupies only one of the dots. This charge decoherence is very fast, acting on timescales around 10 ns [209]. During electron shuttling, the system must pass through this zero detuning point where charge decoherence occurs. As the adiabatic shut-

tling pulses demonstrated in Chapter 2 and 3 are around an order of magnitude faster than this decoherence timescale, charge decoherence may impact the shuttling fidelity.

3.6 Conclusions

In summary, the first half of this chapter showed how to construct constant-adiabaticity control pulses for shuttling single electrons along a 1D chain of QDs. By keeping the adiabatic parameter constant while varying geometric device parameters, for example, we can compare shuttling under different conditions, and optimize for shuttle speed or fidelity. Our method of simulation connects the 3D device model to an effective Hamiltonian in 1D. The second half modeled coherent spin transport by including spin-orbit and valley terms in an effective Hamiltonian, and shuttling one member of a spin-entangled pair. We found that a high-fidelity process requires $t_c > E_z$, $\delta\phi < \delta\phi_{th}$, and $|\Delta| > E_z$. The threshold value $\delta\phi_{th}$ is a function of the ratio t_c/E_z. Shuttle speeds up to 0.3 μm/ns were obtained in the single-valley case, and up to 80 nm/ns in the two-valley case with spin-orbit coupling present. Our results indicate that disorder-induced variation in the valley phase, if sufficiently large, is a primary obstacle to high-fidelity spin shuttling in ^{28}Si. Future work includes designing faster pulses (constant-adiabaticity is not time-optimal), shuttling in larger arrays, and including charge noise [154] and charge dephasing effects. Developing 2D simulations would enable simulating shuttling through a T-junction, a likely feature of realistic device architectures.

Chapter 4

Calculating the exchange interaction in lateral quantum dot networks

Chapter contributions: Bohdan Khromets and Dr. Marek Korkusinski assisted with the derivation of the closed form Coulomb matrix expression (both the symmetric and eccentric expressions). Dr. Marek Korkusinski also helped in developing the model to explain the charge noise sensitivity results in Section 4.3.3.

This chapter is based on the following preprint and is under review for publication in a journal:

Buonacorsi, B., Korkusinski, M., Khromets, B., and Baugh, J. (2020). Optimizing lateral quantum dot geometries for reduced exchange noise. *arXiv preprint arXiv:2012.10512*.

4.1 Introduction

Chapter 3 focused on simulating a key aspect of the stabilizer operation for the network architecture proposed in Chapter 2: electron shuttling. Another key ingredient of the stabilizer operation for the proposed architecture are the two-qubit $\sqrt{\text{SWAP}}$ gates. This chapter focus on developing numerical methods to be able to efficiently and accurately model $\sqrt{\text{SWAP}}$ gates. These methods enable $\sqrt{\text{SWAP}}$ gates to be described in terms of the directly accessible experimental control variables: the set of applied gate voltages $\vec{V}$ used to define the quantum dots (we use vector notation to indicate the set of voltages applied on n gates, $\{V_1, V_2, ..., V_n\}$).

In arrays of singly-occupied quantum dots, the inter-dot Coulomb interaction together with fermionic statistics leads to the effective spin exchange interaction. The dynamics of exchange enable SWAP and $\sqrt{\text{SWAP}}$ quantum logic gates [170, 58]. In weak spin-orbit materials like silicon, exchange between spins labeled i and j can be described by an effective Heisenberg Hamiltonian [58] with strength J_{ij}. The orbital wavefunctions, especially the overlap between orbitals in adjacent dots, can be manipulated via the gate electrodes that define the dots, so that J_{ij} is determined by $\vec{V}$. Electrostatic control of the exchange interaction in multi-dot systems is routine in lateral GaAs quantum dots [208, 198, 191, 127], and is becoming routine in silicon dots [269, 271, 287, 116, 276] in both MOSFET and Si/SiGe devices. However, it remains a challenge to realize two-spin quantum gates with the high fidelities required for fault-tolerant quantum computing, mainly due to the sensitivity of exchange to charge noise [56, 201]. The relationship between J_{ij} and $\vec{V}$ for a network of dots depends on both $\vec{V}$ and the physical device geometry in ways that are generally hard to accurately predict. Accurate numerical calculation of $J_{ij}(\vec{V})$ for arbitrary device layouts and network topologies is critical to realistic modeling of spin qubit processors. Such realistic modeling is necessary for optimizing device geometries and voltage control sequences that will mitigate the impacts of charge noise on quantum gate fidelity.

In order to accurately model $J_{ij}(\vec{V})$, techniques borrowed from quantum chemistry must be used. Generally, methods for determining J_{ij} offer a trade-off between computational complexity and quantitative accuracy when evaluating the energy spectra of many-electron systems. Approximate computational methods including Hubbard [149, 55], Heitler-London [21, 28], and Hund-Mülliken [113, 261, 103] techniques use only the localized, lowest energy s-orbitals construct the many-electron state. However, these approaches are only accurate over a limited range of device parameters [204] and fail more easily in Si compared to GaAs, due to the larger effective mass in Si [163]. Exact diagonalization of the many-electron Hamiltonian using a full configuration interaction (CI) formalism [53, 239, 111, 194, 7, 54] produces more accurate modeling. In a full CI calculation, the many-electron basis set is constructed by including all configurations of the s-, p-, d-, f-, etc., orbital states for the Hamiltonian diagonalization. A convergent spectrum requires a sufficient number of these excited orbital states. The full CI method is applicable, in principle, to any quantum dot network; however, these calculations are computationally intensive due to the need to evaluate Coulomb matrix elements for all configurations. Calculating the dependence of exchange strength J_{ij} on varying device parameters, such as gate voltages and device layout, tends to be impractical for large parameter spaces.

Methods for determining J_{ij} that are both computationally efficient and numerically accurate are key to designing devices with improved robustness to charge noise. Such

optimization would complement standard charge noise reduction techniques such as dynamical decoupling [22], composite pulses [235, 270, 290], and symmetric point operation [221, 177, 284]. Furthermore, quantum optimal control techniques such as GRAPE [136, 280] and effective Hamiltonian engineering [96], which require many repeated estimations of $\nabla J_{ij}(\vec{V})$, could be applied to exchange operations in quantum dots if efficient CI computations were available. Finally, the dynamics of coupled spins could be simulated directly in terms of the applied gate voltages using such tools.

Section 4.2 presents a modification of the linear combination of harmonic orbitals and configuration interaction (LCHO-CI) approach introduced by Gimenez *et al.* [83]. The modified LCHO-CI provides calculations of J_{ij} with significantly improved efficiency, while retaining quantitative accuracy. In Section 4.2.1, we show how to construct single electron states in a quantum dot network using a large orthogonal basis of harmonic orbitals. Section 4.2.2 describes the full CI calculation that accounts for all electron-electron correlations in the system. By using an orthogonal basis of harmonic orbitals, evaluation of the Coulomb matrix elements (the most computationally intensive part of the calculation) is reduced to a scalar multiplication and subsequent basis transformation of a pre-calculated library of Coulomb matrix elements. This strategy significantly reduces the resources needed to evaluate the Coulomb interactions, reducing the total computation time of the LCHO-CI calculation. The resulting many-electron spectra found with the LCHO-CI method are then mapped to the effective Heisenberg Hamiltonian [83] to obtain J_{ij} for the quantum dot network. Section 4.2.3 describes how the harmonic orbital basis can be optimized to improve the accuracy of the LCHO-CI calculations without increasing the computation time.

Section 4.3 uses the modified LCHO-CI method to study the sensitivity of J with respect to charge noise in a realistic double quantum dot geometry. In Section 4.3.1, we introduce the full 3D device structure and model it with a self-consistent Poisson solver. This allows us to map out how the 2D electronic potential landscape varies with the geometric parameters of the physical gate layout, as well as the applied gate voltages. In Section 4.3.3, these 2D potentials are used to study how the sensitivity of J to charge noise is influenced by the physical device parameters including dot size, tunnel gate width, gate oxide thickness and dot eccentricity. Sensitivity to charge noise is determined by calculating $\frac{\partial J}{\partial V_{bias}}$ as a function of the bias voltage V_{bias} applied across the plunger gates of the double dot. We also convert this bias to an effective inter-dot detuning ϵ to obtain $\frac{\partial J}{\partial \epsilon}$. Overall, the results show that dots with larger charging energies and with smaller plunger gate lever arms tend to be less sensitive to charge noise. The tools developed here can be further utilized to design quantum dot networks with optimal robustness to charge noise.

4.2 The modified LCHO-CI method

In this section we outline a variation of the LCHO-CI approach [83] for calculating many-electron states and energies in a quantum dot network. We present the method using double quantum dot networks, but the approach generalizes to larger quantum dot systems. Each quantum dot (QD) is assumed to be formed electrostatically by surface gate electrodes. In order to directly compare our method to the Heitler-London and Hund-Mülliken approaches [21, 163], we approximate the confining 2D potential experienced by the electrons with the quartic model:

$$V(x,y) = \frac{m^* \omega_0^2}{2} \left[\frac{1}{4d^2}(x^2 - d^2)^2 + y^2 \right] \tag{4.1}$$

where m^* is the material effective mass ($0.067m_0$ for GaAs and $0.191m_0$ for Si where m_0 is the free electron mass), $2d$ is the separation between the two QDs, and ω_0 is the harmonic frequency of the potential wells at $\pm d$. The characteristic width of each potential minima is given by $l_0 = \sqrt{\hbar/m^*\omega_0}$.

Later, in Section 4.3, we move to a more realistic model of the potential landscape by simulating a double QD device structure in a Si/SiO$_2$ material system using self-consistent 3D Poisson calculations. Throughout this chapter we assume that there is no magnetic field; however, this can be included into our calculations by adding a vector potential term to the Hamiltonian in Equation 4.2. We note that adding a magnetic field will impact the convergence of the single electron calculations discussed in Section 4.2.1. In particular, the magnetic field introduces a varying phase component in the orbital wave functions which may require more harmonic orbital states in order to accurately approximate the single-electron orbitals.

4.2.1 Building single electron states in a quantum dot network using harmonic orbitals

We begin the LCHO-CI calculation by evaluating the single electron states for the following Hamiltonian

$$H = -\frac{\hbar^2}{2m^*}\left[\frac{\partial^2}{\partial x^2} + \frac{\partial^2}{\partial y^2}\right] + V(x,y) \tag{4.2}$$

where $\hbar$ is the reduced Planck's constant. The single electron states $|\xi_j\rangle$ are eigenfunctions of H with corresponding eigenenergies ϵ_j which satisfy $H|\xi_j\rangle = \epsilon_j |\xi_j\rangle$. In order to make the LCHO-CI calculation simpler later on, it is useful to approximate the single electron states

$|\xi_j\rangle$ using a basis of radially symmetric 2D harmonic orbitals (HOs) centered at the origin of the quantum dot network. The explicit form of the 2D HO states is $\phi_{nm}(x, y) = \phi_n(x)\phi_m(y)$ where $\phi_q(s) = \frac{1}{\sqrt{2^q q!}}\left(\frac{m^*\omega}{\pi\hbar}\right)^{1/4}\exp\left(-\frac{m^*\omega s^2}{2\hbar}\right)H_q\left(\sqrt{\frac{m^*\omega}{\hbar}}s\right)$, H_q are the Hermite polynomials and ω is the harmonic frequency. The full 2-dimensional HO basis $\{\phi_{nm}(x, y)\}$ is found by taking the Cartesian product of two 1-dimensional HO bases $\{\phi_n(x)\}$ and $\{\phi_m(y)\}$ where each 1D basis is composed of the lowest M_x and M_y energy states respectively. The total number of 2D HO states $\{\phi_i(x, y)\}$ is $M = M_x M_y$. Throughout this work we use $M_x = M_y$.

Next, we find approximations $|\xi'_j\rangle$ of the first N single-electron states $|\xi_j\rangle$ using a linear combination of harmonic orbitals (LCHO)

$$|\xi'_j\rangle = \sum_{i=1}^{M} A_{ij} |\phi_i\rangle \tag{4.3}$$

where i is a composite index describing the n, m indices of the harmonic orbital state and A_{ij} are expansion coefficients. H is then rewritten in the 2D HO basis H^ϕ, and we obtain the generalized eigenvalue problem

$$H^\phi \hat{A} = \epsilon' \hat{A} \tag{4.4}$$

where H^ϕ has matrix elements $H^\phi_{ij} = \langle\phi_i| H |\phi_j\rangle$, $\hat{A} = (\vec{A}_1, \vec{A}_2, \ldots, \vec{A}_M)$ describes the unitary transformation between $\{|\phi_i\rangle\}$ and $\{|\xi'_i\rangle\}$, and ϵ' are approximations of the single electron state energies ϵ. The basis $\{|\xi'_j\rangle\}$ converges to $\{|\xi_j\rangle\}$ as M increases and more harmonic orbital basis states are included in the basis set. A schematic of the transformation between $\{|\phi_i\rangle\}$ and $\{|\xi'_j\rangle\}$ via $\hat{A}$ is shown in Figure 4.1a. The three lowest energy single electron orbitals are shown on the left using the quartic potential given in Equation 4.1 where $m^* = 0.191m_0$ (Si/SiO_2 system), $\hbar\omega_0 = 0.375$ meV ($l_0 = 32.6$ nm), and $d = 50$ nm. Some of the lowest energy harmonic orbital states used in approximating $\{|\xi'_j\rangle\}$ are shown on the right for a harmonic frequency of $\hbar\omega_0 = 0.188$ meV ($l_0 = 46.1$ nm). Figure 4.1b shows how the 12 lowest approximated energies ϵ'_j converge as a function of M for the quartic and harmonic parameters used in Figure 4.1a. The lowest two energy levels rapidly converge while the higher energy levels do not fully converge until $M > 12^2$. The lowest three energy levels are $\epsilon'_0 = 0.3436$ meV, $\epsilon'_1 = 0.3692$ meV, and $\epsilon'_2 = 0.5822$ meV.

Typically, M must be much larger than N in order for $\{|\xi'_j\rangle\}$ to accurately approximate $\{|\xi\rangle\}$. After $\hat{A}$ has been calculated, $\hat{A}$ is subsequently trimmed to have dimension $M \times N$ making $\hat{A}$ semi-unitary ($\hat{A}^\dagger\hat{A} = I$ but $\hat{A}\hat{A}^\dagger \neq I$). This reduces the computational complexity later when transforming the Coulomb matrix element basis in Section 4.2.2. So far, the choice of ω used to construct $\{|\phi_i\rangle\}$ is arbitrary; we will show in Section 4.2.3 how to optimally choose ω to best approximate $\{|\xi_j\rangle\}$.

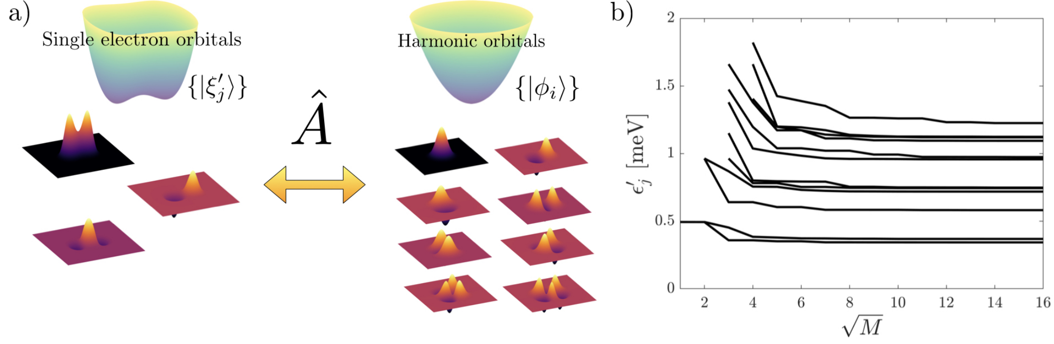

Figure 4.1: Using harmonic orbitals to approximate single electron orbital states. a) Schematic showing how $\hat{A}$ transforms between the harmonic orbital basis $\{|\phi_i\rangle\}$ and the approximated single electron orbitals $\left|\xi'_j\right\rangle$. The first 3 single electron orbitals are shown for an example quartic potential on the left and on the right are 8 of the lower energy HO states. b) Convergence of the first 12 approximated single electron energies ϵ'_j versus the number of harmonic orbitals M used to compose the basis $\{|\phi_i^\omega\rangle\}$. Here, $M = M_x M_y$ where $M_x = M_y$ are the numbers of 1-dimensional HOs taken along the $\hat{x}$ and $\hat{y}$ axes respectively used to construct the 2-dimensional HOs.

4.2.2 Constructing the many-electron Hamiltonian

Here we focus on the construction of the general many-body Hamiltonian for the quantum dot network. When written in second quantization, this Hamiltonian takes the form

$$H = \sum_i \epsilon_i c_i^\dagger c_i + \frac{1}{2} \sum_{ijkl} \langle ij|\, v \,|kl\rangle\, c_i^\dagger c_j^\dagger c_k c_l \tag{4.5}$$

where $c_i^\dagger$ and c_i are the fermionic creation and annihilation operators acting on an electron in the ith spin-orbital state $|i\rangle = |\chi_{m_s}\rangle |\xi_j\rangle$. Here, $|\chi_{m_s}\rangle$ is the spin component of the single electron spin-orbital state taking a value of either $m_s = \pm 1/2$. ϵ_j are the single electron energies as described in Section 4.2.1. Here, i, j, k, and l are composite indices for the spin and orbital components of the corresponding electron spin-orbital state. Lastly, $v = \frac{e^2}{4\pi\epsilon_0\epsilon_r} \frac{1}{|\vec{r}_2 - \vec{r}_1|}$ is the standard Coulomb potential where ϵ_0 is the vacuum permittivity and ϵ_r is the material dielectric constant (12.4 for GaAs and 7.8 for Si/SiO$_2$ where $\epsilon_{\text{Si/SiO}_2} = [\epsilon_{\text{Si}} + \epsilon_{\text{SiO}_2}]/2$).

Evaluating the Coulomb Matrix Elements (CMEs) $\langle ij|\, v \,|kl\rangle$ in the single electron basis is numerically difficult due to the divergent $\frac{1}{|\vec{r}_2 - \vec{r}_1|}$ potential term. However, the CMEs can

be calculated by decomposing them into the HO basis using $\hat{A}$

$$\langle ij|\, v\, |kl\rangle = \langle \chi_i|\chi_l\rangle \langle \chi_j|\chi_k\rangle \sum_{\alpha=1}^{M}\sum_{\beta=1}^{M}\sum_{\gamma=1}^{M}\sum_{\delta=1}^{M} A^*_{i\alpha}A^*_{j\beta}A_{k\gamma}A_{l\delta} \langle \alpha\beta|\, v\, |\gamma\delta\rangle \tag{4.6}$$

where latin indices correspond to single electron states $|\xi\rangle$, greek indices correspond to 2D harmonic orbital states $|\phi\rangle$, and * denotes the complex conjugate.

In the HO basis, the CMEs have a fully analytic solution. The derivation follows similarly to Chapter 3 of Korkusinski's thesis [148]. To begin, we will rewrite the Coulomb potential into plane waves by using the inverse Fourier transform

$$\begin{aligned}\langle \alpha\beta|\, \frac{1}{|\vec{r}_2-\vec{r}_1|}\, |\gamma\delta\rangle &= \langle \alpha\beta|\, \frac{1}{8\pi^2}\int d\vec{q}\, \frac{4\pi}{q} e^{i\vec{q}(\vec{r}_1-\vec{r}_2)}\, |\gamma\delta\rangle \\ &= \frac{1}{2\pi}\int d\vec{q}\, \frac{1}{q} \langle \alpha|\, e^{i\vec{q}\vec{r}_1}\, |\delta\rangle \langle \beta|\, e^{-i\vec{q}\vec{r}_2}\, |\gamma\rangle\, . \end{aligned} \tag{4.7}$$

The 2D harmonic orbital states are products of the 1D harmonic orbital states $|\alpha\rangle = |n_\alpha m_\alpha\rangle$ where n_α and m_α are the harmonic oscillator modes along the $\hat{x}$ and $\hat{y}$ axes respectively. Next, we will rewrite the position coordinates in terms of the canonical harmonic oscillator ladder operators

$$x_i = \frac{1}{\sqrt{2\omega}}(a_i + a_i^\dagger) \qquad y_i = \frac{1}{\sqrt{2\omega}}(b_i + b_i^\dagger) \tag{4.8}$$

where ω is the harmonic oscillator frequency.

We will now focus on the first matrix element in Equation 4.7, $\langle \alpha|\, e^{i\vec{q}\vec{r}_1}\, |\delta\rangle$. After rewriting this matrix element in terms of ladder operators, it becomes

$$\langle \alpha|\, e^{i\vec{q}\vec{r}_1}\, |\delta\rangle = \langle \alpha|\, e^{\frac{iq_x}{\sqrt{2\omega}}(a_1^\dagger + a_1)} e^{\frac{iq_y}{\sqrt{2\omega}}(b_1^\dagger + b_1)}\, |\delta\rangle\, . \tag{4.9}$$

Using both the fact that a and b commute as well as the Baker-Campbell-Hausdorff formula $e^{X+Y} = e^X e^Y e^{-\frac{1}{2}[X,Y]}$ (valid when $[X,[X,Y]] = [Y,[X,Y]] = 0$), the matrix element can be written as

$$\langle \alpha|\, e^{i\vec{q}\vec{r}_1}\, |\delta\rangle = e^{-\frac{1}{4\omega}(q_x^2+q_y^2)} \langle \alpha|\, e^{\frac{iq_x}{\sqrt{2\omega}}a_1^\dagger} e^{\frac{iq_y}{\sqrt{2\omega}}b_1^\dagger} e^{\frac{iq_x}{\sqrt{2\omega}}a_1} e^{\frac{iq_y}{\sqrt{2\omega}}b_1}\, |\delta\rangle$$

with a similar expression for the second matrix element $\langle \beta|\, e^{-i\vec{q}\vec{r}_2}\, |\gamma\rangle$ where $i \to -i$.

Next, each 2D harmonic orbital state $|\alpha\rangle$ can be rewritten as the repeated application of the creation operator on the vacuum state $|00\rangle$

$$|\alpha\rangle = |n_\alpha m_\alpha\rangle = \frac{1}{\sqrt{n_\alpha! m_\alpha!}} \left(a^\dagger\right)^{n_\alpha} \left(b^\dagger\right)^{m_\alpha} |00\rangle \, . \tag{4.10}$$

We will also insert the following identity operator into the middle of the matrix element expression

$$\hat{I} = \sum_{p_1=0}^{\infty} \sum_{p_2=0}^{\infty} |p_1 p_2\rangle \langle p_2 p_1| = \frac{1}{p_1! p_2!} \sum_{p_1=0}^{\infty} \sum_{p_2=0}^{\infty} \left(a_1^\dagger\right)^{p_1} \left(b_1^\dagger\right)^{p_2} |00\rangle \langle 00| \, b_1^{p_2} a_1^{p_1} \tag{4.11}$$

where p_1 and p_2 are two dummy indices swept over. Using these above expressions, as well as Taylor expanding the exponential operator terms, the matrix element becomes

$$\begin{aligned} \langle\alpha| \, e^{i\vec{q}\vec{r}_1} \, |\delta\rangle = {} & \frac{e^{-\frac{1}{4\omega}(q_x^2+q_y^2)}}{\sqrt{n_\alpha! m_\alpha! n_\delta! m_\delta!}} \sum_{p_1=0}^{\infty} \sum_{p_2=0}^{\infty} \frac{1}{p_1! p_2!} \sum_{s_1,s_2,s_3,s_4=0}^{\infty} \frac{\left(\frac{iq_x}{\sqrt{2\omega}}\right)^{s_1+s_3}}{s_1! s_3!} \frac{\left(\frac{iq_y}{\sqrt{2\omega}}\right)^{s_2+s_4}}{s_2! s_4!} \\ & \times \langle 00| \, a_1^{n_\alpha} \left(a_1^\dagger\right)^{p_1+s_1} b_1^{m_\alpha} \left(b_1^\dagger\right)^{p_2+s_2} |00\rangle \langle 00| \, a_1^{p_1+s_3} \left(a_1^\dagger\right)^{n_\delta} b_1^{p_2+s_4} \left(b_1^\dagger\right)^{m_\delta} |00\rangle \end{aligned} \tag{4.12}$$

where s_i are the indices in the Taylor expansions.

There are two things of note which simplify Equation 4.12. The first is that p_1 and p_2 cannot sweep all the way to ∞ and instead, go only up to $\min(n_\alpha, n_\delta)$ and $\min(m_\alpha, m_\delta)$ respectively. Above these limits, there will be indices of s_i which result in the annihilation operator being applied onto the vacuum state. The second thing is that the matrix elements are non-zero only when $p_1 + s_1 = n_\alpha$ with analogous relationships for the other three s_i and p_i indexing pairs. These observations reduce the matrix element to

$$\begin{aligned} \langle\alpha| \, e^{i\vec{q}\vec{r}_1} \, |\delta\rangle = {} & \frac{e^{-\frac{1}{4\omega}(q_x^2+q_y^2)}}{\sqrt{n_\alpha! m_\alpha! n_\delta! m_\delta!}} \\ & \times \sum_{p_1=0}^{\min(n_\alpha,n_\delta)} \sum_{p_2=0}^{\min(m_\alpha,m_\delta)} \frac{1}{p_1! p_2!} \frac{\left(\frac{iq_x}{\sqrt{2\omega}}\right)^{n_\alpha+n_\delta-2p_1}}{(n_\alpha-p_1)!(n_\delta-p_1)!} \frac{\left(\frac{iq_y}{\sqrt{2\omega}}\right)^{m_\alpha+m_\delta-2p_2}}{(m_\alpha-p_2)!(m_\delta-p_2)!} \\ & \times \langle 00| \, a_1^{n_\alpha} \left(a_1^\dagger\right)^{n_\alpha} b_1^{m_\alpha} \left(b_1^\dagger\right)^{m_\alpha} |00\rangle \langle 00| \, a_1^{n_\delta} \left(a_1^\dagger\right)^{n_\delta} b_1^{m_\delta} \left(b_1^\dagger\right)^{m_\delta} |00\rangle \, . \end{aligned} \tag{4.13}$$

Applying the ladder operators introduces a scalar $n_\alpha!m_\alpha!n_\delta!m_\delta!$ term, and the expression simplifies to

$$\langle\alpha| e^{i\vec{q}\vec{r}_1} |\delta\rangle = \frac{e^{-\frac{1}{4\omega}(q_x^2+q_y^2)}}{\sqrt{n_\alpha!m_\alpha!n_\delta!m_\delta!}} \sum_{p_1=0}^{\min(n_\alpha,n_\delta)} \sum_{p_2=0}^{\min(m_\alpha,m_\delta)} \left(\frac{iq_x}{\sqrt{2\omega}}\right)^{n_\alpha+n_\delta-2p_1} \left(\frac{iq_y}{\sqrt{2\omega}}\right)^{m_\alpha+m_\delta-2p_2} \times p_1!p_2! \binom{n_\alpha}{p_1}\binom{n_\delta}{p_1}\binom{m_\alpha}{p_2}\binom{m_\delta}{p_2} \tag{4.14}$$

with an analogous expression for the second matrix element $\langle\beta| e^{-i\vec{q}\vec{r}_2} |\gamma\rangle$ where $i \to -i$ and $p_1, p_2 \to p_3, p_4$.

Assembling everything together gives

$$\begin{aligned}\langle\alpha\beta| \frac{1}{|\vec{r}_2 - \vec{r}_1|} |\gamma\delta\rangle &= \frac{1}{2\pi}\int d\vec{q}\,\frac{1}{q} \langle\alpha| e^{i\vec{q}\vec{r}_1} |\delta\rangle \langle\beta| e^{-i\vec{q}\vec{r}_2} |\gamma\rangle \\ &= \frac{1}{2\pi\sqrt{n_\alpha!m_\alpha!n_\delta!m_\delta!n_\beta!m_\beta!n_\gamma!m_\gamma!}} \sum_{p_1=0}^{\min(n_\alpha,n_\delta)} p_1!\binom{n_\alpha}{p_1}\binom{mn_\delta}{p_1} \\ &\times \sum_{p_2=0}^{\min(m_\alpha,m_\delta)} p_2!\binom{m_\alpha}{p_2}\binom{m_\delta}{p_2} \sum_{p_3=0}^{\min(n_\beta,n_\gamma)} p_3!\binom{n_\beta}{p_3}\binom{m_\gamma}{p_3} \\ &\times \sum_{p_4=0}^{\min(m_\beta,m_\gamma)} p_4!\binom{m_\beta}{p_4}\binom{m_\gamma}{p_4} I_{p_1p_2p_3p_4}\end{aligned} \tag{4.15}$$

where the $I_{p_1p_2p_3p_4}$ is

$$\begin{aligned}I_{p_1p_2p_3p_4} = \int \frac{d\vec{q}}{q} e^{-\frac{1}{2\omega}(q_x^2+q_y^2)} &\left(\frac{iq_x}{\sqrt{2\omega}}\right)^{n_\alpha+n_\delta-2p_1} \left(\frac{iq_y}{\sqrt{2\omega}}\right)^{m_\alpha+m_\delta-2p_2} \\ \times &\left(\frac{-iq_x}{\sqrt{2\omega}}\right)^{n_\beta+n_\gamma-2p_3} \left(\frac{-iq_y}{\sqrt{2\omega}}\right)^{m_\beta+m_\gamma-2p_4}.\end{aligned} \tag{4.16}$$

We will now focus on evaluating $I_{p_1p_2p_3p_4}$. After converting to polar coordinates and using the change of variables $x = q/\sqrt{2\omega}$, the integral can be reduced to

$$I_{p_1p_2p_3p_4} = (-1)^{n_\beta+m_\beta+n_\gamma+m_\gamma+p} \frac{\sqrt{\omega}}{\sqrt{2}} \Gamma\left(p+\frac{1}{2}\right) \int_0^{2\pi} d\theta\,(\cos\theta)^a (\sin\theta)^{2p-a} \tag{4.17}$$

where Γ is the gamma function and the notation has been condensed using parameters

$$
\begin{aligned}
2p &= n_\alpha + m_\alpha + n_\delta + m_\delta + n_\beta + m_\beta + n_\gamma + m_\gamma - 2p_1 - 2p_2 - 2p_3 - 2p_4 \\
a &= n_\alpha + n_\delta + n_\beta + n_\gamma - 2p_1 - 2p_3.
\end{aligned}
$$

The integral over θ can be evaluated analytically using the beta function

$$
\mathrm{B}(x, y) = 2\int_0^{\frac{\pi}{2}} d\theta\, (\sin\theta)^{2x-1} (\cos\theta)^{2y-1} = \frac{\Gamma(x)\Gamma(y)}{\Gamma(x+y)}
$$

giving

$$
\int_0^{2\pi} d\theta\, (\cos\theta)^a\, (\sin\theta)^{2p-a} = \begin{cases} 2\mathrm{B}\left(p - \frac{a-1}{2}, \frac{a+1}{2}\right) & \text{if } a \text{ and } 2p \text{ are even} \\ 0 & \text{otherwise} \end{cases}. \tag{4.18}
$$

Lastly, using the fact that $\Gamma(x) = x\,\Gamma(x-1)$ and $\Gamma(1/2) = \sqrt{\pi}$, the final form of the full CME is

$$
\begin{aligned}
\langle \alpha\beta | \, v \, | \gamma\delta \rangle &= \langle n_\alpha m_\alpha n_\beta m_\beta | \, v \, | n_\gamma m_\gamma n_\delta m_\delta \rangle \\
&= \frac{e^2}{4\pi\epsilon_0\epsilon_r} \int d\vec{r}_1 \int d\vec{r}_2 \; \phi^*_\alpha(\vec{r}_1)\phi^*_\beta(\vec{r}_2) \frac{1}{|\vec{r}_2 - \vec{r}_1|} \phi_\gamma(\vec{r}_2)\phi_\delta(\vec{r}_1) \\
&= \sqrt{\omega} \frac{e^2}{4\pi\epsilon_0\epsilon_r} \frac{\sqrt{\pi}(-1)^{n_\beta + m_\beta + n_\gamma + m_\gamma}}{\sqrt{n_\alpha! m_\alpha! n_\delta! m_\delta! n_\beta! m_\beta! n_\gamma! m_\gamma!}} \sum_{p_1=0}^{\min(n_\alpha, n_\delta)} p_1! \binom{n_\alpha}{p_1} \binom{n_\delta}{p_1} \\
&\quad \times \sum_{p_2=0}^{\min(m_\alpha, m_\delta)} p_2! \binom{m_\alpha}{p_2} \binom{m_\delta}{p_2} \sum_{p_3=0}^{\min(n_\beta, n_\gamma)} p_3! \binom{n_\beta}{p_3} \binom{n_\gamma}{p_3} \\
&\quad \times \sum_{p_4=0}^{\min(m_\beta, m_\gamma)} p_4! \binom{m_\beta}{p_4} \binom{m_\gamma}{p_4} (-1)^p \, \frac{(2p-1)!!(2p-a-1)!!(a-1)!!}{2^{2p}\, p!}
\end{aligned} \tag{4.19}
$$

where $k!! = k(k-2)\cdots 3 \cdot 1$ is the double factorial for odd k. The above expression only holds when both a and $2p$ are even, and $\langle \alpha\beta | \, v \, | \gamma\delta \rangle = 0$ otherwise.

The analytical expression in Equation 4.19 arises due to the use of an orthogonal HO basis. This is a key distinction from the original LCHO-CI approach [83] which used a non-orthogonal set of localized HOs taken from each QD. The CME expression is similar to the equations presented in Hawrylak *et al.* [104] and Kyriakidis *eta al.* [156] which use different orbital basis sets. We denote the full $M^2 \times M^2$-dimensional matrix of CMEs

when written in the HO basis with harmonic frequency ω as $C_{\text{HO},\omega}$. The matrix of CMEs written in the single electron basis is denoted as C_{SE} and has dimension $N^2 \times N^2$. C_{SE} is easily obtained via a basis transformation $C_{\text{SE}} = (A^\dagger \otimes A^\dagger) C_{\text{HO},\omega} (A \otimes A)$.

After finding C_{SE}, we use a full configuration-interaction (CI) approach to calculate the many-electron energy spectra and eigenstates. In the full CI approach, a basis of K-electron states is constructed out of all possible K-electron configurations of single-electron spin-orbital states. After this configuration basis is constructed, the Hamiltonian from Equation 4.5 is rewritten in the configuration basis and subsequently diagonalized to find the corresponding eigenenergies and eigenstates. A detailed example of how to construct the configuration basis as well as how to rewrite the many-electron Hamiltonian in the configuration basis is given in Chapter 3 of Korkusinski's thesis [148]. The total number of configurations n_{C} of K-electron states grows according to $n_{\text{C}} = \binom{2N}{K} = \frac{(2N)!}{K!(2N-K)!}$ where $2N$ is the total number of single electron spin-orbital states. Because H conserves the total spin S_z, rather than diagonalizing the Hamiltonian using all K-electron spin-orbit configurations, the configuration basis can be restricted to a subset of $|S_z|$ subspace to ease computational requirements.

The lowest energy states of the many-electron energy spectra can be mapped onto the effective Heisenberg Hamiltonian $H = \sum_{ij} J_{ij} \vec{\sigma}_i \cdot \vec{\sigma}_j$ where indices correspond to quantum dot sites and $\vec{\sigma}$ are vectors of the 2-level Pauli spin operators. For a 2-electron system, J is the energy difference between the singlet and triplet $|T_0\rangle$ eigenstate. In the presence of no external magnetic field and in the $|S_z| = 0$ spin subspace, the ground and first excited eigenstates are the singlet and $|T_0\rangle$ state respectively giving $J > 0$ according to the Lieb-Mattis theorem [166]. Therefore, parameterizing J for a 2-electron system is done by simply taking the energy difference of the two lowest energy states. An example for parameterizing the Heisenberg Hamiltonian for a 3-electron system is given in Gimenez *et al.* [83].

4.2.3 Choosing an optimal harmonic orbital basis

The accuracy of the evaluated K-electron energy spectra relies on two parameters. The first parameter is N, or how many approximate single-electron states $|\xi'_j\rangle$ are used in the construction of the Hamiltonian in Equation 4.5. As N is increased, higher energy single-electron states can add important corrections to the K-electron energy spectra until N is sufficiently large where the energies have converged. The second parameter is how close the approximate single-electron states $\{|\xi'_j\rangle\}$ are to $\{|\xi_j\rangle\}$. If a large enough basis set of HOs M is used, then $\{|\xi'_j\rangle\}$ will converge to $\{|\xi_j\rangle\}$. However, it is not always computationally

practical to use an arbitrarily large M in order to accurately approximate $\{|\xi_j\rangle\}$ as the total size of $C_{\mathrm{HO},\omega}$ scales as M^4. For a fixed M, an improved approximation of $\{|\xi_j\rangle\}$ can be achieved by using an optimal value of ω when constructing the HO basis states. So far, there has been no discussion on the choice of ω used when building $\{|\phi_i^\omega\rangle\}$ (here we adopt a new notation for the 2D HOs which specifies the choice of ω used to construct the basis). In the LCHO-CI method laid out in Gimenez *et al.* [83], $\{|\phi_i^\omega\rangle\}$ is built by taking localized HOs centered at each respective QD in the network. For the localized HOs, ω is chosen by fitting the minima of each QD potential to a radially symmetric harmonic potential well. In the modified LCHO-CI approach described in this paper, a single collection of HOs centered at the origin constitutes the full HO basis, and there is not a direct analogue for choosing ω. Naively, ω could be chosen by fitting the potential minima of each QD in the network to a harmonic well and using the average ω extracted from each fit; however, there is nothing to suggest that this choice $\{|\phi_i^\omega\rangle\}$ will best approximate $\{|\xi_j\rangle\}$. The idea of optimizing basis orbitals used to approximate $\{|\xi_j\rangle\}$ was also used in Nielsen *et al.* [194] which optimized the relative spacing and width of Gaussian orbitals to improve the accuracy of the full CI calculation.

The optimal choice of ω should maximize the overlap between bases $\{|\xi_j'\rangle\}$ and $\{|\xi_j\rangle\}$ or mathematically $F = \sum_{j=1}^{N} |\langle \xi_j|\xi_j'\rangle|^2$. If $\{|\xi_j'\rangle\}$ perfectly describes $\{|\xi_j\rangle\}$, then $F = N$. We can optimize ω then by recalculating $\{|\xi_j'\rangle\}$ for a given choice of ω and subsequently minimizing $1 - \frac{1}{N}F$. However, evaluating $\{|\xi_j'\rangle\}$ during each optimization step means H_ϕ must be constructed and subsequently diagonalized as described in Section 4.2.1. The construction of H_ϕ alone requires the evaluation of $M(M+1)/2$ inner products $H_{ij}^\phi = \langle\phi_i| H |\phi_j\rangle$. Optimizing ω this way can be very slow due to the large choice of M typically required for the LCHO-CI calculations. We note that the exact length of time it takes to calculate H_ϕ strongly depends on the number of grid points used in constructing the 2D potentials. This is because more grid points increases the computation cost of each individual inner product, a numerical integration over the 2D grid.

To reduce the computational complexity of this optimization, we take a slightly different approach. We note that if the single electron basis states $\{|\xi_j\rangle\}$ can be accurately decomposed into the HO basis $\{|\phi^\omega\rangle\}$, then for each state $|\xi_j\rangle$, we have $\sum_{i=1}^{M} |\langle\xi_j|\phi_i^\omega\rangle|^2 \approx 1$. If instead $\{|\phi^\omega\rangle\}$ poorly describes $|\xi_j\rangle$, then $\sum_{i=1}^{M} |\langle\xi_j|\phi_i^\omega\rangle|^2 < 1$. Therefore for a choice of N' single-electron states $|\xi_j\rangle$, an optimal ω can be found via the following minimization problem

$$\min_\omega \; f_{\min}(\omega) = \min_\omega \; 1 - \frac{1}{N'} \sum_i^{N'} \sum_j^{M} |\langle\xi_i|\phi_j^\omega\rangle|^2 \tag{4.20}$$

where we refer to the optimization function as $f_{\min}(\omega)$. Note that we have specified using a

smaller subset N' of the single-electron orbitals compared to the full number of N orbitals used in the main LCHO-CI calculation. Using $N' < N$ does not significantly impact the final ω value and allows for a slightly faster minimization. The N' single-electron states $|\xi_j\rangle$ need to only be evaluated once at the beginning of the minimization, and only $N' \times M$ inner products are calculated during each minimization step. As N' is usually $\ll M$, this is much faster than directly calculating H^ϕ and does not bottleneck the full LCHO-CI calculation. For minimizations done in this chapter, the minimization is done using a BFGS quasi-Newton search with a first-order optimality tolerance of 1×10^{-6} [70].

Figure 4.2 shows how the optimization function $f_{\min}(\omega)$ depends on ω as well as the size of the HO basis $\{|\phi_i^\omega\rangle\}$. The single electron orbitals $|\xi_j\rangle$ are found using a quartic potential where $m^* = 0.191m_0$ (Si/SiO$_2$ system), $\hbar\omega_0 = 0.375$ meV ($l_0 = 32.6$ nm), and $d = 50$ nm. The first $N' = 6$ single electron states are used in the minimization, and M is stepped from 1 to 16^2. Recall that $M = M_x M_y$ where we have set $M_x = M_y$. Different line colors specify different M values. Non-optimal ω values can yield orders of magnitude worse values of $f_{\min}(\omega)$ compared to the optimal choice of ω. This indicates using the optimal ω is a very useful way to improve the accuracy of the approximated orbitals $\{|\xi'_j\rangle\}$ during the LCHO-CI calculation. At a fixed ω, as M is increased, $f_{\min}(\omega)$ always decreases; this is in accordance with the fact that as the size of $\{|\phi_i^\omega\rangle\}$ increases, better approximations of $\{|\xi_j\rangle\}$ can be obtained no matter the choice of ω. Additionally, as M increases, the optimal choice of ω appears to converge towards a singular overall optimal ω.

After the optimal ω is found, C_{HO} must be evaluated to continue with the LCHO-CI calculation. Typically, evaluation of the CMEs is the most computationally intensive part of the CI calculation, and this is still true here, even though the HO CMEs have an analytical form. However, we make use of the fact that in Equation 4.19 the only dependence on ω is a scalar $\sqrt{\omega}$ term that can be factored out. A large matrix of CMEs can be pre-calculated for a unit choice of $\omega = 1$ ($C_{\text{HO},1}$) and then simply scaled by $\sqrt{\omega}$ to obtain the matrix of CMEs for the optimal HO basis

$$C_{\text{HO},\omega} = \sqrt{\omega} C_{\text{HO},1}. \tag{4.21}$$

Using the pre-calculated library $C_{\text{HO},1}$ allows for numerically quick yet still quantitatively accurate full LCHO-CI calculations across a range of quantum dot network potentials. This is a key computational speed-up in this modified LCHO-CI approach. The longest part of the calculation (evaluating C_{SE}) becomes a simple scalar multiplication of $C_{\text{HO},1}$ and subsequent rotation of $C_{\text{HO},\omega}$ into the single electron basis. The idea of using a pre-calculated library of CMEs to speed up CI calculations was used previously in Pedersen *et al.* [204] for a Gaussian orbital basis; however, the orbital basis was never optimally tuned to improve the accuracy of the results.

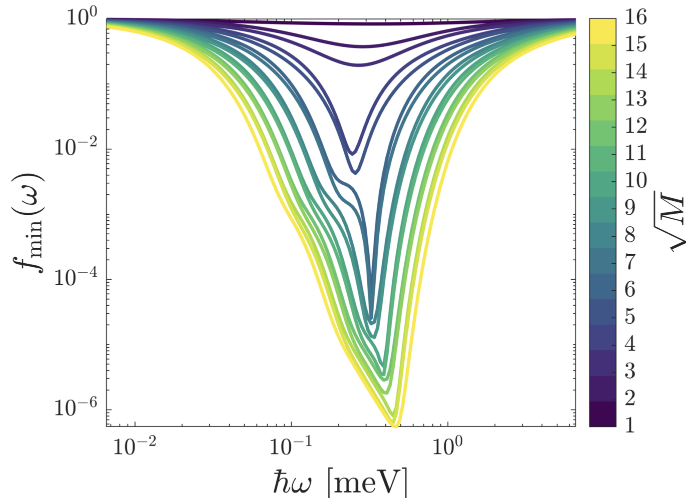

Figure 4.2: Dependence of the optimization function $f_{\min}(\omega)$ on ω and the size of the harmonic orbital basis ($M_x M_y = M$). $N' = 6$ for a quartic potential with parameters $m^* = 0.191m_0$, $\hbar\omega_0 = 0.375$ meV, and $d = 50$ nm. Color indicates a different number of HO basis states ranging from $M_x = M_y = 1$ (purple) to $M_x = M_y$=16 (yellow).

In Section 4.3, we perform modified LCHO-CI calculations of a double quantum dot potential where $M = 16^2$, $N = 18$, and $N' = 6$. The grid spacing of the 2D potential along $\hat{x}$ and $\hat{y}$ axes is 0.5 nm. The choice of M gives a total of 16^8 CMEs to calculate using Equation 4.19. In this chapter, the CME calculations were done in MATLAB using a computer with an Intel Xeon E5-2650 processor and parallelized across 24 cores. It takes us ∼10 hours to evaluate all the CMEs (only half of the CMEs are calculated as $C_{\text{HO},1}$ is Hermitian, and 3/4 of the matrix elements are zero). The scalar multiplication done to convert $C_{\text{HO},1}$ to $C_{\text{HO},\omega}$ is relatively fast, taking only a few seconds. The basis rotation of $C_{\text{HO},\omega}$ into C_{SE} takes tens of seconds and depends on the size of both N and M. For the N and M values used, after the initial long calculation in evaluating $C_{\text{HO},1}$, the total evaluation of C_{SE} takes ∼25 seconds. The other steps in the LCHO-CI which include optimization of ω, evaluation of A, and construction of the second quantization Hamiltonian take approximately 20, 90, and 30 seconds respectively. This gives a total modified LCHO-CI calculation time of ∼3 minutes. These values correspond to a 2D potential with approximately 300×100 grid points. Larger grids will increase the computation time of optimizing ω and evaluating A. The other steps in the modified LCHO-CI calculation are unaffected by the grid size.

It is worthwhile to point out that for some QD networks, such as a linear chain of QDs, it might be more ideal to use an elliptical set of 2D HOs where $\omega_x \neq \omega_y$ in order to better approximate the single-electron states $|\xi_j\rangle$. If $\omega_x \neq \omega_y$, then the HO CMEs still have a closed analytical form; however, ω_x and ω_y cannot be factored out of the CME expression (refer to Appendix A). This means that an elliptical HO basis does not provide the same computational speed performance as the radially symmetric case, and this is why we have chosen to use HOs with $\omega_x = \omega_y$. We note that it is possible to pre-calculate a discrete set of elliptical CME matrices $C_{\text{HO},1,\kappa}$ where $\omega_x = 1$ and $\kappa = \omega_x/\omega_y$ is the HO eccentricity. We can then optimize over a continuous choice of ω_x as well as a discrete set of κ values and subsequently find $C_{\text{HO},\omega_\text{x},\omega_\text{y}} = \sqrt{\omega_x}C_{\text{HO},1,\kappa}$ (see Appendix A). This comes at the cost of storing a pre-calculated $C_{\text{HO},1,\kappa}$ matrix for each choice of κ which, due to the large choice of M typically required for these calculations, may make this impractical. An alternative idea for QD networks where eccentric harmonic orbitals are desirable could be to use an asymmetric choice of $M_x \neq M_y$ when building a 2D HO basis to approximate $\{|\xi'_j\rangle\}$. However, this idea is not explored in this work as we deal with only a small double QD system and use $M_x = M_y$ for all calculations.

4.2.4 Comparison to Heitler-London and Hund-Mülliken methods

We conclude the discussion of the modified LCHO-CI approach by comparing it to the Heitler-London (HL) [21, 28] and Hund-Mülliken (HM) [113, 261, 103] approaches for evaluating J. The system considered is a double quantum dot system with a quartic potential given by Equation 4.1 occupied by 2 electrons. In both the HL and HM approaches, the 2-electron singlet and triplet states are constructed using localized s-orbitals taken from each dot. The HL approach includes only the singly occupied $S(1,1)$ and $T(1,1)$ states while the HM method extends the basis set to include the doubly occupied singlet $S(0,2)$ and $S(2,0)$ states. (n,m) denotes the electron occupancy in each quantum dot. The localized s-orbitals for both the HL and HM methods are found by approximating each potential minimum as a harmonic well with confinement ω_0 located at $\pm d$. Approximating the orbital states this way gives rise to analytical expressions for J when the quartic potential is used, for both the HL and HM methods [21]. The analytical expressions make these methods useful for exploring qualitative behavior under a variety of potential parameters as well as magnetic field B or inter-dot detuning. However, both methods are known to break down at small inter-dot separations $2d$ and give an nonphysical result where J is negative at zero-magnetic field. Quantitatively, the breakdown occurs for potential where the ratio of the Coulomb and confinement energies $c = \sqrt{\pi/2}(e^2/4\pi\epsilon_0\epsilon_r l_0)/\hbar\omega_0 > 2.8$.

Therefore, c is inversely proportional to $l_0 = \sqrt{\hbar/m^*\omega_0}$ and is directly proportional to m^*. This means that the HL and HM methods break down more easily at close inter-dot distances for small dot sizes and in Si/SiO_2 which has a larger m^* compared to GaAs. The inter-dot separation at which breakdown occurs increases with larger dot radii [28]. This limits the parameter space over which the HL and HM methods can be used to study J particularly for Si/SiO_2.

This breakdown occurs due to poor approximations of the localized s-orbitals at small dot separations. Each localized s-orbital is assumed to be taken from a harmonic well (i.e. gaussian) and separated by $2d$. However, at small inter-dot separations, the tunneling barrier in the quartic potential is lowered, and the electrons delocalize towards the center of the double well potential. This effect is shown in Figure 4.3a which compares the ground single electron orbital eigenstate for both the HL/HM and LCHO-CI methods at different dot separations $2d$. We consider a Si/SiO_2 material system with $l_0 = 6$ nm for the quartic potential. The ground eigenstate for the HL/HM methods is found as $|\psi_0\rangle = (|R\rangle + |L\rangle)\sqrt{2}$ where $|R\rangle$ and $|L\rangle$ are the localized s-orbitals taken at $\pm$d respectively. The ground eigenstate for the LCHO-CI method is obtained numerically using the methods outlined in Section 4.2.1. At small dot separations $2d$, the HL/HM clearly overestimate the actual localization of the electron orbitals. As the separation increases, the numerical and HL/HM methods more closely agree. We expect that when d/l_0 is large, that the numerical and HL/HM should produce similar results for J. For these particular potential parameters when $d/l_0 > 10$, we find that the overlap between the approximated HL/HM and numerical LCHO-CI ground state orbitals is $\sim$0.99. Therefore, we anticipate that the LCHO-CI and HL/HM methods should converge to the same J value around $d/l_0 > 10$. Of course, there is no precise comparison between the error in the single electron orbitals and the many-electron spectra, so this is only an estimate.

Figure 4.3b shows the calculated J as the dot separation $2d$ for the quartic potential is varied. In addition to the HL (purple) and HM (dark blue) calculations, we do three modified LCHO-CI calculations where $N = 2$ (blue), 4 (green), and 10 (yellow) single electron orbitals are used to build the two-electron configuration basis. For all LCHO-CI calculations, $M = 15^2$. As the dot separation decreases, J increases due to the enhanced Coulomb interaction as the electrons are brought closer together. The most striking feature of the curves is the anticipated breakdown of the HL and HM approaches where J goes negative around a dot separation of 18 nm for the chosen l_0. All of the three LCHO-CI calculations show no breakdown at small dot separations. This is expected as the LCHO-CI performs an exact diagonalization of the many-electron Hamiltonian as opposed to the approximate approach in the HL/HM methods. As N increases, J decreases for the LCHO-CI calculations until J converges around $N = 10$ (variations are less than 3%).

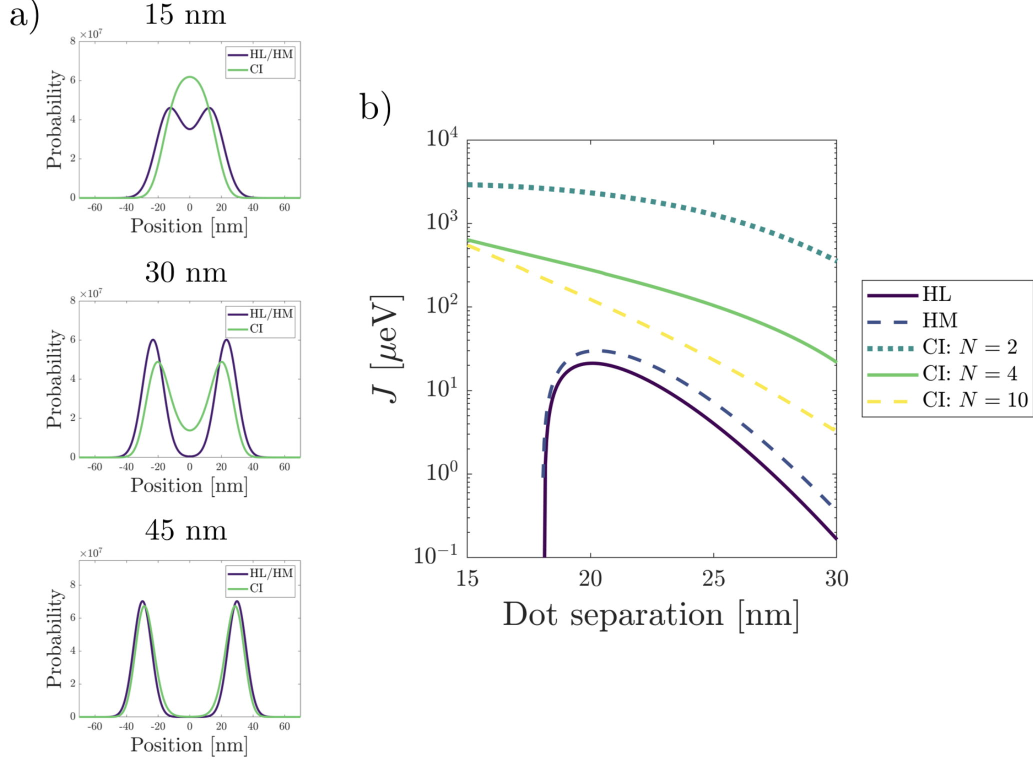

Figure 4.3: Comparison of the HL (purple) and HM (dark blue) methods to the modified LCHO-CI method for evaluating J. The system considered is Si/SiO_2 with a double dot quartic potential where $l_0 = 6$ nm. a) The ground single electron orbital eigenstate for the HL/HM and LCHO-CI calculations at different dot separations. At small dot separations, the HL/HM overestimate the actual separation of the two localized wavefunctions when found numerically for the quartic potential. As dot separation increases, the HL/HM approximated states converge to the numerically obtained orbitals. b) J versus the inter-dot separation $2d$ is plotted. Three different LCHO-CI calculations are done for $N = 2$ (light blue), 4 (green), are 10 (yellow). For all LCHO-CI calculations $M = 15^2$.

For the quartic potential, the HL and HM methods seemingly underestimate the exchange energies found using the LCHO-CI approach. The $N = 2$ LCHO-CI calculation uses a 2-electron configuration basis similar to the HL and HM methods with the exception that the doubly occupied triplet $T(0, 2)$ and $T(2, 0)$ states are added to the basis set. Even though the $N = 2$ and HL/HM basis functions are similar, there are orders of magnitude

of difference in the calculated J values. This is attributed mainly to the fact that the HL/HM methods overestimate the actual dot separation resulting in a lower calculated J. The key takeaway from this section is to demonstrate the necessity of using numerical approaches such as the modified LCHO-CI method to calculate J for general quantum dot networks. Approximate methods like the HL and HM approaches are computationally easy to implement but suffer significant flaws such as breakdown for some dot configurations. As such, HL and HM methods should only be used qualitatively and not for quantitative accuracy, especially when used for larger effective mass material systems like silicon.

4.3 Charge noise sensitivity of a double quantum dot device

In this section, the modified LCHO-CI method is used to investigate the charge noise sensitivity of the exchange interaction in a 2-electron double quantum dot system. Charge noise is composed of two sources: fluctuations in the gate electrode voltages as well as charge fluctuations in background charge traps present in the host material system. Both of these sources perturb the potential minima as well as the tunnel barrier in the double quantum dot system. The potential fluctuations in turn perturb the electron orbitals which causes modulations in J. We investigate which device geometries make J less susceptible to these potential fluctuations coming from the two sources of charge noise. As charge noise is a strong decoherence mechanism for spin qubits, finding optimal device geometries to improve robustness to charge noise is critical for achieving high fidelity multi-spin logic gates.

The calculations are done in a Si/SiO_2 material system where they are particularly relevant because SiO_2 is a known source of charge traps. The silicon valley states are assumed to have a large splitting (100s meV) which is uniform between the two QDs. If the valley splitting Δ is greater than the thermal broadening energy k_BT, then electrons loaded into the double QD system will populate only the ground valley eigenstate. Because Coulomb interactions between opposite valley eigenstates are weak [49], the Hamiltonian in Equation 4.5 does not couple the electrons to excited valley-states, and we can assume a single-valley system for our purposes. We note that at worst, neglecting valley physics means that the exchange interaction strengths J calculated in this section represent the highest possible strengths. We saw in Chapter 3 that differences in the phase of the valley splitting $\delta\phi$ between adjacent quantum dots serve to decrease the effective inter-dot tunnel coupling strength t_c. As it can be shown in the small detuning regime that $J \propto t_c^2$ [221], we anticipate that non-zero $\delta\phi$ would decrease the effective J, resulting in J being maximal

when $\delta\phi = 0$. In our calculations, we additionally neglect any effects of the small but non-zero spin-orbit interaction in silicon which can be fully tuned to zero by appropriately tuning the direction of an external magnetic field [250].

4.3.1 Device model

Rather than use an analytical form for the potential landscape, a full 3D device structure including the Si/SiO_2 heterostructure and the metal gates electrodes used to define the quantum dots is simulated using a self-consistent Poisson solver in nextnano++ [11]. In general, when modelling nanostructures, it is ideal to use Schrödinger-Poisson calculations instead of Poisson calculations as the former method takes into account quantum effects that the accumulated electron density has on the potential landscape. However, during either Poisson or Schrödinger-Poisson calculations the electron density can change continuously as the gate voltages are swept. This does not match the experimental behavior seen in QDs which maintain a fixed electron number as the gate voltages are swept and the QDs are decoupled from an electron reservoir. Because of this, all of our simulations are done below the turn-on voltage threshold of the device where the electron density is zero and therefore fixed as the gate voltages are swept. In the zero-charge regime, Poisson and Schrödinger-Poisson calculations are the same and is why only Poisson calculations are done here. For detail, refer back to Section 3.3.1. There it was shown that for a double quantum dot system, the presence of a single electron in a double well potential reduces the tunnel barrier and increases the orbital spacing. Because the exchange interaction is very sensitive to variations in the electrostatic potential, this approximation is important to consider in the scope of discussing our results. However, we anticipate a proper accounting for this effect would only provide a relatively minor quantitative change in our results and not affect any qualitative behavior.

Figure 4.4a shows a 3D render of the double quantum gate structure with an 2D potential slice taken 1 nm below the Si/SiO_2 interface. Two plunger gates with the corresponding voltages V_{p1} and V_{p2} form a double well potential along with a tunneling gate with voltage V_t that is used to control the tunneling barrier. The gate voltages used to form the particular 2D potential are $V_{p1} = V_{p2} = 0.15$ V and $V_{\text{tun}} = 0.094548$ V. These particular voltages are used because they give an exchange interaction strength $J \approx 1$ μeV. Two outer barrier gates are included in the device structure and are kept grounded for all simulations ($V = 0$ V). The outer barrier gates are included to better model a realistic device which is typically surrounded by other metallic gates. A grounded screening gate ($V = 0$ V) underneath the arms of the plunger and barrier gates restricts the formation of the potential wells underneath the heads of the plunger gates. Figure 4.4b shows a 2D view of the potential overlaid

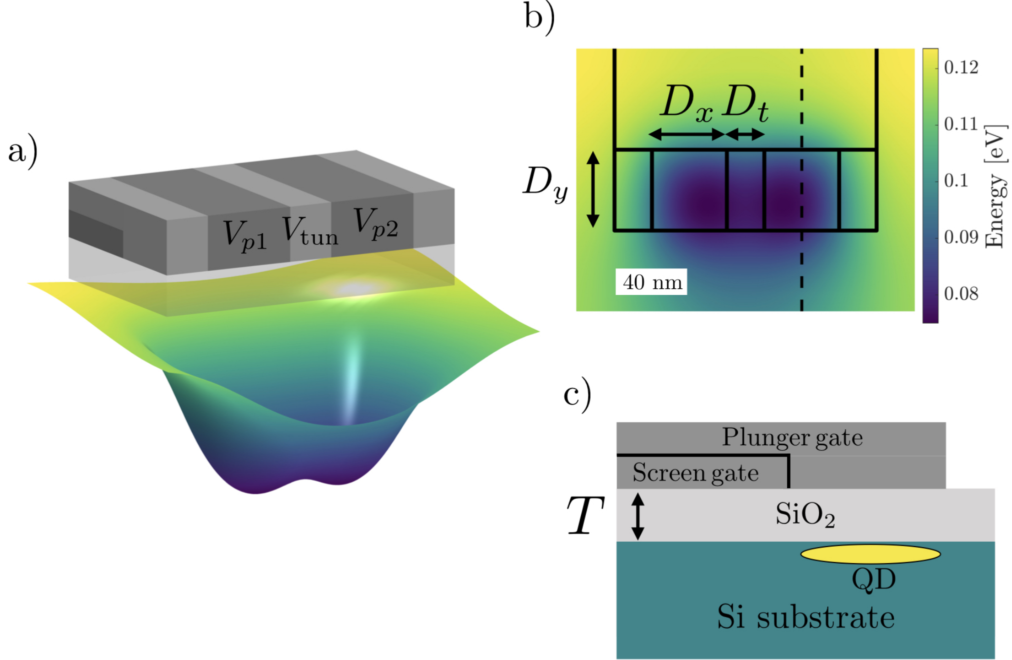

Figure 4.4: Schematic of a double quantum dot gate geometry formed by plunger, tunnel, and screening gates. The device parameters are $D_x = D_y = 40$ nm, $D_t = 20$ nm, $T = 15$ nm $V_{p1} = V_{p2} = 0.150$ V, and $V_{\text{tun}} = 0.094548$ V. a) 3D model of the gate geometry where the plunger, tunnel and screening gates are colored differently for better contrast along with a semi-transparent SiO_2 layer. A simulated electrostatic potential obtained by a 3D self-consistent Poisson calculation is plotted below. b) A 2D view of the potential overlaid with an outline of the gate structure showing the heads of the plunger and tunnel gates as well as the screening gate. The width and length of the plunger gate as well as the width of the tunnel gate are labelled D_x, D_y, and D_t respectively. The potential is taken 1 nm below the Si/SiO_2 interface. c) A side profile of the gate structure taken along the dashed line in b). The SiO_2 layer thickness is labelled T. The quantum dot (yellow ellipse) is formed underneath the head of the plunger gate.

with an outline of the plunger, tunnel and screening gates. The plunger gate widths along the $\hat{x}$ and $\hat{y}$ axes are labelled D_x and D_y, respectively. The tunneling gate width along $\hat{x}$ is labelled D_t, and the $\hat{y}$ dimension of the tunneling gate is chosen to always be equal to D_y. When D_x, D_y or D_t is changed, it is changed for all the corresponding gates in unison so that the gate layout is always symmetric about the central $\hat{y}$ axis. The lack of

a screening gate on the bottom half of the device causes an asymmetry in the potential along the $\hat{y}$ axis seen by the fact the potential wells form slightly off-center of the plunger gate heads. Figure 4.4c shows a 1D cut along the dashed black line in Figure 4.4d to show the screening gate and SiO_2 layer with corresponding thickness T. The screening gate restricts accumulation of the QD to be under the plunger gate head. The device geometric parameters used in Figure 4.4 are $D_x = D_y = 40$ nm, $D_t = 20$ nm, and $T = 15$ nm.

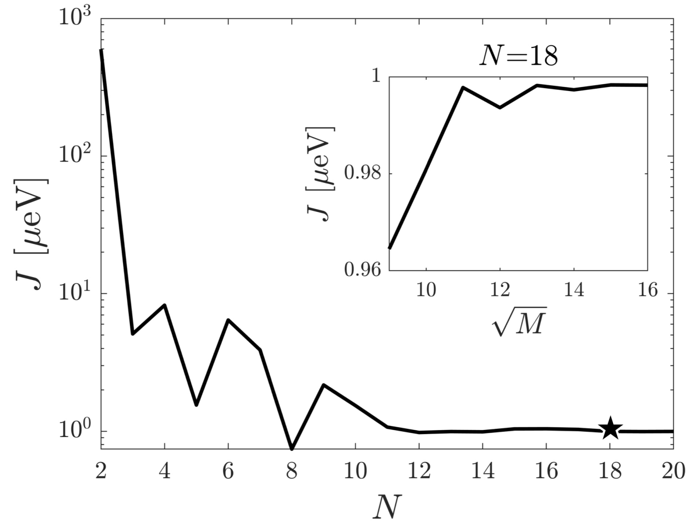

Figure 4.5: Convergence of J with respect to the number of single electron orbitals N when $M = 16^2$. The device parameters are $V_{p1} = V_{p2} = 0.15$ V, $V_t = 0.094548$ V, $D_x = D_y = 40$ nm, $D_t = 20$ nm, and $T = 15$ nm. *Inset:* The convergence of J with respect to M when $N = 18$ (star in the main figure).

The potential shown in Figure 4.4 is used to demonstrate the typical convergence behavior of J using the LCHO-CI method with this device geometry. Figure 4.5 shows J versus the number of single electron orbitals N (main figure) as well as the number of harmonic orbitals M (inset panel). For all data points, ω is reoptimized, and in the main figure, $M = 16^2$. As more single electron orbitals are included, the higher order electron-electron correlations end up reducing the overall exchange splitting. Around $N = 12$, J begins to stabilize but does not stop varying by $< 1\%$ until $N = 18$ where $J \approx 1$ μeV. The inset shows how J converges at $N = 18$ with respect to the number of harmonic orbitals M. Good convergence ($< 1\%$ variation) is achieved when $M > 15^2$. While the device parameters are varied throughout the remainder of this work, the convergence behavior is qualitatively the same as what is shown in Figure 4.5. As such, for every exchange

calculation done from here on out, we use $N = 18$ and $M = 16^2$. These values give $n_C = 630$ two-electron spin-orbital configuration states, $C_{\text{HO},\omega}$ of size 65536×65536, and C_{SE} of size 324×324.

4.3.2 Charging energies and lever arms

Here we show how the charging energies U and lever arms α are extracted for the device geometry introduced in Section 4.3.1. These parameters are used to study the device's sensitivity to charge noise in Section 4.3.3. When evaluating U, we use only symmetric double QD potentials where the plunger gate bias voltage $V_{\text{bias}} = 0$ V. For a double QD system where both dots are the same size, the charging energy U of each QD can be evaluated as [231]

$$U = \left\langle \psi_{L/R}(\vec{r}_1)\psi_{L/R}(\vec{r}_2) \right| v \left| \psi_{L/R}(\vec{r}_2)\psi_{L/R}(\vec{r}_1) \right\rangle \tag{4.22}$$

where v is the standard Coulomb potential as given in Equation 4.5, and $\left|\psi_{L/R}\right\rangle$ are the localized electron orbitals in the left/right QDs. The localized orbitals are found by taking the symmetric and anti-symmetric combinations of the ground and first excited orbital eigenstates of the double QD potential: $\left|\psi_{L/R}\right\rangle = \frac{1}{\sqrt{2}}(\left|\psi_0\right\rangle \pm \left|\psi_1\right\rangle)$. The charging energy U can be found by following the procedure outlined in Section 4.2 to find the Coulomb matrix elements of these new single electron orbitals $\left|\psi_{L/R}\right\rangle$. The specific charging energies U that are calculated for each device geometry are given in the tables of Figures 4.7, 4.8, 4.9, and 4.10 of Section 4.3.3.

Next, we show how to evaluate the lever arm α for each device geometry. The lever arm connects the plunger gate bias voltage to the effective inter-dot detuning $\epsilon = \epsilon_R - \epsilon_L$ as $\epsilon = \alpha V_{\text{bias}}$ where $\epsilon_{L/R}$ is the localized ground state energy in the left/right QD. To find α, V_{bias} is varied and the tunnel gate voltage V_{tun} remains fixed. We model the double QD system with the simple two-level Hamiltonian

$$H = \begin{bmatrix} \epsilon_L & t_c \\ t_c & \epsilon_R \end{bmatrix}. \tag{4.23}$$

where the basis states are $\{\left|\psi_L\right\rangle, \left|\psi_R\right\rangle\}$. The energy difference between the ground and first excited energy levels of H is given as

$$\epsilon_1 - \epsilon_0 = \sqrt{\epsilon^2 + 4\,t_c^2}. \tag{4.24}$$

The eigenenergies ϵ_0 and ϵ_1 are found by solving the Schrödinger equation from Equation 4.2. The inter-dot tunnel coupling t_c is found when $V_{\text{bias}} = 0$, which corresponds to

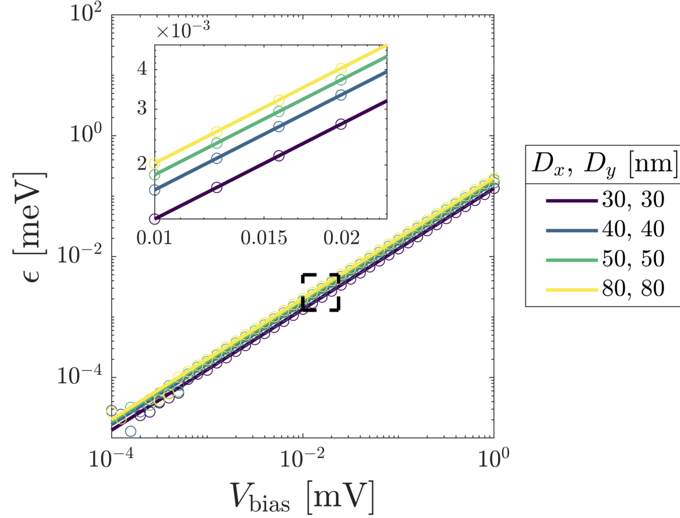

Figure 4.6: Relationship between bias voltage V_{bias} and inter-dot detuning ϵ for different dot sizes. The calculated data points are indicated by circles and the solid line is a fit to the equation $\epsilon = \alpha V_{\mathrm{bias}}$ where α is the lever arm. The region in the dashed black box is enlarged and shown in the inset to demonstrate the linearity of the fitted data.

an effective inter-dot detuning of $\epsilon = 0$. t_c is assumed to remain fixed as V_{bias} is varied. Equation 4.24 is used to find the corresponding ϵ value for each V_{bias} data point.

The resulting data are fit to the linear relationship $\epsilon = \alpha V_{\mathrm{bias}}$ to find α for the corresponding device geometry. Figure 4.6 shows data of detuning versus bias voltage for a few different device geometries where the dot size $D_x = D_y$ was varied. The other device parameters are $D_t = 20$ nm, $T = 15$ nm, and $V_p = 0.150$ V. Circles are actual data points, and solid lines correspond to $\epsilon = \alpha V_{\mathrm{bias}}$ fits. For all data sets, the data is only fit in the interval $V_{\mathrm{bias}} = [10^{-3}, 10^{-1}]$ mV to avoid noise at low bias voltages and prevent fitting in any non-linear high bias regimes. The region shown in the figure inset (dashed black box in the main figure) demonstrates the accuracy of the linear fit to the data. Only a handful of device geometries are presented here for visual clarity, but all fitted data sets used throughout this chapter show similar behavior and fit quality. The specific α values extracted for each device geometry are given in the tables of Figures 4.7, 4.8, 4.9, and 4.10 of Section 4.3.3.

4.3.3 Exchange calculations for different gate geometries

The 3D model of the device structure discussed in Section 4.3.1 allows us to study how the physical gate geometry impacts the exchange interaction's sensitivity to charge noise. It is quantified using the derivative of the exchange interaction with respect to a bias voltage V_{bias} applied between the two plunger gates which form the quantum dots. The bias is also converted into the effective inter-dot detuning ϵ. Here, $\epsilon = \epsilon_2 - \epsilon_1$ where ϵ_j is the ground state energy in the jth QD. $\partial J/\partial V_{\text{bias}}$ highlights J's sensitivity to the raw voltage noise. On the other hand, $\partial J/\partial \epsilon$ highlights J's sensitivity to more general electrostatic fluctuations in the surrounding material system such as charge traps.

We now outline the general procedure used to study J throughout this section. First, for a series of varying device geometries, we sweep the tunneling gate voltage V_{tun} at a fixed plunger gate voltage $V_p = V_{p1} = V_{p2}$. For each device geometry, $J(V_{\text{tun}})$ is linearly interpolated to find V_{tun} which yields $J = 1$ μeV (corresponding to ∼2 ns SWAP pulse). At each interpolated V_{tun} value, a symmetric bias voltage V_{bias} is applied between the plunger gates such that $V_{p1} \to V_p - V_{\text{bias}}/2$ and $V_{p2} \to V_p + V_{\text{bias}}/2$. From the biased potentials the plunger gate lever arm α is calculated which connects V_{bias} and ϵ as $\epsilon = \alpha V_{\text{bias}}$ (refer back to Section 4.3.2 for details). This produces two resulting exchange derivatives for each device geometry: $\partial J/\partial V_{\text{bias}}$ and $\partial J/\partial \epsilon$. Additionally for each device geometry, we calculate the charging energy U of each QD using the 2D potentials that give $J = 1$ μeV at zero bias. The derivative of J is a non-trivial relationship between the bias voltage, tunnel gate voltage, and device geometry. This chapter focuses in particular on exploring the impact that the device geometry has on J's sensitivity to charge noise. In order to make a systematic comparison and remove the effect of V_{tun} on J, we tune all geometries to the same reference J value at zero bias. As a reminder, for all simulations, we use $N = 18$ and $M = 16^2$ for the modified LCHO-CI calculations. In this 2-electron system with no magnetic field, J is the energy difference between the two lowest eigenenergies and is always greater than zero.

Varying plunger gate size

We first study how varying the plunger gate size D_x and D_y impacts the exchange interaction's sensitivity to charge noise. The results are summarized in Figure 4.7. Both D_x and D_y are varied simultaneously from 30 nm (purple) to 80 nm (yellow) in steps of 10 nm so that the plunger gate head is square for each device geometry. The tunnel gate width $D_t = 20$ nm, and the oxide thickness $T = 15$ nm. Figure 4.7a shows how J varies with V_{tun} when $V_p = 0.150$ V. For all curves, J increases as V_{tun} increases. As V_{tun} is increased,

the tunnel barrier decreases, and the localized electron orbitals have a larger probability of being in the tunnel barrier region. This in turn enhances the Coulomb interaction and subsequently raises J. For a fixed V_{tun}, J decreases as the dot size increases. This is because as the area of the plunger gate head increases, there are additional electric field contributions that come from the edge of the plunger gate. These contributions further push the potential minima lower with respect to the tunnel barrier gate, creating an effectively higher tunnel barrier. This is the same as saying the capacitive coupling between the plunger gate and the QD potential increases with bigger plunger gates. In addition, the wider plunger gates further separate the electron orbitals which reduces their overlap and Coulomb interaction. Lastly, the increasing plunger gate size also directly increases the dot size. The wider QD potentials further localize the electron orbital more within the potential minima. This suppresses the electron orbital overlap in the tunnel barrier region and reduces the Coulomb interaction strength. Taking all these effects together explains why J decreases with increasing dot size. The V_{tun} values where $J = 1$ μeV for each device geometry (indicated by the dashed black line) are given in Section 4.3.4.

Figures 4.7b-c show the derivative of J with respect to V_{bias} and ϵ when $J = 1$ μeV at zero bias. In both figures, the derivative increases with a larger bias. This is due to the accumulated dipole characteristic of the singlet-like ground state with respect to the triplet-state [163, 218]. At $V_{\mathrm{bias}} = \epsilon = 0$, both the low energy singlet- and triplet-like states are in the $(1,1)$ charge configuration. As a bias is applied, the singlet $S(1,1)$ state starts to tunnel into the $S(0,2)$ charge configuration and acquires a non-zero dipole moment. However, the $T(1,1)$ state remains unaffected by the bias as the $T(0,2)$ state is energetically unavailable. Therefore, the triplet state acquires no dipole moment as the bias increases. The accumulated dipole moment in the singlet state makes the ground state more sensitive to electrostatic fluctuations. As the bias increases, so does the accumulated dipole which increases that sensitivity. In Figures 4.7b-c where $D_x = D_y \geq 60$ the second derivative can be seen to increase near $V_{\mathrm{bias}} = 10^{-2}$ V. This happens because the singlet state is biased near the $S(1,1)$-$S(0,2)$ anticrossing.

Figures 4.7b-c show that the charge noise sensitivity with respect to both V_{bias} and ϵ increases as the dot size $D_x = D_y$ increases. The physical reason is straightforward and can be understood by considering the simple Hubbard model. The Hubbard Hamiltonian for a double quantum dot system is

$$H_{\mathrm{Hub}} = \sum_{j=1,2;\chi} \epsilon_j n_{j,\chi} + U n_{j,\chi}(n_{j,\chi} - 1) + \frac{t_c}{\sqrt{2}}(c^\dagger_{1,\chi} c_{2,\chi} + c^\dagger_{2,\chi} c_{1,\chi}) \tag{4.25}$$

where $c^\dagger_{j,\chi}$ creates an electron in the jth QD with spin state χ and $n = c^\dagger c$. ϵ_j is the QD's ground state energy, U is the QD's charging energy (both dots are assumed to be identical

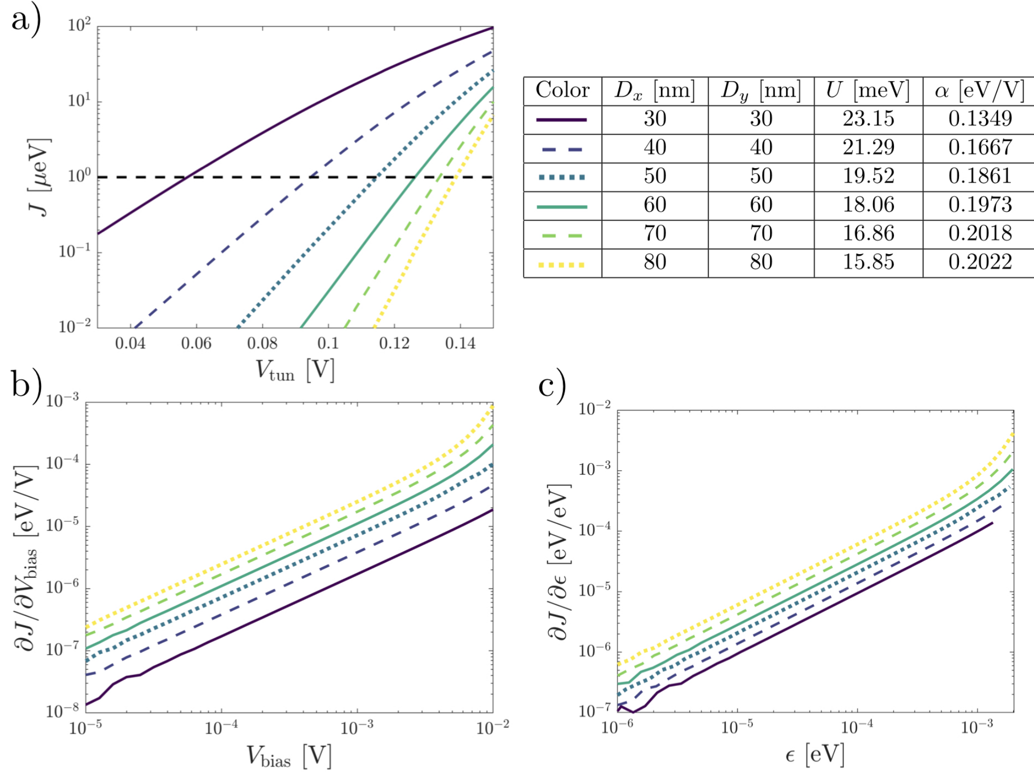

Color	D_x [nm]	D_y [nm]	U [meV]	α [eV/V]
	30	30	23.15	0.1349
	40	40	21.29	0.1667
	50	50	19.52	0.1861
	60	60	18.06	0.1973
	70	70	16.86	0.2018
	80	80	15.85	0.2022

Figure 4.7: Dependence of J as the dot size D_x, D_y is varied. a) J as V_{tun} is swept from 0.03−0.150 V. The other fixed device parameters are $V_p = 0.150$ V, $V_{\mathrm{bias}} = 0$ V, $D_t = 20$ nm, and $T = 15$ nm. The dashed black line indicates where $J = 1$ μeV. b) Derivative of J with respect to V_{bias}. For each device geometry, V_{tun} is tuned so that $J = 1$ μeV at $V_{\mathrm{bias}} = 0$. c) Derivative of J with respect to ϵ where $\epsilon = \alpha V_{\mathrm{bias}}$ and α is the lever arm between the raw bias voltage and the effective inter-dot detuning. The upper-right table indicates the corresponding varied device parameters, charging energy U, and lever arm α.

so $U_1 = U_2$), and t_c is the inter-dot tunnel coupling. J is the difference between the ground and first excited states of H_{Hub} in the 2-electron basis. Typically, $t_c \ll U$ and in the small detuning limit where $\epsilon = \epsilon_2 - \epsilon_1 \ll U$, the ground state energy difference is [221]

$$J = \frac{2t_c^2 U}{U^2 - \epsilon^2} \tag{4.26}$$

which gives the derivatives

$$\frac{\partial J}{\partial \epsilon} = \frac{4t_c^2\, U\, \epsilon}{(U^2 - \epsilon^2)^2} \qquad \frac{\partial J}{\partial V_{\text{bias}}} = \frac{4t_c^2\, U\, \alpha^2\, V_{\text{bias}}}{(U^2 - \alpha^2 V_{\text{bias}}^2)^2} \tag{4.27}$$

where in the second derivative ϵ is converted into terms of the raw bias voltage V_{bias} and lever arm α using $\epsilon = \alpha V_{\text{bias}}$. From Equation 4.27, we can see that the derivatives equal 0 when $V_{\text{bias}} = \epsilon = 0$. From there, the derivatives increase until either $\epsilon \approx U$ or $\alpha V_{\text{bias}} \approx U$. The width of this [0,$U$] interval clearly depends on the magnitude of U in the case of ϵ and depends both on U and α in the case of V_{bias}. If U is large, then $\partial J/\partial\epsilon$ will require larger detuning values until it becomes appreciable. However if U is small, then $\partial J/\partial\epsilon$ is larger for smaller values of ϵ. Therefore, in order to improve the sensitivity of J to fluctuations in ϵ, U must be large. Similar arguments imply that in order to improve the sensitivity of J to fluctuations in V_{bias}, both U must be large and α be small. These results are not entirely surprising. If the charging energy is small, then the singlet state can more easily tunnel into the $S(0,2)$ charge configuration increasing the sensitivity of J. Additionally, if the plunger gates have smaller lever arms, then fluctuations in the gate voltage will perturb the potential and, subsequently, J less.

The table in Figure 4.7 shows that the charging energy U decreases and that α increases as the dot size increases. Both effects are unsurprising. The charging energy is inversely proportional to the QD radius [150], and the capacitive coupling between the plunger gate and potential landscape should increase with plunger gate surface area. Even when the capacitive coupling is accounted for by converting V_{bias} into ϵ using α (see table in Figure 4.7), the same behavior remains where $\partial J/\partial\epsilon$ increases with larger dot size. As the dot size increases in the double quantum dot system, the charging energy decreases as well. The smaller U causes an increase in $\partial J/\partial\epsilon$ as dot size increases. In summary, Figures 4.7b-c show that smaller QDs are less susceptible to charge noise coming from both V_{bias} and ϵ.

Varying tunnel gate width

Next, we study how varying the tunnel gate width D_t impacts the exchange interaction's sensitivity to charge noise. The results are summarized in Figure 4.8. D_t is stepped from 15 nm (purple) to 40 nm (yellow) in increments of 5 nm. The other fixed device parameters are $D_x = D_y = 40$ nm, $T = 15$ nm, and $V_p = 0.150$ V. Figure 4.8a shows how J varies with V_{tun}. For all curves, J increases with increasing V_{tun}, as expected due to the decreasing tunnel barrier height. At a fixed V_{tun}, J decreases as D_t increases. This is because the tunnel barrier region gets wider and further separates the QDs. As the

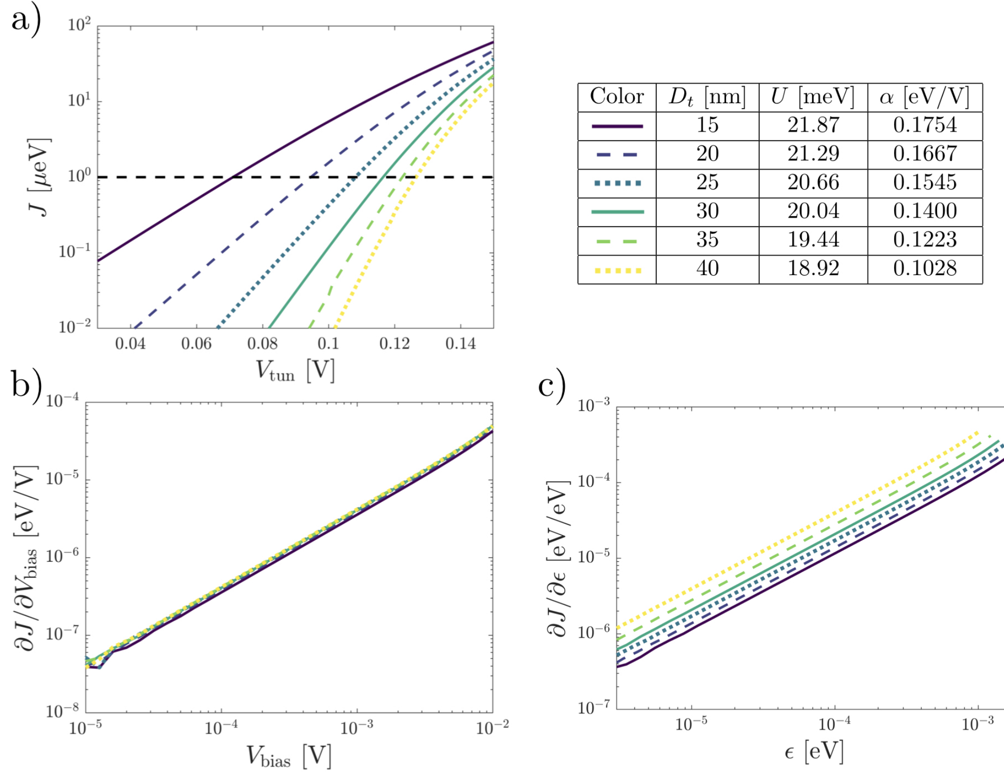

Figure 4.8: Dependence of J as the tunnel gate width D_t is varied. a) J as V_{tun} is swept from 0.03−0.150 V. The other fixed device parameters are $V_p = 0.150$ V, $V_{\text{bias}} = 0$ V, $D_x = D_y = 40$ nm, and $T = 15$ nm. The dashed black line indicates where $J = 1$ μeV. b) Derivative of J with respect to V_{bias}. For each device geometry, V_{tun} is tuned so that $J = 1$ μeV at $V_{\text{bias}} = 0$. c) Derivative of J with respect to ϵ where $\epsilon = \alpha V_{\text{bias}}$ and α is the lever arm between the raw bias voltage and the effective inter-dot detuning. The upper-right table indicates the corresponding varied device parameters, charging energy U, and lever arm α.

electron orbitals move further apart, the orbital overlap in the tunnel barrier region is reduced. This decreases the Coulomb interaction and subsequently J. The specific V_{tun} values at which $J = 1$ μeV are given in Section 4.3.4.

Figures 4.8b-c show the derivative of J with respect to V_{bias} and ϵ for different tunnel gate widths. For all curves, $J = 1$ μeV at $V_{\text{bias}} = 0$. There is clear difference between the V_{bias} and ϵ derivatives. While the plunger gate size remains fixed across the varied

geometries, U decreases with the increasing tunnel gate width. This is because for larger D_t, V_{tun} must be tuned to higher voltages to reach $J = 1$ μeV at zero bias voltage as shown in Figure 4.8a, . Both the higher V_{tun} value and increased width of the tunnel gate cause the tunnel barrier to 'flatten' as D_t increases. The flattening of the tunnel barrier actually widens the QD potentials at the plunger/tunnel gate interface As the potential opens, the localized electron orbitals broaden. This in turn decreases the charging energy as the QD is effectively bigger. The explicit potentials for $J = 1$ μeV are given in Section 4.3.4 to more clearly explain this behavior. The table in Figure 4.8 shows that the lever arm α decreases with increases D_t. We attribute this to the fact that increasing D_t will screen the effect of the constant sized plunger gate. The plunger gates have to work harder in order to overcome the additional electric field contributions from the added tunnel gate material.

The fact that both U and α decrease with increasing D_t has an interesting effect on $\partial J/\partial V_{\text{bias}}$. Recall that $\partial J/\partial V_{\text{bias}}$ increases when U decreases and when α increases. As D_t increases, U and α fight against each other to both increase and reduce the sensitivity with respect to V_{bias}. Interestingly, they both cancel out in this device geometry so that D_t has minimal impact on the sensitivity to the raw bias voltage. When the bias voltage is translated into the effective dot detuning, then J becomes more sensitive to ϵ as the tunnel gate widens. This is due to the fact that U decreases with increasing D_t as discussed above. In summary, Figures 4.8b-c show that narrower tunnel gates are less susceptible to charge noise coming from ϵ and has minimal impact on charge noise coming from V_{bias}.

Varying oxide thickness

Next, we study how varying the oxide thickness T impacts the exchange interaction's sensitivity to charge noise. The results are shown in Figure 4.9 where T is stepped from 1 nm (purple) to 15 nm (yellow). The other fixed device parameters are $D_x = D_y = 40$ nm, $D_t = 20$ nm, and $V_p = 0.100$ V. Figure 4.9a shows how J varies with V_{tun}. For all device geometries, J increases with V_{tun} and is caused by a reduction in tunnel barrier height. At a fixed V_{tun}, J decreases as the oxide thickness decreases. This occurs because the plunger and tunnel gates acquire a stronger capacitive coupling to the potential landscape as they move closer to the Si/SiO_2 interface. Because $V_{\text{tun}} < V_p$ and the plunger gates are larger than the tunnel gate, the plunger gates push the QD potentials much lower than the tunnel gate lowers the tunnel barrier height. This effect results in an overall higher effective tunnel barrier. The higher barrier suppresses probability of the electron orbital in the tunnel barrier region thereby reducing the Coulomb interaction and J. The V_{tun} values which yield $J = 1$ μeV are given in Section 4.3.4.

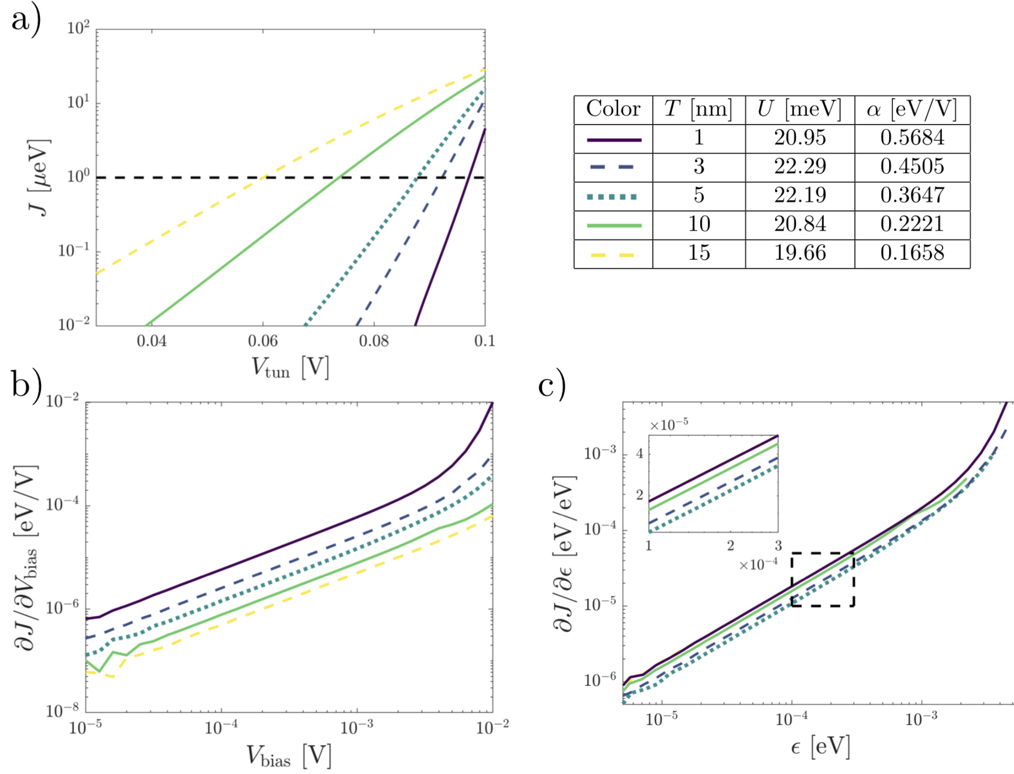

Figure 4.9: Dependence of J as the oxide thickness T is varied. a) J as $V_{\rm tun}$ is swept from 0.0−0.100 V. The other fixed device parameters are $V_p = 0.100$ V, $V_{\rm bias} = 0$ V, $D_x = D_y =$ 40 nm, and $D_t = 20$ nm. b) Derivative of J with respect to $V_{\rm bias}$. Each device has $V_{\rm tun}$ tuned so that $J = 1$ μeV at $V_{\rm bias} = 0$ as indicated by the dashed black line in panel a). c) Derivative of J with respect to ϵ where $\epsilon = \alpha V_{\rm bias}$ and α is the lever arm between the raw bias voltage and the effective inter-dot detuning. The upper-right table indicates the corresponding varied device parameters, charging energy U, and lever arm α.

Figures 4.9b-c show the derivatives of J with respect to $V_{\rm bias}$ and ϵ as T is varied. For all curves, $J = 1$ μeV at zero bias. $\partial J/\partial V_{\rm bias}$ can be seen to strongly depend on the oxide thickness. This occurs because the plunger gate lever arm α significantly increases as T decreases. Notice that the increase in α overshadows any impact from U which varies non-monotonically with T. Figure 4.9c shows a tighter spread in the $\partial J/\partial \epsilon$ curves compared to $\partial J/\partial V_{\rm bias}$. The individual $\partial J/\partial \epsilon$ curves are ordered according to the charging energy U specified in the table (inset panel in Figure 4.9c). The non-monotonic behavior of U

with respect to T is surprising. As T decreases, the image of the gates are mapped more clearly onto the underlying potential landscape. This means that in the limit $T \to 0$, the potential would be two square potential wells connected by a square tunnel barrier. We expect naively that as T decreases, the potential should open up reducing the confinement strength as it transitions from a $\cup$-like to a $\sqcup$-like shape. The more open $\sqcup$-like shape would result in a smaller charging energy. However, we see that U actually increases as T decreases initially from 15 nm to 3 nm. From 3 nm and lower, U decreases as expected. The potentials at zero-bias are shown in Section 4.3.4. As T is reduced, the tunnel barrier transitions from $\cap$-like to $\sqcap$-like as expected. However, the slope of the outer edges of the QD potentials remain relatively unaffected until $T \approx 3$ nm. From $T = 15$ nm to 5 nm, the outer edges of the potential actually move towards the center of the QD. This creates a tighter confinement in the QD and raises U. As $T = 3$ nm to 1 nm, the outer edges of the potential shift back outward and begin opening up into the expected $\sqcup$-like shape. This opens the confinement in the QD and lowers U.

It is possible that the non-monotonic behavior of U is caused by a few of our choices in the device model itself. The first potential cause could be our choice to ground the outer tunnel barrier gates in the full device geometry (see Figure 4.4). Allowing those voltages to vary or be non-zero will certainly impact the exact shape of the QD potentials. Another potential cause could be that the self-consistent 3D Poisson calculations were done in the zero-charge regime. Incorporating the impact of an electron using a Schrödinger-Poisson calculation would also change the exact shape of the QD potential. Even if those effects are accounted for, the behavior of $\partial J/\partial V_{\mathrm{bias}}$ should not qualitatively change. This is because the dominating mechanism in determining charge sensitivity with respect to V_{bias} is the lever arm and not the charging energy. However, the behavior observed of $\partial J/\partial \epsilon$ may change if these effects are considered. We would expect any change in $\partial J/\partial \epsilon$ to still follow how the charging energy U changes. Additionally, we have neglected the fact in an actual device, reducing the oxide thickness also reduces the total amount of charge defects present in the material system. This in turn reduces the total amount of fluctuations in ϵ, but we do not explore that trade-off here. In summary, using our device model, reducing the oxide thickness increases the sensitivity to charge noise caused by V_{bias} and has a relatively smaller effect on the sensitivity to charge noise caused by ϵ.

Varying plunger gate eccentricity

Lastly, we study how varying the plunger gate eccentricity D_y/D_x impacts the exchange interaction's sensitivity to charge noise. The results are shown in Figure 4.10. Eccentricities $D_y/D_x > 1.0$ mean the plunger gate is being elongated along the $\hat{y}$ axis while values < 1.0

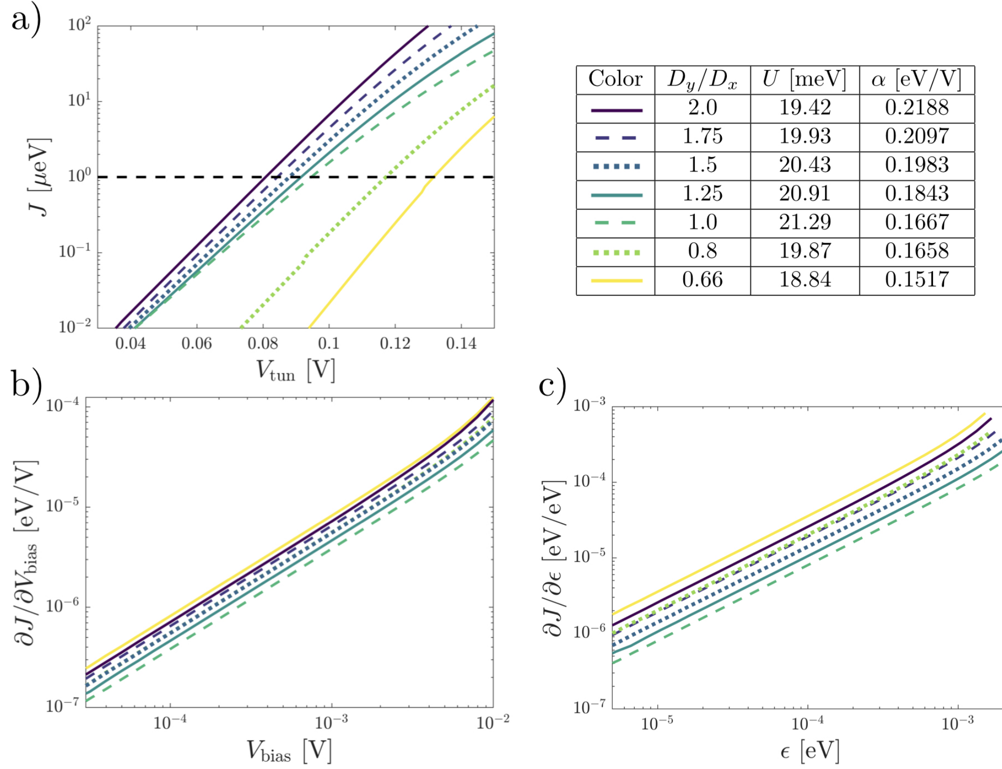

Color	D_y/D_x	U [meV]	α [eV/V]
	2.0	19.42	0.2188
	1.75	19.93	0.2097
	1.5	20.43	0.1983
	1.25	20.91	0.1843
	1.0	21.29	0.1667
	0.8	19.87	0.1658
	0.66	18.84	0.1517

Figure 4.10: Dependence of J as the eccentricity D_y/D_x is varied. For $D_y/D_x > 1.0$, $D_x =$ 40 nm, while for $D_y/D_x < 1.0$, $D_y = 40$ nm. a) J as V_{tun} is swept from 0.03−0.150 V. The other fixed device parameters are $V_p = 0.150$ V, $V_{\text{bias}} = 0$ V, $D_t = 20$ nm, and $T =$ 15 nm. b) Derivative of J with respect to V_{bias}. Each device has V_{tun} tuned so that $J =$ 1 μeV at $V_{\text{bias}} = 0$ as indicated by the dashed black line in panel a). c) Derivative of J with respect to ϵ where $\epsilon = \alpha V_{\text{bias}}$ and α is the lever arm between the raw bias voltage and the effective inter-dot detuning. The upper-right table indicates the corresponding varied device parameters, charging energy U, and lever arm α.

mean the plunger gate is being elongated along the $\hat{x}$ axis. For $D_y/D_x > 1.0$, $D_x = 40$ nm while D_y is varied. Conversely, for $D_y/D_x < 1.0$, $D_y = 40$ nm while D_x is varied. At $D_y/D_x = 1.0$, $D_x = D_y = 40$ nm. For all geometries, $D_t = 20$ nm, $T = 15$ nm, and $V_p = 0.150$ V. Figure 4.10a shows how J varies with V_{tun}. For all curves, J increases with V_{tun} again as expected. Interestingly, at a fixed value of V_{tun}, J decreases monotonically with the eccentricity. This is because for $D_y/D_x > 1.0$, the plunger gate has more electric

field contributions along the $\hat{y}$ axis of the device. These additional field contributions push both the QD potential minima and the tunnel barrier lower. Overall, the tunnel barrier is pushed lower than the potential minima are, which results in a lower overall tunnel barrier height. For $D_y/D_x < 1.0$, the plunger gate acquires more electric field contributions along the $\hat{x}$ axis instead. These additional contributions affect the QD potential minima more than they affect the tunnel barrier. Subsequently, the effective tunnel barrier height increases and D_y/D_x decreases. The dashed black line shows where $J = 1$ μeV, and the corresponding V_{tun} values are given in Section 4.3.4.

Figures 4.10b-c show the derivatives of J with respect to V_{bias} and ϵ as D_y/D_x is varied. For all geometries, $J = 1$ μeV at zero bias. In Figures 4.10b-c, both $\partial J/\partial V_{\text{bias}}$ and $\partial J/\partial \epsilon$ show the same dependence with respect to the eccentricity. The least sensitive geometry has $D_y/D_x = 1.0$ where the plunger gates have the smallest total area and, therefore, the largest U. As the plunger gates acquire an eccentricity not equal to 1.0, the plunger gate area increases. The increased surface area reduces U and causes those device geometries to be more susceptible to fluctuations in V_{bias} and ϵ. The behavior observed for $\partial J/\partial V_{\text{bias}}$ occurs even though the lever arm α decreases monotonically with D_y/D_x. This shows that U is the dominating factor in determining the sensitivity of J with respect to V_{bias} as the eccentricity is varied. In summary, symmetric QDs with no eccentricity are the least susceptible to charge noise coming from both V_{bias} and ϵ.

4.3.4 Zero bias potentials

Here we show the zero bias potentials for the varied device geometries discussed in Section 4.3.3. 1D slices of the potentials along the $\hat{x}$ axis are plotted in Figure 4.11. The y-coordinate at which the slice is taken is chosen such that the 1D slice goes through the minima of the double quantum dot potential. Note from Figure 4.4b that this point is not necessarily directly underneath the center of the plunger gate head and changes with the device geometry. Table 4.1 lists the varied geometry parameters and the V_{tun} value where $J = 1$ μeV at $V_{\text{bias}} = 0$ V.

Figure 4.11a shows 1D potential slices as the dot size D_x, D_y is varied. The other geometry parameters are $D_t = 20$ nm, $T = 15$ nm, and $V_p = 0.150$ V. As the dot size increases, the tunnel barrier flattens and the potential confinement decreases causing a larger charging energy U as discussed in the main text. Interestingly, the minima of the potential wells seem to remain in the same $\hat{x}$-coordinate location even as the plunger gate get larger.

Figure 4.11b shows 1D potential slices as the tunnel gate width D_t is varied. The other

D_x, D_y [nm]	V_{tun} [V]	D_t [nm]	V_{tun} [V]	T [nm]	V_{tun} [V]	D_y/D_x	V_{tun} [V]
30, 30	0.057228	15	0.070977	3	0.060071	2.0	0.080796
40, 40	0.094548	20	0.094548	5	0.073663	1.75	0.084305
50, 50	0.114617	25	0.108097	10	0.087739	1.5	0.087954
60, 60	0.126211	30	0.116451	15	0.092118	1.25	0.091506
70, 70	0.133647	35	0.122298			1.0	0.094548
80, 80	0.138619	40	0.126458			0.8	0.117165
						0.66	0.131638

Table 4.1: Corresponding tunnel gate voltages V_{tun} which yield $J = 1$ μeV at $V_{\text{bias}} = 0$ V for different device geometries. The default device geometry parameters unless varied are $D_x = D_y = 40$ nm, $D_t = 20$ nm, and $T = 15$ nm. For $D_y/D_x > 1.0$, $D_x = 40$ nm, and for $D_y/D_x < 1.0$, $D_y = 40$ nm. $V_p = 0.150$ V for all geometries except when T is varied where $V_p = 0.100$ V. 1D slices of the corresponding potentials are shown in Figure 4.11.

geometry parameters are $D_x = D_y = 40$ nm, $T = 15$ nm, and $V_p = 0.150$ V. As the tunnel gate widens the tunnel barrier flattens. This reduces the potential confinement of each QD thereby increasing the charging energy U as described in the main text.

Figure 4.11c shows 1D potential slices as the oxide thickness T is varied. The other geometry parameters are $D_x = D_y = 40$ nm, $D_t = 20$ nm, and $V_p = 0.100$ V. As the oxide thickness decreases, the image of the square plunger gate head is mapped more strongly onto the potential landscape. In the limit where $T = 0$, the double QD potential would be two square wells with a square tunnel barrier between them. As this transition towards a more 'square' potential occurs, the slope of the tunnel barrier increases and slightly widens. This effect suppresses the wavefunction overlap in the tunnel barrier region as the electrons are more localized to each QD. Additionally, the effective confinement of each QD increases which slightly increases the charging energy U as shown in the main text.

Figure 4.11d shows 1D potential slices as the oxide thickness T is varied. The other geometry parameters are $D_t = 20$ nm, $T = 15$ nm, and $V_p = 0.150$ V. For $D_y/D_x > 1.0$, $D_x = 40$ nm, while for $D_y/D_x < 1.0$, $D_y = 40$ nm. It is clear from these potentials that U decreases when $D_y/D_x < 1.0$ as the QD potentials open. However due to the fact that we are taking 1D slices along the $\hat{x}$ axis, it is difficult to see the same effect when $D_y/D_x > 1.0$ even though U is decreasing as well. The potentials do show that the tunnel barrier height increases as the plunger gate eccentricity increases due to the additional plunger gate material along the $\hat{y}$ axis which pushes the QD minima lower. For sensitivity to charge noise, the relevant parameter is the charging energy U which increases whether or not the plunger gates are elongated along the $\hat{x}$ or $\hat{y}$ axes.

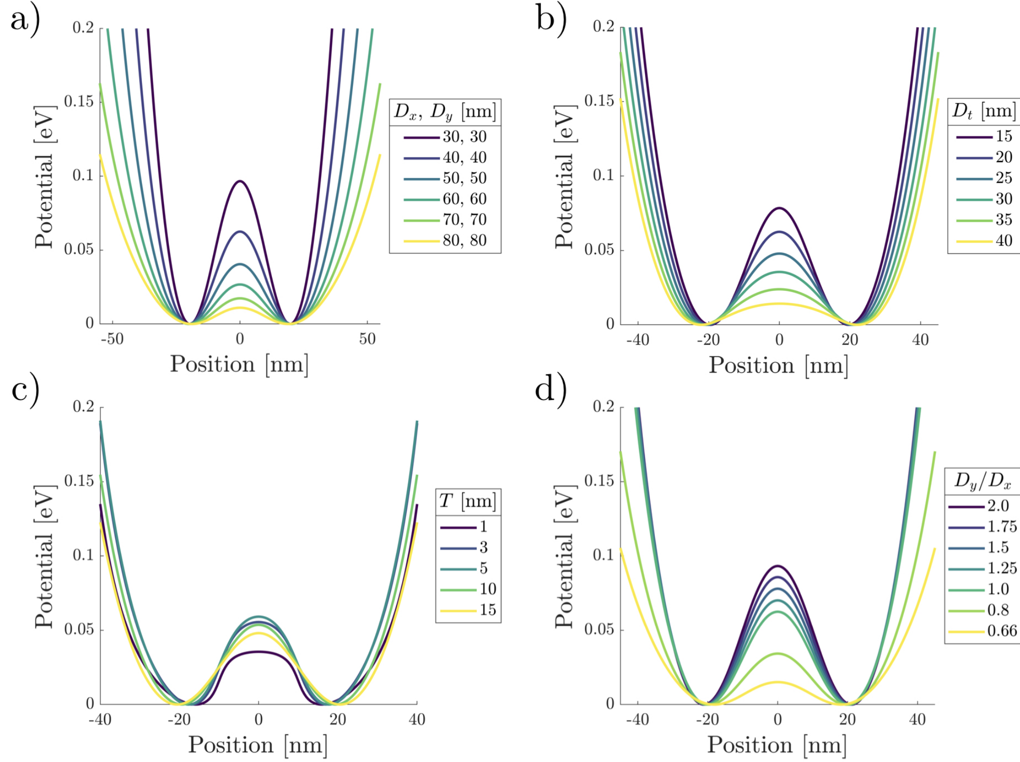

Figure 4.11: 1D potential slices of the 2D potentials which gives $J = 1$ μeV at $V_{\text{bias}} = 0$ V. Unless varied, the default device parameters are $D_x = D_y = 40$ nm, $D_t = 20$ nm, and $T = 15$ nm. For $D_y/D_x > 1.0$, $D_x = 40$ nm, and for $D_y/D_x < 1.0$, $D_y = 40$ nm. The corresponding gate voltages are given in Table 4.1. The 1D slices are taken along the $\hat{x}$ axis where the slice passes through the lowest potential minima in the 2D potential.

4.4 Conclusion

In summary, a modified LCHO-CI method was presented for calculating the many-electron states and energy spectra of a quantum dot network. Using an orthogonal basis of harmonic orbitals to approximate single electron orbitals, the evaluation of the Coulomb matrix elements requires significantly less computational resources. Additionally, we demonstrated an efficient method for optimizing the choice of harmonic orbital basis in order to better approximate the single electron orbitals and improve the accuracy of the CI calculation. Our modified LCHO-CI approach provides a significant reduction in computation time

that can be exploited to obtain a large number of accurate energy spectra as a function of varying model parameters. The energy spectra can be mapped to an effective Heisenberg Hamiltonian to obtain the pairwise exchange interaction energies J_{ij} in arbitrary quantum dot networks.

The modified LCHO-CI approach was then used to investigate how the physical gate geometry of a quantum dot device impacts the sensitivity of exchange to charge noise. A 3D model of a double dot device structure on Si/SiO_2 is simulated using a self-consistent Poisson calculation. From these 3D simulations, planar 2D potentials were used in the LCHO-CI calculations to determine how J varies with respect to an applied bias voltage between the two plunger gates, and also with respect to the effective inter-dot detuning. The charge noise sensitivity was calculated as a function of plunger gate size, tunnel gate width, SiO_2 (gate dielectric) thickness and dot eccentricity. Generally, device geometries that maximize the dot charging energy and reduce the lever arm of the plunger gates are found to be less sensitive to charge noise. For the device layout chosen in this work, this means that small and symmetric plunger gates, narrow tunnel gates, and suitably thick SiO_2 will improve the robustness to charge noise. Future work includes obtaining better approximations the electronic potential landscape by using self-consistent Schrödinger-Poisson calculations. There are many device geometries that are ripe for exploration using our methods, such as asymmetric double quantum dots [108]. We envision these methods enabling the realistic modeling of exchange in larger quantum dot networks such as multi-qubit processor nodes.

Chapter 5

Electron transport in dopant-free GaAs

Chapter contributions: The Hall bar devices in Section 5.2 were fabricated and measured by myself, Nachiket Sherlekar, and Dr. François Sfigakis. All of the other devices in Sections 5.3 and 5.4 were fabricated solely by myself with the exception of the device measured in Figure 5.15 where Dr. Arjun Shetty assisted with fabrication. All measurements were done with the assistance of Dr. François Sfigakis.

The section regarding single electron pumps is based on a manuscript currently being prepared for submission to a journal.

5.1 Introduction

The previous chapters in this thesis have so far focused on applied theoretical studies of quantum dots in Si/SiO_2 material systems. In this chapter, we shift focus onto experimental studies of electron and hole transport in dopant-free GaAs material systems. The main result of this chapter is the demonstration of single electron pumping in dopant-free GaAs using a dynamically driven quantum dot. These quantum dot devices are not made for quantum information processing purposes in mind, which was the focus of the silicon quantum dot devices studied in the previous chapters of this thesis. Instead, these dynamically driven quantum dots lay the ground-work for realizing novel on-demand single photon sources for quantum communications and quantum optics. GaAs is a direct bandgap semiconductor which enables electrons to directly emit a photon upon recombination with a hole. This is why GaAs is the material of focus in this chapter rather than silicon.

III-V semiconductors (such as GaAs) have a higher mobility compared to silicon leading III-V's to be a more ideal choice for studying electron transport and mesoscopic physics. The most popular III-V system studied is Gallium-Arsenide/Aluminum-Gallium-Arsenide (GaAs/AlGaAs) where in the second layer, Al replaces some fraction of the Ga in the lattice (typically 0.33 giving $Al_{0.33}Ga_{0.67}As$). The GaAs/AlGaAs interface is called a heterojunction. When there is only one GaAs/AlGaAs interface in the material, we call this system a single heterojunction. Both GaAs and AlGaAs have similar lattice structures which means that a smooth interface layer is formed with few defects and little strain. This enables the high carrier mobilities observed in GaAs [259] as holes or electrons encounter relatively fewer scattering sites travelling through the material.

GaAs has a smaller bandgap than AlGaAs leading to a step-like band structure at the heterojunction. A thin conductive layer of electrons can be formed at the GaAs/AlGaAs interface by bending the conduction band below the Fermi level. This is achieved by intentionally doping the material system [245] or by applying an external electrostatic field using either a doped capping layer [128] or a metallic top gate [101]. The thin conductive layer is called a 2-dimensional electron gas (2DEG). 2DEGs are labelled as 2D because the carriers are confined to a thin region just nanometers thick along the $\hat{z}$ direction of the substrate.

The standard approach to form a 2DEG in GaAs/AlGaAs heterostructures is to add intentional dopants the material system using a technique called modulation doping. In modulation doping, a thin layer of a n-type (electron) dopant (typically Si) is embedded in the AlGaAs layer during the wafer growth using Molecular Beam Epitaxy (MBE) [90]. In the doping layer, dopants replace either Al or Ga in the lattice and leave both a positively charged nucleus and free electron. The positive ions serve to bend the conduction band of the GaAs/AlGaAs interface below the Fermi level where free electrons accumulate to form the 2DEG. Figure 5.1a shows a simulated 1D band structure along the $\hat{z}$ axis of a modulation doped single-heterojunction. The simulation in nextnano++ [11] using a self-consistent Schrödinger-Poisson calculation. The full heterostructure from top-to-bottom is a 10 nm GaAs capping layer, 80 nm of AlGaAs, and 80 nm of GaAs. A 10 nm thick doping layer composed of Si dopants with a concentration of 3×10^{18} cm^{-3} is placed 65 nm away from the GaAs/AlGaAs interface. When exposed to air, AlGaAs oxidizes and is why a capping layer of GaAs is added on top of the heterostructure. The positively charged ions in the doping layer pin the Fermi level (black) near the conduction band (blue), and the ions subsequently bend the conduction band at the heterojunction (blue). Free electrons then collect at the GaAs/AlGaAs interface and form a 2DEG (yellow).

This chapter focuses on an alternative method of realizing a 2DEG in GaAs/AlGaAs heterostructures. Rather than intentionally doping the material, an external electric field

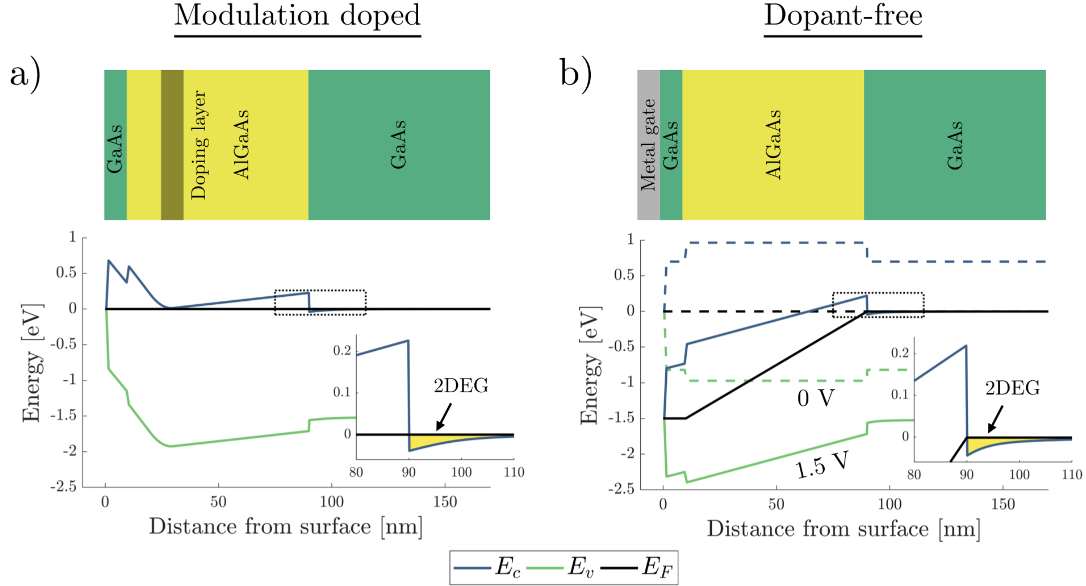

Figure 5.1: Band structures of a modulation doped and dopant-free single heterojunction simulated in nextnano++. a) A modulation doped heterostructure consisting of a 10 nm GaAs cap layer, 80 nm AlGaAs, 80 nm GaAs. A 10 nm thick doping layer of Si dopants is placed 60 nm from the lower GaAs/AlGaAs interface. The conduction band E_c (blue) is bent near the interface to be below the Fermi level E_F (black) and form a 2DEG (yellow). The valence band E_v (green) is far below E_F so that no holes are induced. b) A dopant-free heterostructure capped with a 10 nm thick metal layer to electrostatically gate the heterostructure. When the gate voltage is 0 V (dashed lines), the Fermi level (black) is midgap and no 2DEG is induced in the conduction band (blue). When the gate voltage is increased to 1.5 V (solid lines), the band structure is bent downward so that the conduction band falls below E_F and a 2DEG is induced (yellow).

is used to bend the conduction band and induce a 2DEG. Because the 2DEG is induced without the use of any intentionally placed dopants in the material, the GaAs/AlGaAs structure is labelled *dopant-free*. Figure 5.1b shows a 1D simulation of the band structure along the $\hat{z}$ axis of a single heterojunction dopant-free system. The full heterostructure is a 10 nm metal gate, 10 nm GaAs capping layer, 80 nm of AlGaAs, and 80 nm of GaAs. When 0 V is applied to the metal gate (dashed lines), the conduction bands are horizontal, and the Fermi level (black) is pinned mid-gap. As the Fermi level is well below the conduction band, no 2DEG is induced. When a sufficiently large voltage (+1.5 V in the simulation) is

applied on the gate (solid lines), the conduction band at the heterojunction is pulled below the Fermi level and the 2DEG forms (yellow). In a modulation doped heterostructure, the electrons in the 2DEG were supplied by the n-type dopants. Since these are not present in a dopant-free structure, electrons must be supplied from some other electron reservoir in order to actually form the 2DEG. The reservoir can be realized by locally implanting n-type dopants into the wafer, either by annealing n-type ohmic contacts [101, 229, 35] or by ion implantation [119].

The lack of any intentional dopants in dopant-free structures offers several significant advantages over conventional modulation doped heterostructures. In modulation doped material, high quality wafers with high mobilities require a large concentration of dopants. The density of these intentional dopants is orders of magnitude greater than any background impurity dopants which arise naturally during the MBE growth [258, 172]. Increased scattering from the intentional dopants prevents modulation doped materials from being gated to very low carrier densities. On the other hand, dopant-free materials are only limited by scattering from the background impurity dopants, and as such, can be gated to low carrier densities [114]. Electron-electron interactions are strongest in low density systems, an ideal platform for studying Wigner crystallization [36, 143]. In the opposite regime, dopant-free systems can also be gated to very high carrier densities. High carrier densities are achievable as well in modulation doped samples, but this requires large doping concentrations in order to sufficiently bend the conduction band to obtain the high densities. An external electric field could, in principle, be applied on a modulation doped heterostructure to even further increase the carrier density; however, in practice this can problematic. Gating very highly doped structures can induce a parallel conducting path through the doping layer or cause leakage between the dopants and the 2DEG. Dopant-free materials avoid these problems by removing the intentional dopants altogether. Another advantage of dopant-free material systems over their intentionally doped counterparts, is the ability to induce 2DEGs in very shallow heterojunctions. In such shallow systems, the potential from the electrodes used to gate the material is more strongly coupled to the 2DEG allowing better control of the potential landscape of the device. However, bringing the 2DEG closer to surface lowers the carrier mobilities due to scattering from defects present at the surface [145, 160]. In modulation doped heterostructures, the thin spacing layer and doping concentrations required to form a 2DEG makes these shallow devices very difficult to gate, even when realized experimentally [186]. In dopant-free systems, such gate-ability issues are avoided [174, 175] as long as the 2DEG can be properly contacted.

The last advantage of dopant-free systems is the ability to create ambipolar devices, devices with both n- and p-type (hole) carriers. Holes have only been mentioned in passing in this thesis. Whereas a free electron occupies the conduction band, a hole is the absence

of an electron in the valence band. A hole can propagate in the material just like an electron as a free charge; however, the flow of current will be in the opposite direction due to the hole's positive charge. In GaAs, holes have a higher effective mass which means confined holes are more localized and have lower mobilities (higher resistances) compared to electrons. Free holes appear when the valence band is bent above the Fermi level forming a 2-dimensional hole gas (2DHG) at the GaAs/AlGaAs interface. For dopant-free structures, the valence band can be bent upwards simply by applying a negative gate voltage on top of the heterostructure [41] (the reverse direction of what is shown in Figure 5.1b). In a modulation doped wafer, the doping layer provides carriers for either the 2DEG or 2DHG. If the dopants are n-type, then only a 2DEG can form. Conversely, if the dopants are p-type, then only a 2DHG can form. As such, a modulation doped wafer is restricted to realizing only a single carrier type. In dopant-free heterostrtuctures, the carriers must be brought from a local reservoirs. Both n- and p-type reservoirs can be placed locally in the heterostructure while being far apart as to not contaminate each other. Separate metal gates can the be used to induce both a 2DEG and 2DHG within the same heterostructure [35, 48].

This chapter presents experiments done with a variety of devices realized in dopant-free single GaAs/AlGaAs heterojunctions. These are foundational experiments aimed towards realizing ambipolar, single electron/hole devices that will provide a new platform for developing quantum devices where electrons, holes, and electron-hole recombination can be controlled and exploited. Section 5.2 discusses the first step in making these devices: fabricating n- and p-type ohmic contacts to the heterojunction. Magnetotransport experiments show that we can induce both 2DEGs and 2DHGs with low contact resistances in a deep single-heterojunction. In Section 5.3, we use the n-type contacts to demonstrate 1-dimensional electron transport through a quantum point contact (QPC). Quantized conductance persists up to a temperature of 4 K due to the high subband spacing ~4.5 meV measured in our devices. Lastly, in Section 5.4, the QPC device is expanded upon to realize a tunable-barrier quantum dot acting as a single electron pump. We demonstrate the first realization of single electron pumping in dopant-free GaAs heterostructures. Pumping is evident at temperatures of 1.4 K and persists up to 4K.

5.2 n- and p-type ohmic contacts to dopant-free GaAs single heterojunctions

The first step towards making dopant-free devices is to develop recipes for ohmic contacts between the surface and the electrons or holes induced in the conduction layer. Ohmic

contacts allow a bias voltage to be applied to the 2DEG or 2DHG and for current to be monitored through the conduction channel. This is critical in being able to study electron transport through these devices. The ohmic contact resistance must be low and follow Ohm's law $V = IR$ where V is the applied bias voltage, I is the current, and R is the device resistance. This first half of this section outlines the process for fabricating ohmic contacts in deep and shallow dopant-free single heterojunctions. The second half discusses magnetotransport in 2D systems and presents experimental data which demonstrates good quality n- and p-type ohmic contacts to a 310 nm deep single heterojunction.

5.2.1 Overview of ohmic fabrication

In modulation doped devices, developing high yield and high quality ohmic contacts is relatively easy. This is because the 2DEG or 2DHG always exists at the heterojunction due to the free electrons created by the doping layer. To form ohmics, metal is deposited on top of the heterostructure and subsequently annealed at a high temperature. Annealing causes the ohmic material to diffuse into the substrate until it contacts the 2DEG or 2DHG. Typically, for 2DEGs, the ohmic is an alloy of Ni, Au, and Ge. The Ni acts as a catalyst for the AuGe to diffuse into the material where Ge acts as an n-type dopant. This creates a conductive channel of electrons from the surface to the 2DEG. For 2DHGs, the ohmic is an alloy of Au and Be. Similarly when annealed, the AuBe diffuses into the substrate where Be acts as a p-type dopant creating a conduction channel of holes from the surface to the 2DHG. Figure 5.2a shows a schematic of this approach for contacting a 2DEG in a modulation doped heterostructure. The ohmic material is deposited on top of the GaAs cap and annealed. The semi-transparent region schematically depicts the diffusion of the ohmic material from the surface to the 2DEG, connecting both by a conductive channel of free electrons.

Compared to modulation doped devices, ohmic contacts in dopant-free devices are much more difficult. The reason dopant-free devices are harder is because of the top gate required to induce the 2DEG or 2DHG in the substrate. Figure 5.2b shows a schematic of a failed ohmic contact to a would-be 2DEG using the same approach as the modulation doped device. As before, the ohmic contact is annealed so that metal diffuses into the substrate. Unlike the modulation doped structure, a 2DEG can only be induced underneath wherever the top gate is located. Note that the top gate used to induce the 2DEG is no longer directly on the surface of the structure. An insulating layer of SiO_2 allows the top gate to overlap directly with the ohmic contact, bringing the would-be 2DEG as close as possible to the ohmic. In this configuration, the top gate is screened by the ohmic material preventing the top gate from sufficiently bending the conduction band underneath the ohmic. Therefore,

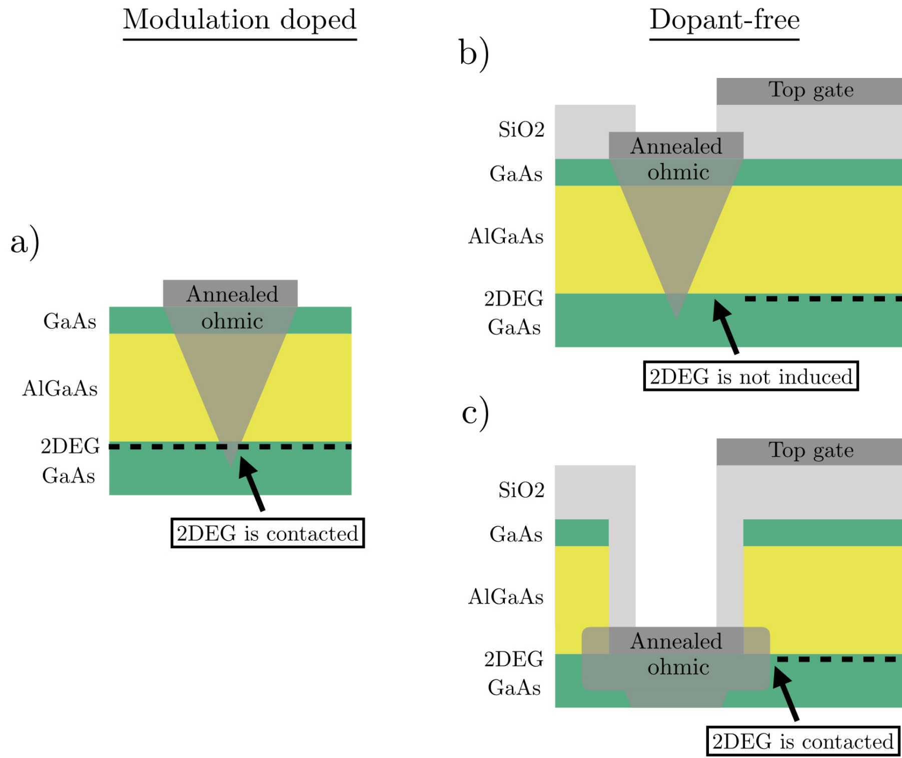

Figure 5.2: Schematic of ohmic contact diffusion after annealing in GaAs/AlGaAs single heterojunctions. a) Successful ohmic contact to a modulation doped single heterojunction. The annealed ohmic diffuses downward yielding a good ohmic contact to the 2DEG. b) Failed ohmic contact in a dopant-free single heterojunction. The ohmic contact screens the top gate which prevents contact of the diffused ohmic material to the where the 2DEG would be induced. c) Successful ohmic contact in a dopant-free single heterojunction. The lateral diffusion of the recessed ohmic does not screen the top gate allowing a 2DEG to be induced with a good electrical contact to the ohmic.

there is high potential barrier between the diffused ohmic material and where the top gate can induce a 2DEG. As such, electrons cannot populate the region underneath the top gate and no 2DEG can be induced.

The solution to achieving ohmic contacts in dopant-free materials is to recess the ohmic contact into the material. A schematic of this technique is shown in Figure 5.2c. Part of the heterostructure has been etched away so that the ohmic material is now deposited directly at the heterojunction. Because of this, the material can diffuse laterally through

the side walls of substrate in addition to the downward diffusion. The lateral diffusion does not screen the top gate from bending the conduction band all the way up to the diffused ohmic material. As such there is no potential barrier preventing electrons from populating underneath the top gate, and a 2DEG is induced with a good electrical contact to the ohmic.

Fabricating a recessed ohmic is not a straightforward process due to technical fabrication constraints such as photoresist overhang, etching profiles of the recess pit, roughness of the annealed ohmic, and placement of the deposited ohmic material. Figure 5.3 shows a schematic of a self-aligned ohmic fabrication process for deep and shallow single-heterojunction devices. Using a self-aligned process is critical to making high quality ohmic contacts. In the self-aligned process, a layer of photoresist (purple) is spun on the sample and subsequently patterned using optical lithography to act as an etching mask. A wet etch is done using a solution of 1:1:20 H_2O_2:H_3PO_4:H_2O to form the recess pit. An ohmic metal alloy (grey) is deposited at an angle, ending up on top of the photoresist layer and within the recesses pit. Depositing the metal at an angle is critical as it places ohmic material directly at the GaAs/AlGaAs interface. The angled profile of the wet etch creates an undercut underneath the photoresist. The undercut ensures that the metal deposited directly on top of the photoresist and in the etch pit are not connected which is necessary for good metal liftoff during fabrication. Because the wet etch and the metal deposition are done using the same photoresist layer, the process is self-aligned, and the metal pattern exactly matches the etched pattern.

There are a few subtle, yet important, differences when fabricating ohmics in deep and shallow single heterojunctions. Figure 5.3a shows the 'standard' ohmic process that was outlined above applied in a deep heterojunction. The etch is done just past the GaAs/AlGaAs heterojunction, and the metal deposition is done at a 45° angle. The etch depth and deposition angle allows the metal to slightly climb the AlGaAs side wall. When the ohmic is later annealed, the metal will diffuse laterally into the side walls to provide a good contact to the induced 2DEG or 2DHG. Figure 5.3b shows a slightly modified ohmic process required for a shallower heterojunction. The etched pit for the shallow heterojunction is the same depth as the deep heterojunction, even though this places the bottom of the etched pit far past the GaAs/AlGaAs interface. This is done to standardize the ohmic fabrication process across heterojunctions of various depths to make a more reproducible fabrication recipe. Applying the 'standard' ohmic process to the shallow heterojunction would result in all the ohmic metal being deposited below the GaAs/AlGaAs interface. In order to fix this, we do two things: a plasma etch of the photoresist and a shallower angle metal deposition. The plasma etch removes some of the photoresist allowing the metal to climb further up the side walls. The shallower deposition

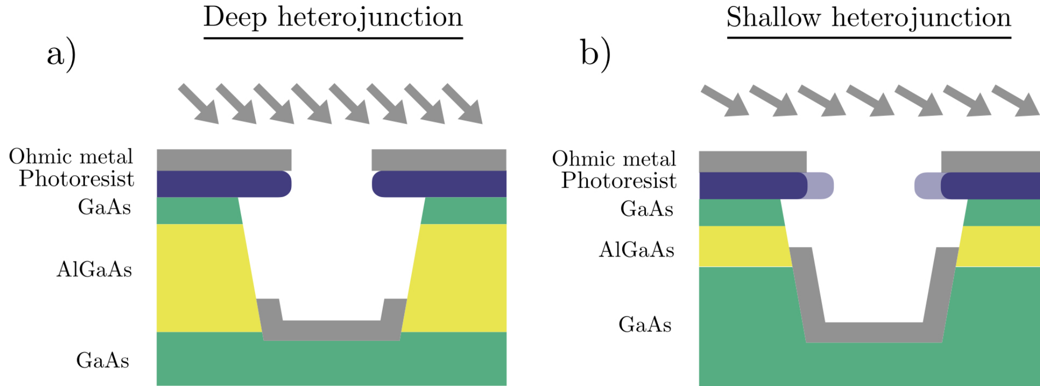

Figure 5.3: Schematic of ohmic fabrication for deep and shallow single heterojunctions. a) For a deep heterojunction, a recessed pit is etched and the metal is deposited at a 45° angle so that metal slightly climbs the side walls. b) For a shallow heterojunction, a recessed is etched to the same depth as the deep heterojunction to provide consistency between different heterostructure recipes. The resist is slightly etched using a plasma etch and the metal is deposited at a 60° angle to ensure the metal climbs up all the way to the heterojunction interface.

angle (60° for the shallow heterojunction) also deposits metal further up the side wall. Both of these modifications increase the risk of a bad metal liftoff as the metal can climb too high and subsequently connect the metal on top of the photoresist and within the recessed pit. Proper tuning of the plasma etch duration is required to ensure that ohmics are produced with high yield.

After the ohmics are deposited, they must be subsequently annealed in order to diffuse the metal into the material. Annealing must be done at sufficiently high temperatures in order to allow the metal to react with the substrate. The reaction causes the ohmic material to become very rough (particularly for n-type ohmics where the AuGe alloy experiences a liquid phase transition during the anneal). This causes issues later in the device fabrication as we need the top gate to overlap the ohmic contact in order to induce a 2DEG right next to the ohmic (as discussed in Figure 5.2c). If the roughness is bad enough, the insulating SiO_2 layer will not prevent shorts between the ohmics and top gate, subsequently killing the device. In order to reduce the roughness for n-type ohmics, a capping layer of Ni is added on top of the ohmic before annealing. The Ni layer does not get as rough during

the anneal which suppresses shorts to the top gate. For p-type ohmics, a capping layer of SiO_2 is added before annealing and removed afterwards which keeps the AuBe material relatively smooth during the entire annealing process.

Detailed fabrication notes for n- and p-type ohmic contacts, along with recipes for all the other steps in realizing a dopant-free device, are given in the Appendix B.

5.2.2 Magnetotransport in a 2D system

Once a device has been fabricated, it is important to characterize the quality of ohmic contacts as well as characterize the quality of the induced 2DEG or 2DHG in the heterostructure. Ohmic quality can be deduced by a simple 4 terminal voltage measurement in order to differentiate between the resistance of the ohmic contact and the resistance of the 2DEG or 2DHG. Characterizing the quality of the induced 2DEG or 2DHG can be achieved by studying the transport behavior of the device under an perpendicular magnetic field. At high magnetic fields, transport experiments provide clear measurement signatures that can only be achieved in 2D systems. Additionally, these measurements can be used to extract the electron mobility and electron density to quantify the quality of the 2DEG. It is also important to distinguish that we are only contacting a single 2DEG or 2DHG. A potential issue with our devices is that additional conduction channels could be induced in the system. The desired 2DEG is induced at the intended GaAs/AlGaAs interface yet another is induced at a different interface in the heterostructure. Eliminating these parallel conducting channels is desired in order to ensure that we have proper electrostatic control over the 2DEG of interest. The first half of this section briefly goes over the theory of electron transport in 2D systems in a perpendicular high magnetic field. The second half of this section presents magnetotransport experiments done in a 310 nm deep single heterojunction for both n- and p-type ohmics.

2D electron transport in low magnetic fields

As a starting point, we briefly consider electron transport through a 2DEG in low strength magnetic fields where quantum mechanical effects can be neglected [118]. To begin, we assume the 2DEG lies on the $\hat{x} - \hat{y}$ plane and is subjected to an external electric field along the $\hat{x}$ axis, $\vec{E} = E_x \hat{x}$, and a perpendicular magnetic field along $\hat{z}$, $\vec{B} = B_z \hat{z}$. We assume that the 2DEG is significantly larger than the mean free path l_0 of the system where l_0 quantifies how far an electron travels, on average, before encountering a scattering event. The average amount of time τ between scattering events is termed the scattering time. l_0

and τ are related as $l_0 = v_{\text{avg}}\tau$ where v_{avg} is the average drift velocity of the electrons. The electric field along $\hat{x}$ is realized by applying a bias voltage across the 2DEG. The drift velocity v of the electrons along $\hat{x}$ and $\hat{y}$ is

$$v_x = -E_x \frac{e\tau}{m^*(1+\omega_c^2\tau^2)} \quad (5.1)$$

$$v_y = -v_{\text{avg}} \left(1 - \frac{1}{1+\omega_c^2\tau^2}\right) \quad (5.2)$$

where m^* is the electron effective mass and $\omega_c = eB_z/m^*$. When $B_z = 0$ T, $v_y = 0$, and $v_x = -E_x\mu = -E_x e\tau/m^*$ where $\mu = e\tau/m^*$ is the electron mobility. It is clear from this definition of μ that cleaner material systems with longer scattering times τ directly correspond to higher electron mobilities.

The current density is related to the drift velocity as $\vec{\mathrm{j}} = -n_{2D}e\vec{v}$ where n_{2D} is the electron density. The negative sign accounts for the electron's negative charge. $\vec{\mathrm{j}}$ is related to the applied electric field via the conductivity tensor $\hat{\sigma}$ as $\vec{\mathrm{j}} = \hat{\sigma}\vec{E}$. The inverse of the conductivity is the resistivity $\hat{\sigma}^{-1} = \rho$. Equating $\vec{\mathrm{j}} = -n_{2D}e\vec{v}$ with $\vec{\mathrm{j}} = \hat{\sigma}\vec{E}$ and solving for ρ yields the longitudinal and transverse resistivities respectively as

$$\rho_{xx} = \frac{\sigma_{xx}}{\sigma_{xx}^2 + \sigma_{xy}^2} = \frac{\mu}{n_{2D}e} \quad (5.3)$$

$$\rho_{xy} = \frac{\sigma_{xy}}{\sigma_{xx}^2 + \sigma_{xy}^2} = \frac{B_z}{en_{2D}} \quad (5.4)$$

Measuring both resitivities as a function of B allows us to extract the electron mobility and density of a 2DEG.

Shubnikov-de Haas oscillations and the integer quantum Hall effect

In the high magnetic field regime, quantum effects come into play [2]. In a 2DEG confined along the $\hat{z}$ axis, the energy levels are discretized into 2D subbands. Due to the small confinement along z, the subband energy spacing is large enough so that at low temperatures, the 2DEG occupies only the lowest subband. For a 2DEG in a perpendicular magnetic field (i.e. $\vec{\mathbf{B}} = B_z\hat{z}$), the eigenenergies along $\hat{x}$ and $\hat{y}$ are the solutions to the Schrödinger equation

$$\frac{1}{2m^*}(\vec{\mathbf{p}} + e\vec{\mathbf{A}})^2\psi = E\psi \quad (5.5)$$

where $\vec{\mathbf{p}}$ is the momentum operator and $\vec{\mathbf{A}} = \nabla \times \vec{\mathbf{B}}$ is the magnetic vector potential. The subsequent eigenergies are

$$E_n = \hbar\omega_c\left(n + \frac{1}{2}\right) \tag{5.6}$$

Each energy subband is referred to as a Landau level, and they are separated by a constant energy spacing $\hbar\omega_c$. Accounting for Zeeman splitting of the spin $\uparrow$ and $\downarrow$ states will further split the Landau levels as

$$E_n = \hbar\omega_c\left(n + \frac{1}{2}\right) \pm \frac{1}{2}g\mu_B B_z \tag{5.7}$$

where $\pm$ correspond to the $\uparrow$ and $\downarrow$ spin states respectively, g is the electron g-factor, and μ_B is the Bohr magneton. The number of occupied Landau levels is termed the filling factor ν and can be expressed as

$$\nu = \frac{hn_{2D}}{eB_z} \tag{5.8}$$

At low magnetic field strengths and in highly disordered samples, ν can vary continuously with B_z. As the material quality increases and B_z is sufficiently large, ν takes on discrete integer values as will be discussed in the following paragraph.

In theory, the density of states $g(E)$ for each Landau level is a perfect delta function, schematically shown in Figure 5.4a In practice, scattering impurities in the material broaden each Landau level by Γ. As B_z increases, the Landau levels separate in energy until they have an energy spacing $> \Gamma$ where individual Landau level peaks appear in the density of states (see Figure 5.4b). When Landau levels pass above the Fermi level E_F, electrons occupying those levels depopulate into lower energy states which decreases ν. As the total electron density n_{2D} must remain fixed, $g(E)$ for each Landau increases as ν decreases. ν takes on integer values when E_F lies in between Landau levels (Figure 5.4b) and will remain fixed until B_z is swept further until E_F reaches the next Landau level (Figure 5.4c). When E_F lies within a Landau level (Figure 5.4d), ν changes continuously.

The behavior of the sample's longitudinal resistivity ρ_{xx} depends on whether or not E_F lies within a Landau level. When ν is an integer and E_F lies in between Landau levels, there are no accessible energy levels for the electrons to conduct through when a bias voltage is applied. As such $\sigma_{xx} = 0$, and by Equation 5.3, $\rho_{xx} = 0$ (we note that at non-zero magnetic fields, $\rho_{xy} \neq 0$). On the other hand, when E_F lies within a Landau level, there are available states for the electron to conduct and scatter into. This produces a non-zero longitudinal resistivity that reaches a maximum when ν is in the middle of a Landau level (i.e. $\nu \approx 3.5$). Therefore as B_z is swept, ρ_{xx} will alternate between periods of

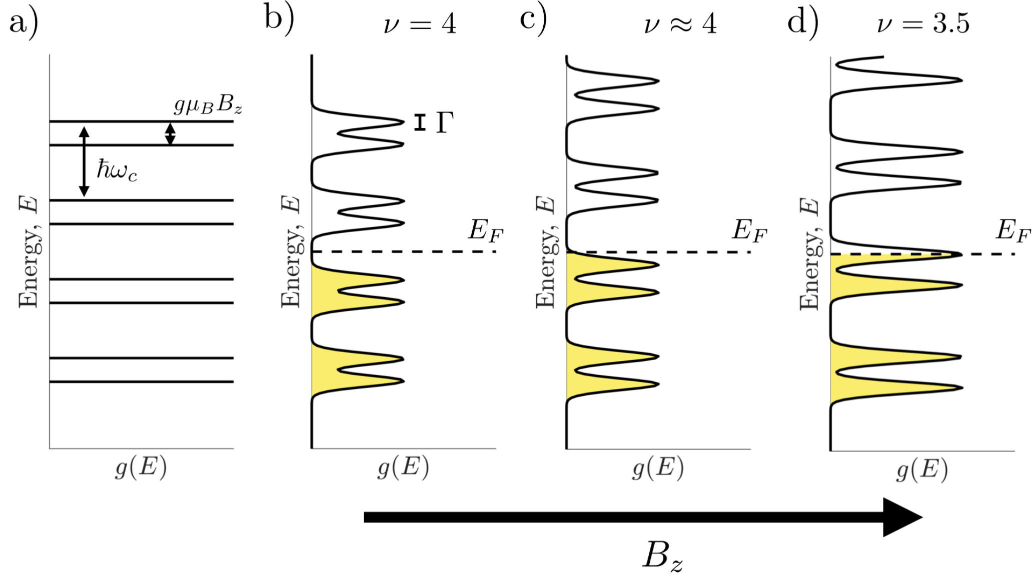

Figure 5.4: Schematic showing the formation of Landau levels in a 2D system. a) In a ideal system, each Landau level is a δ function and separated by the cyclotron frequency $\hbar\omega_c$. A perpendicular magnetic field causes a spin-slitting of each Landau level separated by $g\mu_B B_z$. b-d) In a real sample, disorder in the system broadens each Landau level. Levels below the Fermi level E_F (dashed line) are occupied by electrons. As the magnetic field increases, the Fermi level shifts and electrons drop into lower energy Landau levels which decreases the amount of filled Landau levels ν.

zero and non-zero resistivity. These oscillations are called Shubnikov-de Haas oscillations. As B_z increases, the maximum value of ρ_{xx} will increase due to stronger localization of the electron orbits which suppresses conduction through the sample.

Next, we discuss the behavior of the transverse resistivity ρ_{xy}. In the low field regime given by Equation 5.4, ρ_{xy} is expected to increase continuously with B_z. In the high field regime where the Landau levels are sufficiently separated, ρ_{xy} takes on quantized values given by

$$\rho_{xy} = \frac{h}{e^2}\frac{1}{\nu} \tag{5.9}$$

This quantization is called the integer quantum Hall effect. As B_z increases and Landau levels are depopulated, ρ_{xy} increases as well. Understanding the integer quantum Hall requires a discussion of edge states using Landauer-Buttiker formalism [24]. The confining

potential of the sample edge raises the Landau levels above E_F near the side wall. Electrons now have states accessible for conduction through a 1-dimensional edge channel along the side wall. This conduction occurs even if middle of the sample is insulating when E_F resides in between Landau levels. Electrons propagate in opposite directions on the sample edges [98]. Because these oppositely propagating channels are spatially separated by the sample width, back-scattering is greatly suppressed, and the longitudinal resistivity is $\rho_{xx} = 0$. Each 1D channel contributes e^2/h to the total conductance [24], and therefore, the total conductance caused by these edge states is $\nu e^2/h$ giving the transverse resistivity relation in Equation 5.9.

As touched on earlier, if the material is too disordered (i.e. mobility μ is low), then level broadening Γ will cause Landau levels to overlap. As such ν cannot take on discrete integer values both the integer quantum Hall effect and Shubnikov-de Haas oscillations will be suppressed. In addition to material quality, the temperature of the system is important in whether or not these effects are observed. If thermal broadening is comparable to the Landau level spacing (i.e. $k_BT \approx \hbar\omega_c$), then electrons can freely jump between Landau levels. This suppresses any localization effects that would otherwise be present and both the quantum hall and Shubnikov-de Haas effects will be suppressed. Observing these effects in a sample is a straightforward way of demonstrating the presence of a 2DEG or 2DHG, as the effects are quantum in nature. Bulk transport through the material would not show this behavior. More detailed discussions of Shubnikov-de Haas oscillations and the quantum hall effect can be found in Frieß [74] and Baer *et al.* [5].

5.2.3 Experimental results

Here, we characterize both n- and p-type ohmic contacts to a 2DEG and 2DHG respectively. Both a n-type and p-type Hall bar was fabricated on a 310 nm deep single heterojunction. The full heterostructure consists of a 10 nm GaAs cap, followed by 300 nm of AlGaAs, and then a GaAs substrate. This is considered a 'deep' heterostructure, and the ohmic contacts are easier to fabricate. An optical image of a nominally similar Hall bar is shown in Figure 5.5a. A zoomed image in Figure 5.5b better highlights the different regions of the device. The ohmic square regions are darker and rougher due to the ohmic annealing process during fabrication. A top gate (smooth gold) overlaps the ohmics and is used to induce the 2DEG or 2DHG at the GaAs/AlGaAs heterojunction. During fabrication, a mesa pattern is etched 350 nm deep past the heterojunction restricting formation of the 2DEG or 2DHG within the mesa area. The mesa prevents accumulation of the conduction layer underneath the bondpads which could otherwise short together during wirebonding when preparing the sample for measurement. Figure 5.5a also shows a schematic of the

circuit for measuring Shubnikov-de Haas oscillations and the integer quantum Hall effect in the Hall bar. A current source passes a constant current through the two ends of the Hall bar. Two voltage probes measure the respective longitudinal and Hall voltage drops, V_{xx} and V_H respectively, as we sweep a perpendicular magnetic field B_z.

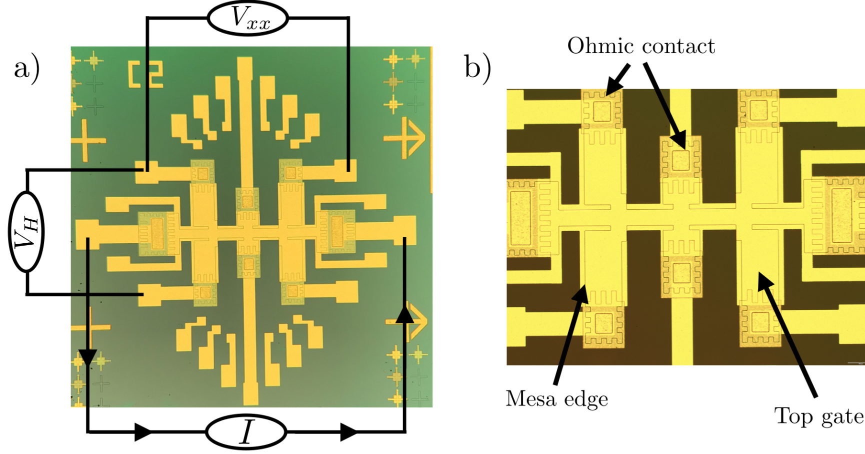

Figure 5.5: Optical image of a Hall bar used to characterize induced 2DEGs and 2DHGs in a dopant-free GaAs heterostructure. a) Shows the full device layout as well as the general circuit measurement used to perform Hall measurements of the device. Current is passed longitudinally through the device and two voltage probes measure the longitudinal V_{xx} and lateral Hall V_H voltage in the sample. b) A zoomed in view of the device structure. Ohmic contacts, the top gate, and the mesa edge are labelled accordingly.

The first device is a n-type Hall bar with a 300 nm thick SiO_2 insulating layer measured at 1.4 K. The results are summarized in Figure 5.6. It can be shown that the measured Hall resistance $R_H = V_H/I = \rho_{xy}$, which gives a direct relation between the Hall voltage V_H and electron density n_{2D} using Equation 5.4. For measurements of n_{2D}, we set $B =$ 0.1 T. Figure 5.6a shows how n_{2D} changes with the top gate voltage V_g. Below the turn on threshold $V_g = 0.6$ V, the top gate voltage is not strong enough to induce a 2DEG, and $n_{2D} = 0$ cm^{-2}. Above $V_g = 0.6$ V, the electron density increases linearly with V_g until a maximum value of $n_{2D} = 2.85{\times}10^{11}$ cm^{-2}. The fact that n_{2D} increases linearly indicates that there is no top gate current leakage to the ohmic contact or the 2DEG through the SiO_2 insulating layer. Such leakage can occur when the ohmics are very rough causing the SiO_2 to deposit non-uniformly. The longitudinal resistivity ρ_{xx} can be expressed as $\rho_{xx} = V_{xx}|_{B=0\ \mathrm{T}}/(I(l/w))$ where l and w are the length and width of the Hall bar. For the Hall bar in Figure 5.5, $l = 480$ μm and $w = 60$ μm. Combining this

expression with Equation 5.3 allows us to determine the electron mobility μ_e. Figure 5.6b shows μ_e at different electron densities n_{2D}. The mobility increases monotonically until reaching a maximum value of 7.5×10^6 cm^2/V·s at an electron density of 2.85×10^{11} cm^{-2}. As the electron density increases, there is higher Thomas-Fermi screening of background impurities which increases the electron mobility [4].

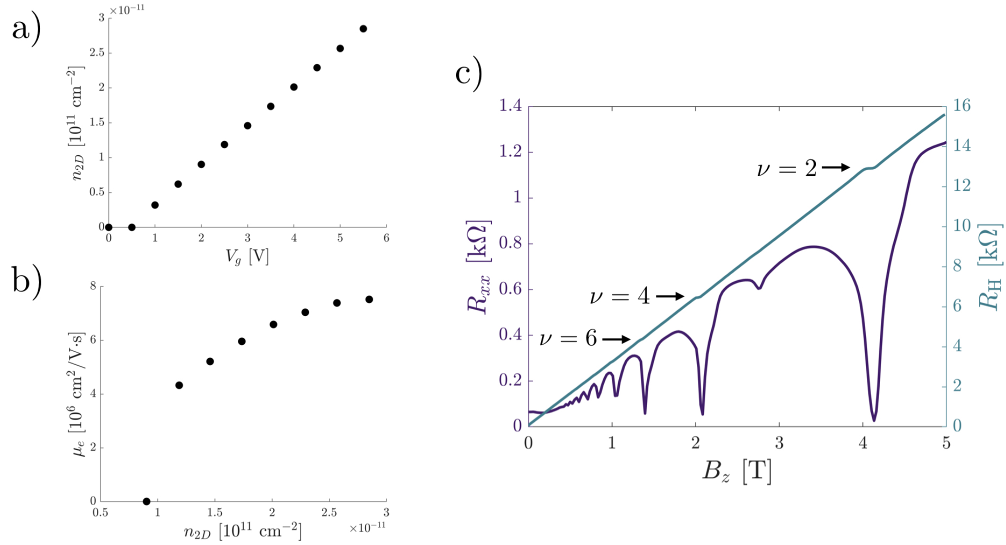

Figure 5.6: Characterization of a n-type Hall bar in a 310 nm deep single heterojunction at $T = 1.4$ K. a) Electron density n_{2D} versus the top gate voltage V_g. Below the turn-on threshold $V_g = 0.7$ V, there is no induced 2DEG. Above the turn-on threshold, the electron density increases linearly with top gate voltage suggesting that there is no leakage to the top gate. b) Electron mobility μ_e versus the electron density. The electron mobility increases monotonically with the density as higher electron concentrations screen scattering events in the material. At the peak density of $n_{2D} = 2.5\times10^{11}$ cm^{-2} the mobility is $\mu_e = 4\times10^6$ cm^2/V·s. c) Shubnikov-de Haas oscillations and integer quantum Hall measurements with a perpendicular magnetic field. Oscillations in the longitudinal resistance R_{xx} (purple) appear at high magnetic fields and correspond to narrow quantized hall plateaus in the Hall resistance R_H (blue). The corresponding filling factors are given for each oscillation and plateau.

Now that the mobility and electron density of the 2DEG have been characterized, we need to check that there is no parallel conduction in the device. This is achieved by observing the integer quantum Hall effect and Shubnikov-de Haas oscillations. Figure 5.6c

show magnetotransport measurements as the magnetic field is swept from 0 to 5.5 T. The left axis (purple) plots the longitudinal resistance $R_{xx} = V_{xx}/I$ and the right axis (blue) plots the Hall resistance $R_H = V_H/I$ of the device. At high magnetic fields, Shubnikov-de Haas oscillations oscillations appear with the minima of each oscillation approaching 0 as B_z increases. Near the minima of the last three oscillations, narrow plateaus in R_H appear corresponding to $\nu = 6$, 4 and 2 (labelled accordingly in the figure). The narrowness of the Shubnikov-de Hass minima and the quantum hall plateaus is due to the high measurement temperature $T = 1.4$ K. The quality of the Shubnikov-de Has and integer quantum Hall effects correspond directly to the mobility of the material (as this is a direct indication of the amount of disorder in the sample). Measurements of a lower quality dopant-free heterostructure ($\mu_e = 1.68{\times}10^6$ cm^2/V·s) were done at $T = 300$ mK where the Shubnikov-de Haas oscillations and quantum hall plateaus are very prominent [174]. As the mobility we report here is even higher than that work, we believe measurements at lower temperatures would greatly enhance our features. At the temperatures for this experiment, k_BT is greater than the Zeeman splitting $g\mu_BB$, and odd filling factors are not observable although a Shubnikov-de Haas oscillation does just begin to appear at around $\nu = 3$. As the Shubnikov-de Haas oscillations essentially reach zero in Figure 5.6c, we conclude that there is only a single 2DEG present. If there was a second conduction channel present, then current flow through that other channel would mask these features in R_{xx} and R_H. All of the measurements in Figure 5.6 could only have been achieved using high quality ohmics where there is no leakage to the top gate, a linear response in current with the applied bias, and a low contact resistance. A series of I-V measurements (not shown) indicate that the ohmic contact resistance is very low ∼110 Ω.

The second device is a p-type Hall bar with a 300 nm thick SiO_2 insulating layer measured at 1.4 K. The results are summarized in Figure 5.7. Figure 5.7a shows the hole density p_{2D} versus the top gate voltage V_g at $B = 0.1$ T. The 2DHG is induced when $V_g = -1.5$ V. At the highest top gate voltage $V_g = -5.5$ V, $p_{2D} = 2.26{\times}10^{11}$ cm^{-2}. We note that the turn-on voltage for the 2DHG is more negative than the corresponding positive turn-on voltage for the 2DEG (0.6 V). This is not surprising as surface states, device fabrication variability, and oxide quality (among others) can cause the Fermi level of the surface to be pinned non-mid gap. As such, the turn-on voltages for 2DEGs and 2DHGs is anticipated to not be symmetric around $V_g = 0$ V. As with the n-type Hall bar, the linear relation between p_{2D} and V_g shows that there is no top gate leakage to either the 2DHG or ohmic contact. The hole mobility μ_h versus p_{2D} is plotted in Figure 5.7b and reaches a maximum of $\mu_h = 0.64{\times}10^6$ cm^2/V·s. Hole mobility is roughly an order of magnitude less than electron mobility at equal carrier densities. This is because in GaAs a hole has a larger effective mass ($m^* = 0.45m_e$) compared to an electron ($m^* = 0.067m_e$). Because mobility

$\mu \propto 1/m^*$, it is clear that higher effective masses have a lower mobility. One artifact of lower mobilities is that hole resistances will be higher than their electron counterparts. Figure 5.7c shows the longitudinal R_{xx} and Hall R_H resistances as the magnetic field is swept. For the 2DHG, no quantum hall plateaus appear while a Shubnikov-de Haas oscillation does begin to appear around $\nu = 2$; however, this oscillation does not drop fully to zero longitudinal resistance. The absence of the anticipated R_{xx} and R_H behavior is due to either the presence of another conduction layer in the heterostructure or due to the high temperature of the experiment $T = 1.4$ K. We already argued that this temperature was too high to clearly resolve these features for a 2DEG. As holes have a higher effective mass, all their effective energy scales decrease accordingly. This means holes require an even lower measurement temperature to clearly resolve these features, typically tens of mK. Nevertheless, the data in Figures 5.7a-b indicate that we can contact the 2DHG and tune its density and mobility. A series of I-V measurements (not shown) indicate that our contact resistance is very low ∼500 Ω.

5.3 Quantum point contacts in dopant-free GaAs single heterojunctions

This section explores electron transport through quantum point contacts (QPCs) where the electrons are confined within a 1D system. Quantum point contacts can be realized either by using a split top gate or split etched pit to restrict the conductive channel to 1D. QPCs have been experimentally studied in detail for both intentionally doped [253, 263] and dopant-free [230] GaAs heterostructures. As before in the 2D case, electrons confined to a 1D channel occupy discrete energy subbands. Each spin-degenerate subband contributes exactly $2e^2/h$ to the conductance G of the channel. If the length of the 1D channel is less than the mean free path of the system, then the electron transport is ballistic (meaning the electron experiences no scattering events). In this case, the conductance G is quantized into integer multiples of $2e^2/h$. The first half of this section will briefly introduce the theory behind electron transport through these 1D channels. The second half will present experiments done with QPCs using an induced 2DEG in a shallow single heterojunction. In particular, our devices show a large subband spacing of 4.5 meV which allows the conductance quantization to persist up to temperatures of 4 K.

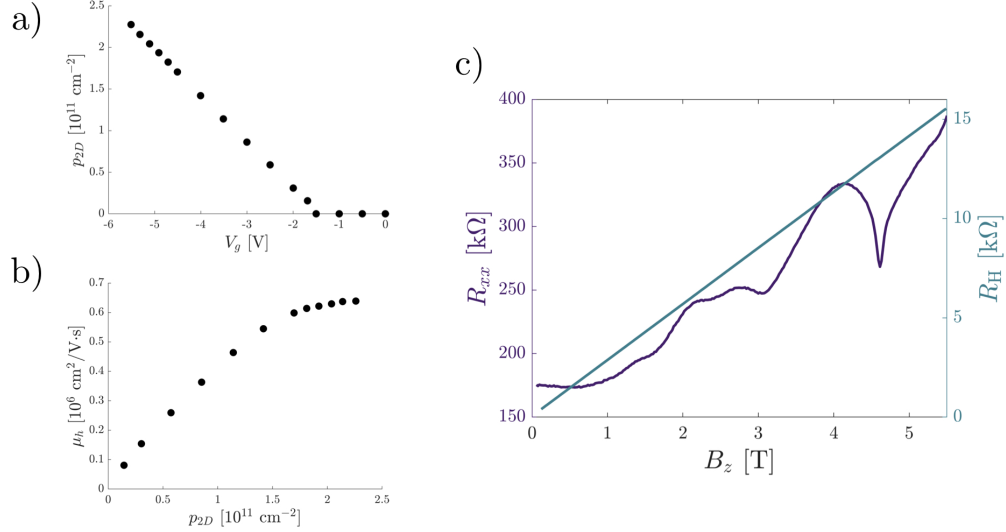

Figure 5.7: Characterization of a p-type Hall bar in a 310 nm deep single heterojunction at $T = 1.4$ K. a) Hole density p_{2D} versus the top gate voltage V_g. Above the turn-on threshold $V_g = -1.5$ V, there is no induced 2DHG. Below the turn-on threshold, the hole density increases linearly with top gate voltage suggesting that there is no leakage to the top gate. b) Hole mobility μ_h versus the hole density. The hole mobility increases monotonically with the density as higher hole concentrations screen scattering events in the material. At the peak density of $p_{2D} = 2.26\times10^{11}$ cm^{-2} the mobility is $\mu_h = 0.64\times10^{6}$ cm^2/V·s. c) Shubnikov-de Haas oscillations and integer quantum Hall measurements with a perpendicular magnetic field. A small oscillation starts to appear in the longitudinal resistance R_{xx} (purple) near a filling factor of $\nu = 2$. No quantized plateaus in the Hall resistance R_H (blue) are seen. This suggests either the measurement temperature is too high to resolve the oscillations or there is a parallel conducting layer.

5.3.1 Electron transport in 1D

Here, we will derive the expression for conductance quantization in a 1D channel following Bagwell *et al.* [6]. To begin, we assume an arbitrary 1D potential denoted as $U(x, V_{\text{bias}})$ where x is the position and V_{bias} describes an external bias voltage applied across the channel. The 1D channel is contacted on both the left and right sides by electron reservoirs (2DEGs). The bias voltage induces an electric field which drives electrons across the 1D channel $U(x, V_{\text{bias}})$ with a transmission coefficient T_{1D}. A unit coefficient $T_{1D} = 1$ implies

that the electrons experience ballistic transport meaning they experience no scattering events.

At a finite temperature T, the current through the 1D channel can be written as

$$I = e \int v(E)\, T_{1D}(E, V_{\text{bias}})\, g_{1D}(E) \times [f(E - (\mu + eV_{\text{bias}}), T) - f(E - \mu, T)]\, dE \tag{5.10}$$

where $v(E)$ is the electron drift velocity in the $+\hat{x}$ direction, $g_{1D}(E)$ is the 1D density of states for both spin species, μ is the Fermi level in the right electron reservoir, and f is the Fermi function. The $f(E - (\mu + eV_{\text{bias}}), T)$ term corresponds to current induced by electrons flowing from the left-to-right electron reservoirs ($+\hat{x}$ direction). The $f(E - \mu, T)$ term corresponds to current induced by electrons flowing from the right-to-left electron reservoirs ($-\hat{x}$ direction). In 1D, we have that $v(E) = \frac{1}{\hbar}\left|\frac{dE}{dk}\right|$ and $g_{1D}(E) = \frac{1}{\pi}\left|\frac{dk}{dE}\right|$ where k is the wave vector of an electron in the conduction band. Both of these terms exactly cancel to leave a constant $\frac{1}{\pi\hbar}$ in the integral. The Fermi function can be rewritten as a composite probability function

$$f(E - \mu, T) = [1 - \Theta(E - \mu)] \otimes \left[-\frac{df}{dE}(E, T)\right] \tag{5.11}$$

where Θ is the Heavyside step function and $\otimes$ is a convolution over E. This allows the Fermi term in the integral to be rewritten as

$$f(E - (\mu + eV_{\text{bias}}), T) - f(E - \mu, T) = [\Theta(E - \mu) - \Theta(E - (\mu + eV_{\text{bias}}))] \otimes \left[-\frac{df}{dE}(E, T)\right] \tag{5.12}$$

The left bracket term can be interpreted as an energy broadening due to the applied bias voltage, while the right bracketed term can be interpreted as an energy broadening caused by temperature smearing. Physically, this separates the effects of voltage and thermal broadening on the current implying that they are statistically independent. Combining all these together leads to the reduced expression

$$\begin{aligned} I &= \frac{2e^2}{h} T_{1D}(E, V_{\text{bias}})[\Theta(E - \mu) - \Theta(E - (\mu + eV_{\text{bias}}))] \otimes \left[-\frac{df}{dE}(E, T)\right] \\ &= \frac{2e^2 V_{\text{bias}}}{h} \bar{T}_{1D}(E, V_{\text{bias}}) \end{aligned} \tag{5.13}$$

where $\bar{T}$ denotes the energy averaged transmission coefficient of the 1D channel $U(x, V_{\text{bias}})$. The conductance G of the 1D channel is simply $G = I/V_{\text{bias}}$. If T and V_{bias} are small such that they induce relatively little smearing, then the expression reduces to the well known Landauer formula [158]

$$G = \frac{2e^2}{h} T_{1D}(E, V_{\text{bias}}) \tag{5.14}$$

The result shows that when an electron transport is ballistic through 1D channel ($T_{1D} = 1$), then each 1D channel contributes exactly $\frac{2e^2}{h}$ to the overall conductance. If many 1D channels are accessible for electrons to conduct through then the total conductance is given by

$$G = \frac{2e^2}{h} \sum_{i,j} T_{ij}(E, V_{\text{bias}}) \tag{5.15}$$

where T_{ij} denotes the transmission coefficient of an electron travelling from the ith channel in the left electron reservoir into the jth channel in the right electron reservoir [246].

There are two things to note in this above derivation. The first is the factor of 2 in the conductance quantization coefficient which arises due to the spin-degeneracy in the absence of a magnetic field. In a non-zero magnetic field, the 1D subbands are no longer spin-degenerate, and the conductance quantization instead becomes e^2/h for each 1D subband. The second thing is that nowhere did we require an explicit form of U. As long as U is a 1D potential, then the drift velocity and 1D density of states will cancel as evident in the derivation.

A useful model of U used to understand conductance quantization is the saddle point potential [23]

$$U(x, y) = V_0 - \frac{1}{2} m^* \omega_x^2 x^2 + \frac{1}{2} m^* \omega_y^2 y^2 \tag{5.16}$$

The ω_x term describes the tunneling energy of electrons through saddle point barrier while ω_y describes the transverse confinement of the 1D channel. The 1D channel subband spacings are given by the harmonic confinement along $\hat{y}$, $E_y = \hbar\omega_y(n + 1/2)$. It can be shown [180, 43] that the transmission coefficient of this channel is given as

$$T_{nm}(E) = \delta_{nm} \frac{1}{1 + e^{-\pi E_n}} \tag{5.17}$$

$$E_n = 2[E - \hbar\omega_y(n + 1/2) - V_0]/\hbar\omega_x \tag{5.18}$$

when $T = 0$ K. This transmission coefficient takes into account the electron scattering caused directly by the saddle point potential.

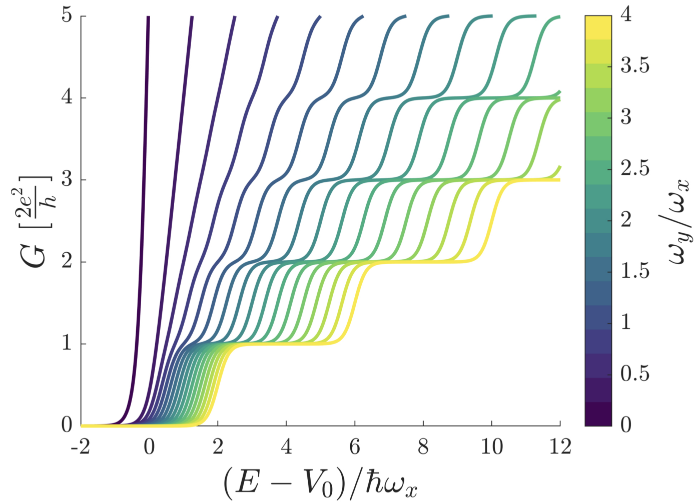

Figure 5.8: Quantum conductance through a saddle point 1D potential. The $\hat{x}$ axis corresponds to energy in the 1D channel and the $\hat{y}$ axis corresponds to the channel's conductance G in units of $2e^2/h$. Line color corresponds to the ratio of ω_y/ω_x. As the ratio increases, conductance quantization appears.

Figure 5.8 shows simulated conductance curves using the saddle point potential for different ratios of the confinement and tunneling energies ω_y/ω_x. The $\hat{x}$ axis is in normalized energy units and line color denotes the ω_y/ω_x value. When $\omega_y \ll \omega_x$ (purple), there is no quantized conductance. This is because electrons have a higher transmission probability to tunnel directly through the saddle point barrier rather than conduct through the 1D channel. The quantized conductance transport that does occur in the system is smeared out by the electron tunneling events through the barrier. When the transmission probability of tunneling through the barrier is suppressed (i.e. ω_x decreases thereby increasing ω_y/ω_x), the quantized conductance is no longer smeared and shows clear conductance plateaus (yellow). Therefore, conductance quantization is most clearly observable when $\omega_y \gg \omega_x$. The particular values of ω_y and ω_x are not important as long as $\omega_y/\omega_x > 1$ is maintained. Practically, ω_x can be decreased by lengthening the 1D channel, creating an effectively wider tunneling barrier. However, conductance quantization occurs only when the electron transport in the 1D channel is ballistic and no scattering events occur. As a result, the physical 1D channel length should not exceed the mean free path l_0 of the material. Clean material systems, such as dopant-free heterostructures, have larger l_0 values. This means that longer QPC channels can be realized, reducing ω_x and increasing ω_y/ω_x to yield clearer

conductance quantization.

5.3.2 1D subband spectroscopy of a quantum point contact

Here, we present experimental results for an etched QPC in a 90 nm deep single heterojunction. A scanning electron microscope (SEM) image of a nominally similar device is shown in Figure 5.9a. The QPC gates are composed of a metal bilayer of 10/10 nm of Ti/Au and were patterned using Electron Beam Lithography (EBL). The region in between the QPC gates has dimension 500×500 nm. A $20 - 30$ nm etch using a solution of 1:1:20 H_2O_2:H_3PO_4:H_2O was done right before the metal deposition so that the QPC gates are slightly recessed. Ohmic contacts (denoted by squares with a cross in the figure) on both sides of the QPC were fabricated using techniques described in Section 5.2.1. On top of the device, 300 nm of SiO_2 was deposited as an insulating layer and subsequently capped by a 20/80 nm Ti/Au top gate used to induce the 2DEG. The QPC gates screen the electric field coming from the top gate voltage and prevent a 2DEG from being induced under the QPC gates. The top gate only induces a 1D channel in between the opening of the QPC gates. By applying a voltage to the two QPC gates (denoted V_{qpc}), the energy of the 1D channel can be shifted in order to move 1D subbands below and above the Fermi level. This changes the number of 1D subbands contributing to the total conductance. If V_{qpc} is raised too high ($\gtrapprox 0.75$ V), a 2DEG can be induced underneath the QPC gates and suppress the 1D channel.

Figure 5.9a shows the circuit used to measure the conductance through the QPC. The sample itself is placed in a liquid Helium cryostat with a base temperature of 1.4 K. Electrical wires connect the sample to voltage sources and measurement equipment outside of the cryostat at room temperature. A lock-in amplifier with a reference frequency of 100 Hz supplies an AC bias voltage onto the leftmost ohmic with a peak-to-peak amplitude of 200 μV. The right-hand ohmic is connected to the lock-in's current pre-amp to monitor the current I through the device. Line resistance from the cryostat wiring and the ohmic contacts cause only part of the 200 μV to drop in amplitude before reaching the 1D channel. Therefore, another ohmic pair, split across the 1D channel, is connected to a voltage pre-amp in another lock-in amplifier in order to monitor the real voltage drop V directly across the 1D channel. The conductance through the 1D channel is found as $G = I/V$. Voltages to the QPC gates V_{qpc} and top gate V_g are supplied by a DC voltage source.

Figure 5.9b shows the measured conductance of the 1D channel in units of $2e^2/h$ as V_{qpc} is swept. The top gate is set to $V_g = 9.0$ V and the sample is at a temperature of 1.4 K. The first 6 conductance plateaus are clearly visible and match well to the expected

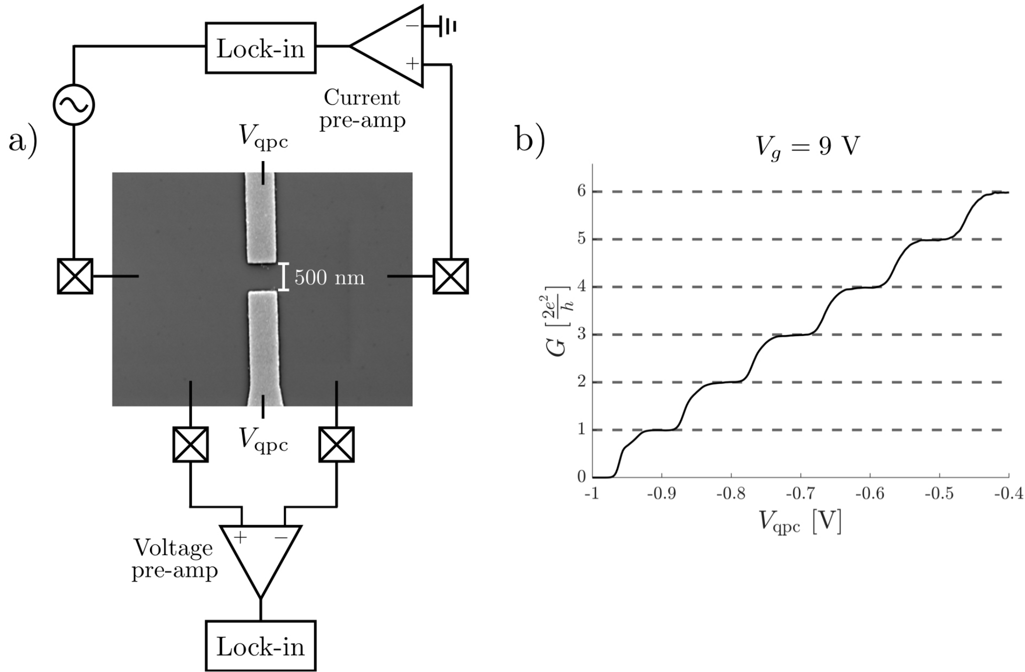

Figure 5.9: Quantized conductance of an etched QPC in a 90 nm deep single heterojunction. a) SEM image of a 20 nm deep etched QPC nominally similar to the device measured. A schematic of the measurement circuit is overlaid on the SEM image. A small AC bias is applied across the 1D channel using a lock-in reference signal and a current pre-amplifier monitors the current flow through the device. The voltage dropped across the device is measured using voltage pre-amp fed into another lock-in. DC voltages are supplied to the QPC gates V_{qpc} and a global top gate V_g. b) Measured conductance in units of $2e^2/h$ versus V_{qpc} at $T = 1.4$ K at $V_g = 9.0$ V. Up to 6 quantized plateaus are seen in the given voltage range. The kink below the first plateau corresponds to the 0.7 structure readily observed in QPCs.

integer quantized values. Just below the first plateau is the 0.7 structure, a not yet fully understood phenomenon that forms near $\sim 0.7\times 2e^2/h$. The 0.7 structure is believed to either be an artifact of a partial spin-polarization at zero magnetic field [252] or due to a Kondo-like correlated spin state [47]. The turn on of the 1D channel occurs at around $V_{\mathrm{qpc}} = -0.96$ V. While data is not shown here, quantized conductance was observed at lower top gate voltages all the way down to $V_g = 3.0$ V.

The QPC is tuned to a high top gate voltage V_g in order to increase the 1D subband spacing as much as possible. Increasing the top gate voltage pulls the potential along the

central axis of the QPC lower with respect to the potential along the edges of the QPC, due to the screening of the top gate electric field by the QPC gates. This change induces an effectively stronger confinement in the 1D potential which increases the subband spacing. Increasing V_g shifts the turn-on of the channel to more negative QPC voltages. At $V_g =$ 3.0 V, the top gate cannot induce a 1D channel due to the screening of the QPC gates when $V_{\text{qpc}} = 0$ V. There are no 1D subbands accessible for electrons to tunnel through in the channel. V_{qpc} must have a positive voltage in order to assist the top gate and open the channel. When V_g is increased all the way to 9.0 V, as in Figure 5.9b, the top gate supplies enough of an electric field to induce a 1D channel even when $V_{\text{qpc}} = 0$ V. In order to pinch off the channel, V_{qpc} must be tuned to negative voltages which is more ideal for operating a QPC. Electrons are repelled by the negative voltage which makes an effectively 'tighter' 1D channel with a higher subband spacing.

It is not possible to directly evaluate the subband spacing from a single 1D trace of the quantized conductance. This is because we do not know the lever arm between the change in V_{qpc} and the change in energy of the 1D subbands. The fact that such clear quantization is observable in our device at 1.4 K indicates that the 1D subband spacing is at least higher than the thermal energy $k_B T = 0.125$ meV. A general rule of thumb is that the subband spacing must be higher than $\approx 10\, k_B T$ in order to see clear conductance plateaus. In order to measure the true subband spacing, we need to do an energy resolved measurement [203]. This is achieved by adding a DC bias voltage V_{bias} to the measurement circuit shown in Figure 5.9a. By sweeping V_{bias}, we can bring additional subbands within the bias voltage window to increase the measured conductance through the channel. As with the small AC bias, V_{bias} does not all drop directly across the 1D channel due to line and ohmic contact resistances. A DC voltage probe is used to monitor the actual bias voltage $\tilde{V}_{\text{bias}}$ dropped across the channel.

Figure 5.10 summarizes the results of a 1D subband spectroscopy experiment done at 1.4 K. The DC bias V_{bias} was stepped from -15 to $+15$ mV in steps of 0.2 mV. At each V_{bias} value, V_{qpc} was swept to measure the quantized conductance plateaus. From analyzing the G versus V_{bias} and V_{qpc} we can extract the subband spacing. The above steps were repeated at different V_g values to measure how the subband spacing changes with top gate voltage. Raw conductance data are plotted in Figure 5.10a for $V_g = 6.0$ V in units of μS. Starting from the leftmost curve which corresponds to $V_{\text{bias}} = -15$ mV, each conductance curve is shifted by $+4$ mV on the $\hat{x}$ axis for visual clarity. The rightmost curve corresponds to $V_{\text{bias}} = +15$ mV. As V_{bias} is increased, additional conductance plateaus appear at half-integer quantized conductance values. Additional plateaus are appropriately labelled by their scalar multiple of the fundamental quantized conductance value $G_0 = 2e^2/h = 77.4$ μS.

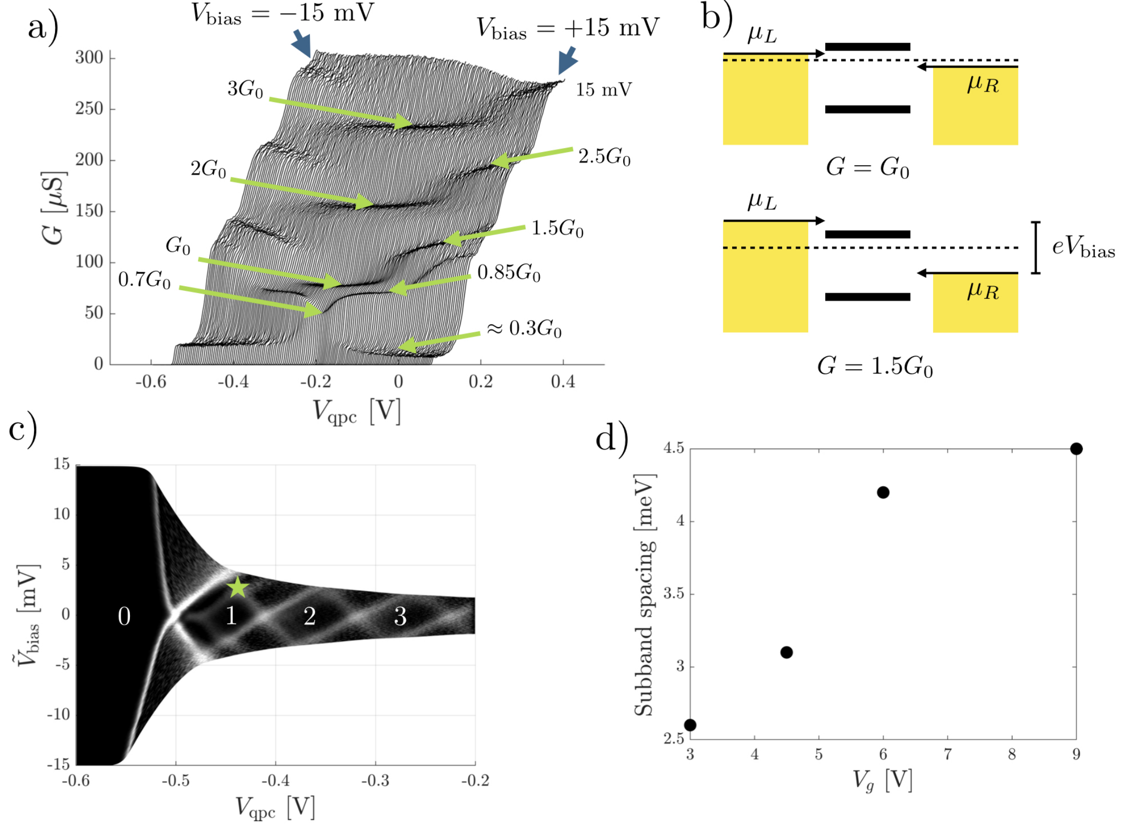

Figure 5.10: Subband spectroscopy measurement of an etched QPC. a) Device conductance in μS versus V_{qpc} at different DC bias voltage V_{bias}. Starting at $V_{\text{bias}} = -15$ mV on the left-most curve, each curve is offset laterally by +4 mV for visual clarity. The rightmost curve corresponds to $V_{\text{bias}} = +15$ mV. Quantized conductance plateaus are labelled according to their scalar multiple of the fundamental quantized conductance value $G_0 = 2e^2/h$. b) Schematic showing how a large DC bias voltage causes fractional quantized conductance values. When the bias window contains a single subband level, electrons can only conduct through the second subband from the left reservoir and not the right. c) Plot of dG/dV_{qpc} versus V_{bias} and $\tilde{V}_{\text{bias}}$ when $V_g = 6.0$ V. $\tilde{V}_{\text{bias}}$ is the actual bias applied across the device which changes as the device resistance changes with V_{qpc}. Each conductance plateau is labelled according to their correspond integer multiple of the fundamental conductance value G_0. The first subband spacing is found at the vertex of the first conductance diamond. d) Measured subband spacing versus the top gate voltage V_g.

The appearance of these half-integer plateaus can be explained using the schematic shown in Figure 5.10b. The energy of the 1D channel is tuned such that the first 1D subband falls below the Fermi level (dashed black line) when $V_{\text{bias}} = 0$ V. We assume that V_{bias} is applied symmetrically across the 1D channel [203]. When V_{bias} is very small or zero, no 1D subbands lie within the bias window. Electrons from travelling in both the left-to-right and right-to-left directions have the same number of subbands to conduct through, giving rise to an integer quantized conductance $G = G_0$ value. When V_{bias} is increased to values comparable to the subband spacing, a single 1D subband can be brought within the bias window. Now, there is an asymmetry in the channel conductance as electrons in the right reservoir can only conduct through the lowest 1D subband while electrons in the left reservoir can conduct through two 1D subbands [87, 202]. This averages the total conductance through the channel to be 1/2 of the G_0 and $2G_0$ integer conductance values. By sweeping V_{bias} and tracking the appearance of these half-integer plateaus, we can extract the subband spacing.

Figure 5.10c shows a 2D map of dG/dV_{qpc} for the data shown in Figure 5.10a. However, the $\hat{y}$ axis corresponds to the bias voltage actually applied across the device $\tilde{V}_{\text{bias}}$. When V_{qpc} is low and the channel is pinched off, the channel resistance is very high and dominates the total line resistance of the measurement circuit. Therefore, all of the bias is dropped directly across the channel and $V_{\text{bias}} \approx \tilde{V}_{\text{bias}}$. As the channel opens and the resistance decreases, $\tilde{V}_{\text{bias}}$ reduces as demonstrated by the 'pinching' of the 2D data along the $\hat{x}$ axis. Black corresponds to flat regions of conductance, and white corresponds to transitions between conductance plateaus. Diamonds indicate regions where the conductance is quantized. Along the central axis of the graph, diamonds correspond to integer conductance values $G = 0G_0$, G_0, $2G_0$, and $3G_0$. The 1D subband spacing can be easily determined by finding $\tilde{V}_{\text{bias}}$ at the top of an integer conductance diamond (green star). For this data set, we measure a subband spacing $\sim$4.2 meV.

The subband spacing can be modified using the top gate voltage. By changing the top gate voltage, we directly control the shape of the 1D channel potential. When V_g is small, the 1D potential will be shallower with sloped side walls which create an effectively wider lateral confinement (ω_y in Equation 5.16). When V_g is large, the 1D potential will be deeper with sharper side walls creating a tighter 1D channel constriction. Therefore, larger V_g values will increase the subband spacing. Figure 5.10d shows data for the measured subband spacing in our etched QPC device at four different V_g values. As V_g increases, the subband spacing increases until converging towards a maximum value of $\sim$4.5 meV near $V_g = 9.0$ V. We could not go to higher top gate voltages due to charging of the SiO_2 insulator layer. A subband spacing of $\sim$4.5 meV for a etched QPC is higher than any published result for dopant-free devices [173] but is far from the current record of $\sim$20

meV for modulation doped devices [153]. This high of a subband spacing easily allows for observable conductance quantization at 4 K. We believe the device could be even further optimized to significantly raise the subband spacing. The etch was very shallow, only $20-30$ nm. A deeper etch would increase the lateral confinement of the 1D channel thereby increasing the subband spacing. Additionally, the device measured had a 500×500 nm physical gate dimension; however, by making the channel width narrower, the subband spacing could also be further increased.

5.4 Single electron pumping in dopant-free GaAs single heterojunctions

The previous section explored quantized conductance in a QPC. Here, in this section, we study quantized current using a one-parameter single electron pump (SEP). In a SEP, electrons are moved through the device in response to a AC driving signal. The current flow through the device is given as $I = nef$ where f is the frequency of the driving signal, e is the electron charge, and n is the number of electrons moved per driving cycle [125]. Single electron pumps have been realized experimentally a number of different ways including one-parameter tunable-barrier pumps [123, 81], 2-parameter turnstile pumps [152, 188, 33], arrays of metallic islands [135], Josephson junction arrays [196, 265], or surface acoustic waves [238, 110]. Such devices are particularly interesting for metrological purposes as a method for standardizing one of the base SI units, the ampere. Originally, the ampere was defined as the amount of force generated between two infinitely long conducting rods placed 1 m apart. As this is difficult to realize in practice, the ampere was redefined in May 2019 as the number of electrons that pass a given point in 1 second (specifically 1 A corresponds to 6.241×10^{18} electrons travelling past a given point in 1 second). This definition corresponds more intuitively to what an ampere means and is more practical to realize in a lab setting. However, the electron charge is very small, and precisely counting individual electrons over an extended period of time is challenging. In order for single electron pumps to be useful for metrology, the pump must have a high operating frequency f to produce large measurable currents as well as low error rates per driving cycle (i.e. only 1 electron is moved per cycle with very high fidelity). Aside from metrological purposes, a single electron pump with high operating frequency and low error rates could have practical usage in optoelectronics applications. A device which deterministically pumps an electron can be integrated with a PN junction to realize a on-demand single photon source as proposed for both tunable-barrier pumps [237] and surface acoustic waves [71, 34]. Such a device has recently been demonstrated experimentally using surface acoustic waves [110].

Indistinguishably of the emitted photons from a single-photon requires the photon energy spread to be very narrow. For these types of novel photon sources which combine SEPs and PN junctions, the photon energy spread is directly related to the energy spread of the pumped electrons. One-parameter SEPs (which are the focus of this section) have demonstrated energy spreads of $\Delta E = 1.8$ meV [257], but theory predicts that this could be reduced all the way to a few μeV [161].

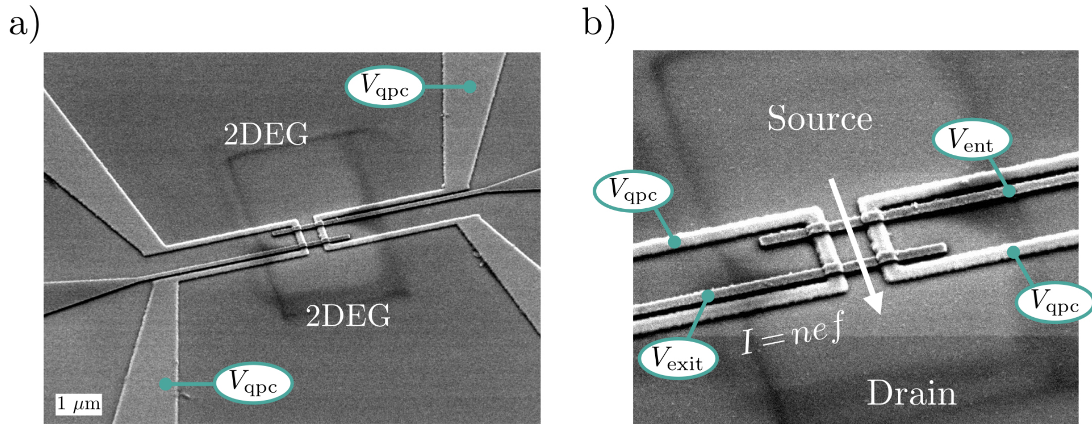

Figure 5.11: SEM image of a tunable-barrier single electron pump on a 90 nm deep single heterojunction. a) Two QPC gate with voltages V_{qpc} can be used to realize a 1D channel. The 1D channel is contacted on both sides by an induced 2DEG using a global top gate deposited on top the device (not shown in the image). b) Zoomed view showing the active pump device. Entrance and exit barrier gates are used to form a dynamically driven quantum dot. By RF modulating entrance barrier voltage V_{ent}, electrons are collected from the source and pumped into the drain resulting in a quantized current $I = nef$ where n is the number of pumped electrons per RF cycle and f is the RF frequency.

One-parameter tunable-barrier SEPs have demonstrated the highest operating frequencies [277] and lowest error rates at frequencies > 100 MHz (0.2 ppm [243]) out of all types of single electron pumps. Higher operating frequencies are preferred as they result in larger quantized current magnitudes which are easier to measure. For the devices considered in this Section, the SEP geometry consists of a quantum dot. A 1D channel formed by QPC gates provides lateral confinement and two additional gate electrodes form additional tunnel barriers to realize the quantum dot. A SEM image of a fabricated SEP device is shown in Figure 5.11a where the QPC gates have corresponding voltages V_{qpc} similar to the devices studied in Section 5.3. The device was fabricated on a 90 nm deep dopant-free

GaAs/AlGaAs single heterojunction. The 1D channel is contacted by 2DEGs induced on both sides of the device which provide electron reservoirs. Figure 5.11b is a zoomed in image of the device highlighting the additional tunnel barrier gates where electrons will enter and exit the pump.

The operation of the single-parameter tunable-barrier pump is depicted schematically in Figure 5.12. In the upper left panel is a rough depiction of the entrance and exit gates where an RF signal is applied to the entrance gate. For each panel, the black line corresponds to the potential landscape of the device, the dashed line is the Fermi level in the adjoining 2DEGs, and blue circles are individual electrons. The close physical proximity of the entrance and exit gates means there is inherent cross coupling of the gate voltages in the device. There are four stages of electron pumping during a single RF cycle. The start of the cycle is the loading stage. The entrance tunnel barrier is lowered below the Fermi level and electrons are 'scooped' into the QD potential. During the back-tunneling stage, the entrance potential begins to rise. Each electron has a corresponding back-tunneling rate Γ_i describing how long it takes to tunnel into the left electron reservoir. Given that $\Gamma_i < \Gamma_{i+1}$, higher energy electrons tunnel out of the QD while the lower energy electrons remain. The remaining electrons are then captured as the entrance barrier increases and reduces the remaining back-tunneling rates. In the ejection stage, the tunnel barrier gate is brought sufficiently high so that the remaining electron's energy rate is higher than the exit barrier gate and the electron is ejected into the right electron reservoir. The cycle is then repeated.

The Fermi level in both the source and drain electron reservoirs are the same, meaning there is no external bias applied across the device. The reason why current still occurs even in the absence of a bias voltage is because the electrons are pumped non-adiabatically through our device. A SEPs ability to produce quantized current with a high accuracy is determined in the back-tunneling stage. When the ratio $\Gamma_1/\Gamma_0 \gg 1$, only a single electron will be captured each pumping cycle with high probability. In the limit where $\Gamma_1 = \infty$ and $\Gamma_0 = 0$, the device would pump a single electron with perfect fidelity every RF cycle. Deviations away from those ideal values lower the pump accuracy. The ratio Γ_1/Γ_0 is affected mainly by two device parameters: the width of the tunneling barriers and the energy level spacing of the QD (which is determined by the charging energy) [130, 69]. A wider tunnel barrier will reduce Γ_0 and a higher energy spacing will increase Γ_1.

The number of electrons ejected per RF cycle is dependent on how many electrons are captured and ejected during those respective stages. Both the entrance and exit gates have a corresponding DC voltage component used to tune the SEP device. By adjusting the DC offset on the entrance gate, more or fewer electrons can be captured in the respective stage. Similarly, by adjusting the DC voltage on the exit gate, the exit tunnel barrier

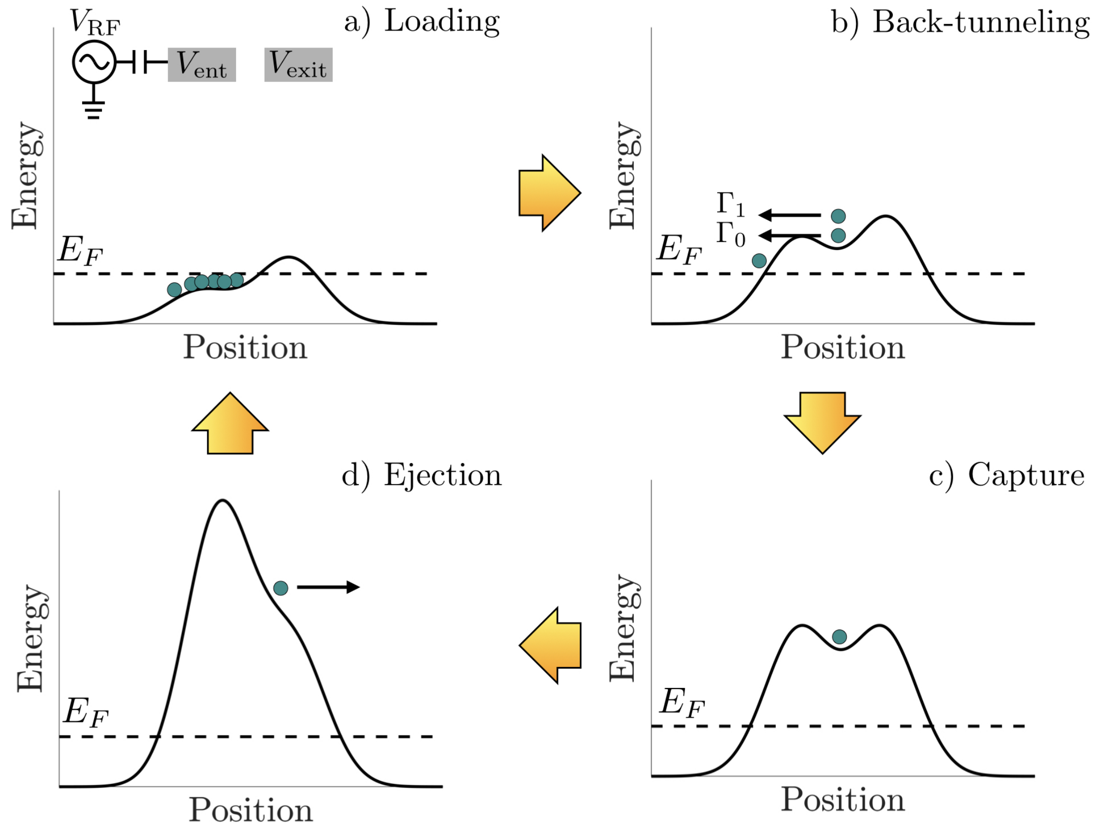

Figure 5.12: The four stages of a tunable-barrier pump operation. a) **Loading stage**. Schematic of the circuit and gate electrodes controlling the pump where an RF signal is applied to the entrance gate. During the loading stage, the entrance barrier is brought below the Fermi level E_F (dashed black line) and many electrons load into the dot. b) **Back-tunneling stage**. As the entrance gate is raised, electrons back-tunnel into the left electron reservoir. Higher energy electrons have faster back-tunneling rates $\Gamma_{i+1} > \Gamma_i$. c) **Capture stage**. After back-tunneling only a small integer number of electrons are captured in the quantum dot as the entrance barrier is raised. d) **Ejection stage**. When the entrance barrier is raised sufficiently high, the electron energy is increased beyond the exit barrier height, and the electron is ejected from the quantum dot. The entrance barrier is then lowered back to the loading stage.

can be shifted lower and higher to allow more or fewer electrons to be ejected each RF cycle. This allows the n in the $I = nef$ current to be directly tuned by V_{ent} and V_{exit}. We emphasize here that V_{ent} has both an RF and DC voltage component while V_{exit} has purely a DC voltage component. A typical model used to describe the back-tunneling dynamics during the non-adiabatic electron pumping is the universal decay cascade model [130]. The model provides a formula for fitting quantized current plateaus where

$$I/ef = \sum_{i=0}^{1} \exp[-\exp(-aV + \ln \Gamma_i)] \tag{5.19}$$

where V is a swept gate voltage (either V_{ent} or V_{exit} but is typically V_{exit}), Γ_i is the back-tunneling rates, and a is a fitting parameter [130]. The fitted ratio $\delta = \ln(\Gamma_1/\Gamma_0)$ is a useful figure of merit when discussing the quality of the SEP as δ is related to the predicted pumping accuracy [130, 81]. Of course, the real pumping accuracy is the more consequential value; however, measuring the accuracy requires lengthy experiments at a fixed pumping configuration in order to average out noise in the measurement setup. The highest accuracy SEPs are measured at cryogenic temperatures where the thermal energy is much less than the charging energy. SEPs in silicon have been shown to operate up to 17 K [279] while in GaAs temperature most pumps are operated at cryogenic temperatures limited to <300 mK [123, 81, 73]. By increasing the charging energy E_c of the quantum dot, SEPs can be operated at higher temperatures as long as $k_B T \ll E_c$.

5.4.1 Experimental results

Here we experimentally realize a SEP in a 90 nm deep single heterojunction. While many SEPs have been realized in intentionally doped GaAs heterostructures, to our knowledge, this is the first realization of a SEP in a dopant-free GaAs system. The device geometry is similar to that shown in Figure 5.11. The QPC gates are deposited directly onto the surface, followed by a 30 nm layer of SiO_2, and followed again by the entrance and exit tunneling gates. These fine metal gate layers were patterned using EBL. The dimensions of the QPC channel are 1000×400 nm and the inner edge-to-edge separation of the entrance and exit gates is 400 nm. This results in an effective quantum dot size of 400×400 nm according to the physical gate dimensions. Ohmic contacts were fabricated as described in Section 5.2.1, and a 300 nm layer of SiO_2 was deposited on top of the device and subsequently capped with a metal top gate. The top gate both induces the 2DEGs on either side of the device as well as helps shape the quantum dot potential. The source reservoir is grounded, and the drain reservoir is connected to a current pre-amplifier to

monitor the pumped current. All the V_{qpc}, V_{exit}, and V_g (top gate) voltages are supplied using a DC voltage source. The entrance gate is connected to a bias tee so that applied the entrance voltage $V_{\text{ent}} = V_{\text{AC}}\sin(2\pi f t) + V_{\text{DC}}$ has an AC component in addition to a DC offset. Throughout this section, we will refer to the DC component as simply V_{ent} and the RF component of this signal as V_{pp} corresponding to the peak-to-peak voltage amplitude of the signal.

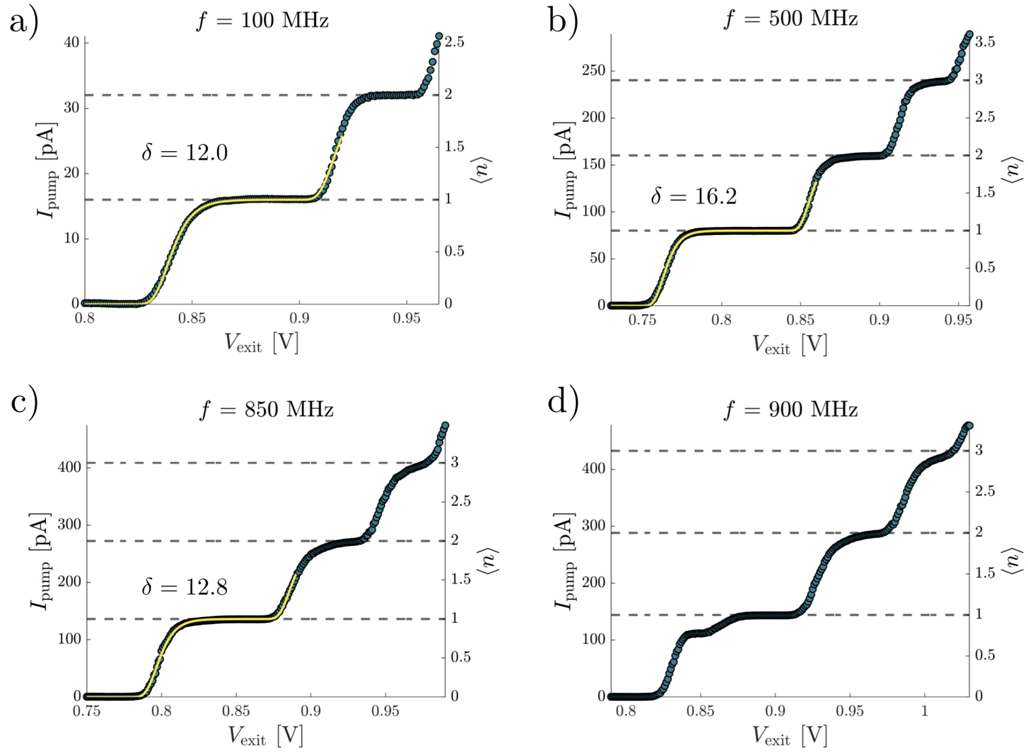

Figure 5.13: Single electron pumping at $T = 1.4$ K for different driving frequencies f. Fits of the first plateau to the electron cascade model (yellow) are done for panels a)-c). a) $f = 100$ MHz. Fitting gives $\delta = 12.0$. b) $f = 500$ MHz. Fitting gives $\delta = 16.2$. c) $f = 850$ MHz. Fitting gives $\delta = 12.8$. d) $f = 900$ MHz. The kink below the first plateau occurs when the electron is non-adiabatically excited to a higher orbital state during the back-tunneling stage. Exciting the electron increases its back-tunneling rate allowing it to escape which suppresses the current.

Figure 5.14 shows measurements of electron pumping at $T = 1.4$ K for driving frequen-

cies from 100 MHz up to 900 MHz. The $\hat{x}$ axis corresponds to the exit barrier gate voltage. On the left $\hat{y}$ axis the raw current is plotted and the right $\hat{y}$ axis converts the raw current to the average number of electrons pumped per RF cycle $\langle n \rangle$. Dashed lines are added for visual clarity to highlight where the current plateaus are expected to appear. For all data sets, $V_g = 6.0$ V and $V_{\text{qpc}} = 0.18$ V. For the 100, 500, 850, and 900 MHz data sets, $V_{\text{rf}} =$ 0.80 V, 0.87 V, 0.94 V, and 0.90 V, and $V_{pp} = 0.7$ V, 1.0 V, 1.6 V, and 1.75 V. At higher driving frequencies, transmission line losses are greater. To compensate for these losses, V_{pp} is increased with f in order to maintain the same effective peak-to-peak voltage at the actual device. In all figures, the current is quantized at expected integer values of $\langle n \rangle$. The highest quality plateaus occur at $\langle n \rangle = 1$ and reduce in quality as $\langle n \rangle$ increases where the back-tunneling ratios Γ_{i+1}/Γ_i are lower. In the 900 MHz data set, there is a kink in the current quantization just below the the first plateau. The kink arises because at high frequencies, the electron in the ground orbital state is non-adiabatically excited to a higher energy orbital state due to the fast modulation of the potential [132, 223]. When excited, the back-tunneling rate increases and the electron tunnels back into the source reservoir causing a decrease in the averaged pumped current. The magnitude of the current drop in the kink is directly proportional to the probability of inducing an excitation.

For all data sets, the first plateau (except for $f = 900$ MHz) is fit to Equation 5.19 to extract δ. The resulting fit and corresponding δ value is overlaid on the figure. Using the fit, we can estimate the expected error $\epsilon_{p,\text{est}}$ of the SEP which is found as $\epsilon_p = 1 - \langle n_{\text{fit}} \rangle$ at the inflection point of the fitted first plateau [130]. For $f = 100$, 500 and 850 MHz, $\epsilon_{p,\text{est}} =$ 74.8, 1.87, 41.5 ppm. While these are only estimated values, we expect the true pump error to be within an order of magnitude of $\epsilon_{p,\text{est}}$. Previous experiments even suggest that $\epsilon_{p,\text{est}}$ is actually an overestimation of the true pumping accuracy [82, 81].

Figure 5.14 shows a 2D map of single electron pumping at $f = 500$ MHz taken at $T =$ 1.4 K. Other device parameters are $V_{\text{qpc}} = 0.18$ V, $V_g = 6.0$ V, and $V_{pp} = 1.1$ V. The $\hat{x}$ and $\hat{y}$ axes corresponds to V_{exit} and V_{ent} respectively. The raw current data is plotted in Figure 5.14a, and $|dI/dV_{\text{exit}}|$ is plotted in Figure 5.14b to emphasize the current plateaus. The plateaus in Figure 5.14b are labelled according to the number of pumped electrons per RF cycle. The plateaus are very stable in voltage space: 0.1 V wide with respect to V_{exit} and > 0.35 V with respect to V_{ent}. The slant in the plateau boundary lines is attributed to RF coupling between the entrance and exit gates mediated through the QPC gate.

There are three things could be done to improve the accuracy of the measured SEP without any modifications to the current device design. The first is operating a lower cryogenic temperature. All the data taken here was done at $T = 1.4$ K. Going to a dilution fridge would enable tens of mK temperatures which would reduce thermal broadening effects on the pumping accuracy. The second improvement is to apply a large perpendicular

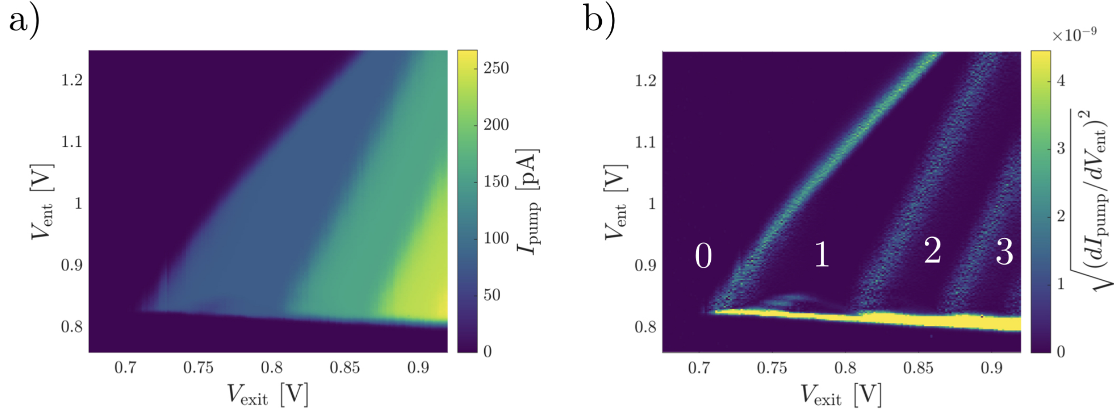

Figure 5.14: 2D pumping map of a single electron pump at $T = 1.4$ K. The driving frequency is $f = 500$ MHz. Other device parameters are $V_{\rm qpc} = 0.18$ V, $V_g = 6.0$ V, and $V_{pp} = 1.1$ V. a) Raw pumped current data showing three current plateaus. b) Plot of the derivative $|dI_{\rm pump}/dV_{\rm ent}|$. Current plateaus are labelled according to the number of electrons pumped per RF cycle. The pronounced slope of the transition line between plateaus is attributed to RF coupling between the entrance and exit gate voltages.

magnetic field during pumping. While the full underlying mechanism is not understood, large magnetic fields have been seen to enhance pump accuracy in GaAs SEPs [273, 124]. It is typically attributed to a increased sensitivity of the tunnel rate to the varying potential landscape as well as a suppression of non-adiabatic excitations of the last electron to higher energy states [69]. There does appear to be a limit in the benefits of a higher magnetic field as [161, 69] both show almost no improvement in pump accuracy above $B = 12 - 15$ T. The last improvement to improve pump accuracy is to use shaped RF pulses. So far during our experiments, we have used a regular sine wave for the RF signal. At higher frequencies, non-adiabatic excitations can cause electrons to tunnel out of the dot during the back-tunneling stage which increases the pumping error [132]. An arbitrary waveform generator can be used to shape the RF pulse so that a larger portion of the clock cycle is spent in the back-tunneling and capture stages while less time is spent during the ejection stage [77, 81]. The overall clock cycle of the pulse still remains f, so the overall pumped current has the same magnitude $I = nef$. Such shaped pulses have shown significant improvements of the pumping accuracy by orders of magnitude [81]. Even without these improvements, the data shown in Figure 5.13 for $f = 500$ MHz suggested an estimated pump error rate $\epsilon_{p,\rm est} = 1.87$ ppm which would be comparable to the state of the art pumps

in GaAs operating at similar frequencies. In Giblin *et al.* [81], a pump error of $\epsilon_p = 1.2$ ppm was achieved at $f = 1$ GHz using all three of the above mentioned improvement. Another experiment in Stein *et al.* [243] demonstrated a pump error of $\epsilon_p = 0.2$ ppm at $f = 545$ MHz using all of the above improvements as well.

In addition to these three improvements, higher pump accuracy can, in principle, be obtained by better tuning of the gate voltages used to control the SEP. One advantage of dopant-free SEPs over their modulation doped equivalents is the ability to strongly gate the device. Both the QPC gates and top gate can be used in conjunction with the entrance and exit barrier gates to better control the shape of the SEP's potential landscape. Such tunability has proven to be very effective in improving pumping accuracy in silicon SEPs by shaping the potential to increase the QD charging energy [234]. However, tunability comes at the cost of increasing the dimension of the control parameter space, making it more difficult to find the most optimal tuning regime where the SEP accuracy is highest. In general, we find for our devices that pump accuracy improves when V_g is largest and V_{qpc} is smallest. The former condition pulls the quantum dot potential lower which increases the charging energy of the quantum dot (analogous to the QPC subband spacing results from Section 5.3). The latter condition serves to constrict the 1D channel which again raises the charging energy of the quantum dot. Increasing the charging energy will increase the ratio of the back-tunneling rates δ.

We conclude our discussion of SEPs by demonstrating single electron pumping at higher temperatures. SEPs in silicon have demonstrated the highest pumping temperatures up to even 36 K using donor-based QDs [159]. High temperatures in GaAs are more difficult due to the fact that the 2DEG is induced deeper in the substrate where the gates are more weakly coupled to the potential landscape and the doping layer screens the gate electrodes. The device measured is one similar to that in Figure 5.11 with the exception that the entrance and exit gates are shorter in order to reduce RF coupling between the gates. Additionally, this device was fabricated on a 75 nm deep single heterojunction. The device temperature was varied from 1.4 K to 5 K. The device parameters are $V_{\text{qpc}} = 0.15$ V, $V_{\text{ent}} = 1.0$ V, and $V_g = 5.0$ V, and $V_{pp} = 1.2$ V. The RF pumping frequency is $f =$ 150 MHz. The ohmics on this device were very high in resistance (>100 kΩ) and low quality which introduced much more noise into the current data. Traces of I versus V_{exit} are shown for five different temperatures. At lower temperatures, the current plateaus are well defined, and for $T = 1.4$ K, the first plateau has a fitted $\delta = 11.4$ ($\epsilon_{p,\text{est}} = 42.5$ ppm). Even all the way up to $T = 5$ K, the first plateau is still noticeable and gives a fitted $\delta =$ 5.9 ($\epsilon_{p,\text{est}} = 20100$ ppm). Above these temperatures, the first plateau is too smeared to resolve any pumping. While pumping at 5 K is evident, the pump accuracy is obviously lacking; however this could be increased using the techniques discussed in the previous two

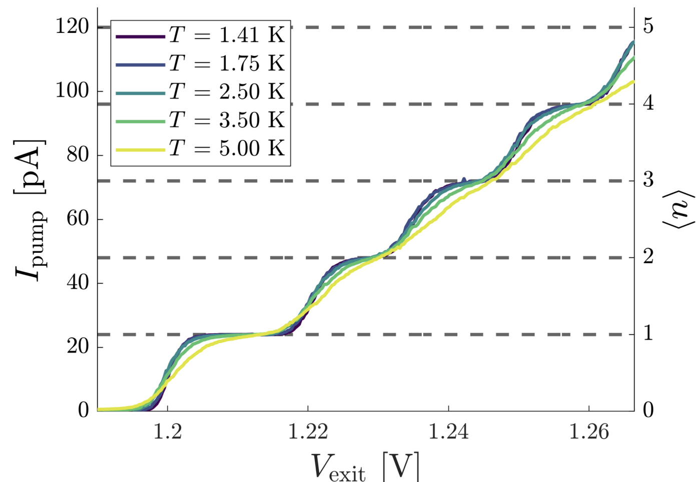

Figure 5.15: Electron pumping dependence on temperature. This device is a slightly modified device structure of the one shown in Figure 5.11 (see main text for details). The device parameters are $V_{\text{qpc}} = 0.15$ V, $V_{\text{ent}} = 1.0$ V, and $V_g = 5.0$ V, $V_{pp} = 1.2$ V, and $f = 150$ MHz. At $T = 1.4$ K (purple) the plateaus are best defined. As the temperature increases up to $T = 5.0$ K (yellow) the plateaus are thermally broadened and the current is less quantized. The current curves are noticeable noise because the ohmics of this device were low quality with high contact resistance.

paragraphs.

5.5 Conclusions

In this chapter, we explored electron transport in dopant-free GaAs. We first introduced dopant-free GaAs heterostructures and explained their utility for studying mesoscopic physics. Next, we showed why device are difficult to fabricate with these heterostructures due to complications in making ohmic contacts to an induced 2DEG. Hall bar devices on a 310 nm deep heterostructure are fabricated using both n- and p-type ohmic recipes and are measured to study the ohmic contact quality as well as study the induced 2DEG and 2DHG quality. For both the n- and p-type Hall bar, the ohmics have a low contact resistance and do not leak to the top gate. The lack of any intention dopants in the material enables high electron and hole mobilities to be realized up to 7.5 million $\text{cm}^2/\text{V}{\cdot}\text{s}$ and 0.64

million $cm^2/V{\cdot}s$. Shubnikov-de Haas oscillations and quantum hall measurements suggest that show that only a single 2DEG layer is contacted in the n-type Hall bar. Lack of oscillations in the p-type Hall bar suggest that the measurement temperature is too high to resolve oscillations. Next we moved to a 1D system and studied quantized conductance through a shallow etched QPC. The first 6 conductance plateaus are seen at at $T = 1.4$ K. Subband spectroscopy measurements show that the device's subband spacing can be tuned by the top gate voltage V_g and reaches value of 4.5 meV when $V_g = 9.0$ V. We conclude the dopant-free experiments by studying a single electron pump, a device capable of producing quantized current in steps of $I = nef$ where n is the number of pumped electrons per RF cycle and f is the driving frequency. Measurements show current plateaus indicating single electron pumping at $T = 1.4$ K with driving frequencies of $f = 100$ MHz up to 900 MHz. Fits to the electron cascade model indicate that the device tuning at $f = 500$ MHz yields the highest single electron pumping accuracy with an estimated pump error rate of 1.87 ppm which is comparable to current state of the art electron pumps in GaAs. The tunability of the single electron pump allows to realize large quantum dot charging energies so that single electron pumping is visible up to $T = 5$ K. By lowering the pumping temperature, applying a perpendicular magnetic field, and shaping the RF pulse, the accuracy of these devices can be significantly improved.

Chapter 6

Conclusions

Single spins in silicon quantum dots are a promising candidate for building a scalable quantum processor due to their compact size, high coherence times, and ease of integration into existing microchip fabrication technology. Chapter 1 introduces these devices by first discussing electron transport, showing how electrons can be loaded onto and off of the dot by appropriate electrostatic tuning. The chapter continues with an introduction of using single spins in quantum dots as qubits by discussing qubit initialization, single spin rotations, two spin rotations, and spin measurement.

Chapter 2 of this thesis proposes a scalable network architecture for single spin quantum dot qubits in silicon. Local nodes of quantum dots are spatially separated on the order of microns to create ample space for the high density of physical wiring needed to control each quantum dot. Nodes are connected by electron shuttling lines in order to facilitate entanglement distribution between nodes in the network. Each node consists of just seven quantum dots used to host a data qubit, two ancilla qubits, two measurement qubits, and a shuttled qubit. The network architecture is mapped to a surface code, and an explicit circuit for realizing stabilizer operations amongst four local nodes is presented in terms of fundamental quantum dot gate operations. A key element of the stabilizer circuit, shuttling of one electron from an entangled singlet state from one node to a neighboring node, is simulated. Electron shuttling is achieved by sequential tunneling of an electron through a quantum dot chain. We find that an electron can be shuttled adiabatically across a micron in tens of nanoseconds, meaning shuttling is not a bottleneck to the overall processor speed. The small but non-zero spin orbit coupling in silicon causes a Stark shift of the electron's g-factor during shuttling which induces a Z rotation of the shuttled spin state. However, proper electrostatic tuning of the second electron's g-factor can completely suppress this rotation enabling high fidelity shuttling. Error models for the fundamental gate operations

of the stabilizer circuit are proposed and used to estimate the error thresholds for the network architecture. Dephasing errors due to electron shuttling are found to have the highest error thresholds. The strictest error thresholds are for entangling $\sqrt{\text{SWAP}}$ errors, which are almost an order of magnitude less than single qubit errors.

Chapter 3 expands on the electron shuttling simulations of Chapter 2. Electrons are shuttled by sequential tunneling through a linear chain of quantum dots where each quantum dot is formed using a simplified gate geometry. An algorithm for finding constant-adiabatic shuttling pulses is introduced, which allows for a systematic comparison of shuttling speeds and fidelities as the system Hamiltonian parameters are varied. Self-consistent 3D Poisson calculations are done to approximate how the electrostatic potential of the quantum dot device varies as a function of applied gate voltage. These potentials are used to simulate charge shuttling through a triple quantum dot chain. We show that both the shuttling speed and fidelity are directly proportional to the adiabatic parameter ξ maintained throughout the shuttling pulse. These constant-adiabatic shuttling pulses are then used to optimize the quantum dot geometry in order to maximize the shuttling speed. We find that speeds of $\sim$300 nm/ns are achievable using realistic fabrication constraints for the device geometry. We switch to an effective Hamiltonian representation where valley and spin degrees of freedom can be included into the shuttling simulations. One electron from an entangled singlet pair is shuttled from one dot to another. High fidelity spin shuttling can be achieved when the Zeeman splitting is less than the interdot tunnel coupling strength. In order to achieve high fidelity shuttling, the valley phase difference between neighboring quantum dots must be below some threshold value, determined by the ratio of the tunneling and Zeeman energies. In the high fidelity parameter space, the shuttling infidelity is due to a coherent rotation of the shuttled spin, caused by the effective magnetic field axis induced by the spin-orbit Hamiltonian terms. The coherent rotation is correctable, in principle, by single spin rotations applied after shuttling.

Chapter 4 lays the groundwork towards simulating another part of the network architecture presented in Chapter 2, two-spin quantum gates implemented using the exchange interaction. We present a modified LCHO-CI approach for calculating the many-electron energy spectra of a general quantum dot network. Single electron orbitals are approximated using an orthogonal basis of harmonic orbitals centered at the origin of the network. Using an orthogonal harmonic orbital basis allows for numerically quick evaluation of the Coulomb interactions, which are required for the LCHO-CI calculation. The accuracy of the modified LCHO-CI calculation can be improved by optimizing the confinement energy $\hbar\omega$ of the harmonic orbital basis. We present a method for optimizing ω without significantly impacting the total LCHO-CI computation time. The modified LCHO-CI method is used to study charge noise sensitivty of a silicon double quantum dot device. The full

device structure is simulated using a self-consistent Poisson calculation to study how the physical device parameters, such as plunger gate size, tunneling barrier size, and SiO_2 thickness, impact the charge noise sensitivity. By modelling the system using an effective Hubbard Hamiltonian, we find that geometries which increase the dot charging energy and decrease the gate lever arm will reduce the device's sensitivity to charge noise. For the device geometry studied, this means that smaller plunger gates, wider tunneling gates, and thicker SiO_2 will produce less sensitive devices.

Chapter 5 departs from the previous chapters which focused on applied theoretical studies of silicon double quantum dot devices. In Chapter 5, we experimentally study electron transport through devices fabricated in dopant-free GaAs heterostructures. One of the most difficult parts of realizing these devices is fabricating high quality ohmic contacts. By depositing the ohmic material in an etched recess pit, the ohmic material can diffuse laterally through the material and not screen the top gate used to the induce a 2DEG. Magnetotransport experiments, done using a Hall bar fabricated on a 310 nm deep single heterojunction, show that we can realize both n- and p-type ohmic contacts. Carrier mobilities and densities can be tuned using the top gate, and we measure mobilities up to 7.5 million $cm^2/V{\cdot}s$ for electrons and 0.64 million $cm^2/V{\cdot}s$ for holes. Next, we move to a 1D transport system and study an 20 nm etched QPC in a 90 nm deep single heterojunction. A 1D subband spacing of 4.5 meV is measured, enabling clear conductance quantization at $T = 1.4$ K. Lastly, we move to a 0D system and study a dynamically driven quantum dot acting as a single electron pump. The device is fabricated on a 90 nm deep single heterojunction. Current quantization is observed at 1.4 K and fits to an electron cascade model suggest single electron pumping errors on the order of 1.87 ppm at a driving frequency $f = 500$ MHz. The ability for us to finely tune the single electron pump using the top gate and QPC gates, allows the quantum dot to have a high charging energy enabling quantized pumping up to $T = 5$ K.

6.1 Outlook and future work

Much of this thesis focuses on work towards simulating a node or even a small group of nodes in the network architecture proposed in Chapter 2. One of the key next steps is to experimentally realize the basic building blocks of the network architecture: a 7 dot node and electron shuttling over ~ 1 um. Silicon quantum dot devices consisting of six [214] and up to twelve [289] quantum dots have been demonstrated implying that realizing a single node is within current experimental reach. Single qubit gate and two qubit gate fidelities of >0.999 [280] and 0.98 [116] respectively have been achieved experimentally, moving silicon

quantum dot devices closer towards fault tolerance thresholds required for operating the network architecture.

Both charge shuttling [181] and spin shuttling [285] have been demonstrated experimentally in quantum dot devices; however, the spin shuttling experiment only shuttled an electron repeatedly between two quantum dots. The spin-orbit coupling causes a fixed spin rotation during shuttling from one dot to the next. Shuttling in the other direction would induce the same rotation but in the opposite direction. Repeatedly shuttling a spin between two dots would cancel the effective rotation and does not show the impact that spin-orbit coupling has on shuttling through a long quantum dot chain. Therefore, it remains to be seen how important the spin-orbit coupling is experimentally in longer chains of dots. Additionally, all the demonstrations of shuttling use a standard, yet complicated, gate geometry to define the quantum dots. In Chapter 3, we showed that shuttling can be realized with a simplified gate geometry that does not use any tunnel barrier gates. Work has been done towards realizing quantum dots defined using the simplified gate geometry [217], yet experimentally demonstrating electron shuttling in such a device remains to be seen. A simplified gate geometry is critical to reduce the total control line density in the network architecture.

The modified LCHO-CI method presented in Chapter 4 offers a numerically efficient method for quantitatively accurate calculations of J in general quantum dot networks. A key take away of the modified LCHO-CI method is the ability to map out the individual exchange interaction pairs J_{ij} as a function of the applied gate voltage $\vec{V}$, creating a J_{ij} look-up library. Interpolation can be used to find J_{ij} values at arbitrary gate voltage configurations which would enable both real time exchange simulations of a device in terms of $\vec{V}$ as well as the study of optimal control techniques for improved robustness to charge noise. In real quantum dot devices, even when fabricated using the same physical gate pattern, local disorder of the either the physical metal gate or material system causes small amounts of disorder in the electrostatic potential. An interesting question is if optimal control pulses can be designed to be robust to this potential disorder. For the device simulations of charge noise sensitivity done in the latter half of Chapter 4, a very simple device geometry was assumed. Different geometries such as asymmetric [108], triple, or quadruple quantum dots would be interesting to explore using the techniques adopted in the chapter. We only considered the impact of charge noise on a single spin qubit, but it would interesting to explore charge noise sensitivity of these devices for other qubit encodings, such as exchange-only qubits [58, 221].

The experiments done in Chapter 5 lay the groundwork for numerous future experimental studies of dopant-free GaAs devices. The ability to realize both a 2DEG and 2DHG in dopant-free GaAs directly leads into realizing lateral PN junctions with these heterostruc-

tures. We have actually already realized such devices experimentally in conjunction with the QPD group at the University of Waterloo [237], although we did not discuss these experiments in this thesis. Integrating the single electron pump (SEP) device presented in this thesis with a lateral PN junction would create an all-electrical, on-demand, single photon source as proposed in [237]. A more exotic possibility of an on-demand photon source involves using a leviton electron source. When a Lorentzian shaped pulse is applied directly to an ohmic contact, it is possible to generate a single electron soliton (leviton) whose wave function does not spread out as it propagates [134, 60]. The leviton source can replace the role of the SEP in the lateral PN junction to inject few (or one) electrons on-demand into a p-type region. Such a device, if it works, would have the advantage of simpler and more robust operation compared to the complex gate layout and parameter space of the traditional SEP. With a 20 nm etched QPC device we were able to realize a subband spacing of 4.5 meV which roughly suggests that quantized conductance could be observed near $T \approx 4.5$ meV$/10\, k_B \approx 5$ K. Pushing the operating temperature further towards the current GaAs record of $T = 30$ K [153] requires a larger subband spacing. This could be achieved by etching a deeper QPC, bringing the 2DEG closer to the surface with a shallower heterojunction, and reducing the separation between QPC gates. There are fabrication considerations for each of those three improvements; however, higher QPC operating temperatures are certainly possible. Raising the QPC operating temperature will also raise the operating temperature of the SEP above $1.4 - 4$ K as the QPC dimensions are utilized in the SEP gate layout. Before such experiments are done, we need to first perform measurements of the true pumping error in our devices and compare with the theoretical estimates from the electron cascade model. Another promising research avenue lies in realizing single hole pumping in GaAs using a tunable-barrier device. Single hole pumps require smaller gate dimensions and colder operating temperatures, due to the hole's higher effective mass compared to the electron in GaAs. The tunability of our pump design, as well as our ability to realize p-type ohmics, mean that hole pumping may be possible. Single hole pumping using a tunable-barrier pump has been demonstrated in silicon [278] but not yet in GaAs.

References

[1] Scott Aaronson and Daniel Gottesman. Improved simulation of stabilizer circuits. *Physical Review A*, 70(5):052328, 2004.

[2] Tsuneya Ando, Alan B Fowler, and Frank Stern. Electronic properties of two-dimensional systems. *Reviews of Modern Physics*, 54(2):437, 1982.

[3] Frank Arute, Kunal Arya, Ryan Babbush, Dave Bacon, Joseph C Bardin, Rami Barends, Rupak Biswas, Sergio Boixo, Fernando GSL Brandao, David A Buell, et al. Quantum supremacy using a programmable superconducting processor. *Nature*, 574(7779):505–510, 2019.

[4] NW Ashcroft and ND Mermin. *Solid State Physics*. Thomson Learning, Toronto, 1976.

[5] Stephan Baer and Klaus Ensslin. *Transport spectroscopy of confined fractional quantum hall systems*, volume 183. Springer, 2015.

[6] Philip F Bagwell and Terry P Orlando. Landauer's conductance formula and its generalization to finite voltages. *Physical Review B*, 40(3):1456, 1989.

[7] Edwin Barnes, JP Kestner, NTT Nguyen, and S Das Sarma. Screening of charged impurities with multielectron singlet-triplet spin qubits in quantum dots. *Physical Review B*, 84(23):235309, 2011.

[8] Carlo WJ Beenakker. Theory of coulomb-blockade oscillations in the conductance of a quantum dot. *Physical Review B*, 44(4):1646, 1991.

[9] Charles H Bennett, David P DiVincenzo, John A Smolin, and William K Wootters. Mixed-state entanglement and quantum error correction. *Physical Review A*, 54(5):3824, 1996.

[10] Benoit Bertrand, Sylvain Hermelin, Pierre-André Mortemousque, Shintaro Takada, Michihisa Yamamoto, Seigo Tarucha, Arne Ludwig, Andreas D Wieck, Christopher Bäuerle, and Tristan Meunier. Injection of a single electron from static to moving quantum dots. *Nanotechnology*, 27(21):214001, 2016.

[11] Stefan Birner, Tobias Zibold, Till Andlauer, Tillmann Kubis, Matthias Sabathil, Alex Trellakis, and Peter Vogl. Nextnano: general purpose 3-d simulations. *IEEE Transactions on Electron Devices*, 54(9):2137–2142, 2007.

[12] Mark David Blumenthal, B Kaestner, L Li, S Giblin, TJBM Janssen, M Pepper, D Anderson, G Jones, and DA Ritchie. Gigahertz quantized charge pumping. *Nature Physics*, 3(5):343–347, 2007.

[13] F Borjans, DM Zajac, TM Hazard, and JR Petta. Single-spin relaxation in a synthetic spin-orbit field. *Physical Review Applied*, 11(4):044063, 2019.

[14] Matthew G Borselli, Kevin Eng, Richard S Ross, Thomas M Hazard, Kevin S Holabird, Biqin Huang, Andrey A Kiselev, Peter W Deelman, Leslie D Warren, Ivan Milosavljevic, et al. Undoped accumulation-mode si/sige quantum dots. *Nanotechnology*, 26(37):375202, 2015.

[15] Matthew G Borselli, Richard S Ross, Andrey A Kiselev, Edward T Croke, Kevin S Holabird, Peter W Deelman, Leslie D Warren, Ivan Alvarado-Rodriguez, Ivan Milosavljevic, Fiona C Ku, et al. Measurement of valley splitting in high-symmetry si/sige quantum dots. *Applied Physics Letters*, 98(12):123118, 2011.

[16] Jelmer M Boter, Juan P Dehollain, Jeroen PG van Dijk, Toivo Hensgens, Richard Versluis, James S Clarke, Menno Veldhorst, Fabio Sebastiano, and Lieven MK Vandersypen. A sparse spin qubit array with integrated control electronics. In *2019 IEEE International Electron Devices Meeting (IEDM)*, pages 31–4. IEEE, 2019.

[17] Kenneth R Brown, Jungsang Kim, and Christopher Monroe. Co-designing a scalable quantum computer with trapped atomic ions. *npj Quantum Information*, 2(1):1–10, 2016.

[18] Brandon Buonacorsi, Zhenyu Cai, Eduardo Barrera Ramirez, Kyle S Willick, Sean M Walker, Jiahao Li, Benjamin D Shaw, Xiaosi Xu, Simon C Benjamin, and Jonathan Baugh. Network architecture for a topological quantum computer in silicon. *Quantum Science and Technology*, 2018.

[19] Brandon Buonacorsi, Marek Korkusinski, Bohdan Khromets, and Jonathan Baugh. Optimizing lateral quantum dot geometries for reduced exchange noise. *arXiv preprint arXiv:2012.10512*, 2020.

[20] Brandon Buonacorsi, Benjamin Shaw, and Jonathan Baugh. Simulated coherent electron shuttling in silicon quantum dots. *Physical Review B*, 102(12):125406, 2020.

[21] Guido Burkard, Daniel Loss, and David P DiVincenzo. Coupled quantum dots as quantum gates. *Physical Review B*, 59(3):2070, 1999.

[22] Donovan Buterakos, Robert E Throckmorton, and S Das Sarma. Crosstalk error correction through dynamical decoupling of single-qubit gates in capacitively coupled singlet-triplet semiconductor spin qubits. *Physical Review B*, 97(4):045431, 2018.

[23] M Büttiker. Quantized transmission of a saddle-point constriction. *Physical Review B*, 41(11):7906, 1990.

[24] Markus Büttiker. Absence of backscattering in the quantum hall effect in multiprobe conductors. *Physical Review B*, 38(14):9375, 1988.

[25] S Büyükköse, B Vratzov, Jelle van der Veen, PV Santos, and Wilfred Gerard van der Wiel. Ultrahigh-frequency surface acoustic wave generation for acoustic charge transport in silicon. *Applied physics letters*, 102(1):013112, 2013.

[26] Yu A Bychkov and Emmanuel I Rashba. Oscillatory effects and the magnetic susceptibility of carriers in inversion layers. *Journal of physics C: Solid state physics*, 17(33):6039, 1984.

[27] Zhenyu Cai and Simon C Benjamin. Constructing smaller pauli twirling sets for arbitrary error channels. *Scientific reports*, 9(1):1–11, 2019.

[28] MJ Calderón, Belita Koiller, and S Das Sarma. Exchange coupling in semiconductor nanostructures: Validity and limitations of the Heitler-London approach. *Physical Review B*, 74(4):045310, 2006.

[29] FA Calderon-Vargas, George S Barron, Xiu-Hao Deng, AJ Sigillito, Edwin Barnes, and Sophia E Economou. Fast high-fidelity entangling gates for spin qubits in si double quantum dots. *Physical Review B*, 100(3):035304, 2019.

[30] Pascal Cerfontaine, Tim Botzem, Julian Ritzmann, Simon Sebastian Humpohl, Arne Ludwig, Dieter Schuh, Dominique Bougeard, Andreas D Wieck, and Hendrik Bluhm.

Closed-loop control of a GaAs-based singlet-triplet spin qubit with 99.5% gate fidelity and low leakage. *arXiv preprint arXiv:1906.06169*, 2019.

[31] Pascal Cerfontaine, Tim Botzem, Julian Ritzmann, Simon Sebastian Humpohl, Arne Ludwig, Dieter Schuh, Dominique Bougeard, Andreas D Wieck, and Hendrik Bluhm. Closed-loop control of a gaas-based singlet-triplet spin qubit with 99.5% gate fidelity and low leakage. *Nature communications*, 11(1):1–6, 2020.

[32] Christopher Chamberland, Pavithran Iyer, and David Poulin. Fault-tolerant quantum computing in the pauli or clifford frame with slow error diagnostics. *Quantum*, 2:43, 2018.

[33] KW Chan, M Möttönen, Antti Kemppinen, NS Lai, KY Tan, WH Lim, and AS Dzurak. Single-electron shuttle based on a silicon quantum dot. *Applied Physics Letters*, 98(21):212103, 2011.

[34] JCH Chen, O Klochan, AP Micolich, K Das Gupta, F Sfigakis, DA Ritchie, K Trunov, D Reuter, AD Wieck, and AR Hamilton. Fabrication and characterisation of gallium arsenide ambipolar quantum point contacts. *Applied Physics Letters*, 106(18):183504, 2015.

[35] JCH Chen, DQ Wang, O Klochan, AP Micolich, K Das Gupta, F Sfigakis, DA Ritchie, D Reuter, AD Wieck, and AR Hamilton. Fabrication and characterization of ambipolar devices on an undoped algaas/gaas heterostructure. *Applied Physics Letters*, 100(5):052101, 2012.

[36] Yong P Chen, G Sambandamurthy, ZH Wang, RM Lewis, LW Engel, DC Tsui, PD Ye, LN Pfeiffer, and KW West. Melting of a 2d quantum electron solid in high magnetic field. *Nature Physics*, 2(7):452–455, 2006.

[37] Lilian Childress and Ronald Hanson. Diamond nv centers for quantum computing and quantum networks. *MRS bulletin*, 38(2):134–138, 2013.

[38] M Ciorga, AS Sachrajda, Pawel Hawrylak, C Gould, Piotr Zawadzki, S Jullian, Y Feng, and Zbigniew Wasilewski. Addition spectrum of a lateral dot from coulomb and spin-blockade spectroscopy. *Physical Review B*, 61(24):R16315, 2000.

[39] JI Cirac, AK Ekert, SF Huelga, and Chiara Macchiavello. Distributed quantum computation over noisy channels. *Physical Review A*, 59(6):4249, 1999.

[40] John Clarke and Frank K Wilhelm. Superconducting quantum bits. *Nature*, 453(7198):1031–1042, 2008.

[41] WR Clarke, AP Micolich, AR Hamilton, MY Simmons, K Muraki, and Y Hirayama. Fabrication of induced two-dimensional hole systems on (311) a gaas. *Journal of applied physics*, 99(2):023707, 2006.

[42] Daniel Comparat. General conditions for quantum adiabatic evolution. *Physical Review A*, 80(1):012106, 2009.

[43] JNL Connor. On the analytical description of resonance tunnelling reactions. *Molecular Physics*, 15(1):37–46, 1968.

[44] Andrea Corna, Léo Bourdet, Romain Maurand, Alessandro Crippa, Dharmraj Kotekar-Patil, Heorhii Bohuslavskyi, Romain Laviéville, Louis Hutin, Sylvain Barraud, Xavier Jehl, et al. Electrically driven electron spin resonance mediated by spin–valley–orbit coupling in a silicon quantum dot. *npj quantum information*, 4(1):1–7, 2018.

[45] David G Cory, Amr F Fahmy, and Timothy F Havel. Ensemble quantum computing by nmr spectroscopy. *Proceedings of the National Academy of Sciences*, 94(5):1634–1639, 1997.

[46] Alessandro Crippa, Romain Maurand, Dharmraj Kotekar-Patil, Andrea Corna, Heorhii Bohuslavskyi, Alexei O Orlov, Patrick Fay, Romain Laviéville, Sylvain Barraud, Maud Vinet, et al. Level spectrum and charge relaxation in a silicon double quantum dot probed by dual-gate reflectometry. *Nano letters*, 17(2):1001–1006, 2017.

[47] SM Cronenwett, HJ Lynch, D Goldhaber-Gordon, LP Kouwenhoven, CM Marcus, K Hirose, NS Wingreen, and V Umansky. Low-temperature fate of the 0.7 structure in a point contact: A kondo-like correlated state in an open system. *Physical review letters*, 88(22):226805, 2002.

[48] AF Croxall, B Zheng, F Sfigakis, K Das Gupta, I Farrer, CA Nicoll, HE Beere, and DA Ritchie. Demonstration and characterization of an ambipolar high mobility transistor in an undoped gaas/algaas quantum well. *Applied Physics Letters*, 102(8):082105, 2013.

[49] Dimitrie Culcer, Łukasz Cywiński, Qiuzi Li, Xuedong Hu, and S Das Sarma. Quantum dot spin qubits in silicon: Multivalley physics. *Physical Review B*, 82(15):155312, 2010.

[50] Dimitrie Culcer, Xuedong Hu, and S Das Sarma. Dephasing of si spin qubits due to charge noise. *Applied Physics Letters*, 95(7):073102, 2009.

[51] Dimitrie Culcer, Xuedong Hu, and S Das Sarma. Interface roughness, valley-orbit coupling, and valley manipulation in quantum dots. *Physical Review B*, 82(20):205315, 2010.

[52] Christian L Degen, F Reinhard, and Paola Cappellaro. Quantum sensing. *Reviews of modern physics*, 89(3):035002, 2017.

[53] F Delgado, Y-P Shim, Marek Korkusinski, and Pawel Hawrylak. Theory of spin, electronic, and transport properties of the lateral triple quantum dot molecule in a magnetic field. *Physical Review B*, 76(11):115332, 2007.

[54] Kuangyin Deng and Edwin Barnes. Interplay of exchange and superexchange in triple quantum dots. *arXiv preprint arXiv:2003.03416*, 2020.

[55] Kuangyin Deng, FA Calderon-Vargas, Nicholas J Mayhall, and Edwin Barnes. Negative exchange interactions in coupled few-electron quantum dots. *Physical Review B*, 97(24):245301, 2018.

[56] OE Dial, Michael Dean Shulman, Shannon Pasca Harvey, H Bluhm, V Umansky, and Amir Yacoby. Charge noise spectroscopy using coherent exchange oscillations in a singlet-triplet qubit. *Physical review letters*, 110(14):146804, 2013.

[57] Claude M Dion, Avazeh Hashemloo, and Ghosne Rahali. Program for quantum wave-packet dynamics with time-dependent potentials. *Computer Physics Communications*, 185(1):407–414, 2014.

[58] David P DiVincenzo, Dave Bacon, Julia Kempe, Guido Burkard, and K Birgitta Whaley. Universal quantum computation with the exchange interaction. *nature*, 408(6810):339–342, 2000.

[59] Gene Dresselhaus. Spin-orbit coupling effects in zinc blende structures. *Physical Review*, 100(2):580, 1955.

[60] J Dubois, T Jullien, F Portier, P Roche, A Cavanna, Y Jin, W Wegscheider, P Roulleau, and DC Glattli. Minimal-excitation states for electron quantum optics using levitons. *Nature*, 502(7473):659–663, 2013.

[61] Wolfgang Dür, Marc Hein, J Ignacio Cirac, and H-J Briegel. Standard forms of noisy quantum operations via depolarization. *Physical Review A*, 72(5):052326, 2005.

[62] W Dybalski and P Hawrylak. Two electrons in a strongly coupled double quantum dot: From an artificial helium atom to a hydrogen molecule. *Physical Review B*, 72(20):205432, 2005.

[63] JM Elzerman, R Hanson, LH Willems Van Beveren, B Witkamp, LMK Vandersypen, and Leo P Kouwenhoven. Single-shot read-out of an individual electron spin in a quantum dot. *nature*, 430(6998):431–435, 2004.

[64] Kevin Eng, Thaddeus D Ladd, Aaron Smith, Matthew G Borselli, Andrey A Kiselev, Bryan H Fong, Kevin S Holabird, Thomas M Hazard, Biqin Huang, Peter W Deelman, et al. Isotopically enhanced triple-quantum-dot qubit. *Science Advances*, 1(4):e1500214, 2015.

[65] Rifat Ferdous, Kok W Chan, Menno Veldhorst, JCC Hwang, CH Yang, Harshad Sahasrabudhe, Gerhard Klimeck, Andrea Morello, Andrew S Dzurak, and Rajib Rahman. Interface-induced spin-orbit interaction in silicon quantum dots and prospects for scalability. *Physical Review B*, 97(24):241401, 2018.

[66] Rifat Ferdous, Erika Kawakami, Pasquale Scarlino, Michał P Nowak, DR Ward, DE Savage, MG Lagally, SN Coppersmith, Mark Friesen, Mark A Eriksson, et al. Valley dependent anisotropic spin splitting in silicon quantum dots. *npj Quantum Information*, 4(1):26, 2018.

[67] Richard P Feynman. Simulating physics with computers. *Int. J. Theor. Phys*, 21(6/7), 1982.

[68] H Flentje, P-A Mortemousque, R Thalineau, A Ludwig, AD Wieck, C Bäuerle, and T Meunier. Coherent long-distance displacement of individual electron spins. *Nature communications*, 8(1):501, 2017.

[69] JD Fletcher, M Kataoka, SP Giblin, Sunghun Park, H-S Sim, P See, DA Ritchie, JP Griffiths, GAC Jones, HE Beere, et al. Stabilization of single-electron pumps by high magnetic fields. *Physical Review B*, 86(15):155311, 2012.

[70] Roger Fletcher. *Practical methods of optimization*. John Wiley & Sons, 2013.

[71] Clare L Foden, VI Talyanskii, Gerard J Milburn, ML Leadbeater, and M Pepper. High-frequency acousto-electric single-photon source. *Physical Review A*, 62(1):011803, 2000.

[72] Austin G Fowler, Matteo Mariantoni, John M Martinis, and Andrew N Cleland. Surface codes: Towards practical large-scale quantum computation. *Physical Review A*, 86(3):032324, 2012.

[73] Lukas Fricke, Michael Wulf, Bernd Kaestner, Vyacheslavs Kashcheyevs, Janis Timoshenko, Pavel Nazarov, Frank Hohls, Philipp Mirovsky, Brigitte Mackrodt, Ralf Dolata, et al. Counting statistics for electron capture in a dynamic quantum dot. *Physical review letters*, 110(12):126803, 2013.

[74] Benedikt Frieß. *Spin and Charge Ordering in the Quantum Hall Regime*. Springer, 2016.

[75] Keisuke Fujii. *Quantum computation with topological codes: from qubit to topological fault-tolerance*, volume 8. Springer, 2015.

[76] Takafumi Fujita, Timothy Alexander Baart, Christian Reichl, Werner Wegscheider, and Lieven Mark Koenraad Vandersypen. Coherent shuttle of electron-spin states. *npj Quantum Information*, 3(1):22, 2017.

[77] Akira Fujiwara, Katsuhiko Nishiguchi, and Yukinori Ono. Nanoampere charge pump by single-electron ratchet using silicon nanowire metal-oxide-semiconductor field-effect transistor. *Applied Physics Letters*, 92(4):042102, 2008.

[78] Jay M Gambetta, Jerry M Chow, and Matthias Steffen. Building logical qubits in a superconducting quantum computing system. *npj Quantum Information*, 3(1):1–7, 2017.

[79] John King Gamble, Patrick Harvey-Collard, N Tobias Jacobson, Andrew D Baczewski, Erik Nielsen, Leon Maurer, Inès Montaño, Martin Rudolph, MS Carroll, CH Yang, et al. Valley splitting of single-electron si mos quantum dots. *Applied Physics Letters*, 109(25):253101, 2016.

[80] Michael R Geller and Zhongyuan Zhou. Efficient error models for fault-tolerant architectures and the pauli twirling approximation. *Physical Review A*, 88(1):012314, 2013.

[81] SP Giblin, M Kataoka, JD Fletcher, P See, TJBM Janssen, JP Griffiths, GAC Jones, I Farrer, and DA Ritchie. Towards a quantum representation of the ampere using single electron pumps. *Nature communications*, 3(1):1–6, 2012.

[82] SP Giblin, SJ Wright, JD Fletcher, M Kataoka, M Pepper, TJBM Janssen, DA Ritchie, CA Nicoll, D Anderson, and GAC Jones. An accurate high-speed single-electron quantum dot pump. *New Journal of Physics*, 12(7):073013, 2010.

[83] Irene Puerto Gimenez, Marek Korkusinski, and Pawel Hawrylak. Linear combination of harmonic orbitals and configuration interaction method for the voltage control of exchange interaction in gated lateral quantum dot networks. *Physical Review B*, 76(7):075336, 2007.

[84] Florian Ginzel, Adam R Mills, Jason R Petta, and Guido Burkard. Spin shuttling in a silicon double quantum dot. *arXiv preprint arXiv:2007.03598*, 2020.

[85] Vittorio Giovannetti, Seth Lloyd, and Lorenzo Maccone. Advances in quantum metrology. *Nature photonics*, 5(4):222, 2011.

[86] Nicolas Gisin and Rob Thew. Quantum communication. *Nature photonics*, 1(3):165–171, 2007.

[87] LI Glazman and AV Khaetskii. Nonlinear quantum conductance of a lateral microconstraint in a heterostructure. *EPL (Europhysics Letters)*, 9(3):263, 1989.

[88] M Fernando Gonzalez-Zalba, Sergey N Shevchenko, Sylvain Barraud, J Robert Johansson, Andrew J Ferguson, Franco Nori, and Andreas C Betz. Gate-sensing coherent charge oscillations in a silicon field-effect transistor. *Nano letters*, 16(3):1614–1619, 2016.

[89] MF Gonzalez-Zalba, S Barraud, AJ Ferguson, and AC Betz. Probing the limits of gate-based charge sensing. *Nature communications*, 6(1):1–8, 2015.

[90] AC Gossard. Modulation doping of semiconductor heterostructures. In *Molecular Beam Epitaxy and Heterostructures*, pages 499–531. Springer, 1985.

[91] Daniel Gottesman. The heisenberg representation of quantum computers. *arXiv preprint quant-ph/9807006*, 1998.

[92] Andrew D Greentree, Jared H Cole, AR Hamilton, and Lloyd CL Hollenberg. Coherent electronic transfer in quantum dot systems using adiabatic passage. *Physical Review B*, 70(23):235317, 2004.

[93] Lov K Grover. A fast quantum mechanical algorithm for database search. In *Proceedings of the twenty-eighth annual ACM symposium on Theory of computing*, pages 212–219, 1996.

[94] Utkan Güngördü and JP Kestner. Pulse sequence designed for robust c-phase gates in simos and si/sige double quantum dots. *Physical Review B*, 98(16):165301, 2018.

[95] Mauricio Gutiérrez and Kenneth R Brown. Comparison of a quantum error-correction threshold for exact and approximate errors. *Physical Review A*, 91(2):022335, 2015.

[96] Holger Haas, Daniel Puzzuoli, Feihao Zhang, and David G Cory. Engineering effective hamiltonians. *New Journal of Physics*, 21(10):103011, 2019.

[97] Hartmut Häffner, Christian F Roos, and Rainer Blatt. Quantum computing with trapped ions. *Physics reports*, 469(4):155–203, 2008.

[98] Bertrand I Halperin. Quantized hall conductance, current-carrying edge states, and the existence of extended states in a two-dimensional disordered potential. *Physical Review B*, 25(4):2185, 1982.

[99] Ronald Hanson, Leo P Kouwenhoven, Jason R Petta, Seigo Tarucha, and Lieven MK Vandersypen. Spins in few-electron quantum dots. *Reviews of modern physics*, 79(4):1217, 2007.

[100] Xiaojie Hao, Rusko Ruskov, Ming Xiao, Charles Tahan, and HongWen Jiang. Electron spin resonance and spin–valley physics in a silicon double quantum dot. *Nature communications*, 5:3860, 2014.

[101] RH Harrell, KS Pyshkin, MY Simmons, DA Ritchie, CJB Ford, GAC Jones, and M Pepper. Fabrication of high-quality one-and two-dimensional electron gases in undoped gaas/algaas heterostructures. *Applied physics letters*, 74(16):2328–2330, 1999.

[102] Patrick Harvey-Collard, Benjamin D'Anjou, Martin Rudolph, N Tobias Jacobson, Jason Dominguez, Gregory A Ten Eyck, Joel R Wendt, Tammy Pluym, Michael P Lilly, William A Coish, et al. High-fidelity single-shot readout for a spin qubit via an enhanced latching mechanism. *Physical Review X*, 8(2):021046, 2018.

[103] T Hatano, S Amaha, T Kubo, Y Tokura, Y Nishi, Y Hirayama, and S Tarucha. Manipulation of exchange coupling energy in a few-electron double quantum dot. *Physical Review B*, 77(24):241301, 2008.

[104] Pawel Hawrylak. Far infrared absorption by screened d- states in quantum wells in a strong magnetic field. *Solid state communications*, 88(6):475–479, 1993.

[105] Pawel Hawrylak and Marek Korkusinski. Voltage-controlled coded qubit based on electron spin. *Solid state communications*, 136(9-10):508–512, 2005.

[106] Toivo Hensgens, Takafumi Fujita, Laurens Janssen, Xiao Li, CJ Van Diepen, Christian Reichl, Werner Wegscheider, S Das Sarma, and Lieven MK Vandersypen. Quantum simulation of a fermi–hubbard model using a semiconductor quantum dot array. *Nature*, 548(7665):70–73, 2017.

[107] Charles D Hill, Eldad Peretz, Samuel J Hile, Matthew G House, Martin Fuechsle, Sven Rogge, Michelle Y Simmons, and Lloyd CL Hollenberg. A surface code quantum computer in silicon. *Science advances*, 1(9):e1500707, 2015.

[108] Tuukka Hiltunen, Hendrik Bluhm, Sebastian Mehl, and Ari Harju. Charge-noise tolerant exchange gates of singlet-triplet qubits in asymmetric double quantum dots. *Physical Review B*, 91(7):075301, 2015.

[109] Gregory Holloway. *Electron transport in semiconducting nanowires and quantum dots*. University of Waterloo, 2017.

[110] Tzu-Kan Hsiao, Antonio Rubino, Yousun Chung, Seok-Kyun Son, Hangtian Hou, Jorge Pedrós, Ateeq Nasir, Gabriel Éthier-Majcher, Megan J Stanley, Richard T Phillips, et al. Single-photon emission from single-electron transport in a saw-driven lateral light-emitting diode. *Nature communications*, 11(1):1–7, 2020.

[111] Chang-Yu Hsieh and Pawel Hawrylak. Quantum circuits based on coded qubits encoded in chirality of electron spin complexes in triple quantum dots. *Physical Review B*, 82(20):205311, 2010.

[112] Chang-Yu Hsieh, Yun-Pil Shim, Marek Korkusinski, and Pawel Hawrylak. Physics of lateral triple quantum-dot molecules with controlled electron numbers. *Reports on Progress in Physics*, 75(11):114501, 2012.

[113] Xuedong Hu and S Das Sarma. Hilbert-space structure of a solid-state quantum computer: Two-electron states of a double-quantum-dot artificial molecule. *Physical Review A*, 61(6):062301, 2000.

[114] Jian Huang, DS Novikov, DC Tsui, LN Pfeiffer, and KW West. Nonactivated transport of strongly interacting two-dimensional holes in gaas. *Physical Review B*, 74(20):201302, 2006.

[115] Peihao Huang and Xuedong Hu. Spin relaxation in a si quantum dot due to spin-valley mixing. *Physical Review B*, 90(23):235315, 2014.

[116] W Huang, CH Yang, KW Chan, T Tanttu, B Hensen, RCC Leon, MA Fogarty, JCC Hwang, FE Hudson, Kohei M Itoh, et al. Fidelity benchmarks for two-qubit gates in silicon. *Nature*, 569(7757):532, 2019.

[117] David Hucul, Ismail V Inlek, Grahame Vittorini, Clayton Crocker, Shantanu Debnath, Susan M Clark, and Christopher Monroe. Modular entanglement of atomic qubits using photons and phonons. *Nature Physics*, 11(1):37, 2015.

[118] Thomas Ihn. *Semiconductor Nanostructures: Quantum states and electronic transport*. Oxford University Press, 2010.

[119] Taroh Inada, Shigeki Kato, Tohru Hara, and Nobuyuki Toyoda. Ohmic contacts on ion-implanted n-type gaas layers. *Journal of Applied Physics*, 50(6):4466–4468, 1979.

[120] HW Jiang and Eli Yablonovitch. Gate-controlled electron spin resonance in g a a s/a l x ga 1- x as heterostructures. *Physical Review B*, 64(4):041307, 2001.

[121] Ryan M Jock, N Tobias Jacobson, Patrick Harvey-Collard, Andrew M Mounce, Vanita Srinivasa, Dan R Ward, John Anderson, Ron Manginell, Joel R Wendt, Martin Rudolph, et al. A silicon metal-oxide-semiconductor electron spin-orbit qubit. *Nature communications*, 9(1):1–8, 2018.

[122] Cody Jones, Michael A Fogarty, Andrea Morello, Mark F Gyure, Andrew S Dzurak, and Thaddeus D Ladd. Logical qubit in a linear array of semiconductor quantum dots. *Physical Review X*, 8(2):021058, 2018.

[123] B Kaestner, V Kashcheyevs, S Amakawa, MD Blumenthal, L Li, TJBM Janssen, G Hein, K Pierz, T Weimann, U Siegner, et al. Single-parameter nonadiabatic quantized charge pumping. *Physical Review B*, 77(15):153301, 2008.

[124] B Kaestner, Ch Leicht, V Kashcheyevs, K Pierz, U Siegner, and HW Schumacher. Single-parameter quantized charge pumping in high magnetic fields. *Applied Physics Letters*, 94(1):012106, 2009.

[125] Bernd Kaestner and Vyacheslavs Kashcheyevs. Non-adiabatic quantized charge pumping with tunable-barrier quantum dots: a review of current progress. *Reports on Progress in Physics*, 78(10):103901, 2015.

[126] Abhinav Kandala, Antonio Mezzacapo, Kristan Temme, Maika Takita, Markus Brink, Jerry M Chow, and Jay M Gambetta. Hardware-efficient variational quantum eigensolver for small molecules and quantum magnets. *Nature*, 549(7671):242–246, 2017.

[127] Yadav P Kandel, Haifeng Qiao, Saeed Fallahi, Geoffrey C Gardner, Michael J Manfra, and John M Nichol. Coherent spin-state transfer via heisenberg exchange. *Nature*, 573(7775):553–557, 2019.

[128] BE Kane, LN Pfeiffer, KW West, and CK Harnett. Variable density high mobility two-dimensional electron and hole gases in a gated gaas/al x ga1- x as heterostructure. *Applied physics letters*, 63(15):2132–2134, 1993.

[129] Bruce E Kane. A silicon-based nuclear spin quantum computer. *nature*, 393(6681):133–137, 1998.

[130] Vyacheslavs Kashcheyevs and Bernd Kaestner. Universal decay cascade model for dynamic quantum dot initialization. *Physical review letters*, 104(18):186805, 2010.

[131] M Kataoka, MR Astley, AL Thorn, DKL Oi, CHW Barnes, CJB Ford, D Anderson, GAC Jones, I Farrer, DA Ritchie, et al. Coherent time evolution of a single-electron wave function. *Physical review letters*, 102(15):156801, 2009.

[132] M Kataoka, JD Fletcher, P See, SP Giblin, TJBM Janssen, JP Griffiths, GAC Jones, I Farrer, and DA Ritchie. Tunable nonadiabatic excitation in a single-electron quantum dot. *Physical review letters*, 106(12):126801, 2011.

[133] Erika Kawakami, Thibaut Jullien, Pasquale Scarlino, Daniel R Ward, Donald E Savage, Max G Lagally, Viatcheslav V Dobrovitski, Mark Friesen, Susan N Coppersmith, Mark A Eriksson, et al. Gate fidelity and coherence of an electron spin in an si/sige quantum dot with micromagnet. *Proceedings of the National Academy of Sciences*, 113(42):11738–11743, 2016.

[134] J Keeling, I Klich, and LS Levitov. Minimal excitation states of electrons in one-dimensional wires. *Physical review letters*, 97(11):116403, 2006.

[135] Mark W Keller, John M Martinis, Neil M Zimmerman, and Andrew H Steinbach. Accuracy of electron counting using a 7-junction electron pump. *Applied Physics Letters*, 69(12):1804–1806, 1996.

[136] Navin Khaneja, Timo Reiss, Cindie Kehlet, Thomas Schulte-Herbrüggen, and Steffen J Glaser. Optimal control of coupled spin dynamics: design of nmr pulse sequences by gradient ascent algorithms. *Journal of magnetic resonance*, 172(2):296–305, 2005.

[137] Dohun Kim, Daniel R Ward, Christie B Simmons, Don E Savage, Max G Lagally, Mark Friesen, Susan N Coppersmith, and Mark A Eriksson. High-fidelity resonant gating of a silicon-based quantum dot hybrid qubit. *Npj Quantum Information*, 1(1):1–6, 2015.

[138] J-S Kim, Thomas M Hazard, Andrew A Houck, and Stephen A Lyon. A low-disorder metal-oxide-silicon double quantum dot. *Applied Physics Letters*, 114(4):043501, 2019.

[139] J-S Kim, Alexei M Tyryshkin, and Stephen A Lyon. Annealing shallow si/sio2 interface traps in electron-beam irradiated high-mobility metal-oxide-silicon transistors. *Applied Physics Letters*, 110(12):123505, 2017.

[140] H Jeff Kimble. The quantum internet. *Nature*, 453(7198):1023–1030, 2008.

[141] K v Klitzing, Gerhard Dorda, and Michael Pepper. New method for high-accuracy determination of the fine-structure constant based on quantized hall resistance. *Physical Review Letters*, 45(6):494, 1980.

[142] Christoph Kloeffel and Daniel Loss. Prospects for spin-based quantum computing in quantum dots. *Annu. Rev. Condens. Matter Phys.*, 4(1):51–81, 2013.

[143] Talbot Knighton, Zhe Wu, Jian Huang, Alessandro Serafin, JS Xia, LN Pfeiffer, and KW West. Evidence of two-stage melting of wigner solids. *Physical Review B*, 97(8):085135, 2018.

[144] Emanuel Knill, Raymond Laflamme, and Gerald J Milburn. A scheme for efficient quantum computation with linear optics. *nature*, 409(6816):46–52, 2001.

[145] G Kopnov, VY Umansky, H Cohen, D Shahar, and R Naaman. Effect of the surface on the electronic properties of a two-dimensional electron gas as measured by the quantum hall effect. *Physical Review B*, 81(4):045316, 2010.

[146] FHL Koppens, KC Nowack, and LMK Vandersypen. Spin echo of a single electron spin in a quantum dot. *Physical Review Letters*, 100(23):236802, 2008.

[147] Frank HL Koppens, Christo Buizert, Klaas-Jan Tielrooij, Ivo T Vink, Katja C Nowack, Tristan Meunier, LP Kouwenhoven, and LMK Vandersypen. Driven coherent oscillations of a single electron spin in a quantum dot. *Nature*, 442(7104):766–771, 2006.

[148] Marek Korkusinski. *Correlations in semiconductor quantum dots.* University of Ottawa, 2004.

[149] Marek Korkusinski, Irene Puerto Gimenez, Pawel Hawrylak, Louis Gaudreau, Sergei A Studenikin, and Andrew S Sachrajda. Topological hunds rules and the electronic properties of a triple lateral quantum dot molecule. *Physical Review B*, 75(11):115301, 2007.

[150] Leo P Kouwenhoven, Charles M Marcus, Paul L McEuen, Seigo Tarucha, Robert M Westervelt, and Ned S Wingreen. Electron transport in quantum dots. In *Mesoscopic electron transport*, pages 105–214. Springer, 1997.

[151] LP Kouwenhoven, S Jauhar, K McCormick, D Dixon, PL McEuen, Yu V Nazarov, NC Van Der Vaart, and CT Foxon. Photon-assisted tunneling through a quantum dot. *Physical Review B*, 50(3):2019, 1994.

[152] LP Kouwenhoven, AT Johnson, NC Van der Vaart, CJPM Harmans, and CT Foxon. Quantized current in a quantum-dot turnstile using oscillating tunnel barriers. *Physical Review Letters*, 67(12):1626, 1991.

[153] A Kristensen, J Bo Jensen, M Zaffalon, CB So/rensen, SM Reimann, PE Lindelof, M Michel, and A Forchel. Conductance quantization above 30 k in gaalas shallow-etched quantum point contacts smoothly joined to the background 2deg. *Journal of applied physics*, 83(1):607–609, 1998.

[154] Jan A Krzywda and Łukasz Cywiński. Adiabatic electron charge transfer between two quantum dots in presence of 1/f noise. *Physical Review B*, 101(3):035303, 2020.

[155] Ferdinand Kuemmeth and Hendrik Bluhm. Roadmap for gallium arsenide spin qubits. *arXiv preprint arXiv:2011.13907*, 2020.

[156] Jordan Kyriakidis, M Pioro-Ladriere, M Ciorga, AS Sachrajda, and Pawel Hawrylak. Voltage-tunable singlet-triplet transition in lateral quantum dots. *Physical Review B*, 66(3):035320, 2002.

[157] NS Lai, WH Lim, CH Yang, FA Zwanenburg, WA Coish, F Qassemi, A Morello, and AS Dzurak. Pauli spin blockade in a highly tunable silicon double quantum dot. *Scientific reports*, 1:110, 2011.

[158] Rolf Landauer. Spatial variation of currents and fields due to localized scatterers in metallic conduction. *IBM Journal of research and development*, 1(3):223–231, 1957.

[159] GP Lansbergen, Y Ono, and A Fujiwara. Donor-based single electron pumps with tunable donor binding energy. *Nano letters*, 12(2):763–768, 2012.

[160] D Laroche, S Das Sarma, G Gervais, MP Lilly, and JL Reno. Scattering mechanism in modulation-doped shallow two-dimensional electron gases. *Applied Physics Letters*, 96(16):162112, 2010.

[161] Ch Leicht, P Mirovsky, B Kaestner, F Hohls, V Kashcheyevs, EV Kurganova, U Zeitler, T Weimann, K Pierz, and HW Schumacher. Generation of energy selective excitations in quantum hall edge states. *Semiconductor science and technology*, 26(5):055010, 2011.

[162] RCC Leon, Chih Heng Yang, JCC Hwang, J Camirand Lemyre, Tuomo Tanttu, Wister Huang, Kok Wai Chan, KY Tan, FE Hudson, KM Itoh, et al. Coherent spin control of s-, p-, d-and f-electrons in a silicon quantum dot. *Nature communications*, 11(1):1–7, 2020.

[163] Qiuzi Li, Łukasz Cywiński, Dimitrie Culcer, Xuedong Hu, and S Das Sarma. Exchange coupling in silicon quantum dots: Theoretical considerations for quantum computation. *Physical Review B*, 81(8):085313, 2010.

[164] Ruoyu Li, Luca Petit, David P Franke, Juan Pablo Dehollain, Jonas Helsen, Mark Steudtner, Nicole K Thomas, Zachary R Yoscovits, Kanwal J Singh, Stephanie Wehner, et al. A crossbar network for silicon quantum dot qubits. *Science advances*, 4(7):eaar3960, 2018.

[165] Xiao Li, Edwin Barnes, Jason P Kestner, and S Das Sarma. Intrinsic errors in transporting a single-spin qubit through a double quantum dot. *Physical Review A*, 96(1):012309, 2017.

[166] Elliott Lieb and Daniel Mattis. Ordering energy levels of interacting spin systems. *Journal of Mathematical Physics*, 3(4):749–751, 1962.

[167] SD Liles, R Li, CH Yang, FE Hudson, M Veldhorst, Andrew S Dzurak, and AR Hamilton. Spin and orbital structure of the first six holes in a silicon metal-oxide-semiconductor quantum dot. *Nature communications*, 9(1):1–7, 2018.

[168] WH Lim, CH Yang, FA Zwanenburg, and AS Dzurak. Spin filling of valley–orbit states in a silicon quantum dot. *Nanotechnology*, 22(33):335704, 2011.

[169] Seth Lloyd. Enhanced sensitivity of photodetection via quantum illumination. *Science*, 321(5895):1463–1465, 2008.

[170] Daniel Loss and David P DiVincenzo. Quantum computation with quantum dots. *Physical Review A*, 57(1):120, 1998.

[171] Dawei Lu, Keren Li, Jun Li, Hemant Katiyar, Annie Jihyun Park, Guanru Feng, Tao Xin, Hang Li, Guilu Long, Aharon Brodutch, et al. Enhancing quantum control by bootstrapping a quantum processor of 12 qubits. *npj Quantum Information*, 3(1):1–7, 2017.

[172] SJ MacLeod, K Chan, TP Martin, AR Hamilton, A See, AP Micolich, M Aagesen, and PE Lindelof. Role of background impurities in the single-particle relaxation lifetime of a two-dimensional electron gas. *Physical Review B*, 80(3):035310, 2009.

[173] Wing Yee Mak. *Transport experiments in undoped GaAs/A1GaAs heterostructures*. PhD thesis, University of Cambridge, 2013.

[174] WY Mak, K Das Gupta, HE Beere, I Farrer, F Sfigakis, and DA Ritchie. Distinguishing impurity concentrations in gaas and algaas using very shallow undoped heterostructures. *Applied Physics Letters*, 97(24):242107, 2010.

[175] WY Mak, F Sfigakis, K Das Gupta, O Klochan, HE Beere, I Farrer, JP Griffiths, GAC Jones, AR Hamilton, and DA Ritchie. Ultra-shallow quantum dots in an undoped gaas/algaas two-dimensional electron gas. *Applied Physics Letters*, 102(10):103507, 2013.

[176] Filip K Malinowski, Frederico Martins, Peter D Nissen, Edwin Barnes, Łukasz Cywiński, Mark S Rudner, Saeed Fallahi, Geoffrey C Gardner, Michael J Manfra, Charles M Marcus, et al. Notch filtering the nuclear environment of a spin qubit. *Nature nanotechnology*, 12(1):16, 2017.

[177] Frederico Martins, Filip K Malinowski, Peter D Nissen, Edwin Barnes, Saeed Fallahi, Geoffrey C Gardner, Michael J Manfra, Charles M Marcus, and Ferdinand Kuemmeth. Noise suppression using symmetric exchange gates in spin qubits. *Physical review letters*, 116(11):116801, 2016.

[178] Brett M Maune, Matthew G Borselli, Biqin Huang, Thaddeus D Ladd, Peter W Deelman, Kevin S Holabird, Andrey A Kiselev, Ivan Alvarado-Rodriguez, Richard S Ross, Adele E Schmitz, et al. Coherent singlet-triplet oscillations in a silicon-based double quantum dot. *Nature*, 481(7381):344–347, 2012.

[179] R Maurand, X Jehl, D Kotekar-Patil, A Corna, H Bohuslavskyi, R Laviéville, L Hutin, S Barraud, M Vinet, M Sanquer, et al. A cmos silicon spin qubit. *Nature communications*, 7(1):1–6, 2016.

[180] William H Miller. Semiclassical treatment of multiple turning-point problems—phase shifts and eigenvalues. *The Journal of Chemical Physics*, 48(4):1651–1658, 1968.

[181] AR Mills, DM Zajac, MJ Gullans, FJ Schupp, TM Hazard, and JR Petta. Shuttling a single charge across a one-dimensional array of silicon quantum dots. *Nature Communications*, 10(1):1063, 2019.

[182] R Mizuta, RM Otxoa, AC Betz, and MF Gonzalez-Zalba. Quantum and tunneling capacitance in charge and spin qubits. *Physical Review B*, 95(4):045414, 2017.

[183] C Monroe, R Raussendorf, A Ruthven, KR Brown, P Maunz, L-M Duan, and J Kim. Large-scale modular quantum-computer architecture with atomic memory and photonic interconnects. *Physical Review A*, 89(2):022317, 2014.

[184] Andrea Morello, Jarryd J Pla, Floris A Zwanenburg, Kok W Chan, Kuan Y Tan, Hans Huebl, Mikko Möttönen, Christopher D Nugroho, Changyi Yang, Jessica A van Donkelaar, et al. Single-shot readout of an electron spin in silicon. *Nature*, 467(7316):687–691, 2010.

[185] Pierre-André Mortemousque, Baptiste Jadot, Emmanuel Chanrion, Vivien Thiney, Christopher Bäuerle, Arne Ludwig, Andreas D Wieck, Matias Urdampilleta, and Tristan Meunier. Enhanced spin coherence while displacing electron in a 2d array of quantum dots. *arXiv preprint arXiv:2101.05968*, 2021.

[186] A Mühle, Werner Wegscheider, and Rolf J Haug. Quantum dots formed in a ga as/ al ga as quantum ring. *Applied Physics Letters*, 92(1):013126, 2008.

[187] Juha T Muhonen, Juan P Dehollain, Arne Laucht, Fay E Hudson, Rachpon Kalra, Takeharu Sekiguchi, Kohei M Itoh, David N Jamieson, Jeffrey C McCallum, Andrew S Dzurak, et al. Storing quantum information for 30 seconds in a nanoelectronic device. *Nature nanotechnology*, 9(12):986–991, 2014.

[188] Y Nagamune, H Sakaki, LP Kouwenhoven, LC Mur, CJPM Harmans, J Motohisa, and H Noge. Single electron transport and current quantization in a novel quantum dot structure. *Applied physics letters*, 64(18):2379–2381, 1994.

[189] Charles Neill, Pedran Roushan, K Kechedzhi, Sergio Boixo, Sergei V Isakov, V Smelyanskiy, A Megrant, B Chiaro, A Dunsworth, K Arya, et al. A blueprint for demonstrating quantum supremacy with superconducting qubits. *Science*, 360(6385):195–199, 2018.

[190] Samuel F Neyens, Ryan H Foote, Brandur Thorgrimsson, TJ Knapp, Thomas McJunkin, LMK Vandersypen, Payam Amin, Nicole K Thomas, James S Clarke, DE Savage, et al. The critical role of substrate disorder in valley splitting in si quantum wells. *Applied Physics Letters*, 112(24):243107, 2018.

[191] John M Nichol, Lucas A Orona, Shannon P Harvey, Saeed Fallahi, Geoffrey C Gardner, Michael J Manfra, and Amir Yacoby. High-fidelity entangling gate for double-quantum-dot spin qubits. *npj Quantum Information*, 3(1):1–5, 2017.

[192] Naomi H Nickerson, Joseph F Fitzsimons, and Simon C Benjamin. Freely scalable quantum technologies using cells of 5-to-50 qubits with very lossy and noisy photonic links. *Physical Review X*, 4(4):041041, 2014.

[193] Naomi H Nickerson, Ying Li, and Simon C Benjamin. Topological quantum computing with a very noisy network and local error rates approaching one percent. *Nature communications*, 4(1):1–5, 2013.

[194] Erik Nielsen, Ralph W Young, Richard P Muller, and MS Carroll. Implications of simultaneous requirements for low-noise exchange gates in double quantum dots. *Physical Review B*, 82(7):075319, 2010.

[195] Michael A Nielsen and Isaac Chuang. Quantum computation and quantum information, 2002.

[196] Antti O Niskanen, Jani M Kivioja, Heikki Seppä, and Jukka P Pekola. Evidence of cooper-pair pumping with combined flux and voltage control. *Physical Review B*, 71(1):012513, 2005.

[197] Katja C Nowack, FHL Koppens, Yu V Nazarov, and LMK Vandersypen. Coherent control of a single electron spin with electric fields. *Science*, 318(5855):1430–1433, 2007.

[198] KC Nowack, M Shafiei, M Laforest, GEDK Prawiroatmodjo, LR Schreiber, C Reichl, W Wegscheider, and LMK Vandersypen. Single-shot correlations and two-qubit gate of solid-state spins. *Science*, 333(6047):1269–1272, 2011.

[199] Toshiaki Obata, Michel Pioro-Ladrière, Yasuhiro Tokura, Yun-Sok Shin, Toshihiro Kubo, Katsuharu Yoshida, Tomoyasu Taniyama, and Seigo Tarucha. Coherent manipulation of individual electron spin in a double quantum dot integrated with a micromagnet. *Physical Review B*, 81(8):085317, 2010.

[200] Joe O'Gorman, Naomi H Nickerson, Philipp Ross, John JL Morton, and Simon C Benjamin. A silicon-based surface code quantum computer. *npj Quantum Information*, 2(1):1–14, 2016.

[201] E Paladino, YM Galperin, G Falci, and BL Altshuler. 1/f noise: Implications for solid-state quantum information. *Reviews of Modern Physics*, 86(2):361, 2014.

[202] NK Patel, L Martin-Moreno, M Pepper, R Newbury, JEF Frost, DA Ritchie, GAC Jones, JTMB Janssen, J Singleton, and JAAJ Perenboom. Ballistic transport in one dimension: additional quantisation produced by an electric field. *Journal of Physics: Condensed Matter*, 2(34):7247, 1990.

[203] NK Patel, JT Nicholls, L Martn-Moreno, M Pepper, JEF Frost, DA Ritchie, and GAC Jones. Evolution of half plateaus as a function of electric field in a ballistic quasi-one-dimensional constriction. *Physical Review B*, 44(24):13549, 1991.

[204] Jesper Pedersen, Christian Flindt, Niels Asger Mortensen, and Antti-Pekka Jauho. Failure of standard approximations of the exchange coupling in nanostructures. *Physical Review B*, 76(12):125323, 2007.

[205] KD Petersson, CG Smith, D Anderson, P Atkinson, GAC Jones, and DA Ritchie. Charge and spin state readout of a double quantum dot coupled to a resonator. *Nano letters*, 10(8):2789–2793, 2010.

[206] L Petit, HGJ Eenink, M Russ, WIL Lawrie, NW Hendrickx, SGJ Philips, JS Clarke, LMK Vandersypen, and M Veldhorst. Universal quantum logic in hot silicon qubits. *Nature*, 580(7803):355–359, 2020.

[207] L Petit, M Russ, HGJ Eenink, WIL Lawrie, JS Clarke, LMK Vandersypen, and M Veldhorst. High-fidelity two-qubit gates in silicon above one kelvin. *arXiv preprint arXiv:2007.09034*, 2020.

[208] Jason R Petta, Alexander Comstock Johnson, Jacob M Taylor, Edward A Laird, Amir Yacoby, Mikhail D Lukin, Charles M Marcus, Micah P Hanson, and Arthur C Gossard. Coherent manipulation of coupled electron spins in semiconductor quantum dots. *Science*, 309(5744):2180–2184, 2005.

[209] JR Petta, AC Johnson, CM Marcus, MP Hanson, and AC Gossard. Manipulation of a single charge in a double quantum dot. *Physical review letters*, 93(18):186802, 2004.

[210] Giuseppe Pica, Brendon William Lovett, Ravindra N Bhatt, T Schenkel, and Stephen A Lyon. Surface code architecture for donors and dots in silicon with imprecise and nonuniform qubit couplings. *Physical Review B*, 93(3):035306, 2016.

[211] Jarryd J Pla, Kuan Y Tan, Juan P Dehollain, Wee H Lim, John JL Morton, David N Jamieson, Andrew S Dzurak, and Andrea Morello. A single-atom electron spin qubit in silicon. *Nature*, 489(7417):541–545, 2012.

[212] GJ Podd, SJ Angus, DA Williams, and AJ Ferguson. Charge sensing in intrinsic silicon quantum dots. *Applied Physics Letters*, 96(8):082104, 2010.

[213] M Prada, G Klimeck, and R Joynt. Spin–orbit splittings in si/sige quantum wells: from ideal si membranes to realistic heterostructures. *New Journal of Physics*, 13(1):013009, 2011.

[214] Haifeng Qiao, Yadav P Kandel, Sreenath K Manikandan, Andrew N Jordan, Saeed Fallahi, Geoffrey C Gardner, Michael J Manfra, and John M Nichol. Conditional teleportation of quantum-dot spin states. *Nature communications*, 11(1):1–9, 2020.

[215] Rajib Rahman, Seung H Park, Timothy B Boykin, Gerhard Klimeck, Sven Rogge, and Lloyd CL Hollenberg. Gate-induced g-factor control and dimensional transition for donors in multivalley semiconductors. *Physical Review B*, 80(15):155301, 2009.

[216] Rajib Rahman, Seung H Park, Jared H Cole, Andrew D Greentree, Richard P Muller, Gerhard Klimeck, and Lloyd CL Hollenberg. Atomistic simulations of adiabatic coherent electron transport in triple donor systems. *Physical Review B*, 80(3):035302, 2009.

[217] Eduardo B Ramirez, Francois Sfigakis, Sukanya Kudva, and Jonathan Baugh. Few-electrode design for silicon mos quantum dots. *Semiconductor Science and Technology*, 35(1):015002, 2019.

[218] Guy Ramon and Xuedong Hu. Decoherence of spin qubits due to a nearby charge fluctuator in gate-defined double dots. *Physical Review B*, 81(4):045304, 2010.

[219] Gianluca Rastelli. Semiclassical formula for quantum tunneling in asymmetric double-well potentials. *Physical Review A*, 86(1):012106, 2012.

[220] Robert Raussendorf, Jim Harrington, and Kovid Goyal. A fault-tolerant one-way quantum computer. *Annals of physics*, 321(9):2242–2270, 2006.

[221] MD Reed, BM Maune, RW Andrews, MG Borselli, K Eng, MP Jura, AA Kiselev, TD Ladd, ST Merkel, I Milosavljevic, et al. Reduced sensitivity to charge noise in semiconductor spin qubits via symmetric operation. *Physical review letters*, 116(11):110402, 2016.

[222] S Rochette, M Rudolph, A-M Roy, M Curry, G Ten Eyck, R Manginell, J Wendt, T Pluym, SM Carr, D Ward, et al. Single-electron-occupation metal-oxide-semiconductor quantum dots formed from efficient poly-silicon gate layout. *arXiv preprint arXiv:1707.03895*, 2017.

[223] Alessandro Rossi, Tuomo Tanttu, Kuan Yen Tan, Ilkka Iisakka, Ruichen Zhao, Kok Wai Chan, Giuseppe C Tettamanzi, Sven Rogge, Andrew S Dzurak, and Mikko Möttönon. An accurate single-electron pump based on a highly tunable silicon quantum dot. *Nano letters*, 14(6):3405–3411, 2014.

[224] Alessandro Rossi, R Zhao, AS Dzurak, and MF Gonzalez-Zalba. Dispersive readout of a silicon quantum dot with an accumulation-mode gate sensor. *Applied Physics Letters*, 110(21):212101, 2017.

[225] Davide Rotta, Fabio Sebastiano, Edoardo Charbon, and Enrico Prati. Quantum information density scaling and qubit operation time constraints of cmos silicon-based quantum computer architectures. *npj Quantum Information*, 3(1):1–14, 2017.

[226] Rusko Ruskov, Menno Veldhorst, Andrew S Dzurak, and Charles Tahan. Electron g-factor of valley states in realistic silicon quantum dots. *Physical Review B*, 98(24):245424, 2018.

[227] Arnau Sala, Jørgen Holme Qvist, and Jeroen Danon. Highly tunable exchange-only singlet-only qubit in a gaas triple quantum dot. *arXiv preprint arXiv:1911.08345*, 2019.

[228] AL Saraiva, MJ Calderón, Rodrigo B Capaz, Xuedong Hu, S Das Sarma, and Belita Koiller. Intervalley coupling for interface-bound electrons in silicon: an effective mass study. *Physical Review B*, 84(15):155320, 2011.

[229] S Sarkozy, K Das Gupta, C Siegert, A Ghosh, M Pepper, I Farrer, HE Beere, DA Ritchie, and GAC Jones. Low temperature transport in undoped mesoscopic structures. *Applied Physics Letters*, 94(17):172105, 2009.

[230] Stephen J Sarkozy, Kantimay Das Gupta, Francois Sfigakis, Ian Farrer, David Ritchie, Geb Jones, Po-Hsin Liu, Helen Quach, and Michael Pepper. Mesoscopic transport in undoped heterostructures. *ECS Transactions*, 16(7):59, 2008.

[231] S Das Sarma, Xin Wang, and Shuo Yang. Hubbard model description of silicon spin qubits: Charge stability diagram and tunnel coupling in si double quantum dots. *Physical Review B*, 83(23):235314, 2011.

[232] Sankar Das Sarma, Michael Freedman, and Chetan Nayak. Majorana zero modes and topological quantum computation. *npj Quantum Information*, 1(1):1–13, 2015.

[233] P Scarlino, E Kawakami, P Stano, M Shafiei, C Reichl, Werner Wegscheider, and LMK Vandersypen. Spin-relaxation anisotropy in a gaas quantum dot. *Physical review letters*, 113(25):256802, 2014.

[234] Minky Seo, Ye-Hwan Ahn, Youngheon Oh, Yunchul Chung, Sungguen Ryu, H-S Sim, In-Ho Lee, Myung-Ho Bae, and Nam Kim. Improvement of electron pump accuracy by a potential-shape-tunable quantum dot pump. *Physical Review B*, 90(8):085307, 2014.

[235] F Setiawan, Hoi-Yin Hui, JP Kestner, Xin Wang, and S Das Sarma. Robust two-qubit gates for exchange-coupled qubits. *Physical Review B*, 89(8):085314, 2014.

[236] LJ Sham and M Nakayama. Effective-mass approximation in the presence of an interface. *Physical Review B*, 20(2):734, 1979.

[237] Nachiket Sunil Sherlekar. Next-generation solid-state quantum emitters. Master's thesis, University of Waterloo, 2019.

[238] JM Shilton, VI Talyanskii, M Pepper, DA Ritchie, JEF Frost, CJB Ford, CG Smith, and GAC Jones. High-frequency single-electron transport in a quasi-one-dimensional gaas channel induced by surface acoustic waves. *Journal of Physics: Condensed Matter*, 8(38):L531, 1996.

[239] Yun-Pil Shim and Pawel Hawrylak. Gate-controlled spin-spin interactions in lateral quantum dot molecules. *Physical Review B*, 78(16):165317, 2008.

[240] Peter W Shor. Algorithms for quantum computation: discrete logarithms and factoring. In *Proceedings 35th annual symposium on foundations of computer science*, pages 124–134. Ieee, 1994.

[241] AJ Sigillito, MJ Gullans, LF Edge, M Borselli, and JR Petta. Coherent transfer of quantum information in a silicon double quantum dot using resonant SWAP gates. *npj Quantum Information*, 5(1):1–7, 2019.

[242] Chao Song, Kai Xu, Wuxin Liu, Chui-ping Yang, Shi-Biao Zheng, Hui Deng, Qiwei Xie, Keqiang Huang, Qiujiang Guo, Libo Zhang, et al. 10-qubit entanglement and parallel logic operations with a superconducting circuit. *Physical review letters*, 119(18):180511, 2017.

[243] Friederike Stein, Dietmar Drung, Lukas Fricke, Hansjörg Scherer, Frank Hohls, Christoph Leicht, Martin Götz, Christian Krause, Ralf Behr, Eckart Pesel, et al. Validation of a quantized-current source with 0.2 ppm uncertainty. *Applied Physics Letters*, 107(10):103501, 2015.

[244] Ashley M Stephens. Fault-tolerant thresholds for quantum error correction with the surface code. *Physical Review A*, 89(2):022321, 2014.

[245] HL Störmer, R Dingle, AC Gossard, W Wiegmann, and MD Sturge. Two-dimensional electron gas at a semiconductor-semiconductor interface. *Solid state communications*, 29(10):705–709, 1979.

[246] Aaron Szafer and A Douglas Stone. Theory of quantum conduction through a constriction. *Physical Review Letters*, 62(3):300, 1989.

[247] MLV Tagliaferri, PL Bavdaz, W Huang, AS Dzurak, Dimitrie Culcer, and Menno Veldhorst. Impact of valley phase and splitting on readout of silicon spin qubits. *Physical Review B*, 97(24):245412, 2018.

[248] Shintaro Takada, Hermann Edlbauer, Hugo V Lepage, Junliang Wang, Pierre-André Mortemousque, Giorgos Georgiou, Crispin HW Barnes, Christopher JB Ford, Mingyun Yuan, Paulo V Santos, et al. Sound-driven single-electron transfer in a circuit of coupled quantum rails. *Nature communications*, 10(1):1–9, 2019.

[249] Kenta Takeda, Jun Kamioka, Tomohiro Otsuka, Jun Yoneda, Takashi Nakajima, Matthieu R Delbecq, Shinichi Amaha, Giles Allison, Tetsuo Kodera, Shunri Oda, et al. A fault-tolerant addressable spin qubit in a natural silicon quantum dot. *Science advances*, 2(8):e1600694, 2016.

[250] Tuomo Tanttu, Bas Hensen, Kok Wai Chan, Chih Hwan Yang, Wister Wei Huang, Michael Fogarty, Fay Hudson, Kohei Itoh, Dimitrie Culcer, Arne Laucht, et al. Controlling spin-orbit interactions in silicon quantum dots using magnetic field direction. *Physical Review X*, 9(2):021028, 2019.

[251] MJ Testolin, JH Cole, and LCL Hollenberg. Modelling the effect of charge noise on the exchange interaction between spins. *arXiv preprint arXiv:0904.0060*, 2009.

[252] KJ Thomas, JT Nicholls, MY Simmons, M Pepper, DR Mace, and DA Ritchie. Possible spin polarization in a one-dimensional electron gas. *Physical Review Letters*, 77(1):135, 1996.

[253] TJ Thornton, M Pepper, H Ahmed, D Andrews, and GJ Davies. One-dimensional conduction in the 2d electron gas of a gaas-algaas heterojunction. *Physical review letters*, 56(11):1198, 1986.

[254] Géza Tóth and Iagoba Apellaniz. Quantum metrology from a quantum information science perspective. *Journal of Physics A: Mathematical and Theoretical*, 47(42):424006, 2014.

[255] JL Truitt, KA Slinker, KLM Lewis, DE Savage, Charles Tahan, LJ Klein, JO Chu, PM Mooney, AM Tyryshkin, DW vanáder Weide, et al. Si/sige quantum devices, quantum wells, and electron-spin coherence. *Electron Spin Resonance and Related Phenomena in Low-Dimensional Structures*, pages 101–127, 2009.

[256] Alexei M Tyryshkin, Shinichi Tojo, John JL Morton, Helge Riemann, Nikolai V Abrosimov, Peter Becker, Hans-Joachim Pohl, Thomas Schenkel, Michael LW Thewalt, Kohei M Itoh, et al. Electron spin coherence exceeding seconds in high-purity silicon. *Nature materials*, 11(2):143–147, 2012.

[257] Niels Ubbelohde, Frank Hohls, Vyacheslavs Kashcheyevs, Timo Wagner, Lukas Fricke, Bernd Kästner, Klaus Pierz, Hans W Schumacher, and Rolf J Haug. Partitioning of on-demand electron pairs. *Nature Nanotechnology*, 10(1):46, 2015.

[258] V Umansky, R De-Picciotto, and M Heiblum. Extremely high-mobility two dimensional electron gas: Evaluation of scattering mechanisms. *Applied physics letters*, 71(5):683–685, 1997.

[259] V Umansky, M Heiblum, Y Levinson, J Smet, J Nübler, and M Dolev. Mbe growth of ultra-low disorder 2deg with mobility exceeding 35× 106 cm2/v s. *Journal of Crystal Growth*, 311(7):1658–1661, 2009.

[260] Pawel Utko, J Bindslev Hansen, Poul Erik Lindelof, Claus Birger Sørensen, and K Gloos. Single-electron transport driven by surface acoustic waves: moving quantum dots versus short barriers. *Journal of Low Temperature Physics*, 146(5-6):607–627, 2007.

[261] WG van der Wiel, M Stopa, T Kodera, T Hatano, and S Tarucha. Semiconductor quantum dots for electron spin qubits. *New journal of physics*, 8(2):28, 2006.

[262] Wilfred G Van der Wiel, Silvano De Franceschi, Jeroen M Elzerman, Toshimasa Fujisawa, Seigo Tarucha, and Leo P Kouwenhoven. Electron transport through double quantum dots. *Reviews of Modern Physics*, 75(1):1, 2002.

[263] BJ Van Wees, H Van Houten, CWJ Beenakker, J Gr Williamson, LP Kouwenhoven, D Van der Marel, and CT Foxon. Quantized conductance of point contacts in a two-dimensional electron gas. *Physical Review Letters*, 60(9):848, 1988.

[264] LMK Vandersypen, H Bluhm, JS Clarke, AS Dzurak, R Ishihara, A Morello, DJ Reilly, LR Schreiber, and M Veldhorst. Interfacing spin qubits in quantum dots and donors—hot, dense, and coherent. *npj Quantum Information*, 3(1):34, 2017.

[265] Juha J Vartiainen, Mikko Möttönen, Jukka P Pekola, and Antti Kemppinen. Nanoampere pumping of cooper pairs. *Applied Physics Letters*, 90(8):082102, 2007.

[266] M Veldhorst, HGJ Eenink, CH Yang, and Andrew S Dzurak. Silicon cmos architecture for a spin-based quantum computer. *Nature communications*, 8(1):1–8, 2017.

[267] M Veldhorst, JCC Hwang, CH Yang, AW Leenstra, Bob de Ronde, JP Dehollain, JT Muhonen, FE Hudson, Kohei M Itoh, A Morello, et al. An addressable quantum dot qubit with fault-tolerant control-fidelity. *Nature Nanotechnology*, 9(12):981, 2014.

[268] M Veldhorst, R Ruskov, CH Yang, JCC Hwang, FE Hudson, ME Flatté, C Tahan, Kohei M Itoh, A Morello, and AS Dzurak. Spin-orbit coupling and operation of multivalley spin qubits. *Physical Review B*, 92(20):201401, 2015.

[269] Menno Veldhorst, CH Yang, JCC Hwang, W Huang, JP Dehollain, JT Muhonen, S Simmons, A Laucht, FE Hudson, Kohei M Itoh, et al. A two-qubit logic gate in silicon. *Nature*, 526(7573):410–414, 2015.

[270] Xin Wang, Lev S Bishop, Edwin Barnes, JP Kestner, and S Das Sarma. Robust quantum gates for singlet-triplet spin qubits using composite pulses. *Physical Review A*, 89(2):022310, 2014.

[271] TF Watson, SGJ Philips, Erika Kawakami, DR Ward, Pasquale Scarlino, Menno Veldhorst, DE Savage, MG Lagally, Mark Friesen, SN Coppersmith, et al. A programmable two-qubit quantum processor in silicon. *Nature*, 555(7698):633–637, 2018.

[272] Göran Wendin. Quantum information processing with superconducting circuits: a review. *Reports on Progress in Physics*, 80(10):106001, 2017.

[273] SJ Wright, MD Blumenthal, Godfrey Gumbs, AL Thorn, M Pepper, TJBM Janssen, SN Holmes, D Anderson, GAC Jones, CA Nicoll, et al. Enhanced current quantization in high-frequency electron pumps in a perpendicular magnetic field. *Physical Review B*, 78(23):233311, 2008.

[274] Xian Wu, Daniel R Ward, JR Prance, Dohun Kim, John King Gamble, RT Mohr, Zhan Shi, DE Savage, MG Lagally, Mark Friesen, et al. Two-axis control of a singlet–triplet qubit with an integrated micromagnet. *Proceedings of the National Academy of Sciences*, 111(33):11938–11942, 2014.

[275] B Paquelet Wuetz, PL Bavdaz, LA Yeoh, R Schouten, H van der Does, M Tiggelman, D Sabbagh, A Sammak, Carmen G Almudever, F Sebastiano, et al. Multiplexed quantum transport using commercial off-the-shelf cmos at sub-kelvin temperatures. *npj Quantum Information*, 6(1):1–8, 2020.

[276] X Xue, TF Watson, J Helsen, Daniel R Ward, Donald E Savage, Max G Lagally, Susan N Coppersmith, MA Eriksson, S Wehner, and LMK Vandersypen. Benchmarking gate fidelities in a Si/SiGe two-qubit device. *Physical Review X*, 9(2):021011, 2019.

[277] Gento Yamahata, Stephen P Giblin, Masaya Kataoka, Takeshi Karasawa, and Akira Fujiwara. Gigahertz single-electron pumping in silicon with an accuracy better than 9.2 parts in 107. *Applied Physics Letters*, 109(1):013101, 2016.

[278] Gento Yamahata, Takeshi Karasawa, and Akira Fujiwara. Gigahertz single-hole transfer in si tunable-barrier pumps. *Applied Physics Letters*, 106(2):023112, 2015.

[279] Gento Yamahata, Katsuhiko Nishiguchi, and Akira Fujiwara. Gigahertz single-trap electron pumps in silicon. *Nature communications*, 5(1):1–7, 2014.

[280] CH Yang, KW Chan, R Harper, W Huang, T Evans, JCC Hwang, B Hensen, A Laucht, T Tanttu, FE Hudson, et al. Silicon qubit fidelities approaching incoherent noise limits via pulse engineering. *Nature Electronics*, 2(4):151–158, 2019.

[281] CH Yang, WH Lim, FA Zwanenburg, and AS Dzurak. Dynamically controlled charge sensing of a few-electron silicon quantum dot. *AIP Advances*, 1(4):042111, 2011.

[282] CH Yang, A Rossi, R Ruskov, NS Lai, FA Mohiyaddin, S Lee, C Tahan, Gerhard Klimeck, A Morello, and AS Dzurak. Spin-valley lifetimes in a silicon quantum dot with tunable valley splitting. *Nature communications*, 4:2069, 2013.

[283] Chih Heng Yang, RCC Leon, JCC Hwang, Andre Saraiva, Tuomo Tanttu, Wister Huang, J Camirand Lemyre, Kok Wai Chan, KY Tan, Fay E Hudson, et al. Operation of a silicon quantum processor unit cell above one kelvin. *Nature*, 580(7803):350–354, 2020.

[284] Xu-Chen Yang and Xin Wang. Suppression of charge noise using barrier control of a singlet-triplet qubit. *Physical Review A*, 96(1):012318, 2017.

[285] J Yoneda, W Huang, M Feng, CH Yang, KW Chan, T Tanttu, W Gilbert, RCC Leon, FE Hudson, KM Itoh, et al. Coherent spin qubit transport in silicon. *arXiv preprint arXiv:2008.04020*, 2020.

[286] Jun Yoneda, Kenta Takeda, Tomohiro Otsuka, Takashi Nakajima, Matthieu R Delbecq, Giles Allison, Takumu Honda, Tetsuo Kodera, Shunri Oda, Yusuke Hoshi, et al. A quantum-dot spin qubit with coherence limited by charge noise and fidelity higher than 99.9%. *Nature nanotechnology*, 13(2):102, 2018.

[287] David M Zajac, Anthony J Sigillito, Maximilian Russ, Felix Borjans, Jacob M Taylor, Guido Burkard, and Jason R Petta. Resonantly driven CNOT gate for electron spins. *Science*, 359(6374):439–442, 2018.

[288] DM Zajac, TM Hazard, X Mi, K Wang, and Jason R Petta. A reconfigurable gate architecture for si/sige quantum dots. *Applied Physics Letters*, 106(22):223507, 2015.

[289] DM Zajac, TM Hazard, Xiao Mi, E Nielsen, and Jason R Petta. Scalable gate architecture for a one-dimensional array of semiconductor spin qubits. *Physical Review Applied*, 6(5):054013, 2016.

[290] Chengxian Zhang, Robert E Throckmorton, Xu-Chen Yang, Xin Wang, Edwin Barnes, and S Das Sarma. Randomized benchmarking of barrier versus tilt control of a singlet-triplet qubit. *Physical Review Letters*, 118(21):216802, 2017.

[291] Xinyu Zhao and Xuedong Hu. Coherent electron transport in silicon quantum dots. *arXiv preprint arXiv:1803.00749*, 2018.

[292] Xinyu Zhao and Xuedong Hu. Toward high-fidelity coherent electron spin transport in a gaas double quantum dot. *Scientific reports*, 8(1):13968, 2018.

[293] G Zheng, N Samkharadze, ML Noordam, N Kalhor, D Brousse, A Sammak, G Scappucci, and LMK Vandersypen. Rapid high-fidelity gate-based spin read-out in silicon. *arXiv preprint arXiv:1901.00687*, 2019.

[294] Neil M Zimmerman, Peihao Huang, and Dimitrie Culcer. Valley phase and voltage control of coherent manipulation in si quantum dots. *Nano letters*, 17(7):4461–4465, 2017.

[295] Floris A Zwanenburg, Andrew S Dzurak, Andrea Morello, Michelle Y Simmons, Lloyd CL Hollenberg, Gerhard Klimeck, Sven Rogge, Susan N Coppersmith, and Mark A Eriksson. Silicon quantum electronics. *Reviews of modern physics*, 85(3):961, 2013.

APPENDICES

Appendix A

Elliptical harmonic orbital Coulomb matrix elements

In this Appendix we generalize the formula for the Coulomb matrix elements (CMEs) derived in Section 4.2.2 of the main text for the case of elliptical harmonic orbitals. To start, the coordinate operators are defined as follows:

$$x_i = \frac{A}{\sqrt{2}}(a_i + a_i^\dagger), \quad A = \sqrt{\frac{1}{\omega_x}}; \qquad y_i = \frac{B}{\sqrt{2}}(b_i + b_i^\dagger), \quad B = \sqrt{\frac{1}{\omega_y}}. \tag{A.1}$$

where ω_x and ω_y are the harmonic frequencies along the x- and y- axes respectively.

The first part of the CME derivation is analogous to the derivation of the symmetric harmonic orbital CME formula in Section 4.2.2 and leads to almost the same expression as given in Equation 4.15. For elliptical harmonic orbitals, the integral $I_{p_1p_2p_3p_4}$ is now given by the formula:

$$\begin{aligned} I_{p_1p_2p_3p_4} &= \int \frac{d\vec{q}}{q} e^{-(\frac{A^2}{2}q_x^2 + \frac{B^2}{2}q_y^2)} \left(\frac{iA}{\sqrt{2}}q_x\right)^{n_\alpha+n_\delta-2p_1} \left(\frac{iB}{\sqrt{2}}q_y\right)^{m_\alpha+m_\delta-2p_2} \\ &\quad \times \left(\frac{-iA}{\sqrt{2}}q_x\right)^{n_\beta+n_\gamma-2p_3} \left(\frac{-iB}{\sqrt{2}}q_y\right)^{m_\beta+m_\gamma-2p_4} \qquad (A.2) \\ &= CA^aB^{2p-a}\int_0^{2\pi} d\theta \int_0^\infty dq\, q^{2p}\,(\cos\theta)^a\,(\sin\theta)^{2p-a}\, e^{-\frac{q^2}{2}(A^2\cos^2\theta + B^2\sin^2\theta)}, \qquad (A.3) \end{aligned}$$

where the following parameters are introduced to condense the notation:

$$\begin{aligned}2p &= n_\alpha + m_\alpha + n_\delta + m_\delta + n_\beta + m_\beta + n_\gamma + m_\gamma - 2p_1 - 2p_2 - 2p_3 - 2p_4\\ a &= n_\alpha + n_\delta + n_\beta + n_\gamma - 2p_1 - 2p_3\\ C &= (-1)^{p+n_\beta+n_\gamma+m_\beta+m_\gamma}.\end{aligned}$$

After converting to polar coordinates and substituting $x = q\sqrt{A^2\cos^2\theta + B^2\sin^2\theta}/\sqrt{2}$, the integral over q immediately yields the Gamma function giving

$$I_{p_1p_2p_3p_4}(A,B) = 2\sqrt{2}\,C\,\Gamma\left(p+\frac{1}{2}\right)A^aB^{2p-a}\underbrace{\int_0^{\frac{\pi}{2}}\frac{(\cos\theta)^a(\sin\theta)^{2p-a}}{\left(A^2\cos^2\theta + B^2\sin^2\theta\right)^{p+\frac{1}{2}}}d\theta}_{\tilde{I}_{[0,\frac{\pi}{2}]}(A,B)} \tag{A.4}$$

if a and $2p$ are even, and zero otherwise. To calculate the integral $\tilde{I}_{[0,\frac{\pi}{2}]}(A,B)$, we consider a generating function:

$$G(A,B) = \int_0^{\frac{\pi}{2}}\frac{\mathrm{d}\theta}{\sqrt{\left(A^2\cos^2\theta + B^2\sin^2\theta\right)}} = \frac{\pi}{2M(A,B)}, \tag{A.5}$$

where $M(A,B)$ is the arithmetic-geometric mean of the numbers A, B. The derivative of Equation A.5 with respect to A^2 and B^2 is

$$\frac{\partial^{k+l}G(A,B)}{\partial^k(A^2)\partial^l(B^2)} = \int_0^{\frac{\pi}{2}}d\theta\frac{\left(\cos^2\theta\right)^k\left(\sin^2\theta\right)^l}{\left(A^2\cos^2\theta + B^2\sin^2\theta\right)^{k+l+\frac{1}{2}}}\frac{(-1)^{k+l}(2k+2l-1)!!}{2^{k+l}} \tag{A.6}$$

and is clearly within a constant factor of $\tilde{I}_{[0,\frac{\pi}{2}]}(A,B)$ when $k = \frac{a}{2}$ and $l = p - \frac{a}{2}$. This leads us to the following formula:

$$I_{p_1p_2p_3p_4}(A,B) = \pi\sqrt{2\pi}(-1)^{n_\beta+n_\gamma+m_\beta+m_\gamma}\left(\frac{\partial}{\partial(A^2)}\right)^{\frac{a}{2}}\left(\frac{\partial}{\partial(B^2)}\right)^{p-\frac{a}{2}}\frac{1}{M(A,B)}. \tag{A.7}$$

Here we also utilized the identity $\Gamma\left(p+\frac{1}{2}\right) = \frac{\sqrt{\pi}(2p-1)!!}{2^p}$ that holds for integer p.

Recollecting the definition of A, B from Equation A.1, we are going to obtain the final expression in terms of ω_x, ω_y. To achieve this, we note that the following equality follows from Equation A.4 by factoring out constant terms from the denominator:

$$I_{p_1p_2p_3p_4}(A,B) = \frac{1}{AB}I_{p_1p_2p_3p_4}\left(\frac{1}{B},\frac{1}{A}\right)$$

Then, the Equation A.7 takes the form:

$$
\begin{aligned}
I_{p_1p_2p_3p_4}(A,B) &= \frac{\pi\sqrt{2\pi}(-1)^{n_\beta+n_\gamma+m_\beta+m_\gamma}}{A^{2p-a+1}B^{a+1}}\left(\frac{\partial}{\partial(B^{-2})}\right)^{\frac{a}{2}}\left(\frac{\partial}{\partial(A^{-2})}\right)^{p-\frac{a}{2}}\frac{1}{M\left(\frac{1}{B},\frac{1}{A}\right)} \\
&= \pi\sqrt{2\pi}(-1)^{n_\beta+n_\gamma+m_\beta+m_\gamma}\omega_x^{p-\frac{a-1}{2}}\omega_y^{\frac{a+1}{2}} \\
&\quad\times\left(\frac{\partial}{\partial\omega_y}\right)^{\frac{a}{2}}\left(\frac{\partial}{\partial\omega_x}\right)^{p-\frac{a}{2}}\frac{1}{M\left(\sqrt{\omega_x},\sqrt{\omega_y}\right)}
\end{aligned}
\tag{A.8}
$$

In the end, after substituting Equation A.8 into Equation 4.15, we obtain the final expression for Coulomb matrix elements in case of elliptical harmonic orbitals:

$$
\begin{aligned}
\langle\alpha\beta|\, v\,|\gamma\delta\rangle &= \sqrt{\frac{\pi\omega_x\omega_y}{2}}\frac{e^2}{4\pi\epsilon_0\epsilon_r}\frac{(-1)^{n_\beta+n_\gamma+m_\beta+m_\gamma}}{\sqrt{n_\alpha!m_\alpha!n_\delta!m_\delta!n_\beta!m_\beta!n_\gamma!m_\gamma!}}\sum_{p_1=0}^{\min(n_\alpha,n_\delta)}p_1!\binom{n_\alpha}{p_1}\binom{n_\delta}{p_1} \\
&\times\sum_{p_2=0}^{\min(m_\alpha,m_\delta)}p_2!\binom{m_\alpha}{p_2}\binom{m_\delta}{p_2}\sum_{p_3=0}^{\min(n_\beta,n_\gamma)}p_3!\binom{n_\beta}{p_3}\binom{n_\gamma}{p_3}\sum_{p_4=0}^{\min(m_\beta,m_\gamma)}p_4!\binom{m_\beta}{p_4}\binom{m_\gamma}{p_4} \\
&\times\omega_x^{p-\frac{a}{2}}\left(\frac{\partial}{\partial\omega_x}\right)^{p-\frac{a}{2}}\omega_y^{\frac{a}{2}}\left(\frac{\partial}{\partial\omega_y}\right)^{\frac{a}{2}}\frac{1}{M\left(\sqrt{\omega_x},\sqrt{\omega_y}\right)},
\end{aligned}
\tag{A.9}
$$

where $a = n_\alpha + n_\delta + n_\beta + n_\gamma - 2p_1 - 2p_3$, $2p = a + m_\alpha + m_\delta + m_\beta + m_\gamma - 2p_2 - 2p_4$, and $2p$ and a are even. Otherwise, the matrix elements are equal to zero.

In summary, we find the closed analytic formulas for Coulomb matrix elements in the cases of circular and elliptical orbitals. However, unlike in the expression from Equation 4.19, the terms dependent on ω_x and ω_y do not factor out from Equation A.9. This does not allow us to simply scale the preliminary calculated library of CMEs for unit frequencies and achieve the desired computational efficiency as discussed in Section 4.2.2 of the main text. For this reason, only symmetric harmonic orbitals are used for all simulations described in Chapter 4.

Nevertheless, improvements can be made to Equation A.9 to make it more useful for full LCHO-CI calculations, even if both ω_x and ω_y do not factor out of the expression. We do this by rewriting Equation A.4 as

$$
I_{p_1p_2p_3p_4}(A,\kappa) = \frac{1}{A}\,2\sqrt{2}\,C\,\Gamma\left(p+\frac{1}{2}\right)\kappa^{2p-a}\int_0^{\frac{\pi}{2}}\frac{(\cos\theta)^a\,(\sin\theta)^{2p-a}}{\left(\cos^2\theta+\kappa^2\sin^2\theta\right)^{p+\frac{1}{2}}}d\theta
\tag{A.10}
$$

where $\kappa = B/A = \omega_x/\omega_y$ is the eccentricity of the harmonic orbitals. A easily factors out of the entire expression, and we can write the Coulomb matrix elements as

$$\begin{aligned}\langle \alpha\beta | \, v \, | \gamma\delta \rangle = \sqrt{\omega_x} \frac{e^2}{4\pi\epsilon_0\epsilon_r} \frac{\sqrt{2}(-1)^{n_\beta+n_\gamma+m_\beta+m_\gamma}}{\pi\sqrt{n_\alpha! m_\alpha! n_\delta! m_\delta! n_\beta! m_\beta! n_\gamma! m_\gamma!}} \sum_{p_1=0}^{\min(n_\alpha,n_\delta)} p_1! \binom{n_\alpha}{p_1} \binom{mn_\delta}{p_1} \\ \times \sum_{p_2=0}^{\min(m_\alpha,m_\delta)} p_2! \binom{m_\alpha}{p_2} \binom{m_\delta}{p_2} \sum_{p_3=0}^{\min(n_\beta,n_\gamma)} p_3! \binom{n_\beta}{p_3} \binom{m_\gamma}{p_3} \sum_{p_4=0}^{\min(m_\beta,m_\gamma)} p_4! \binom{m_\beta}{p_4} \binom{m_\gamma}{p_4} \\ \times (-1)^p \, \Gamma\left(p+\frac{1}{2}\right) \kappa^{2p-a} \int_0^{\frac{\pi}{2}} \frac{(\cos\theta)^a (\sin\theta)^{2p-a}}{\left(\cos^2\theta + \kappa^2 \sin^2\theta\right)^{p+\frac{1}{2}}} d\theta \quad \text{(A.11)}\end{aligned}$$

The term within the quadruple summation depends only on κ and can be easily evaluated numerically. A discrete collection of full harmonic orbital Coulomb matrix elements $C_{\text{HO},1,\kappa}$ can be calculated for $\omega_x = 1$ and a select set of κ values (i.e. $\kappa = 0.1, 0.5, 2.0, 10.0$). The harmonic orbital basis can be optimized over a continuous choice of ω_x and a discrete set of κ, and the desired harmonic orbital Coulomb matrix elements are calculated simply as $C_{\text{HO},\omega_x,\kappa} = \sqrt{\omega_x} C_{\text{HO},1,\kappa}$. Utilizing this approach requires the storage of several $C_{,1,\kappa}$, and since these matrices can be quite large (i.e. $M = 16^2$ gives a $C_{\text{HO},1,\kappa}$ size of 65536×65536), it may not be feasible to store several sets of $C_{\text{HO},1,\kappa}$. However, this approach will be critical to apply this method on 3D potential as the confinement along the z-axis is generally much smaller than the confinements along the x- and y- axes. It will be difficult to get converged approximations of the 3D single electron orbitals if $\omega_x = \omega_y = \omega_z$ for the harmonic orbital basis.

Appendix B

Fabrication recipes for dopant-free GaAs devices

Here we give a detailed fabrication recipes for fabricating a Hallbar in a dopant-free GaAs single heterojunction. The QPC and SEP devices described in Chapter 5 are more complicated structures, but still follow these fundamental fabrication steps. The main difference for QPC and SEP devices is the addition of electron beam lithography (EBL) which is used to pattern the fine gates. The general procedure for EBL and subsequent metal deposition is listed at the end of this appendix. All devices in this thesis were fabricated in the Quantum-Nano Fabrication and Characterization Facility (QNFCF) at the University of Waterloo.

B.1 Sample cleaning

This is the first step of any device's fabrication and is important in removing any debris leftover from cleaving of the wafer.

1. Sonicate cleaved wafer for 5 min in Acetone followed by a 5 minute sonication in IPA. *The Acetone helps remove any potential organics left on the wafer. The IPA is more viscuous helps remove any dust left on the sample from the cleaving. Good cleaning is critical for nice adhesion of the photoresist for the lithography steps*

2. Do a 30 s Buffered Oxide Etch (BOE, 1:10 HF:NH_4F by volume) followed by a several minute rinse in H_2O. *There is a thin native oxide layer on the sample that needs to be removed to help adhesion of photoresist.*

B.2 Mesa pattern

This is typically the second step of any device's fabrication.

1. Spin a PMMA A6/ma-N bilayer of resist. *Keep sample covered at all times to prevent dust or other particles from landing on it, even while baking.*

   (a) Pre-bake the sample for 1 min at 120 °C. *Helps remove any layer of moisture on the sample before spinning the first layer of resist. Be careful not to do hotter or longer of a pre-bake as you risk re-forming an oxide layer that will prevent the PMMA from adhering well to the substrate.*

   (b) While **hot**, spin PMMA A6 at 5000 rpm for 60 s, 1000 rpm/s up-ramp and 1000rpm/s down-ramp. *Be as quick and careful as possible when moving the sample from the hot plate to the spinner before it cools. This will help with adhesion of the PMMA to the GaAs cap layer.*

   (c) Bake PMMA for 5 mins at 180 °C.

   (d) While **warm**, spin ma-N at 5000 rpm for 60 s, 1000 rpm/s up-ramp and 1000rpm/s down-ramp.

   (e) Bake ma-N for 90 s at 120 °C.

2. Expose mesa pattern using photolithography. *At QNFCF we use either a SUSS MA6 aligner or a MLA150 Direct Write UV Lithography system for the exposure.*

3. Develop in maD-5335 for 2 mins followed by at least 1 min in H_2O. *We found placing the sample at the bottom of the beaker during development improves results. This eliminates any movement you may introduce which can cause jagged edges and delamination of the two resist layers.*

4. Do a 10 minute plasma ash of the sample. *This is to remove the PMMA from the regions we developed the ma-N. Approximately 5 mins is spent removing the PMMA, and the remaining 5 mins are for forming the undercut.*

5. Reflow bake the sample at 150 °C for 5 mins. *Helps with adhesion of the PMMA to the substrate before we do an etch.*

6. Etch the mesa pattern

   (a) Use a profilometer to measure the resist height.

(b) Dip sample in BOE for ∼15 s and a 1 min dip in H_2O. *This removes any oxide formed from the ashing*

(c) Dip sample in a 1:8:120 solution of H_2SO_4:H_2O_2:H_2O (∼60−80 seconds). Use the Dektak to see how much you have etched. *While we aim for 350 nm, the exact depth does not matter, but you* ***must*** *go past the AlGaAs/GaAs interface (∼310 nm deep). The typical etch rate is between* $3.5 - 5.5$ *nm/s.*

7. Strip the resist by submerging in Acetone or hot Remover PG and sonicating for 5−7 mins. *The sample can be sonicated freely because there is no metal deposited yet.*

8. Measure the sample using a profilometer to find the actual etched height. Confirm using an optical microscope that the mesa pattern is sharp and clean.

B.3 n-type ohmic contacts

1. Mix a solution of 1:1:9 H_2O_2:HCl:H_2O **the night before** doing the ohmic recess etch. *The etch solution is left overnight is to yield a solution with a stable etch rate. When the solution is first mixed, the etch rate decays rapidly for the first few hours until it equilibrates.*

2. Spin a S1811 layer on the main sample, and spin a diluted S1805 layer on an extra sample piece to calibrate the etch rate.

   (a) Pre-bake each sample for 1 min at 120 °C.

   (b) While **warm**, spin resist on each sample at 5000 rpm for 60 s and 1000 rpm/s ramp speed with a ramp down rate of 1000 rpm/s.

   (c) Bake for 90 s at 120 °C.

3. Expose the ohmic pattern using photolithography. *If the exposure is done using a photomask, the alignment distance should be decreased all the way before exposure. This prevents rotation from resist beads that form at at the corners of the wafer during spinning. These act as pivot points when the mask comes into contact with the wafer for exposure.*

4. Develop in MF-319 for 45 s and rinse in H_2O. *Mildly agitate, just enough to get the developed Shipley off of the patterned area.*

5. Do a brief 10 s plasma ash to ensure all resist is removed.

6. Bake sample at 150 °C for 5 mins to reflow the resist and improve adhesion.

7. Etch the ohmic pattern

   (a) Use a profilometer to measure the test etch sample and obtain the resist height. *The diluted Shipley here is thinner so that the measured height is more accurate than it would be for regular S1805.*

   (b) Dip the test etch sample in BOE for 15 s.

   (c) Dip test etch sample in H_2O_2:HCl:H_2O etching solution prepared the night before for ∼70−80 s (record the exact time).

   (d) Use a profilometer to measure the test etch sample again to calibrate the etch rate. Use this rate to calculate how much time it takes to etch to 350 nm. Typical etch rates are ∼5 nm/s.

   (e) Dip the main sample in BOE for 10 s.

   (f) Dip main sample in H_2O_2:HCl:H_2O etching solution for the appropriate amount of time to obtain ∼350 nm deep recess using rate from test etch sample in GaAs/AlGaAs heterostructures.

8. Do a 4 min plasma ash to etch the photoresist on the sample. *The goal is to remove as much of the resist overhang made during the wet etch as possible. This will allow us to deposit ohmic material as high up on the wall of our ohmic etch region as possible, making a more reliable and consistent contact to the AlGaAs/GaAs interface where we want to induce the 2DEG. Without this etching step, we would not deposit any material on the wall and would have to rely on the diffusion of the metal up towards the interface during the ohmic anneal step. The precise amount of ashing time should be calibrated beforehand as resist age and the particulars of the ashing equipment will impact the precise time.*

9. Dip sample in BOE for 10 s. *We want to make sure there is absolutely* ***no*** *oxide between the ohmic and the heterojunction where the 2DEG is formed.*

10. Deposit 10/250/120 nm of Ni/Au+Ge/Ni (0.5/2.0/1.5 Å/s deposition rates). A Rotatilt is used to deposit the metal at an angle of 45° or 60 ° for a deep (310 nm) or shallow (90 nm) deep single heterojunction respectively. The first layer of Ni helps catalyze the reaction that causes the Ge to diffuse into the GaAs substrate to form a conductive channel to the 2DEG. The Au+Ge layer has a 88:12 ratio by weight percentage. The cap layer of Ni helps smooth the ohmics after the annealing step. For all layers, use a small beam amplitude to focus the beam and reduce the

power required for deposition. *At QNFCF the deposition is done with an INTLVAC Nanochrome II e-beam deposition.*

11. After deposition, place sample in Remover PG and perform metal liftoff. *Either let it sit overnight at room temperature or place it on a hot plate at 100 °C for one hour. Use the spray bottle of acetone to remove any metal pieces clinging to the sample surface.*

12. Anneal the ohmics using the rapid thermal annealer (RTA). The anneal consists of a several minute purge with N_2 gas and heats the sample in Ar at 450 °C for 3 mins.

B.4 p-type ohmic contacts

1. Mix a solution of 1:1:20 H_2O_2:H_3PO_4:H_2O **the night before** doing the ohmic recess etch. *The etch solution is left overnight is to yield a solution with a stable etch rate. When the solution is first mixed, the etch rate decays rapidly for the first few hours until it equilibrates.*

2. Spin a S1811 layer on the main sample, and spin a diluted S1805 layer on an extra sample piece to calibrate the etch rate.

   (a) Pre-bake each sample for 1 min at 120°C.

   (b) Spin resist on each sample at 5000 rpm for 60 s and 1000 rpm/s ramp speed with a ramp down rate of 1000 rpm/s.

   (c) Bake for 90 s at 120 °C.

3. Expose the ohmic pattern using photolithography.

4. Develop in MF-319 for 45 s and rinse in H_2O.

5. Do a brief 10 s plasma ash to ensure all resist is removed.

6. Bake sample at 150 °C for 5 mins to reflow the resist and improve adhesion.

7. Etch the ohmic pattern.

   (a) Use a profilometer to measure the test etch sample and obtain the resist height. *The diluted Shipley here is thinner so that the measured height is more accurate than it would be for undiluted S1805.*

(b) Dip the test etch sample in BOE for 15 s.

(c) Dip test etch sample in H_2O_2:H_3PO_4:H_2O etching solution prepared the night before for ∼70−80 s (record the exact time).

(d) Use a profilometer to measure the test etch sample again to calibrate the etch rate. Use this rate to calculate how much time it takes to etch to 350 nm. Typical etch rates are ∼5 nm/s.

(e) Dip the main sample in BOE for 10 s.

(f) Dip main sample in H_2O_2:H_3PO_4:H_2O etching solution for the appropriate amount of time to obtain ∼290 nm deep recess using rate from test etch sample in GaAs/AlGaAs heterostructures.

8. Do a 4 min plasma ash to etch the photoresist on the sample. *The goal is to remove as much of the resist overhang made during the wet etch as possible. This will allow us to deposit ohmic material as high up on the wall of our ohmic etch region as possible, making a more reliable and consistent contact to the AlGaAs/GaAs interface where we want to induce the 2DHG. Without this etching step, we would not deposit any material on the wall and would have to rely on the diffusion of the metal up towards the interface during the ohmic anneal step. The precise amount of ashing time should be calibrated beforehand as resist age and the particulars of the ashing equipment will impact the precise time.*

9. Dip sample in BOE for 10 s. *We want to make sure there is absolutely* ***no*** *oxide between the ohmic and the heterojunction where the 2DHG is formed.*

10. Deposit 160−200nm of Au+Be alloy onto the sample using a slug weighing 1200-1600 mg in a thermal evaporator at an angle of 45° or 60 ° for a deep (310 nm) or shallow (90 nm) single heterojunction respectively. *At QNFCF the deposition is done using an Angstrom Engineering Amod Thermal Evaporator.*

11. After deposition, place sample in Remover PG and perform metal liftoff. *Either let it sit overnight at room temperature or place it on a hot plate at 100 °C for one hour. Use the spray bottle of acetone to remove any metal pieces clinging to the sample surface.*

12. Cap the ohmics with 1 μm of SiO_2 using PECVD to prevent contamination of the rapid thermal annealer (RTA) in the subsequent annealing step.

13. Anneal the ohmics using the RTA. The anneal consists of a several minute purge with N_2 gas and heats the sample in Ar at 520 °C for 3 mins.

B.5 Oxide insulator and etching via holes

1. Deposit 300 nm of SiO_2 via PECVD. *Make sure to clean and condition the chamber prior to deposition even if the previously run process was the same.*

2. Spin a S1811 layer on the sample.

   (a) Pre-bake the sample for 1 min at 120 °C.

   (b) Spin resist on each sample at 5000 rpm for 60 s and 1000 rpm/s ramp speed with a ramp down rate of 1000 rpm/s.

   (c) Bake for 90 s at 120 °C.

3. Pattern the vias using photolithography.

4. Develop in MF-319 for 45 s and rinse in H_2O.

5. Do a brief 10 s plasma ash to ensure all resist is removed.

6. Dip in BOE for 3 mins. *Check under a microscope to make sure you have removed all the oxide in the via areas.*

7. Place the sample in Remover PG and heat to 100 °C for 10 mins. Treat the resist removal as a regular metal liftoff. Dry the sample with N_2. *We have found that the BOE forms a thin hardened layer of resist during the etching which needs to be removed like a layer of metal when the resist is stripped. If you don't, then the resist layer will fall down onto your sample and can delaminate or flake onto your sample.*

B.6 Top gate and bond pads

1. Spin a PMGI/S1811 bilayer.

   (a) Pre-bake the sample for 1 min at 120 °C.

   (b) While **hot**, spin PMGI: 5000 rpm for 60 s and 1000 rpm/s ramp with a ramp down rate of 1000 rpm/s.

   (c) Bake PMGI for 5 mins at 180 °C.

   (d) While **warm**, spin S1811: 5000 rpm for 60 s and 1000 rpm/s ramp with a ramp down rate of 1000 rpm/s.

(e) Bake S1811 for 90 s at 120 °C.

2. Pattern the top gate and bond pads using photolithography.

3. Develop in MF-319 for 2.5 mins and rinse in H_2O. *Do not hold the sample during the development step. Simply place the sample in the beaker and step away for the development time. We found that holding the sample during the development can cause the MF-319 to get in between the resist layer and mess up the pattern profile.*

4. Look at the device under the microscope to see if there is a noticeable undercut ($1-2$ μm). If there is, proceed to the next step. If not, then develop in MF-319 for another 30 seconds and check again. Repeat this until there is a proper undercut.

5. Ash for 10 seconds to remove any resist residue (recipe 5).

6. Dip in 1:4 HCl:H_2O to remove any oxide from ashing. *Do **not** do a BOE dip like you normally would before the deposition. The SiO_2 there will etch away if you do a BOE dip.*

7. Deposit 20/80 nm of Ti/Au (0.5/2.0 Å/s deposition rate). *At QNFCF the deposition is done with an INTLVAC Nanochrome II e-beam deposition.*

8. Place in Remover PG for liftoff. *Either leave overnight or heat at 100 °C for one hour.*

B.7 Electron beam lithography and metal deposition

1. Spin a PMMA A6 monolayer.
   (a) Pre-bake the sample for 1 min at 120 °C.
   (b) While **hot**, spin PMMA: 5000 rpm for 60 s and 1000 rpm/s ramp with a ramp down rate of 1000 rpm/s.
   (c) Bake PMMA for 15 mins at 180 °C.

2. Expose the fine gate pattern using electron beam lithography. *At QNFCF we use the JEOL JBX-6300FS Electron Beam Lithography System with a 100 kV electron beam.*

3. Develop in IPA:H_20 with a ratio of 7:3 by volume for 60 s. Rinse in H_2O for 30 s. *Stir the sample throughout development to ensure all the resist gets developed and removed.*

4. Deposit 10/10 nm of Ti/Au (0.5/0.5 Å/s deposition rate). *At QNFCF the deposition is done with an INTLVAC Nanochrome II e-beam deposition. Notice that we did not do a plasma ash or acid dip right the deposition. The undercut from EBL is very small and ashing or etching, even briefly, can etch enough resist away so that the undercut no longer ensures good liftoff.*

5. Place in Remover PG for liftoff. Either leave at room temperature overnight or heat it at 80 °C for a few hours.

6. Use a small glass pipette to blow the metal off of the sample. Aggressively blow on the sample to remove all of the metal. *When you are done, there should be no loss pieces of metal clinging to the sample. Look around the wafer to see any small bits of flakes left over on the sample.*

7. Place the sample in another beaker of hot Remover PG and blow again with the pipette for a few minutes. *The second beaker of Remover PG helps remove any resist residue and the extra pipetting helps ensure all flakes are knocked off.*

8. Place sample in a beaker and spray the sample with IPA to remove the Remover PG.

9. Spray now with Acetone to remove all of the IPA on the sample. *Feel free to hold the spray bottle far away from the sample in order to make the Acetone stream "rough" to do a very gentle sonication of the sample.*

10. Do a final spray with IPA to remove the Acetone.

11. Completely dry with N_2 gas.

12. Check under the optical microscope to ensure that there are no big metal pieces left on the sample and that there are no residue marks from missed IPA during drying.

13. If some metal is leftover, then you can place the sample back in hot Remover PG and repeat steps 6−10.

14. If the metal continues to cling, then use a paintbrush to knock off the unwanted metal. *Avoid doing this if you can as fine EBL gates are more sensitive to the paint brush than features done with regular photolithography. If you do need to use a paintbrush, make sure to use a real hair paint brush as a faux hair brush can potentially damage the surface. Take caution and avoid doing this with overlapping metal gates as you may puncture the oxide between metal layers creating a short; however, it is definitely possible to do so without causing shorting.*